Synthesis of Bismuth-based Nanocomposites for Photocatalytic Degradation of Pollutants

Thesis submitted for the award of degree of

Doctor of Philosophy

Submitted by

Aashna

Roll No. 901809012

Under the guidance of

Dr. Soumen Basu

Professor

School of Chemistry and Biochemistry

Thapar Institute of Engineering & Technology

Patiala-147004

2022

Certificate

This is to certify that thesis entitled "**Synthesis of Bismuth-based Nanocomposites for Photocatalytic Degradation of Pollutants**", is being submitted by Ms. Aashna in fulfillment of the requirement for the award of the Degree of Doctor of Philosophy in the School of Chemistry and Biochemistry, Thapar Institute of Engineering and Technology, Patiala, is a record of candidate's own independent and original research work carried out by her under my supervision and guidance. The matter presented in the thesis has not been submitted in part or full for the award of any degree in any other University or Institute.

(Supervisor)

Dr. Soumen Basu
Professor
School of Chemistry and Biochemistry
Thapar Institute of Engineering and Technology
Patiala-147004, Punjab, India

(Head) 26/12/2022

Prof. Satnam Singh
Professor
School of Chemistry and Biochemistry
Thapar Institute of Engineering and Technology
Patiala-147004, Punjab, India.

Candidate's Declaration

I, hereby declare that the present work in the thesis entitled **"Synthesis of Bismuth-based Nanocomposites for Photocatalytic Degradation of Pollutants"**, in the fulfillment of the requirement for the award of the Degree of Doctor of Philosophy in the School of Chemistry and Biochemistry, Thapar Institute of Engineering and Technology, Patiala is an authentic record of my work carried out under the supervision of Dr. Soumen Basu, Professor, School of Chemistry and Biochemistry, Thapar Institute of Engineering and Technology, Patiala, India. The matter embodied in the thesis has not been submitted in part or fully to any other University or Institute for the reward of any degree in India or Abroad.

Aashna

.....

Aashna

Acknowledgements

कर्मण्येवाधिकारस्ते मा फलेषु कदाचन ।

मा कर्मफलहेतुर्भुर्मा ते संगोऽस्त्वकर्मणि ॥

May we all acknowledge the God within us

Through this section, I would like to acknowledge every individual who has been part of this incredible journey both in life and work.

First and foremost, I want to express sincere gratitude to my supervisor, **Dr. Soumen Basu** for giving me the opportunity to work on this project and for his constant support and guidance throughout my Ph.D. I take this opportunity to thank him for always motivating me to do better in life.

I am thankful to Prof. Prakash Gopalan, Director, and Prof. Rafat Siddique, Dean of Research & Sponsored Projects, Thapar Institute of Engineering and Technology, Patiala. My sincere gratitude to **Prof. Satnam Singh**, Professor and Head, School of Chemistry and Biochemistry, Thapar Institute of Engineering and Technology, Patiala, for his ever-helping attitude and best wishes. I would also like to thank my doctoral committee members, **Prof. Satnam Singh, Prof. Bonamali Pal, Prof. Puneet Sharma**, for the scientific discussions and valuable suggestions that have always been very helpful. I also want to acknowledge all the faculty members in the School of Chemistry and Biochemistry for their cooperation and support. I express my sincere gratitude to **Mr. Mayank Sharma** for his constant official help and cooperation. I also want to thank Mr. Chander Thakur, Mr. Hemant Sharma, Mr. Vishwanath, Mr. Shekhar for their support.

I want to thank everyone who helped with instrumentation facilities; SAI Labs, TIET

Patiala; ACIRD, TIET, Patiala; Sprint testing solutions, Mumbai; CIL, PU, Chandigarh; CeNS Bangalore; and IIT Roorkee. I also want to thank Prof. Bonamali Pal for the DRS instrument.

A special thanks to Mr. Davis Bansal for the constant motivation and support. Finally, I want to thank my friends, Ms. Khyati, Ms. Nidhi, Ms. Divya, Ms. Sonam, Ms. Riya, Ms. Tanvi, Mr. Kunal, Mr. Abhinav, Mr. Gautam, Mr. Alok, Mr. Shubham, Mr. Suveer, Dr. Shaurya, Mr. Mohit, Mr. Ayush, and Mr. Gagandeep for making this journey fun and easy.

I want to thank my Ph.D. mates, firstly, Ms. Surbhi for her constant support and help; Ms. Anushka Garg, Dr. Divya Monga, and Mr. Zaid bin Siddique for their friendship and for acting as my counselors in all my problems; Ms. Aayushi for our hostel parties; Ms. Neeraj for always making me laugh; Ms. Shelly for helping me when I needed the most; Dr. Shagun for the delicious food; Ms. Rekha Thakur for taking care of me; Ms. Pooja for rescuing me from problems; Ms. Rohini for her smiling nature; Ms. Meenakshi, Ms. Priyanka, Ms. Aastha for just being there.

Lastly, I want to thank my family members, my grandmothers, my nani and dadi; my mother, Dr. Darshna Nagar; my father, Mr. Vinod Nagar; my brother, Mr. Ashutosh Nagar; my bhabhi, Ms. Leena Nagar, my mama, Mr. N.P. Singh; my mami, Mrs. Sunita Singh; my sister, Ms. Parul Singh for always keeping faith in me and for loving me unconditionally. I am here because of them.

This thesis is dedicated to my mother, Dr. Darshna Nagar.

Table of Contents

CHAPTER 2

Fabrication of 3D porous peony flower-like β-Bi_2O_3/BiOCl heterostructure for synergistically boosting the visible-light-driven degradation of organic pollutants

CHAPTER 3

Deciphering the Role of β-phase Bi_2O_3 Nanorods incorporated on g-C_3N_4 Nanosheets for Efficient Pollutant Removal

CHAPTER 5

Novel tablet-like Bi_3TaO_7/BiOCl 2D-2D heterostructure with heightened charge segregation for Visible-light-driven photocatalytic pollutants degradation

CHAPTER 6

Fabrication of carnation flower-like Bi_3TaO_7/Ag/$BiVO_4$ ternary photocatalyst for boosting pollutants degradation under visible light

List of Figures

Chapter 4

Chapter 5

List of Schemes

Chapter 5

Chapter 6

List of Tables

Chapter 4

Chapter 5

Chapter 6

Conclusions and future perspectives

List of Abbreviations

AO II	Azo Orange II
AOP	Advanced Oxidation Process
AB10B	Amido Black 10B
AMX	Amoxycillin
BET	Brunauer-Emmett-Teller
BJH	Barrett-Joyner-Halenda
COD	Chemical oxygen demand
CIP	Ciprofloxacin
Conc.	Concentration
CB	Conduction Band
DMSO	Dimethyl Sulfoxide
DRS	Diffuse reflectance spectroscopy
EDS	Energy dispersive X-ray spectroscopy
EDC	Endocrine-Disrupting Compounds
FIP	Fipronil
FESEM	Field emission scanning electron microscopy
HRTEM	High resolution transmission electron microscopy
IC	Imidacloprid
JCPDS	Joint committee on powder diffraction standards

MB	Methylene blue
MO	Methyl Orange
NO	Nitrogen Oxide
PNP	p-Nitrophenol
PEG	Polyethylene glycol
PL	Photoluminescence
ppm	Parts per million
pzc	Point of zero charge
RB	Reactive Bordeaux
RB 5	Reactive Black-5
CR	Congo Red
CP	Chlorpyriphos
BG	Brilliant Green
EMC	Erythomycin
RhB	Rhodamine-B
TC	Tetracycline
1,4-TPA	1,4-terephthalic acid
TC HCl	Tetracycline Hydrochloride
TOC	Total Organic Carbon
UV-Vis	Ultraviolet-visible
VB	Valence Band
XPS	X-ray photoelectron spectroscopy
XRD	X-ray diffraction
YT	Yellow Tetrazine

List of Symbols

%	Percentage
%wt	Weight Percentage
%D	Percentage degradation or degradation efficiency
A_t	Absorbance of pollutant at a certain time
S_{BET}	BET surface area, m^2/g
C_t	Concentration of pollutant at a certain time
cm^3/g	Centimeter cube per gram
Kα, Kβ	Characteristic X-rays
^{o}	Degree
^oC	Degree Celsius
$^oC/min$	Degree Celsius per minute
e^-	Electrons
E_c	Energy of the free-electron of hydrogen
E_g	Band gap energy
eV	Electron volt
a	Ferrous ammonium sulfate (FAS) used for the titration of the blank sample in mL
b	Ferrous ammonium sulfate (FAS) used for the titration of the sample in mL

g	Gram
g/L	Gram per litre
>	Greater than
h	Planck constant
h	Hour
h^+	Holes
$\bullet OH$	Hydroxide radical
H	Hysteresis Loop
A_0	Initial absorbance of pollutant
C_0	Initial concentration of pollutant
kV	Kilo-volt
K	Kelvin
M	Molar
mg	Milligram
mg/L	Milligram per litre
mL	Millilitre
mM	Millimolar
mW/cm^2	Milliwatt per square centimeter
μg/L	Microgram per litre
m^2/g	Meter square per gram
nm	Nanometer
ng/L	Nanogram per litre
N	Normality of FAS (0.1 N)
n	Optical transition type of semiconductors

O_2	Oxygen
k	Pseudo-first order rate constant min^{-1}
E_{CB}	Position of the conduction band
E_{VB}	Position of the valence band
A	Proportionality constant
R^2	Regression coefficient
X	Semiconductor's absolute electronegativity
$O_2^{\bullet-}$	Superoxide radicals
t	Time, min
V	Total pore volume, cm^3/g
W	Watt
W/m^2	Watt per square meter
α	Absorption coefficient
λ	Wavelength
θ	Theta
ν	Light frequency
α, β, γ	Phases of Bi_2O_3

Abstracts

Chapter 1

This chapter provides a brief introduction to hazardous pollutants and advanced oxidation processes such as semiconductor photocatalysis in the removal of pollutants from toxic water. The mechanism for photocatalysis has also been illustrated and explained in detail. This section emphasizes the historical background and the need for bismuth nanocomposites with different fabrication techniques such as the hydrothermal process and co-precipitation process. Various applications for bismuth compounds have also been discussed. Moreover, the significance and need for bismuth-based heterostructures for overcoming the recombination rate of charge carriers and enhancing photocatalytic performance have been explained. Finally, a tabulated literature study has also been provided for bismuth-related composites for pollutant degradation.

Chapter 2

This chapter presents the fabrication of a flower-like β-Bi_2O_3/BiOCl binary composite via the in-situ precipitation method. Different characterizations such as XRD, XPS, HRTEM, elemental mapping, FESEM with EDS, UV-vis DRS, and PL were conducted, indicating a crystalline flower-like nanostructure with a narrow bandgap (2.25 eV) energy, and low recombination tendency. The BET N_2 adsorption-desorption analysis showed a large surface area (78 m^2/g) along with a mesoporous structure (42.98 nm). The photocatalyst degraded a model dye, methylene blue (MB), and a model insecticide, fipronil (FIP) having ~93% and ~79% degradation efficiency at lofty rate constants ($k = 0.05883\ min^{-1}$ *and* $0.01481\ min^{-1}$ for MB and FIP, respectively). The enhanced photodegradation was attributed to the β-

Bi_2O_3/BiOCl heterojunction promoting the charge carrier segregation. The variation in pH and catalyst concentrations showed degradation efficiency of 93.27% for MB and 79.96% for FIP at pH 8 and 4, respectively, with 0.13 g/L catalyst concentration. The scavenging experiments disclosed the prominent role enacted by $O_2^{\bullet-}$ (superoxide radical) and h^+ (holes) in toxin degradation. The stability of the binary composite was affirmed by the reusability test performed for 4 repetitive cycles and the degradation efficiency was found to be 79.95% for MB and 69.82% for FIP. XRD scrutiny proved its solidity/intact structure after degradation reaction. The as-synthesized catalyst offers a promising binary photocatalyst with a viable design and elevated visible light efficiency for noxious waste removal.

Chapter 3

This chapter discusses the fabrication of β-Bi_2O_3/g-C_3N_4 nanosheets through the in-situ precipitation process. The photocatalysts were studied via XPS, HRTEM, FESEM-EDS, XRD, UV-vis DRS, elemental mapping, and PL analysis. A flaky nanosheets-like structure having a small bandgap (2.02 eV) and less recombination capacity was procured. A mesoporous structure (25.59 nm) with an immense surface area (63 m^2/g) was acquired via the BET N_2 adsorption-desorption technique. The 1:3 β-Bi_2O_3/g-C_3N_4 composite photodegraded fipronil (FIP) and methylene blue (MB) with ~75% and ~97% efficacy ($k = 0.01068\ min^{-1}$ and $0.04066\ min^{-1}$ for FIP and MB, respectively). The results were accredited to the heterojunction between Bi_2O_3 nanorods and g-C_3N_4 nanosheets. The pH, and catalyst concentration studies displayed the maximum efficiency of 97.54% for MB at pH 8 and 74.28% for FIP at pH 4 via a catalyst dose of 0.06 g/L. The scavengers unveiled the involvement of hydroxide radical ($^{\bullet}OH$) in the degradation process. The stability of the composite was tested for four repetitive cycles with 88.99% degradation efficiency for MB, and 71.84% efficiency for FIP with XRD analysis

scrutinizing the structural intactness of the composite. The nanoflake-like composite caters to a competent photocatalyst useful for toxicant removal.

Chapter 4

This chapter elaborates on the designing of a ternary g-C_3N_4/Ag/$BiVO_4$ photocatalyst where Ag nanoparticles act as electron shuttle and Ag/$BiVO_4$ have been fixated on the surface of g-C_3N_4. To study the catalyst, XRD, HRTEM, FESEM along with EDS, elemental mapping, PL, and UV-vis DRS were performed, suggesting crystalline plate-like nanostructures with a low bandgap energy (2.41eV) and recombination rate. The surface area analysis via BET N_2 adsorption-desorption validated a high surface area (~6.68 m^2/g) for the composite comprising mesopores (46.13 nm). The photocatalyst degraded methylene blue (MB), a model dye, and fipronil (FIP), a model colorless insecticide with ~94% and ~74% efficiency at elevated rate constants ($k = 0.083\ min^{-1}$ *and* $0.0167\ min^{-1}$ for MB and FIP, respectively). The heightened activity of the ternary composite was owed to greater electron-hole charge separation and the presence of hetero-junctions while maintaining enough redox properties. The pH and catalyst concentrations were varied and examined, and 94.57% and 72.56% efficiency for MB and FIP at pH 8 and 4 with catalyst concentrations of 0.13 and 0.06 g/L, respectively were found to be optimum. The trapping experiments revealed the eloquent role played by $^{\bullet}OH$ (hydroxyl radical), $O_2^{\bullet-}$ (superoxide radical), and h^+ (holes) in pollutant degradation. To affirm the stability of the ternary composite, a reusability test was performed for 4 successive cycles and the degradation efficiency was found to be 89.85% for MB and 69.87% for FIP. XRD analysis explicated its stability after photodegradation. The ternary composite can be considered a promising photocatalyst owing to its feasible design and efficiency in visible light for toxin deposition.

Chapter 5

This chapter presents a tablet-like Bi_3TaO_7/BiOCl with varying proportions by in-situ precipitation, investigated via characterization techniques such as XRD, HRTEM, FESEM along with EDS, elemental mapping, PL, and UV-vis DRS. The 1:1 Bi_3TaO_7/BiOCl (74 m^2/g) degraded tetracycline (TC) and methylene blue (MB) with ~90% and ~99% degradation efficiency, respectively ($k = 0.02541\ min^{-1}$ *and* $0.05622\ min^{-1}$ for TC and MB, respectively). The pH and pzc studies suggested the maximum removal for MB (99.6%) and TC (90.22%) in the basic and acidic range, respectively, with 0.13 g/L, indicating the electrostatic interaction between the catalyst and pollutants. The feed concentration studies indicated a decrease in efficiency, suggesting a reduced number of active sites. COD studies displayed the high efficiency of the composite in removing organic pollutants. The stability of the composite was confirmed through the reusability studies and the degradation efficiencies were found to be 92.46% for MB and 86.59% for TC with XRD analysis supporting its intactness. The scavenging experiments explored the mechanism indicating the role of $^{\bullet}OH$ and $O_2^{\bullet-}$ in the degradation process. The work provides a novel technique to synthesize Bi_3TaO_7/BiOCl with possible efficiency in pollutant removal.

Chapter 6

This chapter presents Bi_3TaO_7/Ag/$BiVO_4$ nanoflower-like ternary photocatalysts with varying proportions (1:1, 1:3, and 3:1) of Bi_3TaO_7 and $BiVO_4$/Ag by a simple hydrothermal technique. The catalysts were well investigated using XRD, HRTEM, XPS, UV-vis DRS, FESEM-EDS, PL analysis, and elemental mapping. A carnation flower-like composite with a bandgap of 2.1 eV and low reconciliation tendency was obtained. The composite was found to be mesoporous (20.38 nm), comprising an enormous area of 88 m^2/g procured using the BET

N_2 adsorption-desorption analysis. The composite (1:1) degraded tetracycline (TC), and methylene blue (MB) with ~92% and ~99% efficiency, respectively ($k = 0.02128\ min^{-1}$ and $0.05439\ min^{-1}$ for TC and MB, respectively) under visible light. The results were attributed toan Ag-mediated electron shuttle formed between the 2D-2D semiconductors Bi_3TaO_7 and $BiVO_4$, which facilitates visible-light absorption at a longer wavelength and promotes charge carrier separation. Catalyst concentration and pH analysis showed the optimum efficacy at pH9 for MB (99.85%) and pH 3 for TC (92.94%) with 0.06 g/L catalyst concentration. $^{\bullet}OH$, and $O2^{\bullet-}$ were involved in the degradation activity confirmed by scavenger studies. The stability of $Bi_3TaO_7/Ag/BiVO_4$ nanoflower was investigated repetitively for 4 consecutive cycles and the degradation efficiency for MB and TC was found to be 90.99% and 88.84%, respectively.The XRD pattern validated the composite's intactness after the catalysis reaction. COD studiesdisplayed the high efficiency of the composite in removing organic pollutants. The current study furnishes a novel technique to fabricate Ag-mediated $Bi_3TaO_7/BiVO_4$ heterostructure, which perhaps is a plausible visible-light active catalyst for any toxin removal.

Chapter 1

Introduction and literature

1.1 Introduction to Nanoscience and Nanotechnology

Nanoscience and nanotechnology are the most current topics bringing a revolution in different areas of science and technology. The major reason leading this advancement in science is based on the fact that the materials at the nanoscale have optical, mechanical, electrical, chemical, and physical properties different than their corresponding bulk parts. Through nanoscience and technology, it is feasible to create products, materials, and devices in the 1-100 nm scale range.[1]

1.2 Bismuth

Bismuth (Bi) exists as a diamagnetic element in nature having an atomic number of 83. It is a transition metal in the pentavalent state with its oxide ores used as commercial ores. It possesses less thermal conductivity and elevated electrical conductivity, and Hall coefficient. The deposition of bismuth on the material's surface makes it act like a semiconductor.[2] Moreover, it is found to be heavier in its liquid state than its solid state, enabling expansion of 3% upon solidification. The property facilitates bismuth in forming alloys compensating for the reduction in the rest of the constituents of the alloy.[2] Also, it is free of toxicity and has a low melting point of 271 ˚C. About 63% of bismuth is utilized in cosmetics, pigments, and the pharmaceutical industry, 26% in metallurgy for casting and galvanizing, 7% in bismuth alloys, ammunition, and solders, and 4% in research areas.[3]

Bismuth has always been known since the middle-ages. It was first described by a German monk Basil Valentine in 1450. But in the 18th century, bismuth was misunderstood for tin and lead owing to their alike properties. It derived its name from German with its meaning related to possessing antimony's properties (weisse masse or wismuth which means "white mass") which were eventually restated in the 16th century into the Latin word "bisemutum". It was not until 1753 that bismuth was discovered as a separate element by Claude Geoffroy and had secured its position in the top ten elements discovered and classified. It occurs in an uncombined state with other elements forming indistinct crystals.[19]

1.3 Bismuth-Based Nanoparticles

Nanoparticles are particulate substances in the nano range. Owing to their minute size, nanoparticles illustrate typical structural and electronic properties.[4] The utilization of bismuth-based nanoparticles rather than traditional bulk materials in various technological fields has gained widespread attention.[5] The nanoparticles possess unique properties such as high electrical, optical, thermal, magnetic, and photocatalytic properties depending on the particle's minute size and huge surface area.[6] Such bismuth-based nanomaterials can be fabricated through colloidal chemistry where bismuth salts are used as precursors along with reducing agents and surface modifiers for the synthesis of size-controlled-crystalline bismuth nanoparticles.

1.3.1 Bismuth Chalcogenides

Bismuth chalcogenides consist of a group of photoelectric compounds comprising group VI elements and bismuth, depicted as Bi_2E_3 (E = S, O, Te, Se). It mainly comprises bismuth

sulfide (Bi_2S_3), bismuth oxide (Bi_2O_3), bismuth telluride (Bi_2Te_3), and bismuth selenide (Bi_2Se_3).[7] Such catalysts are significant due to their special properties with applicability in industries. Current studies in the visible-light response of bismuth chalcogenides and their enhanced photocatalytic activity have gained widespread attention.

Bi_2O_3 is a p-type semiconductor having six crystallographic polymorphs depicted as β-, α, ω-, γ-, δ-, ε-Bi_2O_3. Generally, α-Bi_2O_3 (monoclinic phase) occurs at room temperature and when heated, converts to face-centered cubic δ-Bi_2O_3. Some other phases of Bi_2O_3 are orthorhombic ε-Bi_2O_3, body-centered cubic γ-Bi_2O_3, triclinic ω-Bi_2O_3, and tetragonal β-Bi_2O_3.[8] It has a refractive index, dielectric permittivity, narrow bandgap energy, and excellent photoconductivity.[9] Based on the method of fabrication, Bi_2O_3 is also said to have both p- and n-type conductivity making it an amphoteric semiconductor enabling it to be utilized as sensors, optical conductivity, electrochromic materials, and photocatalyst.[10]

1.3.2 Bismuth Vanadate

Bismuth vanadate ($BiVO_4$) has three phases: monoclinic scheelite, tetragonal scheelite, and tetragonal zircon. The monoclinic phase of $BiVO_4$ is responsive in visible light owing to its narrow bandgap (2.4 eV). The visible-light absorption has led to a massive investigation in the field of environmental protection through photocatalysis. Moreover, $BiVO_4$ is environmental-friendly, resistant to corrosion, cheap, and non-toxic.[28]

1.3.3 Bismuth Oxyhalides (BiOX)

BiOX (X= Br, I, Cl) comprise semiconductors in a layered structure, crystallized to obtain tetragonal matlockite form. To form the layered structure, one bismuth atom is

neighbored via four halogen atoms and oxygen atoms making an asymmetric tetrahedral symmetry i.e. X-Bi- O-Bi-X.[11] Such a structure makes it possible for BiOX to have optical, catalytic, electrical, and mechanical properties enabling the utilization of BiOX in water splitting, organic synthesis, gas purification, and organic pollutant photodegradation.[12]

Bismuth oxychloride (BiOCl) is a p-type semiconductor showcasing enhanced ionic conduction, electrical, catalytic, and optical properties. BiOCl comprises bismuth ions (Bi^{3+}), chloride ions (Cl^{-}), and oxygen ions (O^{2-}) constituting in a tetragonal layered form i.e. $[Cl\text{-}O\text{-}Bi\text{-}O\text{-}Cl]_n$. It has non-bonding interactions through the chlorine (Cl) atoms via C-axis. In the tetragonal pyramid structure, the four Bi-O and four Bi-Cl are paired contrary to each other with Bi in the center (**Fig. 1.1**). It is active in UV-light with 3.1-3.5 eV as an experimental bandgap and 2.8-2.9 eV as a theoretical bandgap.[13]

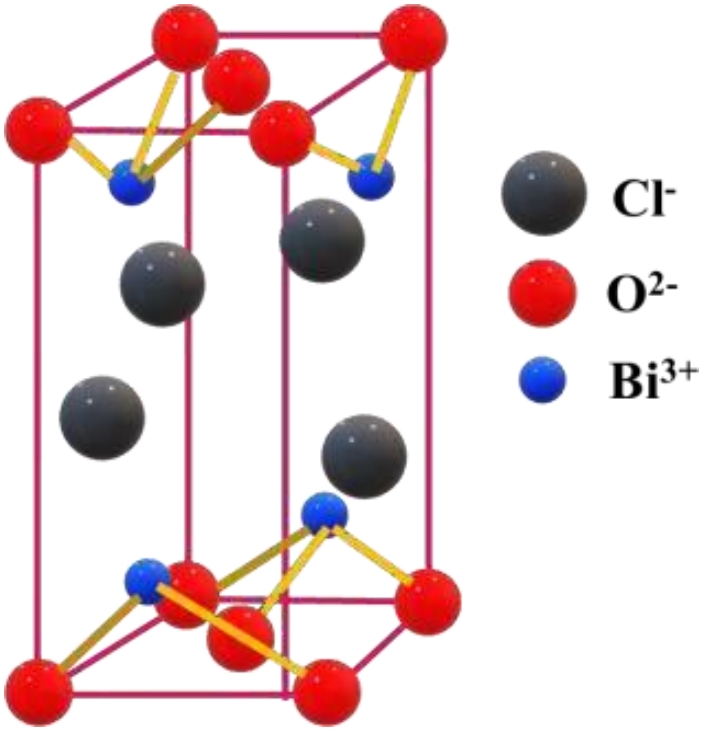

Fig. 1.1. Structure of bismuth oxychloride.

1.3.4 Bismuth Tantalate

Transition metal bismuth salts are the most significant photocatalyst owing to their response toward visible light. The potential of the conduction band (CB) of such catalysts is narrower than the hydrogen reduction position. The orbitals of the bismuth ions and oxygen ion orbitals in the catalyst's structure are susceptible to being hybridized onto the valence band (VB).[14] For bismuth tantalate (Bi_3TaO_7), the semiconductor's valence band and conduction band constitute O 2s and Bi 6s hybridization with the s-p hybridization resulting in minute masses of holes and electrons, facilitating propagation over wider distances.[15] Additionally, there is a hybridization of Bi_3TaO_7's valence band with the bismuth ion's 6s orbital and oxygen ion's 2s orbital leading to a stronger coupling state and therefore, an increase in the valence band energy level and a stronger negative tropism. The decrease in the semiconductor's bandgap makes it visible-light active. Therefore, transition metal bismuth salts display excellent potential for industrial application as visible-light-active photocatalysts.[16] Moreover, since tantalum's ionic radius, is analogous to tungsten ion's radius, therefore, tantalum's 5d orbital is greater as compared to titanate. This is owed to tantalum's peculiarity and a shared octahedral chain of tantalum-oxygen in the crystal structure. Therefore, bismuth tantalate displays good photocatalytic properties.[17]

1.4 Importance of Bismuth-Based Nanomaterials

Bismuth-based nanomaterials are promising materials owing to their visible-light responsive nature. Notably, bismuth-based materials' electronic properties consist of Bi's 6s orbital and O's 2p orbital in the valence band, thus, having a bandgap less than 3 eV. The diffused Bi 6s and O 2p orbitals cause appropriate dispersion of charge carriers, reducing materials' bandgap and thus, decreasing the recombination rate of charge carriers and

improving photocatalytic performance.[18] Therefore, several bismuth-based materials such as BiOX, $BiVO_4$, and Bi_2O_3 have been widely used for photocatalytic applications.

1.4.1 Properties of Bismuth-Based Nanomaterials

Bismuth is hard, lustrous, and brittle in nature. Due to the higher growth rate from the inside to the outer edges, its crystal grows in a strange, stair-shaped formation. It contains one of the lowest levels of thermal conductivity and higher density than its liquid state. Bismuth is utilizedto make allows due to its capacity to expand visibly and compensate for the shrinkage of otherelements in the alloy. It is silvery-white with a distinguished reddish tinge. Bismuth-based materials may have an iridescent tarnish. It is present in hydrothermal veins and pegmatites and its salts are often used as soothing agents for digestive disorders. Bismuth has lower electrical resistance than other metals apart from mercury, therefore, sometimes being called semi-mercury. These semi-metallic properties are applicable for thermoelectric material owing to low atomic mass, and high anisotropic Fermi surface with their capacity to cause semi-metal/semiconductor change with reduced size of crystallite, suitable for soft metals. Lead (Pb) is significant owing to its corrosion resistance property while bismuth (Bi) is important due to its thermoelectric property.[20]

1.4.2 Synthesis of Bismuth-based Nanomaterials

Fabrication of bismuth starts with the reduction or decomposition of a precursor. This results in the formation of nuclei which eventually develops into nanocrystals. The temperatureof the reaction needs to be maintained beyond the metal's melting point for the nanocrystals synthesized via the thermal decomposition method. The nanocrystals are in

liquid form in the entire fabrication step and to make the surface area minimum and therefore, to minimize the total interfacial free energy, the nanocrystals then adopt a spherical shape. By quenching the reaction, the solidification of the liquid nanocrystals to form nanospheres with smooth surfaces occurs.[20]

1.5 Fabrication Techniques

Recently, intensive research has been done in the field of nanomaterials to fabricate photocatalytic materials applicable for both energetic and environmental-related applications like organic pollutant degradation,[21] hydrogen evolution,[22] water disinfectant, and reduction of carbon dioxide to fuels.[23] Various bismuth-based materials, displaying exceptional photocatalytic performance for the degradation of pollutants owing to their morphological characteristic as compared to the surface areas have been designed via different techniques. Different techniques for the fabrication of bismuth nanoparticles have been published in the mid-1990s.[24] The bismuth nanoparticles are synthesized (**Table 1.1**) using laser ablation, high-energy ball milling, electro-hydrodynamic techniques, inverse micelles technique, vapor flow condensation, etc.[25]

Bismuth nanoparticles can be achieved from their bulk counterparts via thermal decomposition, but the method is not sufficient to produce enough yield.[26] While reductive methods to produce bismuth nanoparticles have also been studied. Different precursors of bismuth and reducing agents have been used to synthesize the different crystals of Bi such as the organometallic complex of Bi which is most widely used. Along with the compound's decomposition or salt precursor's reduction, the nanocrystals of low-melting-point metals like Bi can be synthesized via the direct breakage of molten metal's huge droplets by applying shear force. The fabrication of bismuth nanoparticles is split into two groups:

physical methods and chemical methods. Here we discuss only the chemical methods.

Table 1.1. Literature survey showing different bismuth-based nanomaterials and their applications.

Catalyst	**Synthesis Method**	**Application**	**Reference**
g-C_3N_4/$BiVO_4$	Electrodeposition	Photo-electrochemical activity	27
g-C_3N_4/$BiVO_4$	Hydrothermal	Photodecomposition of MO	28
C-$BiVO_4$/Bi_3TaO_7	Hydrothermal	Photodegradation of TC, AMX, CIP	29
Bi_2O_3/BiOCl	Solvothermal	Photodegradation of MO	30
β-Bi_2O_3/BiOCl	Co-precipitation	Photodegradation of RhB	31
Bi_2O_3/BiOCl	Chemical deposition	Photodegradation of MO	32
Bi_2O_3/g-C_3N_4	In-situ growth	Photodegradation of RhB and PNP	33

1.5.1 Chemical Methods

Chemical methods utilized for the synthesis of bismuth nanoparticles depend upon the ability of the reducing agents on the bismuth precursors. The ability of the reducing agent to distribute in the synthesis medium has an impact on the nucleation rate and growth, affecting the creation of polydisperse particles. To decipher the problem, various methods have been employed including the utilization of a strong reducing agent with slow kinetics enabling homogeneous nucleation and growth. To synthesize bismuth nanocrystals different reducing agents such as sodium borohydride,[39] ethylene glycol,[40] ethylenediamine, aqueous hydrazine solution,[41] and sodium hyposphite[42] have been used. Also, bismuth nanoparticles are synthesized using photochemical activation.[43] The most utilized methods in the synthesis of bismuth nanoparticles are the hydrothermal, and co-precipitation methods.

1.5.1.1 Hydrothermal Process

A hydrothermal reaction (**Fig. 1.3**) is described as any heterogeneous chemical reaction with a solvent (non-aqueous or aqueous) at pressure > 1 atm and temperature > 25^{o}C in closed systems. In the process, the morphology,[44] size, and agglomeration can be manipulated via parameters such as pH,[45] the ratio of precursors, temperature, and time of the reactions.[46] It also provides the advantage of phase-change.[47] Bismuth nitrate pentahydrate ($Bi(NO_3)_3.5H_2O$) has been popularly employed as a precursor to synthesize bismuth nanoparticles, particularly, bismuth oxides and bismuth vanadate via the hydrothermal method. The fabricated bismuth nanoparticles exhibit exalting properties such as photocatalytic activity,[48] superconductivity,[49]and magnetic frustration.

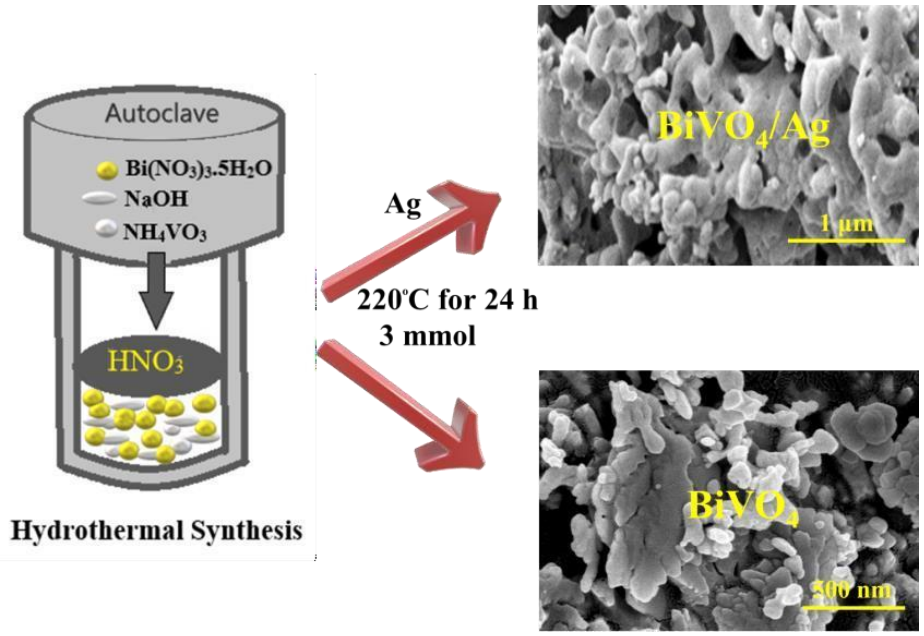

Fig. 1.2. Schematic illustration of hydrothermal synthesis in the preparation of $BiVO_4$ and $BiVO_4$/Ag.

1.5.1.2 Co-precipitation Process

A co-precipitation process is a facile, economically viable, and industrially viable processfor the synthesis of oxide materials (**Fig. 1.3**). The technique provides an easy way to synthesize flowable powders without surplus agglomeration steps. Controlling the pH, temperature, precipitating agents, and solvent used, it can yield products in the micron or nano range. It has been used in the successful synthesis of bismuth nanomaterials.[31]

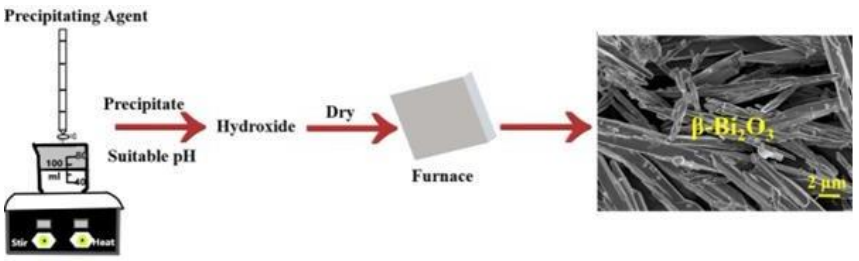

Fig. 1.3. Schematic illustration of co-precipitation synthesis in the preparation of β-Bi_2O_3.

1.5.2 Applications

Bismuth nanomaterials have a variety of applications (**Fig. 1.4**) like photodegradation of organic pollutants, antibiotics, pigments, alloys, and cosmetics owing to their less toxicity as compared to heavy metals.[50] In past years, bismuth salts were widely used in medicines such as bismuth tartrate used in the treatment of syphilis, bismuth sodium triglycollamate in the treatment of warts, respiratory tract infections, and stomatitis.[51] Pepto-Bismol and De-Nol comprising bismuth subsalicylate and colloidal bismuth sub-citrate have been used as gastrointestinal medicines for years. Bismuth compounds are also used as NMR contrast agentsand X-rays.

Apart from these applications, bismuth nanomaterials are widely used in the construction of sensors, pollutant degradation, and anti-bacterial studies owing to their ability in harvesting a wide spectrum of visible light.

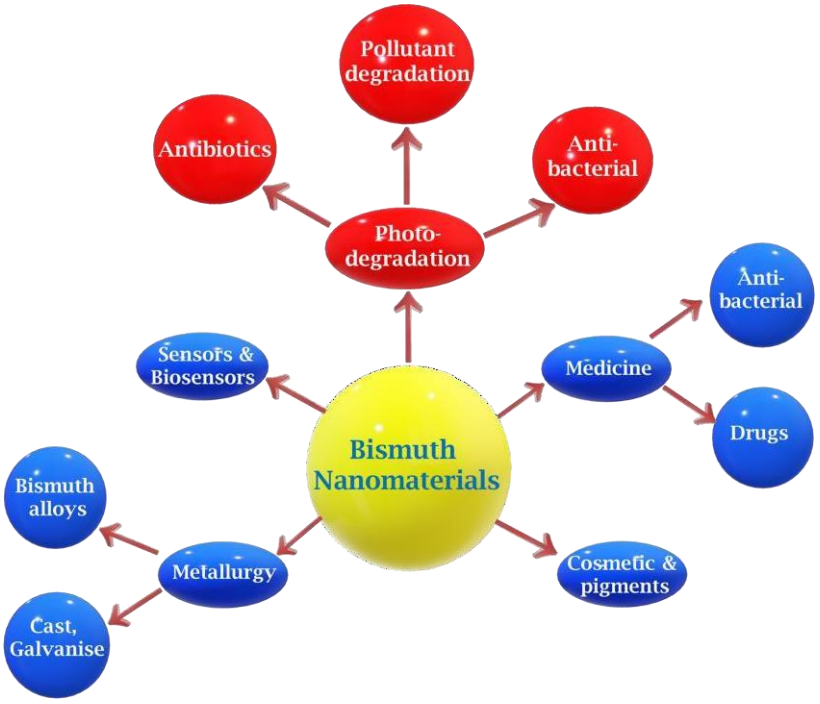

Fig. 1.4. Pathways for applications of Bismuth-based Nanomaterials.

1.6 Water Pollution

Water pollution can be stated as a change in the chemical, physical, and biological characteristics of water having a disastrous effect on human and aquatic life. It can also be defined as excessive amounts of pollutants in water that make the water unfit for cooking, drinking, bathing, and other applications. This could be attributed to the ever-rising industrialization, and urbanization leading to metabolic excretion, extensive industrial waste discharge, and veterinary pharmaceutical contamination.[29]

In past years, the dye industry has shown rapid growth. As per the United States "Color Index", the commodity dyes have reached as high as tens of thousands. About, 60,000 tons ofdye are thrown as industrial waste directly into water bodies every year. Amongst them, 80% are azo dyes. In China, the dye industry is significant for the textile, chemical, and light industry. China's major fuel production is owed majorly to azo dyes.[52] As per the statistics,

about 900 million tons of wastewater are discharged by the textile industry every year. In such printing and dyeing wastewater, the composition of dye is often complex with high concentration and color, and non-degradable components with a variety of organic substances have biological toxicity such as mutagenic, carcinogenic, and teratogenic toxicity. So, the treatment is often difficult using a single treatment technology.[53]

Endocrine-disrupting compounds (EDCs) such as pharmaceuticals are a new group of pollutants that emerged in our world, significantly in wastewater-effected surface water, drinking water, and groundwater. Such compounds penetrate the environment through untreated and treated wastewater. Certain EDCs can also penetrate through agricultural or urban runoff. The concentrations of such effluents in nature are from ng L^{-1} to μg L^{-1}. But their presence in the surface water is quite low. Therefore, due to the different action mechanisms of every substance, their detection, analysis, and removal are quite difficult. Also, their persistent nature in surface water makes their removal challenging. Moreover, intaking phenolic substances even at low concentrations could lead to skin problems, irritation in the eyes, and lack of vision.[54]

Agrochemicals including pesticides and insecticides are vastly used in agriculture to enhance crop yield and reduce post-harvest losses. But the excessive utilization of such agrochemicals has caused major environmental and health problems. Particularly, it has a hazardous effect on the aquatic ecosystem and the water bodies as these chemicals run off andpercolate into the water bodies.[55] It has been observed that the presence of pesticides in human beings even in trace amounts causes severe effects such as decreased fertility, carcinogenic potential, dermatitis, pneumonia, pulmonary diseases, and congenital diseases. Moreover, their degradation efficiency is also quite slow.[56]

Therefore, it is essential to focus on issues concerning organic pollutants with efficient and less time-consuming methods to purify industrial water having rigorous effects on the environment and all living beings.

1.6.1 Methods for Toxin Removal

Various effective techniques for organic pollutant removal from water have gained widespread attention. Numerous methods like filtration with coagulation,[57,58] adsorption,[59] sedimentation,[60] ion exchange,[61] reverse osmosis,[62] precipitation,[63] ultrafiltration,[64] advanced oxidation processes,[65] and biological processes[66] are significantly utilized for the removal of organic pollutants from wastewater. But these processes pose the limitation of slow speed, temperature/pressure control, and formation of side products, and are expensive.[67] However, photodegradation of pollutants seems the most viable method to remove the organic pollutants owing to its feasibility, economic nature, utilization of solar energy, and complete degradation of pollutants.[68]

1.7 Photocatalysis

Photocatalysis, one of the advanced oxidation processes (AOPs)[69] is known as a sustainable, energy-saving, and eco-friendly technique.[70] The method can be employed for highly complex, scarcely biodegradable, and highly concentrated wastewater.[71] The photocatalysts harness the solar light for pollutant degradation which makes the photocatalysistechnique to be viable.[72]

1.7.1 Principle of Photocatalysis

Toxic organic pollutants can be decomposed into lesser harmful products such as CO_2 and H_2O via photocatalysis through photogenerated holes (h^+) and electrons (e^-) and radical species. Bismuth-based nanomaterials photodegrade organic pollutants via the absorption of light of adequate wavelengths such as solar light or visible light source. The light source excites electrons from the photocatalyst's VB to CB. This concludes in the production of

holes on the VB and electrons on the CB, resulting in the electron-hole pair (e^{-}-h^{+}) pairs. Then the hole oxidizes the water molecule into hydroxide radical ($^{\bullet}OH$) while the electrons reduce the oxygen radicals into the superoxide radicals ($O_2^{\bullet-}$). The radicals thus formed finally degrade the pollutants to form harmless products. Although only the photons possess energy higher than the semiconductor's bandgap energy (E_g) can lead to the excitation of electrons in the VB while for the photons having energy lower than Eg, energy is removed in the form of heat.[73]

The mechanism for photocatalysis consists of five major steps, such as (1) photoexcitation (light absorption and charge carrier production), (2) trapping, (3) diffusion, (4) recombination, and (5) oxidation. By irradiating light on the photocatalyst with an energy equalto or greater than the energy of the bandgap, excitation of electrons from VB to CB occurs (**Scheme 1.1**). The photon usually has a wavelength of less than 400 nm. Due to the excitation step, a hole is generated in the VB and thus creating an e^{-}-h^{+} (**Eq. 1.1-1.3**). It was stated that the trapped surface holes and electrons combine at a slower place as compared to the bulk. Without any scavengers (**Eq. 1.4**), the electrons and holes recombine rapidly along with the heat dissipation. Therefore, the existence of scavengers is significant for the reduction in the charge carrier reconciliation and the efficient working of the photocatalytic system. Mostly, photocatalysis occurs in the presence of air, water, pollutant, and photocatalyst. Normally, the holes react with OH^{-} to synthesize surface adsorbed $^{\bullet}OH$ (**Eq. 1.5-1.6**) while a reaction of electrons with O_2 forms $O_2^{\bullet-}$. The superoxide radicals then protonate to form hydroperoxyl radicals ($HO_2^{\bullet}$) and finally produce hydrogen peroxide (H_2O_2) (**Eq. 1.7-1.9**). These radicals have scavenging properties and prolong the charge carrier reconciliation. The photogenerated holes and the produced reactive oxygen species are accountable for organic pollutant degradation (**Eq. 1.91-1.92**).

Photoexcitation: Photocatalyst $+h\nu \longrightarrow e^- + h^+$ (1.1)

Trapping of e^-: $e^-_{CB} \longrightarrow e^-_{TR}$ (1.2)

Trapping of h^+: $h^+_{VB} \longrightarrow h^+_{TR}$ (1.3)

Electron-hole reconciliation: $e^-_{TR} + h^+_{VB}\,(h^+_{TR}) \longrightarrow$ recombine + heat (1.4)

Hydroxyl oxidation: $OH^- + h^+ \longrightarrow {}^{\bullet}OH$ (1.5)

Electron scavenging: $O_2 + e^- \longrightarrow O_2^{\bullet-}$ (1.6)

Protonation of superoxide: $O_2^{\bullet-} + H^+ \longrightarrow HOO^{\bullet}$ (1.7)

Electron co-scavenging: $HOO^{\bullet} + e^- \longrightarrow HO_2^-$ (1.8)

H_2O_2 synthesis: $HOO^- + H^+ \longrightarrow H_2O_2$ (1.9)

Formation of $^{\bullet}OH$: $H_2O_2 + h\nu \longrightarrow 2OH^{\bullet}$ (1.91)

Photodegradation: RH (pollutants) $+h^+/{}^{\bullet}OH/\ O_2^{\bullet-} \longrightarrow CO_2 + H_2O$ (1.92)

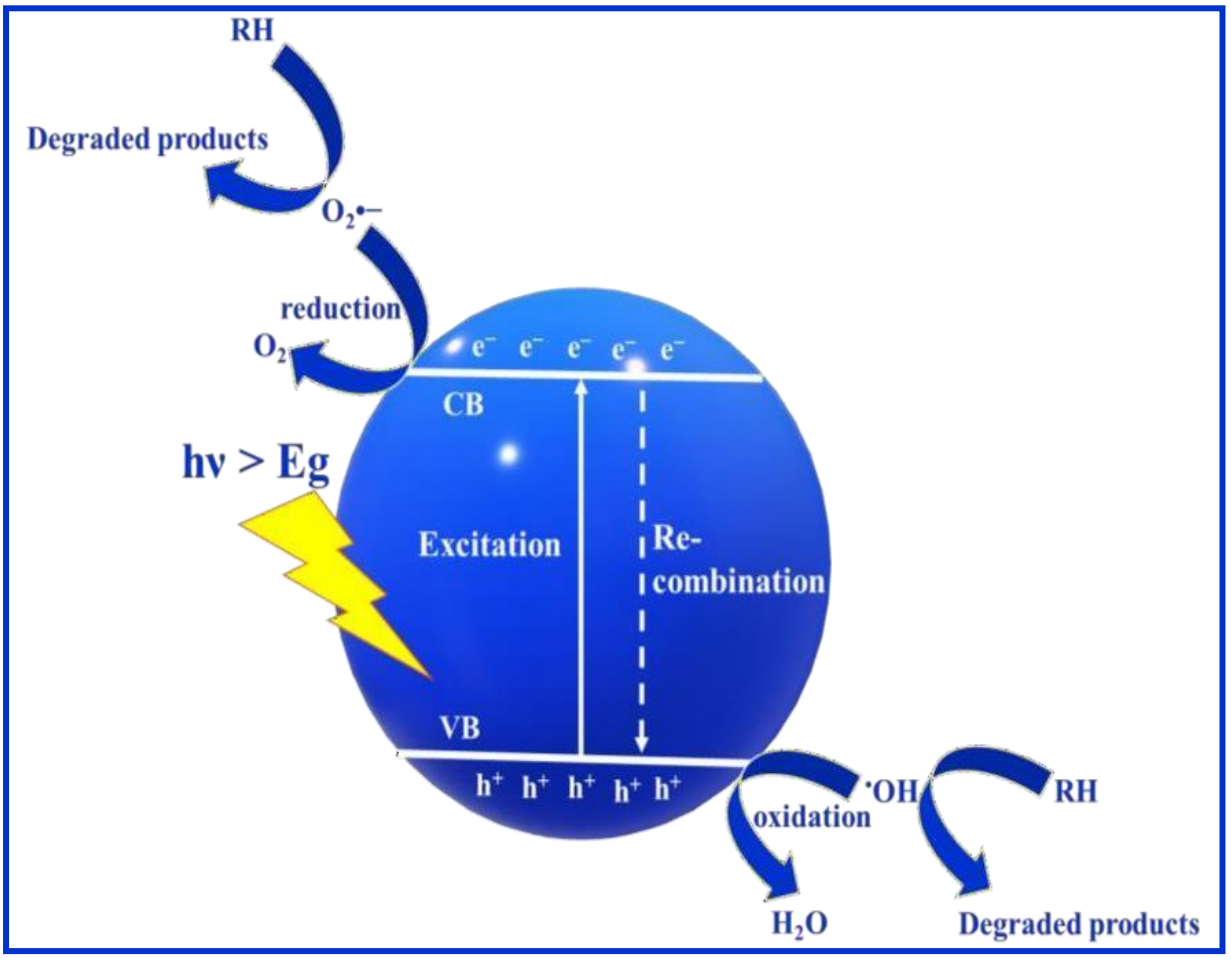

Scheme 1.1. General mechanism for photocatalytic degradation.

TiO_2 is the most widely studied photocatalyst for AOPs as it employs solar radiation for organic pollutant mineralization existing in the air or aquatic systems. But its application poses limitations owing to its slim photocatalytic area (λ < 400nm) and limited capacity to absorb solar radiation (<5%) and visible light owed to its broad bandgap (anatase; ~3.2 eV). To remove this shortcoming, novel photocatalysts are created. Widespread attention is gained via visible-light-induced photocatalysts and their enhanced performance in photodegradation.[74]

1.7.2 Photocatalysts

Photocatalyst is described as a material that facilitates the reaction rate in the presence of light without decomposing itself.[75] The oxidation rates and the efficacy of a photocatalytic system depend on various factors that govern the photodegradation of pollutants. The factors are substrate concentration, amount of photocatalyst, temperature, pH of the solution,[76] the surface area of material, light intensity, dissolved oxygen in the reaction medium, nature of substrate, nature of the photocatalyst, doping of non-metal and metal ions, structure of the catalyst and substrate, electronic band structure, crystallinity. The photocatalytic performance can be enhanced at a low concentration of organic pollutants with an appropriate amount of the photocatalyst, and increased area owing to the enhanced active sites.[77] Also, metal ions which enhance the surface charge of the catalyst are essential. Finally, for optimum efficiency, the degradation activity should be performed at room temperature and the light source should have sufficient energy to excite electrons from VB to CB.[78] Therefore, a photocatalyst is considered optimum if it has a narrow bandgap, optimum light-capturing tendency, high charge carrier separation, and low recombination rate along with a huge surfacearea and appropriate CB and VB positions.[79]

Table 1.2. Different photocatalysts for the photodegradation of pollutants.

Catalyst	Pollutant	Time (min)	Conc. (g/L)	Source	Efficiency (%)	*k* (min^{-1})	Reference
Bi_2O_3/g-C_3N_4	AB10B	120	0.15	Visible light	88.71	0.01722	80
BiOCl-Bi_2S_3	RhB	30	0.05	UV-Visible light	79	0.07166	81
α, β-Bi_2O_3	RhB	210	1	UV-Visible light	80	0.00620	82
AgX (X = I, Br)/$CuBi_2O_4$	TC	60	0.5	Visible light	90, 80	0.03551, 0.02516	83
Boron nitride supported on graphene chitosan	MB, AO II	10, 20	1	Visible light	87, 57	-	84
Bi_2O_3/g-C_3N_4	RB 5	120	1	UV-Visible light	84	-	85

Cellulose nanofibrils doped BiOCl	RhB	16	0.05	Visible light	51	-	86
Cu-doped-Bi_2O_3	Atrazi-ne	120	1	Visible light	28.1	-	87
SiO_2-doped-β- Bi_2O_3	TC	180	0.2	Visible light	80.8	-	88
UVC/H_2O_2/TiO_2, Solar/ H_2O_2/TiO_2	RB, YT	180	0.3	UV-Visible light	99.5, 99.1	0.03, 0.0213	89
Dodecylsulf-ate-intercalated layered double hydroxides	MO, CR, BG	180	0.03	-	98, 96, 92	0.0299, 0.0301, 0.0262	90
Plasmonic Nanostructures (PM-CQDs/TiO_2) [M= Au, Ag]	MB, EMC	20, 150	1	UV-Visible light	96, 52	-	91

[Ni(L1)2]- [Ni(L4)2]	Chlorpyri - phos, parathion -methyl	25	-	UV-Visible light	-	1.5x10- 4, 1.55x10 -4	92

1.8 Research Gaps

Based on the literature study, the following research gaps have been proposed and fulfilled in the current work:

- Not much focus has been given to the synthesis of bismuth-related ternary composites via the hydrothermal process.
- Not much has been reported on the fabrication of β-phased Bi_2O_3 nanocomposites using the in-situ precipitation method.
- As such no significant work has been done in the employment of bismuth-related composites such as Bi_3TaO_7/BiOCl for photocatalytic purposes.
- No significance has been given to the photodegradation of colorless pollutants like pesticides and pharmaceuticals using bismuth-based nanomaterials.

1.9 Objectives

The current work aims to study the photocatalytic activities of bismuth-related composites covering pollutant degradation. The specific objectives are as follows:

- Synthesis and characterization of bismuth-based binary/ternary nanocomposites (e.g., Ag/$BiVO_4$, Bi_2O_3/BiOCl, g-C_3N_4/Ag/$BiVO_4$).
- Photocatalytic degradation of pollutants (e.g., dye, insecticide, CO_2) by the as-synthesized nanocomposites.
- Performance evaluation by varying the operating parameters to optimize the photocatalytic efficiency of the composites.

2.0 Conclusion

The chapter summarizes the significance of bismuth-related nanocomposites for the photocatalytic degradation of organic pollutants. Although numerous catalysts have been reported in the past for various photocatalytic applications, bismuth-based nanocomposites have proved to be highly efficient for photocatalytic purposes owing to their narrow bandgap and better absorption of light in the visible region of the spectrum.

References

(1) Abdelghany, S. F. An Introduction to Mammals. *Nanoscience and Plant-Soil Systems* **2016**, *5*, 1. https://doi.org/10.1007/978-3-319-46835-8.

(2) Jones, H.; A, P. R. S. L. The Theory of the Galvomagnetic Effects in Bismuth. Math. *Phys. Sci.* **1936**, *155*, 653. https://doi.org/10.1098/rspa.1936.0126.

(3) Pistofidis, N.; Vourlias, G.; Konidaris, S.; Pavlidou, E.; Stergiou, A.; Stergioudis, G. The Effect of Bismuth on the Structure of Zinc Hot-Dip Galvanized Coatings. *Mater. Lett.* **2007**, *61*, 994. https://doi.org/10.1016/j.matlet.2006.06.029.

(4) Ganguly, R.; Singh, A. K.; Kumar, R.; Gupta, A.; Pandey, A. K.; Pandey, A. K. Nanoparticles as Modulators of Oxidative Stress. *Nanotechnology in Modern Family Biotechnology* **2019**, *Chapter 3*, 29. https://doi.org/10.1016/B978-0-12-818823-1.00003-X.

(5) Lynall, D.; Nair, S. V.; Gutstein, D.; Shik, A.; Savelyev, I. G.; Blumin, M.; Ruda, H. E. Surface State Dynamics Dictating Transport in InAs Nanowires. *Nano Letters* **2018**, *18*, 1387. https://doi.org/10.1021/acs.nanolett.7b05106.

(6) Kargin, Y. F.; Ivicheva, S. N.; Buslaeva, E. Y.; Kuvshinova, T. B.; Volodin, V. D.; Yurkov, G. Y. Preparation of Bismuth Nanoparticles in Opal Matrices through Reduction of Bismuth Compounds with Supercritical Isopropanol. *Inorg. Mater.* **2006**, *42*, 487. https://doi.org/10.1134/S0020168506050074.

(7) Zhu, C.; Xian, Q.; He, Q.; Chen, C.; Zou, W.; Sun, C.; Wang. S.; Duan, X. Edge-Rich Bicrystalline 1T/2H-MoS_2 Cocatalyst-Decorated {110} Terminated CeO_2 Nanorods for Photocatalytic Hydrogen Evolution. *ACS Applied Materials & Interfaces* **2021**, *13*, 35818. https://doi.org/10.1021/acsami.1c09651.

(8) Liu, G.; Li, S.; Zhang, J.; Feng, Z.; Li, C. Controllable Synthesis of α-Bi_2O_3 andγ-Bi_2O_3 with High Photocatalytic Activity by α-Bi_2O_3→γ-Bi_2O_3→α-Bi_2O_3 transformation in a

Facile Precipitation Method. *J. Alloys Compd.* **2016**, *689*, 787. https://doi.org/10.1016/j.jallcom.2016.08.047.

(9) Structure, F. C. Dielectric Characteristics of Bismuth Oxide Solid Solutions with a Fluorite-Like Crystal Structure. *J. Am. Ceram. Soc.* **2004**, *1061*, 1056. https://doi.org/10.1111/J.1551-2916.2004.01056.X.

(10) Liu, Z.; Yan, F. The Application of Bismuth-Based Oxides in Organic-Inorganic Hybrid Photovoltaic Devices. *J. Am. Ceram. Soc.* **2012**, *95*, 1944. https://doi.org/10.1111/j.1551-2916.2012.05088.x.

(11) Peng, H.; Chan, C. K.; Meister, S.; Zhang, X. F.; Cui, Y. Shape Evolution of Layer-Structured Bismuth Oxychloride Nanostructures via Low-Temperature Chemical Vapor Transport. *Chem. Mater.* **2009**, *21*, 247. https://doi.org/10.1021/cm802041g.

(12) Zhang, J.; Shi, F.; Lin, J.; Chen, D.; Gao, J.; Huang, Z.; Ding, X.; Tang, C. Self-Assembled 3-D Architectures of BiOBr as a Visible Light-Driven Photocatalyst. *Chem. Mater.* **2008**, *20*, 2937. https://doi.org/10.1021/cm7031898.

(13) Zhang, K. L.; Liu, C. M.; Huang, F. Q.; Zheng, C.; Wang, W. D. Study of the Electronic Structure and Photocatalytic Activity of the BiOCl Photocatalyst. *Appl. Catal. B Environ.* **2006**, *68*, 125. https://doi.org/10.1016/j.apcatb.2006.08.002.

(14) Tao, X.; Zhao, Y.; Mu, L.; Wang, S.; Li, R.; Li, C. Bismuth Tantalum Oxyhalogen: A Promising Candidate Photocatalyst for Solar Water Splitting. *Adv. Energy Mater.* **2018**, *8*, 1. https://doi.org/10.1002/aenm.201701392.

(15) Song, Q.; Wu, P.; Sarkar, S.; Zhao, Y.; Liu, Z. T. C. Bi_3TaO_7 Film: A Promising Photoelectrode for Photoelectrochemical Water Splitting. *Dalt. Trans.* **2019**, *49*, 147. https://doi.org/10.1039/c9dt03953h.

(16) Ouyang, S.; Ye, J. β-$AgAl_{1-x}Ga_xO_2$ Solid-Solution Photocatalysts: Continuous Modulation of Electronic Structure toward High-Performance Visible-Light

Photoactivity. J. Am. Chem. Soc. **2011**, *133*, 7757. https://doi.org/10.1021/ja110691t.

(17) Abrahams, I.; Krok, F.; Struzik, M.; Dygas, J. R. Defect Structure and Electrical Conductivity in Bi_3TaO_7. *Solid State Ionics* **2008**, *179*, 1013. https://doi.org/10.1016/j.ssi.2008.02.002.

(18) Bhat, S. S. M.; Jang, H. W. Recent Advances in Bismuth-Based Nanomaterials for Photoelectrochemical Water Splitting. *ChemSusChem* **2017**, *10*, 3001. https://doi.org/10.1002/cssc.201700633.

(19) Shamsedini, N.; Dehghani, M.; Nasseri, S.; Baghapour, M. A. Photocatalytic Degradation of Atrazine Herbicide with Illuminated Fe^{+3}-TiO_2 Nanoparticles. J*ournal of Environmental Health Sciences* **2017**, *15*, 7. https://doi.org/10.1186/s40201-017- 0270-6.

(20) Fowler, B. A.; Sullivan, D. W.; Sexton M. J. Bismuth. *Handbook on the Toxicology of Metals* **2015**, *Chapter 31*, 655. https://doi.org/10.1016/b978-0-444-59453-2.00031-7.

(21) Liu, X.; Pan, L.; Lv, T.; Sun, Z.; Sun, C. Q. Visible Light Photocatalytic Degradation of Dyes by Bismuth Oxide-Reduced Graphene Oxide Composites Prepared via Microwave-Assisted Method. *J. Colloid Interface Sci.* **2013**, *408*, 145. https://doi.org/10.1016/j.jcis.2013.07.045.

(22) Li, C.; Wang, H.; Bonabi, S.; Zhong, J.; Fang, P. Visible Light Driven Hydrogen Evolution by Photocatalytic Reforming of Lignin and Lactic Acid Using One-Dimensional NiS/CdS Nanostructures. *Appl. Catal. B Environ.* **2018**, *227*, 229. https://doi.org/10.1016/j.apcatb.2018.01.038.

(23) Na, B.; Wang, L.; Wang, W. Photocatalytic Hydrogen Production from Aqueous Solutions. *Int. J. Hydrogen Energy* **2011**, *37*, 3041. https://doi.org/10.1016/j.ijhydene.2011.10.105.

(24) Xia, Y.; Xiong, Y.; Lim, B.; Skrabalak, S. E. Shaped-Controlled Synthesis of Metal

Nanocrystals: Simple Chemistry Meets Complex Physics? Angewandte Chemie International Edition 2009, 48, 60. https://doi.org/10.1002/1nie.200802248.

(25) Goia, D. V; Goia, D. V. Preparation and Formation Mechanisms of Uniform Metallic Particles in Homogeneous Solutions. *Journal of Materials Chemistry* **2004**, *14*, 451. htpps://doi.org/10.1039/b311076a.

(26) Zhao, Y.; Zhang, Z.; Dang, H. A Simple Way to Prepare Bismuth Nanoparticles. *Materials Letters* **2004**, *58*, 790. https://doi.org/10.1016/j.matlet.2003.07.013.

(27) Safaei, J.; Ullah, H.; Mohamed, N. A.; Mohamad Noh, M. F.; Soh, M. F.; Tahir, A. A.; Ahmad Ludin, N.; Ibrahim, M. A.; Wan Isahak, W. N. R.; Mat Teridi, M. A. Enhanced Photoelectrochemical Performance of Z-Scheme g-C_3N_4/$BiVO_4$ Photocatalyst. *Appl. Catal. B Environ.* **2018**, *234*, 296. https://doi.org/10.1016/j.apcatb.2018.04.056.

(28) Li, Z.; Jin, C.; Wang, M.; Kang, J.; Wu, Z.; Yang, D.; Zhu, T. Novel Rugby-like g-C_3N_4/$BiVO_4$ Core/Shell Z-Scheme Composites Prepared via Low-Temperature Hydrothermal Method for Enhanced Photocatalytic Performance. *Sep. Purif. Technol.* **2020**, *232*, 115937. https://doi.org/10.1016/j.seppur.2019.115937.

(29) Le, S.; Li, W.; Wang, Y.; Jiang, X.; Yang, X.; Wang, X. Carbon Dots Sensitized 2D-2D Heterojunction of $BiVO_4$/Bi_3TaO_7 for Visible Light Photocatalytic Removal towards the Broad-Spectrum Antibiotics. *J. Hazard. Mater.* **2019**, *376*, 1. https://doi.org/10.1016/j.jhazmat.2019.04.088.

(30) Zhao, Q.; Liu, X.; Xing, Y.; Liu, Z.; Du, C. Synthesizing Bi_2O_3/BiOCl Heterojunctions by Partial Conversion of BiOCl. *J. Mater. Sci.* **2017**, *52*, 2117. https://doi.org/10.1007/s10853-016-0499-y.

(31) Tang, X.; Ma, C.; Liu, N.; Liu, C.; Liu, S. Visible Light β-Bi_2O_3/BiOCl Heterojunction Photocatalyst with Highly Enhanced Photocatalytic Activity. *Chem. Phys. Lett.* **2018**, *709*, 82. https://doi.org/10.1016/j.cplett.2018.08.045.

(32) Zhang, X.; Xu, G.; Hu, J.; Lv, J.; Wang, J.; Wu, Y. Fabrication and Photocatalytic Performances of BiOCl Nanosheets Modified with Ultrafine Bi_2O_3 Nanocrystals. *RSC Adv.* **2016**, *6*, 63241. https://doi.org/10.1039/c6ra09919j.

(33) Wang, D.; Yu, X.; Feng, Q.; Lin, X.; Huang, Y.; Huang, X.; Li, X.; Chen, K.; Zhao, B.; Zhang, Z. In-Situ Growth of β-Bi_2O_3 Nanosheets on g-C_3N_4 to Construct Direct Z-Scheme Heterojunction with Enhanced Photocatalytic Activities. *J. Alloys Compd.* **2021**, *859*, 157795. https://doi.org/10.1016/j.jallcom.2020.157795.

(34) Mitoraj, D.; Lamdab, U.; Kangwansupamonkon, W.; Pacia, M.; Macyk, W.;Wetchakun, N.; Beranek, R. Revisiting the Problem of Using Methylene Blue as a Model Pollutant in Photocatalysis: The Case of $InVO_4/BiVO_4$ Composites. *J. Photochem. Photobiol. A Chem.* **2018**, *366*, 103. https://doi.org/10.1016/j.jphotochem.2018.02.023.

(35) Shan, L. W.; Wang, G. L.; Liu, L. Z.; Wu, Z. Band Alignment and Enhanced Photocatalytic Activation for α-Bi_2O_3/BiOCl (001) Core-Shell Heterojunction. *J. Mol. Catal. A Chem.* **2015**, *406*, 145. https://doi.org/10.1016/j.molcata.2015.05.024.

(36) Si, Y.; Chen, W.; Shang, S.; Xia, Y.; Zeng, X. g-C_3N_4/Pt/$BiVO_4$ Nanocomposites for Highly Efficient Visible-Light Photocatalytic Removal of Contaminants and Hydrogen Generation. *Nanotechnology* **2019**, *31*, 13. https://doi.org/10.1088/1361-6528/ab5bc5.

(37) Ou, M.; Wan, S.; Zhong, Q.; Zhang, S.; Song, Y.; Guo, L.; Cai, W.; Xu, Y. Hierarchical Z-Scheme Photocatalyst of g-C_3N_4@Ag/$BiVO_4$ (040) with Enhanced Visible-Light-Induced Photocatalytic Oxidation Performance. *Appl. Catal. B Environ.* **2018**, *221*, 97. https://doi.org/10.1016/j.apcatb.2017.09.005.

(38) Li, K.; Lu, X.; Zhang, Y.; Liu, K.; Huang, Y.; Liu, H. Bi_3TaO_7/Ti_3C_2 Heterojunctions for Enhanced Photocatalytic Removal of Water-Borne Contaminants. *Environ. Res.* **2020**, *185*, 109409. https://doi.org/10.1016/j.envres.2020.109409.

(39) Wang, Y.; Chen, J.; Chen, L.; Chen, Y.; Wu, L. Shape-Controlled Solventless Syntheses of Nano Bi Disks and Spheres. *Crystal Growth & Design* **2010**, *10*, 1578. https://doi.org/10.1021/cg9010949.

(40) Li, J.; Fan, H.; Chen, J.; Liu, L. C. Synthesis and Characterization of Poly (Vinyl Pyrrolidone)-Capped Bismuth Nanospheres. *Colloids and Surfaces A: Physicochemical and Engineering Aspects* **2009**, *340*, 66. https://doi.org/10.1016/j.colsurfa.2009.03.007.

(41) Ma, D.; Zhao, J.; Li, Y.; Su, X.; Hou, S.; Zhao, Y.; Hao, X.; Li, L. Organic Molecule Directed Synthesis of Bismuth Nanostructures with Varied Shapes in Aqueous Solution and Their Optical Characterization. *Colloids Surfaces A: Physicochemical and Engineering Aspects* **2010**, *368*, 105. https://doi.org/10.1016/j.colsurfa.2010.07.022.

(42) Ma, D.; Zhao, J.; Chu, R.; Yang, S.; Zhao, Y.; Hao, X.; Li, L.; Zhang, L. Novel Synthesis and Characterization of Bismuth Nano/Microcrystals with Sodium Hypophosphite as Reductant. *Adv. Powder Technol.* **2013**, *24*, 79. https://doi.org/10.1016/j.apt.2012.02.004.

(43) Warren, S. C.; Jackson, A. C.; Cater-Cyker, Z. D.; Disalvo, F. J.; Wiesner, U. Nanoparticle Synthesis via the Photochemical Polythiol Process. *Journal of the Americal Chemical Society* **2007**, *129*, 10072. https://doi.org/10.1021/ja0733639.

(44) Yan, Y.; Wu, Y.; Yan, Y.; Guan, W.; Shi, W. Inorganic-Salt-Assisted Morphological Evolution and Visible-Light-Driven Photocatalytic Performance of Bi_2WO_6 Nanostructures. *The Journal of Physical Chemistry C* **2013**, *117*, 20017. https://doi.org/10.1021/jp406574y.

(45) Yu, B. J.; Kudo, A. Effects of Structural Variation on the Photocatalytic Performance of Hydrothermally Synthesized $BiVO_4$. *Advanced Functional Materials* **2006**, *16*, 2163. https://doi.org/10.1002/adfm.200500799.

(46) Lu, H.; Wang, S.; Zhao, L.; Dong, B.; Li, J. Surfactant-Assisted Hydrothermal Synthesis

of Bi_2O_3 Nano/Microstructures. *RSC Advances* **2012**, *2*, 3374. https://doi.org/10.1039/c2ra01203k.

(47) Kumada, N. Preparation and Crystal Structure of New Inorganic Compounds by Hydrothermal Reaction. *Journal of the Ceramic Society of Japan* **2013**, *121*, 135. https://doi.org/10.2109/jcersj2.121.135.

(48) Obregón, S; Caballero, A.; Colón, G. Hydrothermal Synthesis of $BiVO_4$: Structural, and Morphological Influence on the Photocatalytic Activity. Applied Catal. B, Environ. 2012, 117, 59. https://doi.org/10.1016/j.apcatb.2011.12.037.

(49) Rubel, M. H. K.; Takei, T.; Kumada, N.; Ali, M. M.; Miura, A.; Tadanaga, K.; Oka, K.; Azuma, M.; Yashima, M.; Fujii, K.; Moriyoshi, C.; Kuroiwa, Y.; Hester, J. R.; Avdeev, M. Superconductivity of a Double Perovskite Bi-Oxide Hydrothermal Synthesis, Superconductivity of a Double-Perovskite Bi Oxide. *Chemistry of Materials* **2015**, *28*, 459. https://doi.org/10.1021/acs.chemmater.5b02386.

(50) Shevtsov, Y. V; Beizel, N. F. Pb Distribution in Multistep Bismuth Refining Products. *Inorganic Materials* **2011**, *47*, 139. https://doi.org/10.1134/S0020168511020166.

(51) Salvador, J. A. R.; Fiqueiredo, S. A. C.; Pinto, R. M. A. Silvestre S. M. Bismuth Compounds in Medicinal Chemistry. *Future Medicinal Chemistry* **2012**, *4*, 1495. https://doi.org/10.4155/fmc.12.95.

(52) Sarkar, S.; Banerjee, A.; Halder, U.; Biswas, R.; Bandopadhyay, R. Degradation of Synthetic Azo Dyes of Textile Industry: A Sustainable Approach Using Microbial Enzymes. *Water Conserv. Sci. Eng.* **2017**, *2*, 121. https://doi.org/10.1007/s41101-017-0031-5.

(53) Liu, Q. Pollution and Treatment of Dye Waste-Water. *IOP Conf. Ser. Earth Environ. Sci.* **2020**, *514*, 052001. https://doi.org/10.1088/1755-1315/514/5/052001.

(54) McEachran, A. D.; Shea, D.; Bodnar, W.; Nichols, E. G. Pharmaceutical Occurrence in

Groundwater and Surface Waters in Forests Land-Applied with Municipal Wastewater. *Environmental Toxicology and Chemistry* **2015**, *35*, 898. https://doi.org/10.1002/etc.3216.

(55) Nunthasen, W.; Nunthasen, K.; Jaengsaengthong, W. Farmers' Health Effects and Attitude Towards Agrochemicals Use in Rice Production. *IOP Conf. Ser. Earth Environ. Sci.* **2019**, *265*, 012016. https://doi.org/10.1088/1755-1315/265/1/012016.

(56) Nicolopoulou-Stamati, P.; Maipas, S.; Kotampasi, C.; Stamatis, P.; Hens, L. Chemical Pesticides and Human Health: The Urgent Need for a New Concept in Agriculture. *Frontiers in Public Health* **2016**, *4*, 148. https://doi.org/10.3389/fpubh.2016.00148.

(57) Muruganandam, L.; Saravana, K. M. P.; Gulla, S.; Godhwani, B. Treatment of Waste Water by Coagulation and Flocculation Using Biomaterials. *IOP Conference Series: Materials Science and Engineering* **2017**, *263*, 032006. https://doi.org/10.1088/1757-899X/263/3/032006.

(58) Precious, S. N.; Rathilal, S.; Kweinor, T. E. Coagulation Treatment of Wastewater: Kinetics and Natural Coagulant Evaluation. *Molecules* **2021**, *26*, 698. https://doi.org/10.3390/molecule26030698.

(59) Amuda, O.; Ibrahim, A. O. Industrial Wastewater Treatment using Natural Material as Adsorbent. *African Journal of Biotechnology* **2006**, *5*, 1483. https://doi.org/10.5897/AJB05.273.

(60) Wang, Y.; Jin, X.; Zhuo, N.; Zhu, G.; Cai, Z. Interaction-Sedimentation Strategy for Highly Efficient Removal of Refractory Humic Substances in Biologically Treated Wastewater Effluent: From Mechanistic Investigation to Full-Scale Application. *J. Hazard. Mater*. **2021**, *418*, 126415. https://doi.org/10.1016/j.jhazmat.2021.126145.

(61) Fu, F.; Wang, Q. Removal of heavy metal ions from wastewaters: A review. *Journal of Environmental Management* **2011**, *92*, 407.

https://doi.org/10.1016/j.jenvman.2010.11.011.

(62) Trishitman, D.; Cassano, A.; Basile, A.; Rastogi, N. K. Reverse Osmosis Reject for Industrial Wastewater Treatment. *Current Trends and Future Developments on (Bio-) Membranes* **2020**, *Chapter 9*, 207. https://doi.org/10.1016/b978-0-12-816777-9.000095.

(63) Palmer, M.; Hatley, H. The Role of Surfactants in Wastewater Treatment: Impact, Removal and Future Techniques: A Critical Review. *Water Research* **2018**, *147*, 60. https://doi.org/10.1016/j.watres.20218.09.039.

(64) Li, X.; Jiang, L.; Li, H. Application of Ultrafiltration Technology in Water Treatment. *IOP Conference Series: Earth and Environmental* Science **2018**, *186*, 012009. https://doi.org/10.1088/1755-1315/186/3/012009.

(65) Garrido-Cardenas, J. A.; Agüera, A. Wastewater Treatment by Advanced Oxidation Process and Their Worldwide Research Trends. *Internal Journal of Environmental Research and Public Health* **2020**, *17*, 170. https://doi.org/10.3390/ijerph17010170.

(66) Hu, Z.; Houweling, D.; Dold, P. Biological Nutrient Removal in Municipal Wastewater Treatment: New Directions in Sustainability. *Journal of Environmental Engineering* **2012**, *138*, 307. https://doi.org/10.1061/(asce)ee.1943-7870.0000462.

(67) Bhakare, A.; Lokhande, K.; Dhumal, P.; Bondarde, M. Multifunctional heteroatom doped sustainable carbon nanocomposite for rapid removal of persistent organic pollutant and iodine from water. Separation and Purification Technology **2022**, *278*, 119490. https://doi.org/10.1016/j.seppur.2021.119490.

(68) Dong, H.; Zeng, G.; Tang, L.; Fan, C. An Overview on Limitations of TiO_2-Based Particles for Photocatalytic Degradation of Organic Pollutants and the Corresponding Countermeasures. *Water Res.* **2015**, *79*, 128. https://doi.org/10.1016/j.watres.2015.04.038.

(69) Yao, Y.; Yin, H.; Zhang, Y.; Wei, F.; Hu, H.; Tang, Y.; Wang, S. Fe, Cu-coordinated ZIF-derived bimetal encapsulated N-doped carbon nanotube for efficient remediation of various aqueous pollutants. *Chemical Engineering Journal* **2021** *426*, 131801. https://doi.org/10.1016/j.cej.2021.131801.

(70) Chen, D.; Cheng, Y.; Zhou, N.; Chen, P.; Wang, Y.; Li, K.; Huo, S.; Cheng, P.; Peng, P.; Zhang, R.; Wang, L.; Liu, H.; Liu, Y.; Ruan, R. Photocatalytic Degradation of Organic Pollutants Using TiO_2-Based Photocatalysts: A Review. *J. Clean. Prod.* **2020**, *268*, 121725. https://doi.org/10.1016/j.jclepro.2020.121725.

(71) Zare, E. N.; Iftekhar, S.; Park, Y.; Joseph, J.; Srivastava, V.; Khan, M. A.; Makvandi, P.; Sillanpaa, M.; Varma, R. S. An overview on non-spherical semiconductors for heterogeneous photocatalytic degradation of organic water contaminants. *Chemosphere* **2021**, *280*, 130907. https://doi.org/10.1016/j.chemosphere.2021.13.

(72) Wang, S.; Zhang, J.; Li, B.; Sun, H.; Wang, S. Engineered Graphitic Carbon Nitride-Based Photocatalysts for Visible-Light-Driven Water Splitting: A Review. *Energy & Fuels* **2021**, *35*, 6504. https://doi.org/10.1021/acs.energyfuels.1c005.

(73) Dalrymple, O. K.; Stefanakos, E.; Trotz, M. A.; Goswami, D. Y. A Review of the Mechanisms and Modeling of Photocatalytic Disinfection. *Applied Catal. B: Environ.* **2010**, *98*, 27. https://doi.org/10.1016/j.apcatb.2010.05.001.

(74) Tang, K.; Chen, J.; Legaspi, E.; Owh, C.; Lin, M.; Tee, I.; Kai, D.; Loh, X.; Li, Z.; Regulacio, M.; Ye, E. Gold-decorated TiO_2 nanofibrous hybrid for improved solar-driven photocatalytic pollutant degradation. *Chemosphere* **2021**, *265*, 129114. https://doi.org/10.1016/j.chemosphere.2020.129114.

(75) Thakur, I.; Örmeci, B.; verma, A. Inactivation of E. coli in water employing Fe-TiO_2 composite incorporating in-situ dual process of photocatalysis and photo-Fenton in fixed-mode. *Journal of Water Process Engineering* **2020**, *33*, 101085.

https://doi.org/10.1016/j.jwpe.2019.101085.

(76) Berardinelli, A.; Hamrouni, A.; Dirè, S.; Ceccato, R., Camera-Roda; G., Ragni, L.; Palmisano, L.; Parrino, F. Features and application of coupled cold plasma and photocatalysis processes for decontamination of water. *Chemosphere* **2021**, *262*, 128336. https://doi.org/10.1016/j.chemosphere.2020.12.

(77) Kundu, S.; Lau, Liang, H. Shape-Controlled Catalysis by Cetyltrimethylammonium Bromide Terminated Gold Nanospheres, Nanorods, and Nanoprisms. *J. Phys. Chem. C* **2009**, *113*, 5150. https://doi.org/10.1021/jp811331z.

(78) Kumar, A.; Pandey, G. A Review on the Factors Affecting the Photocatalytic Degradation of Hazardous Materials. *Materials Science & Engineering International Journal* **2017**, *1*, 106. https://doi.org/10.15406/mseij.2017.01.00018.

(79) William, W.; Oppong, S. O. B.; Oppong, O. B.; Anku, W.; Govender, P. P.; Govender, P. Bismuth-Based Nanoparticles as Photocatalytic Materials Materials. *Bismuth-Advanced Applications and Defects Characterization* **2018**, *Chapter 2*, 24. https://doi.org/10.5772/intechopen.75104.

(80) Cui, Y.; Zhang, X.; Guo, R.; Zhang, H.; Li, B.; Xie, M.; Cheng, Q.; Cheng, X. Construction of Bi_2O_3/g-C_3N_4 Composite Photocatalyst and Its Enhanced Visible Light Photocatalytic Performance and Mechanism. *Sep. Purif. Technol.* **2018**, *203*, 301. https://doi.org/10.1016/j.seppur.2018.04.061.

(81) Ferreira, V. C.; Neves, M. C.; Hillman, A. R.; Monteiro, O. C. Novel One-Pot Synthesis and Sensitisation of New BiOCl-Bi_2S_3 Nanostructures from Des Medium Displaying High Photocatalytic Activity. *RSC Adv.* **2016**, *6*, 77329. https://doi.org/10.1039/c6ra14474h.

(82) Gadhi, T. A.; Hernández-Gordillo, A.; Bizarro, M.; Jagdale, P.; Tagliaferro, A.; Rodil,S.

E. Efficient α/β-Bi_2O_3 Composite for the Sequential Photodegradation of Two-Dyes Mixture. *Ceram. Int.* **2016**, *42*, 13065. https://doi.org/10.1016/j.ceramint.2016.05.087.

(83) Guo, F.; Shi, W.; Wang, H. B.; Han, M.; Guan, W.; Huang, H.; Liu, Y.; Kang, Z. Study on Highly Enhanced Photocatalytic Tetracycline Degradation of Type II AgI/$CuBi_2O_4$ and Z-Scheme AgBr/$CuBi_2O_4$ Heterojunction Photocatalysts. *J. Hazard. Mater.* **2018**, *349*, 111. https://doi.org/10.1016/j.jhazmat.2018.01.042.

(84) Khose, R. V.; Lokhande, K. D.; Bhakare, M. A.; Dhumal, P. S.; Wadekar, P. H.; Some, S. Boron Nitride Doped Chitosan Functionalized Graphene for an Efficient Dye Degradation. *ChemistrySelect* **2021**, *6*, 7956. https://doi.org/10.1002/slct.202101611.

(85) Shafawi, A. N.; Mahmud, R. A.; Ahmed Ali, K.; Putri, L. K.; Md Rosli, N. I.; Mohamed, A. R. Bi_2O_3 Particles Decorated on Porous g-C_3N_4 Sheets: Enhanced Photocatalytic Activity through a Direct Z-Scheme Mechanism for Degradation of Reactive Black 5 under UV–Vis Light. *J. Photochem. Photobiol. A Chem.* **2020**, *389*. 112289. https://doi.org/10.1016/j.jphotochem.2019.112289.

(86) Tian, C.; Luo, S.; She, J.; Qing, Y.; Yan, N.; Wu, Y.; Liu, Z. Cellulose Nanofibrils Enable Flower-like BiOCl for High-Performance Photocatalysis under Visible-Light Irradiation. *Appl. Surf. Sci.* **2019**, *464*, 606. https://doi.org/10.1016/j.apsusc.2018.09.126.

(87) Sudrajat, H.; Sujaridworakun, P. Insights into Structural Properties of Cu Species Loaded on Bi_2O_3 Hierarchical Structures for Highly Enhanced Photocatalysis. *J. Catal.* **2017**, *352*, 394. https://doi.org/10.1016/j.jcat.2017.05.027.

(88) Ding, S.; Dong, T; Peppel, T.; Steinfeldt, N.; Hu, J.; Strunk, J. Construction of amorphous SiO_2 modified β-Bi_2O_3 porous hierarchical microspheres for photocatalytic antibiotics degradation. *Colloid and Interface Science* **2021**, *607*, 1717. https://doi.org/10.1016/j.jcis.2021.09.029.

(89) Barbosa, A.; Aquino, R; Neves, N.; Dentas, R.; Duarte, M.; Rocha, O. Kinetic study of dye removal using TiO_2 supported on polyethylene terephthalate by advanced oxidation processes through neural networks. *Water Science & Technology* **2019**, *79*, 1134. https://doi.org/10.2166/wst.2019.111.

(90) Grover, A.; Mohiuddin, I; Malik, A. K.; Aulakh, J. S.; Kim, K. H. Zn-Al layered double hydroxides intercalated with surfactant: Synthesis and applications for efficient removal of organic dyes. *Journal of Cleaner Production* **2019**, *240*, 118090. https://doi.org/10.1016/j.jclepro.2019.118090.

(91) Thakur, A.; Kumar, P; Kaur, D. TiO2 nanofibres decorated with green synthesized PAu/Ag@CQDs for the efficient photocatalytic degradation of organic dyes and pharmaceutical drugs. *RSC Advances* **2020**, *10*, 8941. https://doi.org/10.1039/c9ra10804a.

(92) Sidhu, J. S.; Raj, P; Singh, N.; Pandiyan N. Synthesis of Ni(II) Complexes of Novel Naphthalimide Based Heterodipodal Schiff Base Ligands, Structure Characterization and Application for Degradation of Pesticides. *European Journal of Inorganic Chemistry* **2020**, *32*, 461. https://doi.org/10.1002/ejic.202000461.

Chapter 2

Fabrication of 3D porous β-Bi_2O_3/BiOCl heterostructure for synergistically boosting the visible-light-driven degradation of organic pollutants

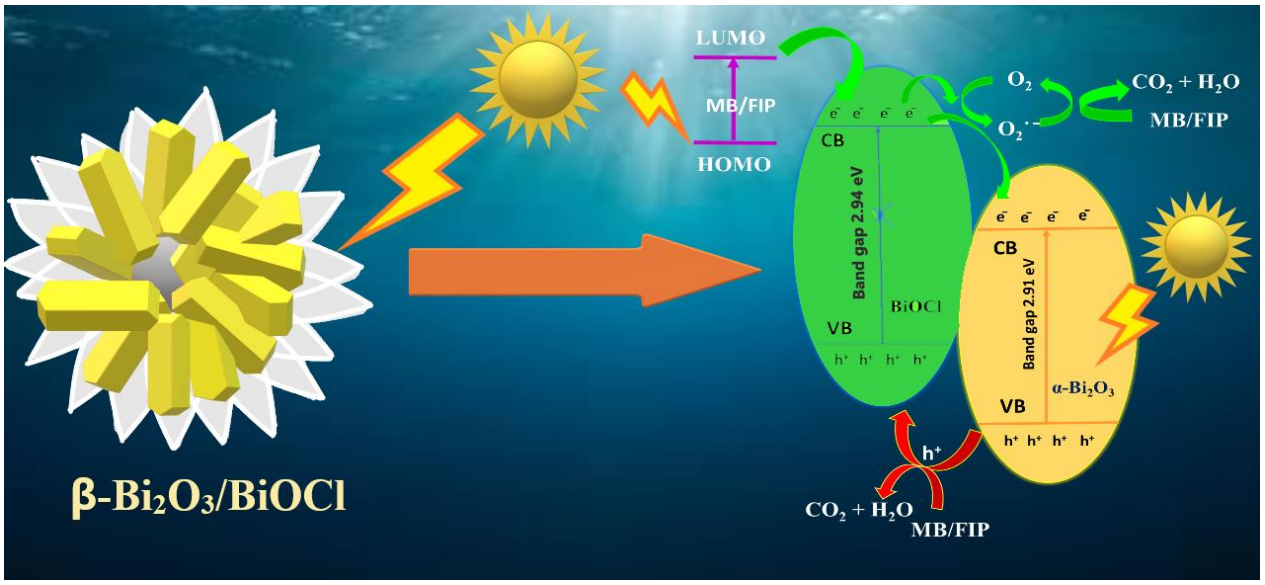

Highlights

- Composites of β-Bi_2O_3/BiOCl nanoflowers were fabricated via the in-situ method.
- Surface active sites unhindered owing to the position of β-Bi_2O_3 nanorods.
- A heterojunction electric field generated via β-Bi_2O_3 enhanced charge separation.
- ~93% and ~79% degradation efficiency was observed in visible light for MB and FIP respectively.

2.1 Introduction

Unabated urbanization and industrialization have led to large-scale energy production and thereby, pollution mainly toxin discharge, needless to say having a tremendous effect on all living beings.[1] Industrial dye discharge mainly via textile and leather industries directly into water bodies without any pre-treatment[2] leads to carcinogenic, mutagenic, and genotoxic effects.[3] Methylene blue (MB) which is a cationic azo dye has pernicious repercussions on the central nervous system and with extended risk can lead to anemia and hypertension.[4] While cardiovascular and metabolic problems arise with the use of fipronil (FIP) in crops.[5] Even their infinitesimal amount can lead to cardiovascular, reproductive, metabolic, and neurological disorders.[6] Therefore, to protect both flora and fauna, these types of contaminant removal are essential.[3]

Plenty of strategies have been reported for water purification such as adsorption, oxidation, sedimentation, and biological and chemical precipitation processes.[1] But they pose limitations of high cost, temperature and pressure barriers, reaction kinetics, and inability to completely eradicate the toxins.[7] Due to the simple procedure and high efficacy, photocatalysisis optimum for pollutant degradation.[8] Photocatalysis includes the eradication of toxic waste and produces less harmful products in addition to CO_2 and H_2O. But heterogeneous photocatalysts are responsive to UV radiation only and therefore have limited use, as UV lightaccounts for merely 5% of the total solar spectrum. To decipher the problem, doping or creating complex heterojunctions between different semiconductors having unequal band gaps was done. This made their utility in visible light possible. Thus, for the complete utilization of solar light, enormous efforts have been taken to design materials that are stable and highly efficientin harvesting a wide spectrum of visible light. These are referred to as visible-light-induced photocatalysts. They are highly feasible owing to the 48% accountability of visible light in thesolar spectrum.[9,10] Over the years, breakthroughs have been made to develop visible-light-induced heterojunction photocatalysts for the

enhancement of photocatalytic activity.[11,12] Amongst them, bismuth-based nanomaterials have played a major role in semiconductor-based photocatalysis.[13] When compared with traditional photocatalysts, Bi_2O_3 has a narrow bandgap(~ 2.5 eV) besides having numerous oxygen vacancies and high optical conductivity. Particularly, β-Bi_2O_3 shows higher photocatalytic efficacy than α-Bi_2O_3 owing to the lower bandgap energy and higher optical absorption in a wider visible light spectrum. However, scarce research is there concerning β-Bi_2O_3 due to the difficulty in the synthesis of the metastable phase of β-Bi_2O_3.[14] Still, pure β-Bi_2O_3 poses a limitation of the rapid electron-hole pair recombination.[13] BiOCl has emerged as a budding semiconductor with an indirect bandgapand high anisotropic layers, good optical activity as well as chemical stability. With a bandgap[13] similar to β-Bi_2O_3, it is a suitable semiconductor for constructing heterostructures. Moreover, owing to its layered structure, the transportation and separation of electron-hole pairs become easier which escalates photocatalytic performance.[15] But BiOCl has a bandgap between 3.2 eVto 3.5 eV[13] and a bad photocatalytic response as compared to β-Bi_2O_3. Given the poor performances of novel β-Bi_2O_3 and BiOCl, the construction of β-Bi_2O_3/BiOCl heterostructure is suggested. Moreover, the heterojunction formation between β-Bi_2O_3 and BiOCl will improvethe charge separation, reduce the recombination rate and enhance the photocatalytic performance. The β-Bi_2O_3/BiOCl heterostructure has an additional advantage for its utility in both UV and visible light and therefore, in a wide solar spectrum. Additionally, the in-situ synthesis method for β-Bi_2O_3/BiOCl composite is not only inexpensive and environment-friendly but also requires no intermediate step, thereby providing a feasible synthesis process.[9] Numerous studies validated the improvement in the photocatalytic performance of Bi_2O_3 when combined with BiOCl. Kong *et al.*[13] fabricated hollow flower-like β-Bi_2O_3/BiOClmicrospheres via the in-situ method of hollow β-Bi_2O_3 spheres. Various composites were synthesized by varying molar contents of BiOCl and the best performance was shown by the binary composite with 85.7% molar contents of HCl and an efficiency of 99.5%. Tang *et al.*[15] synthesized β-

Bi_2O_3/BiOCl heterostructure via β-Bi_2O_3 nanorods and BiOCl nanosheets. The catalyst showed improvement in photocatalytic rhodamine-B deterioration relative to pure β- Bi_2O_3 and BiOCl. The molar content of BiOCl was varied and the composite with 1.5 mol/L ofHCl showed the best performance (99.4%). Zhao *et al.*[16] synthesized Bi_2O_3/BiOCl through consistent BiOCl microspheres via the self-sacrificial template process. BiOCl microspheres composed of nanosheets changed to Bi_2O_3 nanorods with subsequent alkaline addition. The composite showed remarkable performance in degrading methyl orange under visible light. Different composites constructed through varying the time of immersion in NaOH suggested 100% degradation efficiency after 40 min immersion and 80 min illumination. However, limited work has been done for the photocatalytic degradation of pollutants via β-Bi_2O_3/BiOCl,fabricated by a facile and environmental-friendly method.

In the present study, β-Bi_2O_3/BiOCl heterostructures constructed via β-Bi_2O_3 nanorods and flower-like BiOCl by the in-situ method of self-sacrificial precursor BiOCl and using an alkaline path i.e. NaOH. The as-synthesized composite was used to degrade MB and FIP undervisible light. Investigation of numerous factors like pH, catalyst concentration, and reusability study was performed. To determine the photodegradation mechanism, trapping experiments were conducted. For testing the reusability efficiency of the composite, XRD was performed after photodegradation. The originality of the work is attributed to the nanoflower-like β- Bi_2O_3/BiOCl composite designed via the in-situ method employed for MB and FIP degradation with high efficiency. This study provides a facile synthesis step for β-Bi_2O_3 which otherwise poses difficulty owing to its metastable state. Varied weight ratios of Bi_2O_3/BiOCl composite with tetragonal β-phase of Bi_2O_3 for the application of degradation of insecticide FIP have not been reported in the literature to the best of the authors' knowledge.

2.2 Experimental Section

This section consists of the chemicals, materials, and methodologies used for the synthesis of the catalysts.

2.2.1 Chemicals and Materials

Bismuth nitrate pentahydrate ($Bi(NO_3)_3.5H_2O$), polyethylene glycol-5000 (PEG-8000), sodium hydroxide (NaOH), ethylene glycol ($C_2H_6O_2$), and potassium chloride (KCl) were brought via Thermo Fisher Scientific India Pvt. Ltd. and S. D. Fine-Chem Limited, Mumbai. Double distilled water was used while MB was procured from Merck Crop Science Ltd, India, and FIP was purchased from Bayer Crop Science Ltd., India.

2.2.2 Synthesis

This section includes the synthesis methodologies of β-Bi_2O_3, BiOCl, and β-Bi_2O_3/BiOCl.

2.2.2.1 Synthesis of Bi_2O_3

Bi_2O_3 nanorods were designed through the precipitation method. 0.05 M $Bi(NO_3)_3.5H_2O$ and 1 g of PEG-8000 were mixed in water via magnetic stirring and simultaneous heating. 5 M NaOH solution was included dropwise till yellow-colored precipitates appeared with consistent mixing at 80°C. Once cooled, the yellow-colored productwas given a washing with ethanol and distilled water (at least thrice), filtered, and dried at 60°C overnight. The resultant yellow powder was calcined at a temperature of 500°C for 2 h (**Scheme 2.1**).[17]

2.2.2.2 Synthesis of BiOCl

2 mmol $Bi(NO_3)_3.5H_2O$, magnetically stirred with ethylene glycol for 30 min. About

0.149 g KCl in 10 mL water was added dropwise. The solution was warmed in an oil bath for 5 min and stirred overnight. The obtained solution was centrifuged and the white-colored precipitates dried overnight at 60°C **(Scheme 2.1)**.[18]

2.2.2.3 Synthesis of β-Bi_2O_3/BiOCl

β-Bi_2O_3/BiOCl was fabricated via the in-situ precipitation method of BiOCl and NaOH. The obtained white crystals of BiOCl and 0.05 M $Bi(NO_3)_3.5H_2O$ were thoroughly mixed in water by magnetic stirring and simultaneous heating. 1 g of PEG-8000 was included in the solution. Finally, 5 M NaOH solution was put dropwise along with continuous magnetic stirring with a color change from white to pale yellow while maintaining the temperature at 80°C. Once cooled, the pale-yellow product was given washing with ethanol and distilled water (at least thrice), filtered, and dried at 60°C overnight. The resultant pale-yellow powder was calcined at 500°C for 2 h (**Scheme 2.1**).[17] Ratios were varied by varying weights to synthesize different composites of β-Bi_2O_3/BiOCl i.e. 1:1 β-Bi_2O_3/BiOCl, 1:3 β-Bi_2O_3/BiOCl, and 3:1 β-Bi_2O_3/BiOCl.

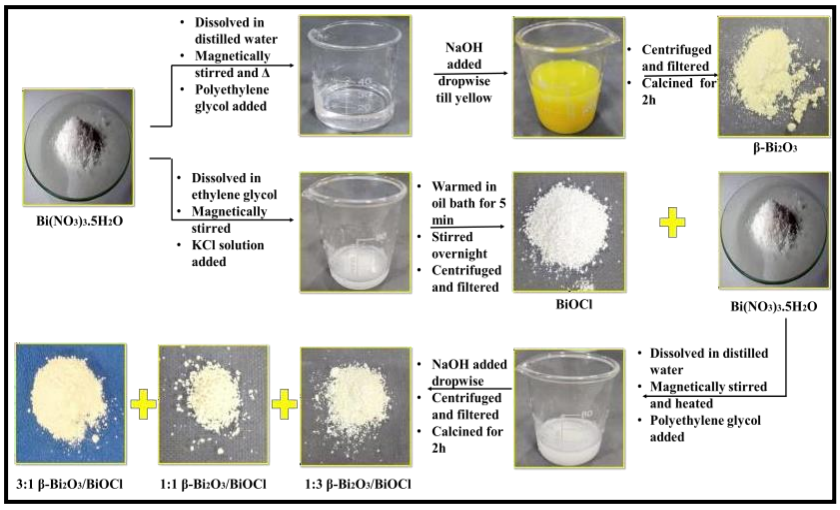

Scheme 2.1. Illustration for the synthesis of β-Bi_2O_3, BiOCl, and β-Bi_2O_3/BiOCl.

2.2.3 Characterization

Microtrac Belsorp Mini-II (Bel, Japan, Inc.) surface analyzer determined the pore-

size distribution and surface area via BET N_2 adsorption-desorption isotherm at 77.3 K. Pre-treatment was performed at 100℃ for 6 h. The pore size distribution curves were scrutinized via Barrett-Joyner-Halenda (BJH) analysis. X-ray diffraction (XRD) method scrutinized the crystallinity of the catalysts by using a PANanalytical X-ray diffractometer using Cu-Kα radiation at a voltage of 45 kV and scan between10-90°. Field emission scanning electron spectroscopy (FESEM SU8180, Hitachi, Tokyo, Japan) with Oxford INCTA energy dispersive spectrometer (EDS) and transmission electron spectroscopy (TEM, JEM-2100F) were availed to scrutinize the surface morphology and microstructure of the binary composite. To get a detailed understanding of the elemental nature of the as-synthesized composite, the PHI-5000 VersaProbe-III system with a monochromatic Al Kα X-ray source (1486.7 eV) was availed for the X-ray photoelectron spectroscopy (XPS). The UV-Vis Diffusion Reflectance Spectroscopy (DRS) was done using the diffuse absorbance mode via a Hitachi-3900H spectrophotometer (Shimadzu, Japan). Photoluminescence (PL) spectra were procured via the fluorescence spectrometer (F-4500, Hitachi, Japan). The cyber scan pH 1100 (Eutech, Singapore) was employed to compute and accommodate pH. Finally, a UV-Vis spectrophotometer (Shimadzu, UV-2600) investigated the photodegradation of the pollutants.

2.2.4 Photocatalytic Activity

The photodegradation of the pollutants FIP and MB was scrutinized by placing the solutions in a photoreactor. 2 mg of the photocatalyst was thoroughly mixed in 15 mL FIP/MB pollutants with 5 ppm concentration. The MB and FIP solutions were kept in dark for 45 min to attain adsorption-desorption equilibrium. It was irradiated in visible light for another 45 min and 90 min (65 W CFL lamp, Phillips, k>400 nm at 125 W/m^2 intensity) for MB and FIP, respectively. The photodegradation activity was noted at the maximum absorption bands i.e. λ_{max} = 664 nmfor MB and 376 nm for FIP via a UV-Vis spectrophotometer.

Lambert Beer's law states that the absorbance depends directly on the concentration of the solution and thus, the percent degradation is as follows (**Eq. (2.1)**)[3]:

$$\% D = \{(A_o-A_t)/A_o\} \times 100 = \{(C_o-C_t)/C_o\} \times 100 \quad (2.1)$$

Where A_o and A_t denote the absorbance of dye/pesticide at a time '0' and 't' respectively, while C_o and C_t denote the concentration of dye/pesticide at a time '0' and 't' respectively.

Mineralization of MB and FIP was evaluated in the terms of TOC removal. 15 mL of MB and FIP with 1:1 Bi_2O_3/BiOCl (0.13 g/L) were irradiated under visible for 45 and 90 min, respectively. TOC was measured before and after the photocatalytic treatment at a time '0' and't', respectively. Percentage TOC reduction can be calculated by **Eq. (2.2)**[3] as follows:

$$\% TOC = \{(TOC_o-TOC_t)/TOC_o\} \times 100 \quad (2.2)$$

2.3 Results and Discussion

2.3.1 Photocatalyst Characterization

2.3.1.1 X-ray Diffraction Studies

XRD study measured the crystal planes of β-Bi_2O_3, BiOCl, and β-Bi_2O_3/BiOCl composites.The β-Bi_2O_3 sample (**Fig. 2.1 (a)**) unveiled the XRD peaks at 27.95°, 31.76°, 32.69°, 42.4°, 46.22°, 52.49°, 54.86°, 56°, 59° and 68.5° corresponding to (201), (211), (220), (212), (222), (411), (203), (421), (402) and (440) planes, respectively correlate with β-Bi_2O_3's tetragonal phase (JCPDS card no. 27-0050) (**Fig. 2.1 (a)**).[15] Pure BiOCl sample exhibited sharp peaks at 12°, 24.15°, 25.93°, 32.58°, 33.5°, 34.81°, 36.5°, 41°, 46.7°, 48.4°, 49.8°, 53.35°, 54.2°, 55.2°, 58.7°, 60.54° and 68.2° corresponding to (001), (002), (101), (110), (102), (111), (003), (112), (200), (201), (113), (202), (211), (104), (212), (114) and (220) planes, respectively suggesting BiOCl's tetragonal phase (JCPDS card no. 06-0249) (**Fig. 2.1(a)**).[15] Finally, the XRD pattern of β-Bi_2O_3/BiOCl displayed the peaks relating to BiOCl and β-Bi_2O_3.

Table 2.1. The Surface area, Mesopore size, and Total pore volume of the as-fabricated photocatalysts.

Photocatalyst	**Surface Area (m^2/g)**	**Total pore volume (cm^3/g)**	**Mesopore size (nm)**
β-Bi_2O_3	18	0.19	22.26
BiOCl	11	0.04	14.68
1:1 β-Bi_2O_3/BiOCl	78	0.43	42.98
1:3 β-Bi_2O_3/BiOCl	47	0.55	46.78
3:1 β-Bi_2O_3/BiOCl	20	0.19	39.46

2.3.1.2 Nitrogen Adsorption/Desorption Studies

N_2 adsorption-desorption work illustrated the type-IV isotherm (**Fig. 2.1 (b)**), suggesting a mesoporous structure of the as-prepared photocatalysts. As shown in **Fig. 2.1 (b)**, BiOCl showsa type H3 hysteresis loop, indicating the presence of porous structure formed between each inter-crossed BiOCl nanosheets.[14] β-Bi_2O_3, 1:1 β-Bi_2O_3/BiOCl, 1:3 β-Bi_2O_3/BiOCl, and 3:1 β-Bi_2O_3/BiOCl display the H1 hysteresis loops consisting of sharp adsorption-desorption branches which validated the constancy and structure of the composite. The mesoporous nature was affirmed by the adsorption isotherms as well as the BJH plot (**Fig. 2 (c)**). The BET surface area studies formulated the surface area, mean pore volume, and mean pore diameter. The observed surface area for β-Bi_2O_3, BiOCl, 1:1 β-Bi_2O_3/BiOCl, 1:3 β-Bi_2O_3/BiOCl, and 3:1 β- Bi_2O_3/BiOCl was measured to be 18, 11, 78, 47, and 20 m^2/g, respectively. Augmentation in the surface area and total pore volume from β-Bi_2O_3 and BiOCl to β-Bi_2O_3/BiOCl composites was noted (**Table 2.1**).

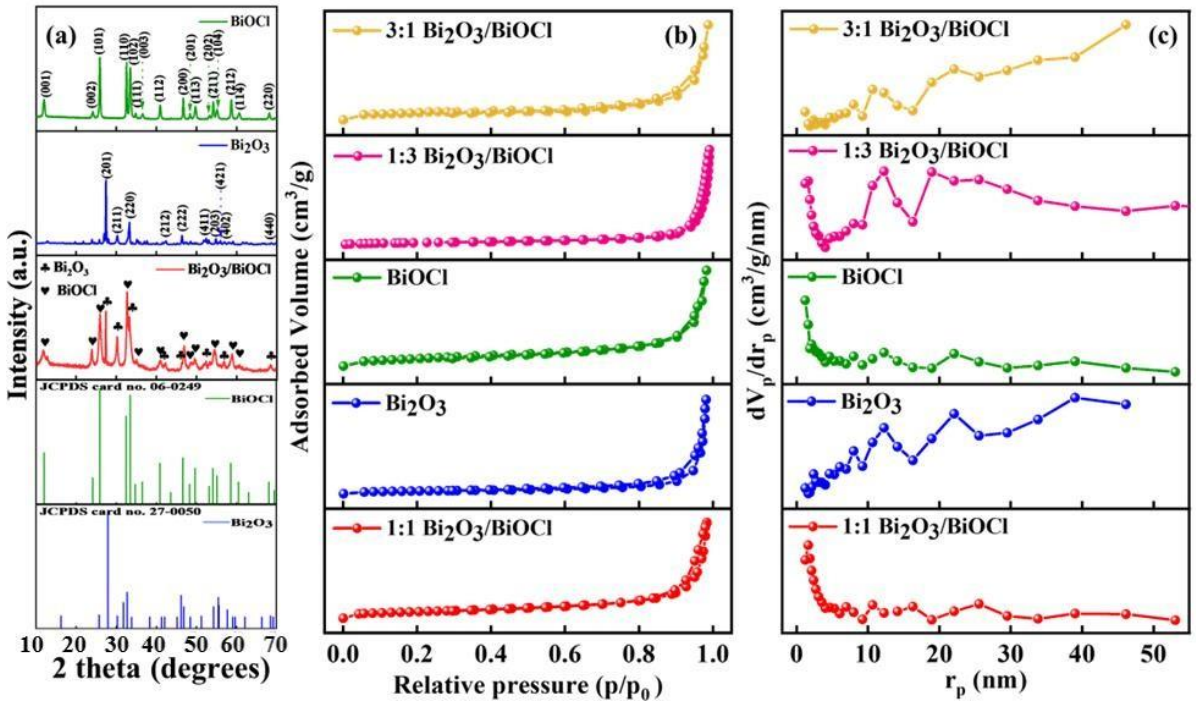

Fig. 2.1. (a) XRD pattern, (b) N_2 adsorption-desorption isotherms, and (c) pore size distribution curves of the as-prepared catalysts.

2.3.1.3 XPS Analysis

For the detailed study of the element's oxidation state in 1:1 β-Bi_2O_3/BiOCl, XPS analysis was employed. The XPS survey spectrum illustrated in **Fig. 2.2 (a)** depicts the presence of Bi, Cl, and O. For the novel β-Bi_2O_3, Bi 4f spectra depicts doublet relating to Bi $4f_{7/2}$ and $4f_{5/2}$ at 158.4eV and 163.7 eV, respectively suggesting the presence of Bi^{3+} in β-Bi_2O_3.[15] The binding energies in BiOCl relating to Bi $4f_{7/2}$ and $4f_{5/2}$ are 159.5 eV and 164.8 eV, respectively indicating the presence of Bi^{3+} in BiOCl.[15] **Fig. 2.2 (b)** depicts Bi 4f spectra with doublet for β-Bi_2O_3/BiOCl, relating to Bi $4f_{7/2}$ and $4f_{5/2}$ at 156.6 eV and 161.8 eV, respectively indicating the existence of Bi^{3+} in β-Bi_2O_3/BiOCl.[15] This indicated the same value of shifting in the heterostructure as compared to novel β-Bi_2O_3 and BiOCl. For β-Bi_2O_3, the O1s spectra display a peak at 529.5 eV, indicating the lattice oxygen (Bi-O) while the other peak is attributed to surface hydroxyl groups and adsorbed H_2O.[15] For the composite,

two convoluted peaks were observed for O1s at 527.4 eV and 531.7 eV (**Fig. 2.2 (c)**). The peak at 527.4 eV depicts the existence of lattice O while the peak at 531.7 eV relates to the binding energy of the adsorbed O on the surface of the composite,[13] suggesting a shift in binding energies with heterojunction formation. For novel BiOCl, two convoluted peaks Cl 2p for $2p_{3/2}$ and $2p_{1/2}$ exist at 198.1 eV and 199.7 eV, respectively[15] while for the heterostructure, two convoluted peaks $2p_{3/2}$ at 195.4eV and $2p_{1/2}$ at 196.7 eV were observed (**Fig. 2.2 (d)**),[13] suggesting the shift to lower binding energies in the composite indicating the strong interaction between β-Bi_2O_3 and BiOCl.

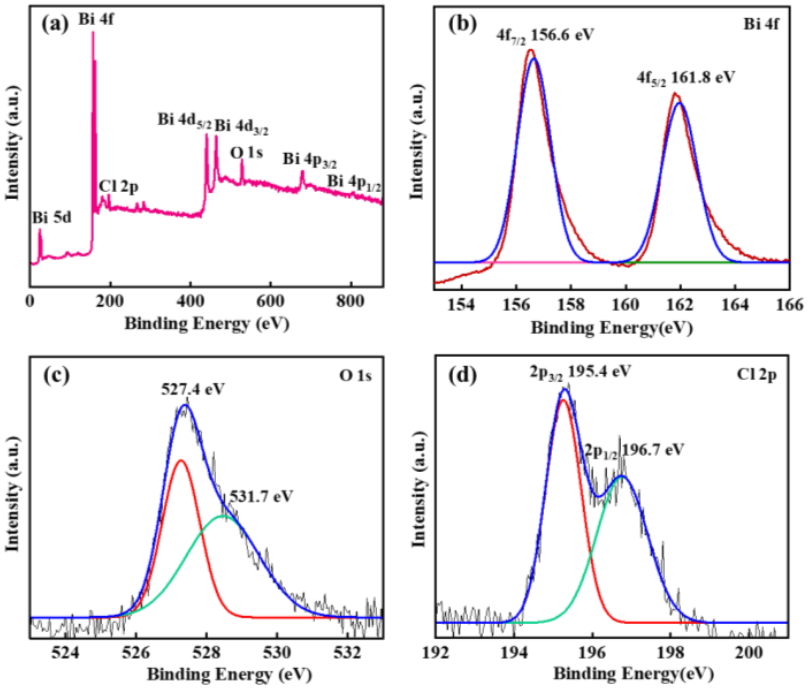

Fig. 2.2. (a) XPS spectrum, deconvoluted peaks of (b) Bi, (c) O, and (d) Cl of 1:1 β-Bi_2O_3/BiOCl binary composite.

2.3.1.4 EDS and Elemental Mapping

For the 1:1 β-Bi_2O_3/BiOCl composite, elemental mapping images are shown in **Fig. 2.3(b-d)**. It confirmed the presence of Bi, Cl, and O in the binary catalyst. The composite was found to be homogeneously dispersed.[13] EDS studies scrutinized the elemental structure

of the composite (**Fig. 2.3 (a)**). The weight percentages in the 1:1 β-Bi_2O_3/BiOCl are Bi with 89.38%, Cl with 8.01%, and O with 2.60%.

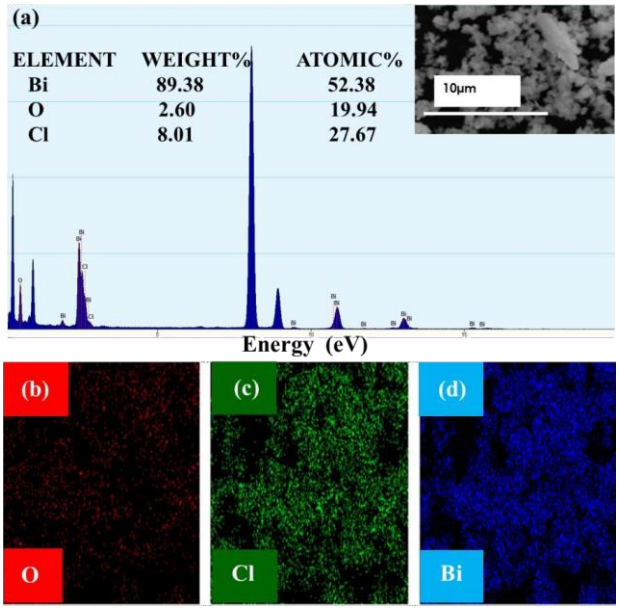

Fig. 2.3. (a) EDS spectrum, elemental mapping images for (b) O, (c) Cl, and (d) Bi of 1:1 β-Bi_2O_3/BiOCl binary composite.

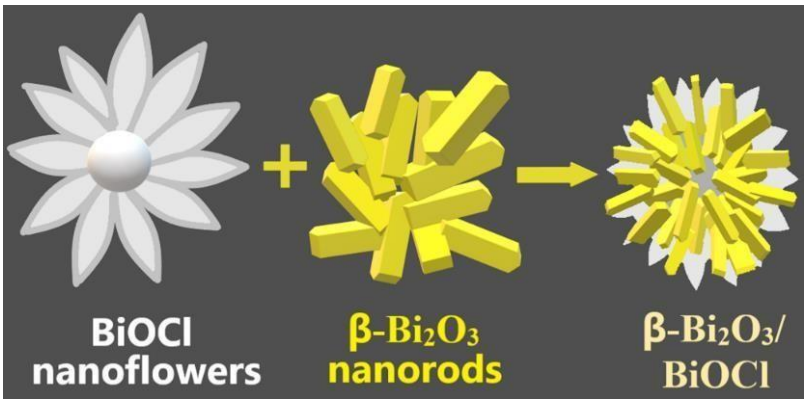

Scheme 2.2. Schematic illustration of β-Bi_2O_3/BiOCl fabrication.

2.3.1.5 FESEM and HRTEM Studies

FESEM studies scrutinized the surface morphology of β-Bi_2O_3/BiOCl, β-Bi_2O_3, and BiOCl. Capsule-like nanostructure was observed in pure BiOCl, accumulated to form nanoflowers (**Fig. 2.4 (a)**). **Fig. 2.4 (b)** depicts nano rod-like structures for pure β-Bi_2O_3.

Finally, it was observed that the β-Bi_2O_3/BiOCl composite showed peony flower-like nanostructures and nanorods (**Fig. 2.4(c-d)**), suggesting the presence of BiOCl and β-Bi_2O_3, respectively. Thus, after the treatment with NaOH, Bi_2O_3 nanorods (correspond with the XRDand XPS data), designed via the in-situ method on BiOCl's surface are visible. The in-situ growth between β-Bi_2O_3 and BiOCl should be close-knitted for the facile electron-hole pair migration.[18] The elaborative structural study of the composite was carried out by HRTEM analysis (**Fig. 2.4 (e-f)**). As depicted in **Fig. 2.4 (e)**, the β-Bi_2O_3/BiOCl composite comprises rod-like β-Bi_2O_3[19] and flower-like BiOCl.[20] **Fig. 2.4 (f)** displays the lattice spacing of 0.32 nm relating to (201) plane and 0.34 nm spacing relating to (210) plane of tetragonal β-Bi_2O_3, while the lattice spacing of 0.35 nm relating to (002) plane and 0.73 nm lattice relating to (001) plane of tetragonal BiOCl.[15] Moreover, the yellow circle depicting the cross lattice fringes indicates the complete heterojunction formation between β-Bi_2O_3 and BiOCl.[21] **Scheme 2.2** illustrated a schematic diagram of β-Bi_2O_3/BiOCl heterostructure synthesis via the in-situ method of BiOCl acting as a self-sacrificial template and NaOH, providing an alkaline medium.

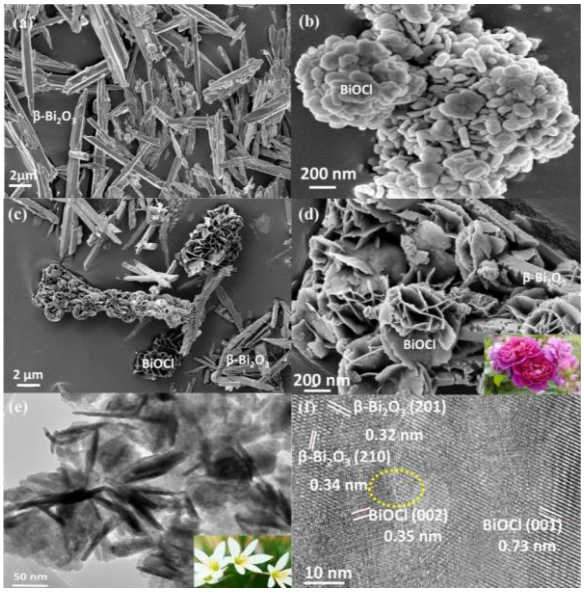

Fig. 2.4. FESEM illustrations (a) β-Bi_2O_3, (b) BiOCl, (c-d) 1:1 β-Bi_2O_3/BiOCl, and (e-f) HRTEM illustrations of 1:1 β-Bi_2O_3/BiOCl.

2.3.1.6 Optical Properties

Charge carrier reconciliation has a significant part in the photodegradation process. With less photoluminescence intensity (PL), the recombination tendency of the electron-hole pair is also low while the charge separation is high.[22] To record the PL spectra, an excitation wavelength of 325 nm was given **Fig. 2.5 (a)**. The emission wavelength for the as-synthesized photocatalysts was found to be 443 nm. The PL intensity of β-Bi_2O_3/BiOCl was lower than the pure β-Bi_2O_3 and pure BiOCl, suggesting efficacy in electron-hole pair partition and suppression of electron-hole pair recombination via heterojunction formation and therefore, an elevated photocatalytic activity was observed.[23]

The bandgap of β-Bi_2O_3/BiOCl was scrutinized by UV-Visible diffuse reflectance spectroscopy (DRS). To formulate bandgap energy, tauc's plot was designed. The equation (**Eq. (2.3)**)[3]:

$$(\alpha h\nu)^{1/2} = A(h\nu - E_g)n/2 \quad (2.3)$$

Where α, h, E_g, ν, A, and n are absorption coefficient, Planck constant, bandgap energy, light frequency, the proportionality constant, and optical transition type of semiconductors, respectively (**Fig. 2.5 (c)**). **Fig. 2.5 (b)** illustrates UV-Vis DRS of β-Bi_2O_3, BiOCl, and β-Bi_2O_3/BiOCl. β- Bi_2O_3 displays evident visible-light absorption at an absorption edge of 570 nm.[24] BiOCl displays only UV-light absorption at an absorption edge of 390 nm.[25] Finally, β- Bi_2O_3/BiOCl displayed visible light absorption at an absorption edge of 540 nm.[21] The optical bandgaps[16] (calculated via **Eq. (2.3)**) for pure β-Bi_2O_3, pure BiOCl, and heterostructure β-Bi_2O_3/BiOCl were found to be 2.5 eV (same as the literature value for β-Bi_2O_3),[26] 2.94 eV, and 2.25 eV, respectively (**Fig. 2.5 (c)**). On account of the large bandgap of BiOCl, the absorption edge of β-Bi_2O_3/BiOCl heterojunction shows a blue shift from that of pure β-Bi_2O_3.[13]

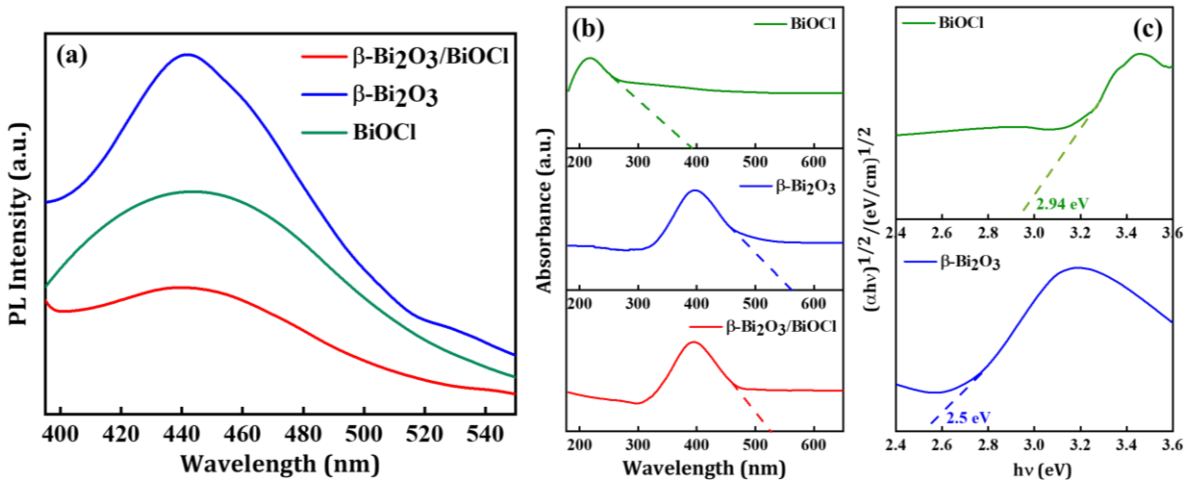

Fig. 2.5. (a) Photoluminescence spectra, (b) UV Visible diffuse reflectance spectra, and (c) Tauc's plot of the as-prepared catalysts.

2.3.2 Methylene Blue and Fipronil Photocatalytic Degradation

The catalytic ability of 1:1 β-Bi_2O_3/BiOCl was scrutinized by photodegrading organic pollutants like MB[27] and FIP[28] under visible light. 5 mg/L of MB and 600 mg/L of FIP were used initially. It took 45 min for the adsorption-desorption equilibrium to set up in dark and then illuminated under visible light (45 min for MB and 90 min for FIP). The photodegradation activity without the 1:1 β-Bi_2O_3/BiOCl was also conducted. It was perceived that with no catalyst, the photodegradation efficiencies for both MB (2.65%) and FIP (4.95%) were very low (**Fig. 2.6 (a), Fig. 2.6 (c)**), revealing the necessity of the composite in the pollutant deterioration activity.

To evaluate the rate constant, **Eq. (2.4)**[3] was used:

$$\ln (C/C_0) = -kt \qquad (2.4)$$

Where k denotes the rate constant, C_0 denotes the concentration at time = '0' and C denotes the concentration at a time 't'.

Fig. 2.6 (a), Fig. 2.6 (c) illustrate the kinetic degradation assessment of FIP and MB, both with and without photocatalyst. Notably, the absorbances devoid of photocatalyst were

merely 2.65% for MB ($k = 6.006 \times 10^{-4}\ min^{-1}$) (**Fig. 2.6 (b)**) and 4.95%for FIP ($k = 6.103 \times 10^{-4}\ min^{-1}$) (**Fig. 2.6 (d)**). The photodegradation activity was found tobe maximum for the 1:1 β-Bi_2O_3/BiOCl composite with 93.7% efficiency for MB ($k = 0.05883\ min^{-1}$) (**Fig. 2.6 (b)**) and 79.8% efficiency for FIP ($k = 0.01481\ min^{-1}$) (**Fig. 2.6 (d)**) in comparison to pure β-Bi_2O_3, pure BiOCl, 1:3 β-Bi_2O_3/BiOCl and 3:1 β- Bi_2O_3/BiOCl. The rate constants of β-Bi_2O_3, BiOCl, 1:1 β-Bi_2O_3/BiOCl, 1:3 β- Bi_2O_3/BiOCl, and 3:1 β-Bi_2O_3/BiOCl for both FIP and MB photodegradation are mentioned in **Table 2.2**. Therefore, the heterojunction 1:1 β-Bi_2O_3/BiOCl showcased commendable efficacy in degrading pollutants under visible light.

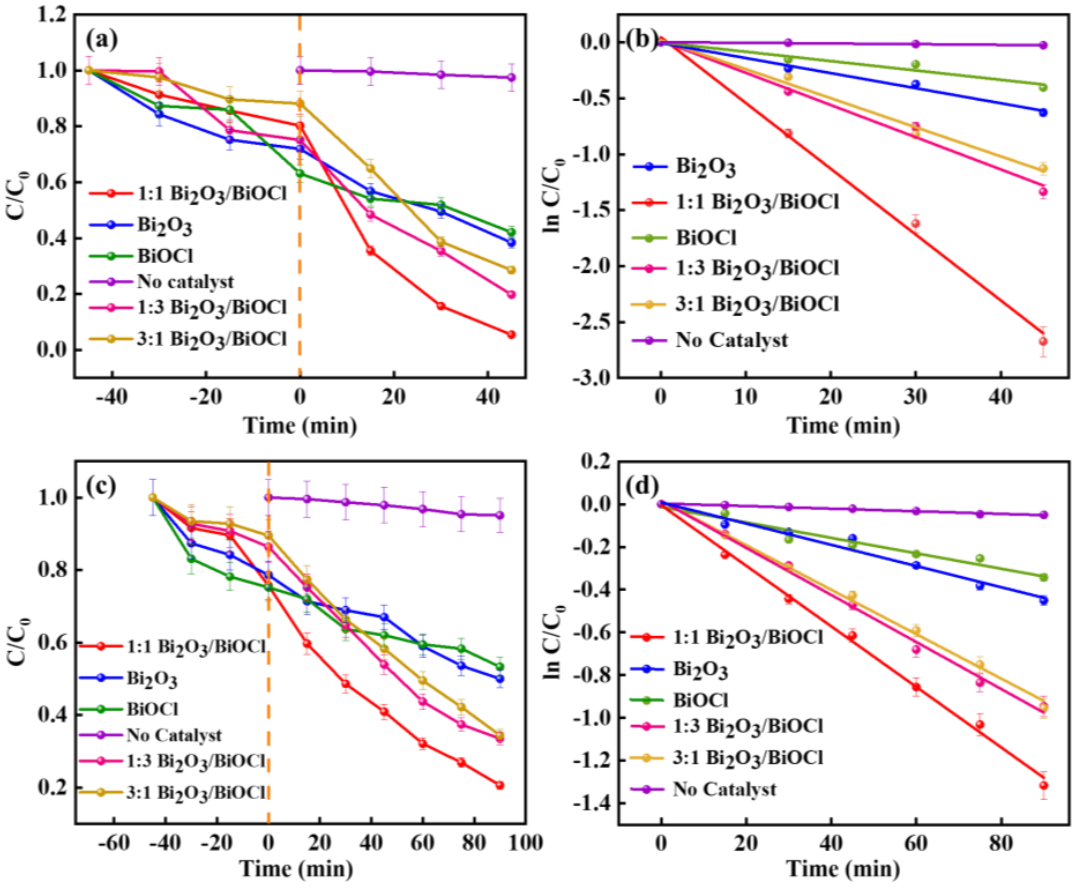

Fig. 2.6. Kinetic assessment of the as-prepared catalysts for photocatalytic degradation (a, b) MB and (c, d) FIP.

Table 2.2. Rate constants for the degradation of MB and FIP.

Photocatalyst	Rate Constants		% Degradation	
	MB (min^{-1})	FIP (min^{-1})	MB	FIP
β-Bi_2O_3	0.01347	0.00503	54.83	49.63
BiOCl	0.00837	0.00384	60.62	45.92
1:1 β-Bi_2O_3/BiOCl	0.05883	0.01481	93.71	79.87
1:3 β-Bi_2O_3/BiOCl	0.04846	0.00974	89.85	67.69
3:1 β-Bi_2O_3/BiOCl	0.0457	0.00927	88.28	65.73

2.3.2.1 Catalyst Concentration Studies

The degradation process of both the pollutants was scrutinized by studying the action of catalyst concentration using. **Fig. 2.7 (a)** displays the degradation activity of different catalyst concentrations ranging from 0.06 to 0.4 g/L in both MB and FIP. The photodegradation activity was highest at 0.13 g/L and gradually decreased from 0.13g/L to 0.40 g/L for both MB and FIP. It was attributed to the deactivation of sites beyond a particular concentration since, in the beginning, the dye adsorption on the catalyst's surface occurs and any additional incorporation will bear no results. It causes the opaqueness of the solution and scattering of light.

2.3.2.2 pH Studies

For β-Bi_2O_3/BiOCl, the pH_{pzc} was formulated[29] to be ~pH 5 (**Fig. 2.7 (b)**), suggesting the surface of the composite to be negatively charged when $pH>pH_{pzc}$ (i.e., pH>5) and positively charged when $pH<pH_{pzc}$.[3] The impact of pH variation (pH 1 to 12) on the

degradation process via 0.13 g/L β-Bi_2O_3/BiOCl composite was recorded (**Fig. 2.7(c)**). To secure the pH, a dilute solution of NaOH and HCl was added. The photodegradation efficiency was maximum at pH 8 (93.27%) for MB which is ascribed tothe interplay between the cationic dye MB[3] and the composite's negative surface.[16] For FIP, the highest degradation activity, that is, 79.96% was achieved at pH 4, attributed to the interplay between the anionic dye FIP[4] and the composite's positive surface.[15]

2.3.2.3 Reusability Studies

The separation of the powder catalyst after the dye degradation process poses a major concern, which could be overcome by centrifugation. Due to the temporary adsorption of MB dye on the surface of the photocatalyst, the as-prepared catalyst couldbe easily separated. To assess the reusability efficiency of the material, the recovered catalyst was washed several times with distilled water, centrifuged, dried, and reused.[2] Itwas perceived that after 4 consecutive cycles of degradation, the efficiency reduced by about 79.95% for MB and 69.82% for FIP[31] (**Fig. 2.7(d)**). To affirm the intactness of thecomposite, XRD analysis was done before and after the degradation activity (**Fig. 2.7 (e)**).[32]

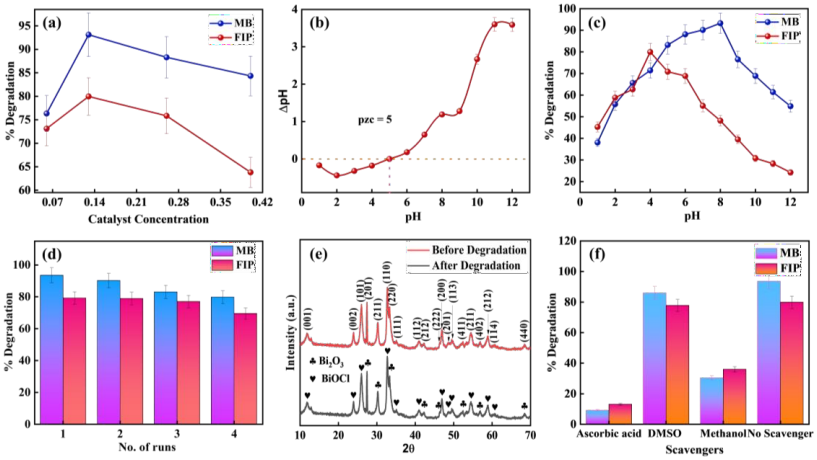

Fig. 2.7. Photocatalytic analysis: (a) catalyst concentration variation, (b) pH_{PZC} formulation, (c) pH changes, (d) reusability studies, (e) XRD patterns of the composite before and after reusability, (f) scavenger analysis by 1:1 β-Bi_2O_3/BiOCl binary composite.

2.3.2.4 Plausible Mechanism

Scavenger studies were employed to scrutinize the prominent radical species involved in the degradation activity by DMSO, methanol, and ascorbic acid, corresponding to hydroxide radical ($^{\bullet}OH$), quenching holes (h^+), superoxide radical ($O_2^{\bullet}$), respectively (**Fig. 2.7 (f)**).[33] Ascorbic acid can scavenge $O_2^{\bullet-}$ as well as $^{\bullet}OH$ but the ascorbyl radical formed by the reaction between ascorbate and $^{\bullet}OH$ has low reactivity.[34] In the process, β-Bi_2O_3/BiOCl was used as a tool (**Fig. 2.7 (f)**). When the inhibition in thephotocatalytic activity by a scavenger is done, then the radical species of the scavenger is accountable for the degradation activity. Equal molars of DMSO, methanol and ascorbic acid were included in the solution. Notably, MB efficiencies by ascorbic acid, DMSO, and methanol were 9.14%, 85.97%, and 30.33%, respectively, indicating the prominent contribution of $O_2^{\bullet-}$ and h^+ in the degradation process. While FIP degradation efficiencies via DMSO, ascorbic acid, and methanol were 77.81%, 13.09%, and 35.97%, respectively, suggesting the eloquent contribution of h^+, and $O_2^{\bullet-}$ in the degradation process.

The band positions of the photocatalyst have a significant impact on the separation of e/h^+ pairs. The positions of the β-Bi_2O_3's and BiOCl's valence band (VB) and the conduction band (CB) can be formulated via **Eqs. (2.5) and (2.6)**[13]:

$$E_{CB} = X - E_c - 0.5E_g \quad (2.5)$$

$$E_{VB} = E_{CB} + E_g \quad (2.6)$$

Where X denotes the absolute electronegativity of the semiconductor, E_{VB} denotes the position of the edge of the valence band, E_{CB} denotes the position of the conduction band,E_g denotes the bandgap of the semiconductor and E_c denotes the energy of the free-electron of hydrogen (~ 4.5 eV). The electronegativity values of β-Bi_2O_3 and BiOCl are 5.95 eV and 5 eV, respectively. From the results of DRS, the band gaps of β-Bi_2O_3 and BiOCl are 2.5 eV and 2.94 eV. Therefore, the positions of the conduction band for β-$Bi_2O_3$and BiOCl are 0.2

eV and -0.97 eV, respectively, and the positions of the valence band for β-Bi_2O_3 and BiOCl are 2.7 eV and 1.97 eV, respectively. Based on these results, it was established that the n-type β-Bi_2O_3 and the p-type BiOCl can create an appropriate B-type heterojunction.

Based on the above analysis, it is inferred that the photocatalytic performance of the composite could be attributed to the p-n type heterojunction formation amongst β- Bi_2O_3 and BiOCl. A mechanism is proposed for the degradation of MB and FIP through β-Bi_2O_3/BiOCl heterostructure in visible light as shown in **Scheme 2.3**. For the n-type β-Bi_2O_3, the fermi level is nearer to the conduction band, and for the p-type BiOCl, the fermi level is nearer to the valence band. Due to the interconnection between β-Bi_2O_3 and BiOCl, there is a diffusion of electrons from the β-Bi_2O_3 to BiOCl and holes from BiOCl to β-Bi_2O_3. Due to this diffusion, there is an aggregation of positive charges in the β- Bi_2O_3 semiconductor region, on the other hand, gathering of negative charges near the BiOCl semiconductor region. With the Fermi level of the semiconductors of β-Bi_2O_3 and BiOCl reaching equilibrium, the generation of a built-in electric field from the β-Bi_2O_3 semiconductor to the BiOCl semiconductor occurs and the internal electric field opposes any further charge to diffuse between the semiconductors.[13] Simultaneously, there is a movement of the energy bands of the semiconductors in the opposite directions as a whole until the Fermi level of the semiconductors becomes flat, which finally results in the generation of a built-in electric field at the p-n junction interface from β-Bi_2O_3 to BiOCl.There is a significant role of the position of the photocatalyst band in the production and separation of photoinduced e^--h^+ pairs. Also, the transfer path of the photogenerated electrons and holes can be reasoned via the conduction band minimum of the photocatalyst and the maximum value of the valence band. After the heterojunction formation, the position of the conduction band of BiOCl is more negative than the position of β-Bi_2O_3's conduction band while the position of β-Bi_2O_3 is more positive than the position of BiOCl's valence band. This is an example of a B-type heterojunction. When the β-

Bi_2O_3/BiOCl heterostructure is irradiated under visible light, β-Bi_2O_3 gets excited via the visible photons to synthesize electrons and holes due to the slim bandgap (2.5 eV) (Eq. (2.9)), and the electrons in β-Bi_2O_3's VB are excited to its CB, producing holes in β-Bi_2O_3's VB. But due to a large bandgap of BiOCl, no excitation via the visible light occurs.[13]

Owing to β-Bi_2O_3's greater positive CB potential than O_2/ $O_2^{\bullet-}$ (-0.33 eV),[35] the electrons on the β-Bi_2O_3's CB are unable to produce $O_2^{\bullet-}$ by reacting with O_2. Due to β-Bi_2O_3's greater VB potential than BiOCl, the holes present on the VB of β-Bi_2O_3 can migrate to the VB of BiOCl by the formation of a heterojunction at the interfaces of the catalysts, leading to great efficacy in segregating the charge carriers.[15] Moreover, the pollutant molecules on the catalyst's surface are sensitized via visible light (**Eq. (2.7)**) to form electrons which eventually transfer to the CB of BiOCl (Eq. (2.8)) because of the greater negative potential of the LUMO of MB[36] and FIP than the CB of BiOCl.[15] The transferred electrons produce $O_2^{\bullet-}$ when reacting with dissolved O_2 (**Eq. (2.10)**) owing to BiOCl's greater negative CB potential as compared to O_2/ $O_2^{\bullet}$.[15] Lastly, the $O_2^{\bullet-}$ radicals and h^+ oxidize the adsorbed pollutant molecules (MB/FIP) and ultimately decompose them into CO_2 and H_2O (**Eq. (2.11-2.12)**).[4] Here, BiOCl acts as a central photocatalyst while β-Bi_2O_3 acts as a photo-sensitizer.[15] The reaction mechanism is as follows:

$$MB/FIP + h\nu \longrightarrow MB´/FIP´ \quad (2.7)$$

$$MB´/FIP´ + \beta\text{-}Bi_2O_3/BiOCl \longrightarrow MB^{+\bullet}/FIP^{+\bullet} + \beta\text{-}Bi_2O_3/BiOCl\ (e^-) \quad (2.8)$$

β-Bi_2O_3/BiOCl + $h\nu$ ⟶ $h^+ + e^-$ (2.9)

$$O_2 + e^- (CB_{BiOCl}) \longrightarrow O_2^{\bullet-} \quad (2.10)$$

$$MB\ (MB^{+\bullet})/FIP\ (FIP^{+\bullet}) + O_2^{\bullet-} (CB_{BiOCl}) \longrightarrow CO_2 + H_2O \quad (2.11)$$

$$MB\ (MB^{+\bullet})/FIP\ (FIP^{+\bullet}) + h^+/{}^{\bullet}OH\ (CB_{BiOCl}) \longrightarrow CO_2 + H_2O \quad (2.12)$$

In conclusion, BiOCl plays important role in photocatalytic activity while β- Bi_2O_3 creates a heterojunction electric field between β-Bi_2O_3 and BiOCl which enhances the charge partition and reduces e^--h^+ pair recombination. The existence of β-Bi_2O_3 facilitates the

broadening of the absorption edge of β-Bi_2O_3/BiOCl for visible light photodegradation and thus a better photocatalytic efficiency than pure β-Bi_2O_3 and pure BiOCl. Moreover, β-Bi_2O_3 nanorods are located outside the β-Bi_2O_3/BiOCl heterostructure, and therefore, the availability of free active sites on the β-Bi_2O_3/BiOCl composite.[15] Finally, it can be said that β- Bi_2O_3/BiOCl heterojunction photocatalyst is environment-friendly, has facile and cheap synthesis, and can have mass production. Thus, it is an efficient catalyst for toxin removal.

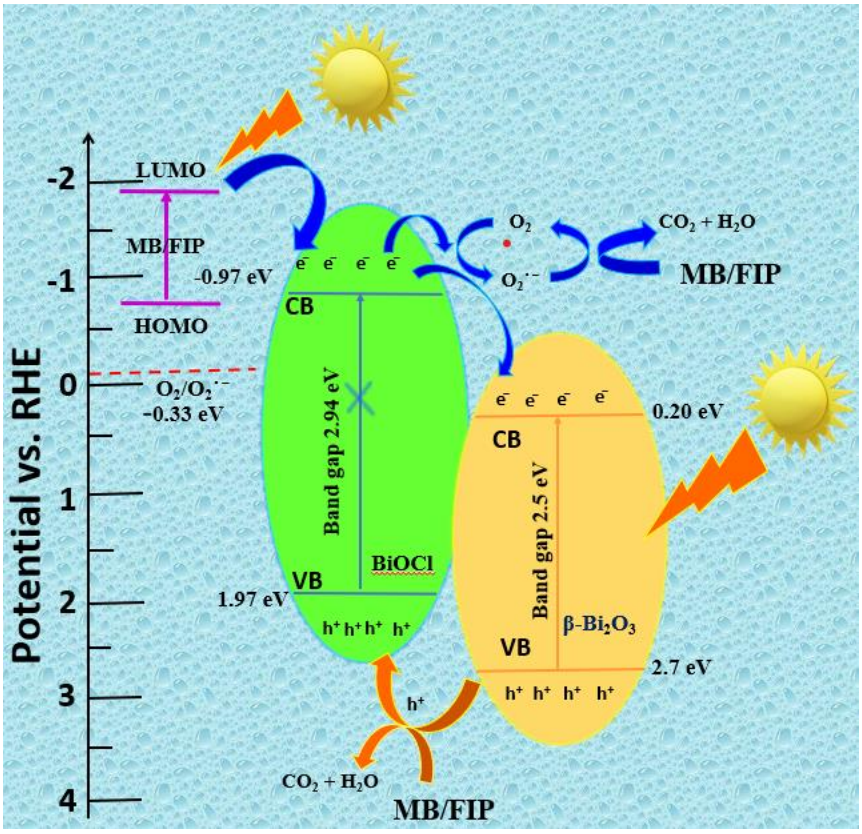

Scheme 2.3. Degradation mechanism of organic pollutants via β-Bi_2O_3/BiOCl heterostructureunder visible light.

A comparative literature study was done on the degradation activity of pollutants via bismuth compounds (**Table 2.3**), affirming the superior efficacy of the synthesized photocatalyst for degradation purposes.

Table 2.3. Comparative study of varied photocatalysts for pollutant degradation.

Catalyst	Pollutant	Conc. (g/L)	Time (min)	Light source	Lamp	*k*	Effici-ency (%)	Reference
Bi_2O_3/ BiOCl	MO	1	6	UV	300 W Hg lamp	-	100	19
Bi_2O_3/ BiOCl	MO	1	80	visible	500 W Xe lamp	3.14 $x10^{-4}$	100	16
Bi_2O_3/BiOCl	1,4-TPA	0.11	60	visible	-	0.064 h^{-1}	-	21
β-Bi_2O_3/BiOCl	TC HCl	0.20	180	visible	300 W Xe lamp	0.025 min^{-1}	99.5	13
β-Bi_2O_3/BiOCl	RhB	0.50	30	visible	300 W Xe lamp	0.052 min^{-1}	99.4	15
BiOCl/ $Bi_{12}O_{17}Cl_2$	NO	-	30	visible	-	-	37.2	25

2.3.2.5 TOC Measurements

The TOC measurement of the pollutants MB and FIP were conducted to analyze the mineralization of toxic pollutants. The TOC removal efficiency of MB and FIP succeeding the photocatalytic treatment was found to be 63.98% and 53.55%,

respectively (**Fig. 2.8**). The reduction in TOC levels indicates the possible utility of the photocatalyst in the degradation of industrial toxic contaminants to relatively simpler compounds.[2]

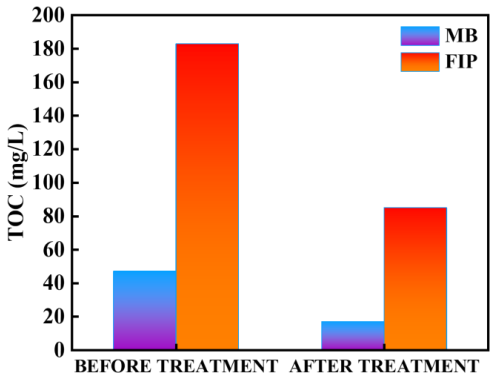

Fig. 2.8. TOC analysis of MB and FIP by 1:1 β-Bi_2O_3/BiOCl binary composite.

2.3.3 Conclusion

The chapter covers the designing of flower-like nanocomposite β-Bi_2O_3/BiOCl through the precipitation process, employed for the photodegradation of MB and FIP. Surface studies showed the accumulation of β-Bi_2O_3 nanorods on BiOCl nanoflowers. The pH and pzc analysis revealed that MB displayed the highest photodegradation in the alkaline pH range while FIP showed maximum efficacy in the acidic pH range. It was owed to the interactions amid the photocatalyst's surface and the surface of cationic MB and anionic FIP, respectively. The reduction in active sites owing to the preliminary complete pollutant adsorption was proved by the lessened degradation efficacy and is illustrated via the feed concentration studies. The reusability test affirmed that the composite is reusable. The scavenging experiments revealed the prominent part of electrons and holes in photodegradation. It was found that BiOCl played a significant partin the degradation process while β-Bi_2O_3 generated a heterojunction electric field at the interfaces of catalysts, separating the charge carriers and deducing electron-hole pair reconciliation and thus, elevating photocatalytic performance. Also, due to the positioning of β-Bi_2O_3 on BiOCl, no

active sites are inhibited. Thus, the technique provides a decent way to design flower-like β-Bi_2O_3/BiOCl photocatalysts with high efficiency.

References

(1) Sharma, S.; Basu, S.; Shetti, N. P.; Nadagouda, M. N.; Aminabhavi, T. M. Microplastics in the Environment: Occurrence, Perils, and Eradication. *Chem. Eng.J.* **2021**, *408*, 127317. https://doi.org/10.1016/j.cej.2020.127317.

(2) Monga, D.; Ilager, D.; Shetti, N. P.; Basu, S.; Aminabhavi, T. M. 2D/2D Heterojunctionof MoS_2/g-C_3N_4 Nanoflowers for Enhanced Visible-Light-Driven Photocatalytic and Electrochemical Degradation of Organic Pollutants. *J. Environ. Manage.* **2020**, *274*, 111208. https://doi.org/10.1016/j.jenvman.2020.111208.

(3) Sharma, S.; Basu, S. Fabrication of Centimeter-Sized Sb_2S_3/SiO_2 MonolithicMimosa Pudica Nanoflowers for Remediation of Hazardous Pollutants from Industrial Wastewater. *J. Clean. Prod.* **2021**, *280*, 124525. https://doi.org/10.1016/j.jclepro.2020.124525.

(4) Nagar, A.; Basu, S. Ternary g-C_3N_4/Ag/$BiVO_4$ Nanocomposite: Fabrication and Implementation to Remove Organic Pollutants. *Environ. Technol. Innov.* **2021**, *23*, 101646. https://doi.org/10.1016/j.eti.2021.101646.

(5) Rathi, A.; Basu, S.; Barman, S. Adsorptive Removal of Fipronil from Its Aqueous Solution by Modified Zeolite HZSM-5: Equilibrium, Kinetic and Thermodynamic Study. *J. Mol. Liq.* **2019**, *283*, 867. https://doi.org/10.1016/j.molliq.2019.02.140.

(6) Sharma, S.; Basu, S. Visible-Light-Driven Efficient Photocatalytic Abatement of Recalcitrant Pollutants by Centimeter-Length MoO_3/SiO_2 Monoliths with Long Service Life. *Appl. Mater. Today* **2021**, *23*, 101033. https://doi.org/10.1016/j.apmt.2021.101033.

(7) Monga, D.; Basu, S. Enhanced Photocatalytic Degradation of Industrial Dye by g-

C_3N_4/TiO_2 Nanocomposite: Role of Shape of TiO_2. *Adv. Powder Technol.* **2019**, *30*, 1089. https://doi.org/10.1016/j.apt.2019.03.004.

(8) Aanchal; Barman, S.; Basu, S. Complete Removal of Endocrine Disrupting Compound and Toxic Dye by Visible Light Active Porous g-C_3N_4/H-ZSM-5 Nanocomposite. *Chemosphere* **2020**, *241*, 124981. https://doi.org/10.1016/j.chemosphere.2019.124981.

(9) Mushtaq, F.; Guerrero, M.; Sakar, M. S.; Hoop, M.; Lindo, A. M.; Sort, J.; Chen, X.; Nelson, B. J.; Pellicer, E.; Pané, S. Magnetically Driven Bi_2O_3/BiOCl-Based Hybrid Microrobots for Photocatalytic Water Remediation. *J. Mater. Chem. A* **2015**, *3*, 23670. https://doi.org/10.1039/c5ta05825b.

(10) Dashairya, L.; Sharma, S.; Rathi, A.; Saha, P.; Basu, S. Solar-Light-Driven Photocatalysis by Sb_2S_3/Carbon Based Composites towards Degradation of Noxious Organic Pollutants. *Mater. Chem. Phys.* **2021**, *273*, 125120. https://doi.org/10.1016/j.matchemphys.2021,125120.

(11) Chen, X.; Shen, S.; Guo, L.; Mao, S. S. Semiconductor-Based Photocatalytic Hydrogen Generation. *Chem. Rev.* **2010**, *110*, 6503. https://doi.org/10.1021/cr1001645.

(12) Sharma, S.; Basu, S. Highly Reusable Visible Light Active Hierarchical Porous WO_3/SiO_2 Monolith in Centimeter Length Scale for Enhanced Photocatalytic Degradation of Toxic Pollutants. *Sep. Purif. Technol.* **2020**, *231*, 115916. https://doi.org/10.1016/j.seppur.2019.115916.

(13) Kong, S.; An, Z.; Zhang, W.; An, Z.; Yuan, M.; Chen, D. Preparation of Hollow Flower-like Microspherical β-Bi_2O_3/BiOCl Heterojunction and High Photocatalytic Property for Tetracycline Hydrochloride Degradation. Nanomater. **2020**, *10*, 1. https://doi.org/10.3390/nano10010057.

(14) Hou, J.; Yang, C.; Wang, Z.; Zhou, W.; Jiao, S.; Zhu, H. Applied Catalysis B:

Environmental In Situ Synthesis of α, β Phase Heterojunction on Bi_2O_3 Nanowireswith Exceptional Visible-Light Photocatalytic Performance. *Applied Catal. B,Environ.* **2013**,*142*, 504. https://doi.org/10.1016/j.apcatb.2013.05.050.

(15) Tang, X.; Ma, C.; Liu, N.; Liu, C.; Liu, S. Visible Light β-Bi_2O_3/BiOCl Heterojunction Photocatalyst with Highly Enhanced Photocatalytic Activity. *Chem. Phys. Lett.* **2018**, *709*, 82. https://doi.org/10.1016/j.cplett.2018.08.045.

(16) Zhao, Q.; Liu, X.; Xing, Y.; Liu, Z.; Du, C. Synthesizing Bi_2O_3/BiOCl Heterojunctionsby Partial Conversion of BiOCl. *J. Mater. Sci.* **2017**, *52*, 2117. https://doi.org/10.1007/s10853-016-0499-y.

(17) Zulkifli, Z. A.; Razak, K. A.; Rahman, W. N. W. A.; Abidin, S. Z. Synthesis and Characterisation of Bismuth Oxide Nanoparticles Using Hydrothermal Method: The Effect of Reactant Concentrations and Application in Radiotherapy. *J. Phys. Conf. Ser.***2018**, *1082*, 012103. https://doi.org/10.1088/1742-6596/1082/1/012103.

(18) Kundu, A.; Sharma, S.; Basu, S. Modulated BiOCl Nanoplates with Porous g-C_3N_4 Nanosheets for Photocatalytic Degradation of Color/Colorless Pollutants in Natural Sunlight. *J. Phys. Chem. Solids* **2021**, *154*, 110064. https://doi.org/10.1016/j.jpcs.2021.110064.

(19) Zhang, X.; Xu, G.; Hu, J.; Lv, J.; Wang, J.; Wu, Y. Fabrication and Photocatalytic Performances of BiOCl Nanosheets Modified with Ultrafine Bi_2O_3 Nanocrystals. *RSC Adv.* **2016**, *6*, 63241. https://doi.org/10.1039/c6ra09919j.

(20) Tian, C.; Luo, S.; She, J.; Qing, Y.; Yan, N.; Wu, Y.; Liu, Z. Cellulose Nanofibrils Enable Flower-like BiOCl for High-Performance Photocatalysis under Visible- Light Irradiation. *Appl. Surf. Sci.* **2019**, *464*, 60. https://doi.org/10.1016/j.apsusc.2018.09.126.

(21) Chai, S. Y.; Kim, Y. J.; Jung, M. H.; Chakraborty, A. K.; Jung, D.; Lee, W. I. Heterojunctioned BiOCl/Bi_2O_3, a New Visible Light Photocatalyst. *J. Catal*. **2009**,

262, 144. https://doi.org/10.1016/j.jcat.2008.12.020.

(22) Nguyen, V. H.; Bui, Q. T. P.; Vo, D. V. N.; Lim, K. T.; Bach, L. G.; Do, S. T.; Van Nguyen, T.; Doan, V. D.; Nguyen, T. D.; Nguyen, T. D. Effective Photocatalytic Activity of Sulfate-Modified $BiVO_4$ for the Decomposition ofMethylene Blue under LED Visible Light. *Materials* **2019**, *12*, 2681. https://doi.org/10.3390/ma12172681.

(23) Zheng, X.; Yuan, J.; Shen, J.; Liang, J.; Che, J.; Tang, B.; He, G.; Chen, H. A Carnation-like RGO/$Bi_2O_2CO_3$/BiOCl Composite: Efficient Photocatalyst for the Degradation of Ciprofloxacin. *J. Mater. Sci. Mater. Electron.* **2019**, *30*, 5986. https://doi.org/10.1007/s10854-019-00898-w.

(24) Oudghiri-Hassani, H.; Rakass, S.; Al Wadaani, F. T.; Al- Ghamdi, K. J.; Omer, A.; Messali, M.; Abboudi, M. Synthesis, Characterization and Photocatalytic Activity of α-Bi_2O_3 Nanoparticles. *J. Taibah Univ. Sci.* **2015**, *9*, 508. https://doi.org/10.1016/j.jtusci.2015.01.009.

(25) Zhang, W.; Dong, X.; Jia, B.; Zhong, J.; Sun, Y.; Dong, F. 2 D BiOCl/$Bi_{12}O_{17}Cl_2$ Nanojunction: Enhanced Visible Light Photocatalytic NO Removal and in Situ DRIFTS Investigation. *Appl. Surf. Sci.* **2018**, *430*, 571. https://doi.org/10.1016/j.apsusc.2017.06.186.

(26) Gadhi, T. A.; Hernández-Gordillo, A.; Bizarro, M.; Jagdale, P.; Tagliaferro, A.; Rodil, S. E. Efficient α/β-Bi_2O_3 Composite for the Sequential Photodegradation of Two-Dyes Mixture. *Ceram. Int.* **2016**, *42*, 13065. https://doi.org/10.1016/j.ceramint.2016.05.087.

(27) Gürses, A.; Doğar, Ç.; Yalçin, M.; Açikyildiz, M.; Bayrak, R.; Karaca, S. The Adsorption Kinetics of the Cationic Dye, Methylene Blue, onto Clay. *J. Hazard. Mater.***2006**, *131*, 217. https://doi.org/10.1016/j.jhazmat.2005.09.036.

(28) Romeh, A. A. A. Green Silver Nanoparticles for Enhancing the Phytoremediation of Soil and Water Contaminated by Fipronil and Degradation Products. *Water. Air.Soil*

Pollut. **2018**, *229*, 147. https://doi.org/10.1007/s11270-018-3792-3.

(29) Ou, M.; Wan, S.; Zhong, Q.; Zhang, S.; Song, Y.; Guo, L.; Cai, W.; Xu, Y. HierarchicalZ-Scheme Photocatalyst of g-C_3N_4@Ag/$BiVO_4$ (040) with Enhanced Visible-Light- Induced Photocatalytic Oxidation Performance. *Appl. Catal. B Environ.* **2018**, *221*, 97. https://doi.org/10.1016/j.apcatb.2017.09.005.

(30) Ambrosio, F.; Wiktor, J.; Pasquarello, A. pH-Dependent Surface Chemistry fromFirst Principles: Application to the $BiVO_4$ (010)-Water Interface. *ACS Appl. Mater. Interfaces* **2018**, *10*, 10011. https://doi.org/10.1021/acsami.7b16545.

(31) Kamble, G. S.; Ling, Y. C. Solvothermal Synthesis of Facet-Dependent $BiVO_4$ Photocatalyst with Enhanced Visible-Light-Driven Photocatalytic Degradation of Organic Pollutant: Assessment of Toxicity by Zebrafish Embryo. *Sci. Rep.* **2020**, *10*, 1. https://doi.org/10.1038/s41598-020-69706-4.

(32) Sorathiya, K.; Mishra, B.; Kalarikkal, A.; Reddy, K. P.; Gopinath, C. S.; Khushalani, D. Enhancement in Rate of Photocatalysis Upon Catalyst Recycling. *Sci. Rep.* **2016**, *6*, 1. https://doi.org/10.1038/srep35075.

(33) Makama, A. B.; Salmiaton, A.; Choong, T. S. Y.; Hamid, M. R. A.; Abdullah, N.; Saion, E. Influence of Parameters and Radical Scavengers on the Visible-Light-Induced Degradation of Ciprofloxacin in ZnO/SnS_2 Nanocomposite Suspension: Identification of Transformation Products. *Chemosphere* **2020**, *253*, 126689. https://doi.org/10.1016/j.chemosphere.2020.126689.

(34) Pehlivan, F. E. Vitamin C: An Antioxidant Agent. *Vitamin C* **2017**, *Chapter 2*, 69660. Heterojunctions for Efficiently Photocatalytic NO in Air Removal: In-Situ Self-Sacrificial Synthesis, Characterizations and Mechanistic Study. *Appl. Catal. B Environ.***2016**, *199*, 123. https://doi.org/10.1016/j.apcatb.2016.06.027.

(35) Wang, Z.; Huang, Y.; Ho, W.; Cao, J.; Shen, Z.; Lee, S. C. Fabrication of $Bi_2O_2CO_3$/g-C_3N_4 Heterojunctions for Efficiently Photocatalytic NO in Air Removal: In-Situ Self-

Sacrificial Synthesis, Characterizations and Mechanistic Study. *Appl. Catal. B Environ.***2016**, *199*, 123. https://doi.org/10.1016/j.apcatb.2016.06.027.

(36) Wang, C. C.; Zhang, Y. Q.; Zhu, T.; Wang, P.; Gao, S. J. Photocatalytic Degradation ofMethylene Blue and Methyl Orange in a Zn (II)-Based Metal– Organic Framework. *Desalin. Water Treat.* **2016**, *57*, 17844. https://doi.org/10.1080/19443994.2015.1088807.

Chapter 3

Deciphering the Role of β-phase Bi_2O_3 Nanorods incorporated on g-C_3N_4 Nanosheets for Efficient Pollutant Removal

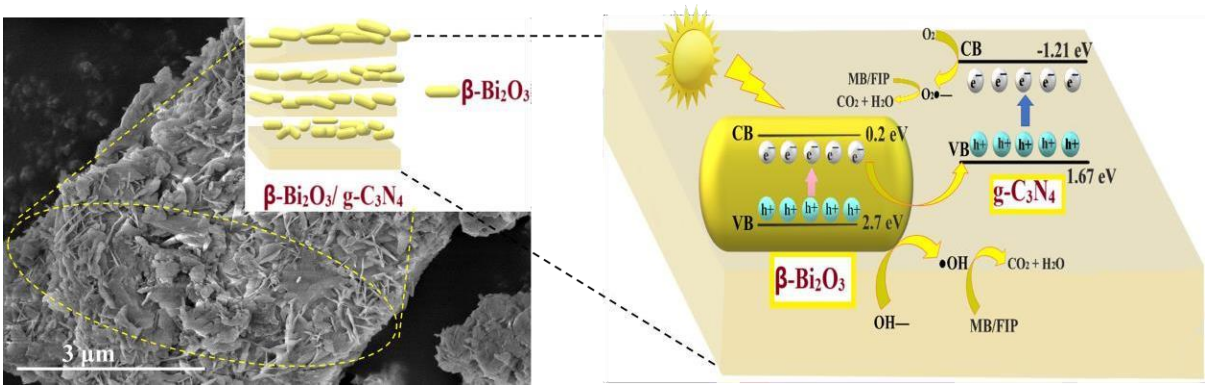

Highlights

- Z-scheme β-Bi_2O_3/g-C_3N_4 composite was designed via the in-situ method.
- β-Bi_2O_3 nanorods deposited on g-C_3N_4 nanolayers.
- ~97% and ~75% degradation efficacy in visible light for MB and FIP respectively.
- Hydroxyl radicals are responsible for the photodegradation process.

3.1 Introduction

With the emergence of the 21st century, recalcitrant urbanization and globalization have invoked large-scale production of both, consumer and industrial goods, which yields exhaustive xenobiotic compounds, such as dyes and insecticides.[1] Such compounds are defiant, laborious to degrade, and poisonous to all living beings. The majority of such pollutants are enduring, and immune to chemical, physical, and biological treatments, suggesting the arduous removal. Moreover, their high solubility in water and discharge in water bodies without any pre-treatment[2] have crippled the environment.[3] Methylene blue (MB),[4] an azo dye, extensively used in dyeing industries, is commonly present in industrial wastewater[5] and has dangerous effects such as nausea, vomiting, abdominal pain, and diarrhea. Fipronil (FIP), a broadly used insecticide, begets significant health issues such as weakness, dizziness, seizures,vomiting, and headache.[6] The consumption of even minute amounts of such toxins can easily result in cardiovascular and biological disorders.[7] Given their stability and solubility in water, processes such as sedimentation, flocculation, oxidation, adsorption, or precipitation have limited effect on such pollutants owing to their ability to transfer matter amongst varied phases without efficient degradation.[8] Photocatalysis is the most significant amongst them due to its cost-effective and competent nature,[9] moreover, it provides a facile fabrication method to yield less toxic products along with CO_2 and H_2O.[10] However, heterogeneous photocatalysts are perceived to respond mainly to UV radiation which constitutes 5% of the entire solar spectrum.[11] The obstacle was overcome by doping or designing heterojunctions amongst varied semiconductors with unequal band gaps, making them visible-light active.[12] Therefore, to efficiently utilize the broad spectrum of visible light, such photocatalysts are constructed.[13] These catalysts are known as visible-light-induced photocatalysts.[14] They are considerably efficient owing to their accountability for 48% of the visible-light spectrum.[14] Researchers have developed

such visible-light catalysts which have better photocatalytic efficacy.[15] Amidst them, bismuth-based compounds have attracted global attention.[15] In contrast with the photocatalysts such as TiO_2, bismuth oxide (Bi_2O_3) possessesa small bandgap energy (2.5 eV)[15] with several vacancies for oxygen with steep optical conductivity. The β-phase displays greater proficiency than the α-phase because of the lesser bandgap and elevated optical visible-light absorption.[16] However, due to the metastable state of the β-phase, synthesis is difficult.[17] Also, therecombination tendency of the e^--h^+ pair is high.[18] Graphitic carbon nitride (g-C_3N_4)[19] has emerged as an assuring photocatalyst comprising of layers and graphene's electronic properties, with a bandgap ~ 2.88 eV, appropriate for activity in visible light, thereby for toxin removal. Its compatibility enhances due to its adaptability in aerobic and aqueous conditions at a wide pH range, along with its inexpensiveness, environmental-friendly nature,[20] and decay-free nature.[21] But g-C_3N_4 procured by calcining nitrogen-rich materials at elevated temperature poses the restriction of feeble light absorption and fasten recombination of e^--h^+ pair.[22] Heterojunctions act as a barrier to the research gap. Due to similar bandgaps, research has been done in the past, coupling Bi_2O_3 with g-C_3N_4 and promoting charge transfer and separation.[23] Recently, considerable research has been conducted regarding the β-Bi_2O_3/g-C_3N_4 heterostructure. Wang *et al.*[22] constructed aggregated layered of β-Bi_2O_3/g-C_3N_4 composite to degrade rhodamine-B and p-nitrophenol and the composite with 0.5 g β-Bi_2O_3 displayed maximum efficacy of 94.8% and 71.6%, respectively. Fan *et al.*[23] utilized the in-situ polymerization technique to deposit γ-phased Bi_2O_3 (supported by XRD analysis and UV-DRS band gap of γ-Bi_2O_3)[24] nanorods on g-C_3N_4 nanosheets. The composite with γ-Bi_2O_3 (0.5 g) displayed only methylene blue degradation efficiency under visible light illumination without validating the indirect mechanism by degrading any colorless pollutant. Zhang *et al.*[25] calcined g-C_3N_4 with $Bi_2O_2CO_3$, to fabricate flower-like β-Bi_2O_3/g-C_3N_4 heterostructure. Different

composites were fabricated by varying the weight ratios such as 70 wt.% g-C_3N_4/$Bi_2O_2CO_3$ displaying the highest degradation efficacy for Rhodamine B (98%) in 80 min. Shafawi *et al.*[26] used impregnation to fabricate Bi_2O_3/g-C_3N_4 for the UV-light degradation of the pollutant Reactive Black 5. The composite with 9 weight percentage of Bi_2O_3/g-C_3N_4 exhibited the highest efficacy of 84% under 120 min. Ghosh *et al.*[27] dispersed nanorods of Bi_2O_3 on nanosheets of g-C_3N_4 via the impregnation method. The composite was varied with 1, 2, 5, and 10 wt %, and the maximum degradation efficiency of methylene blue was shown by 2 wt% Bi_2O_3/g-C_3N_4 (92%) in 80 min. Cui *et al.*[28] designed Bi_2O_3/g-C_3N_4 with 1,2,3,4,5 wt% ratios for the photodegradation of amido black-10 and the composite with 3 wt% showcased maximum efficacy (88.71%) in 120 min. Moreover, the authors did not perform varied reaction parameter studies. To date, there have been some reports regarding the Bi_2O_3/g-C_3N_4 heterostructure for the photodegradation of RhB,[22] MB,[23] and amido black 10B[28] but scarce degradation has beenconducted for the degradation of a colorless pollutant. Moreover, limited research has been done regarding Bi_2O_3/g-C_3N_4 composite with β-phased Bi_2O_3 (2.5 eV) having a bandgap less than α-phased (2.81 eV) and γ-phased (2.75) Bi_2O_3[24] for the degradation of colorless pollutant.Therefore, a β-phased Bi_2O_3/g-C_3N_4 Z-scheme heterostructure is suggested for the visible-light degradation of pollutants.

Presently, β-Bi_2O_3/g-C_3N_4 heterojunction was constructed via g-C_3N_4 nanosheets and β-phased Bi_2O_3 nanorods with the in-situ process of nanoflake g-C_3N_4 and NaOH utilized for MB and FIP degradation. Catalyst concentration, pH, and reusability were the varied parameters. Trapping experiments investigated the degradation mechanism. The reusability of the composite was affirmed by conducting XRD after degradation activity. The novelty of the work is ascribed to the nanosheet-nanorod-like structure of β-Bi_2O_3/g-C_3N_4 prepared by the in-situ process to degrade MB and a colorless pollutant FIP. The paper presents the easy fabrication of the metastable β-Bi_2O_3. Different ratios of the composite, fabricated with

Bi_2O_3 in tetragonal β-phase degraded MB and FIP with varied reaction parameter studies have not been reported to the best of the author's understanding.

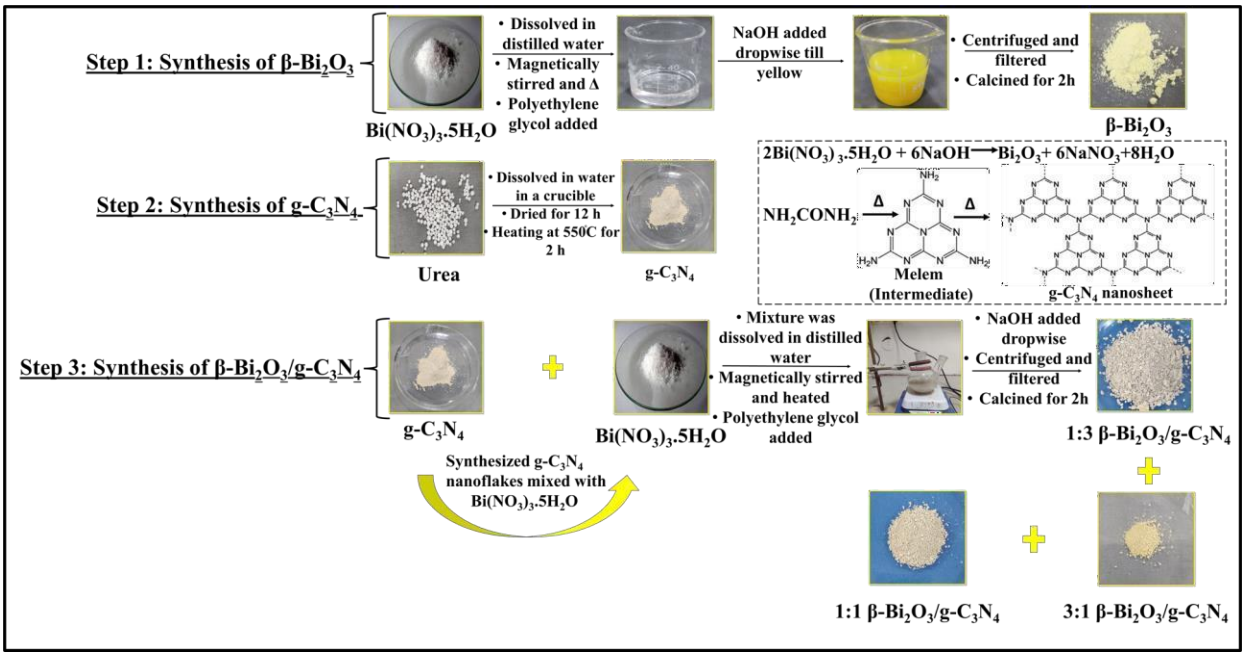

Scheme 3.1. Fabrication of β-Bi_2O_3/g-C_3N_4 heterostructure.

3.2 Experimental

This section consists of the chemicals, materials, and methodologies used for the synthesis of catalysts.

3.2.1 Chemicals and Materials

Urea (NH_2CONH_2), sodium hydroxide (NaOH), bismuth nitrate pentahydrate ($Bi(NO_3)_3.5H_2O$), and polyethylene glycol-8000 (PEG-8000) were purchased from Thermo Fisher Scientific India Pvt. Ltd, and S D Fine-Chem Limited, Mumbai. Merck supplied MB dye while Bayer Crop Science Ltd., India supplied FIP. Double distilled water was also utilized.

3.2.2 Synthesis

This section includes the synthesis methodologies of pure β-Bi_2O_3, pure g-C_3N_4, and β-

Bi_2O_3/g-C_3N_4 composite.

3.2.2.1 Synthesis of β-Bi_2O_3

The precipitation process was employed to fabricate β-Bi_2O_3 nanorods. 10 mL $Bi(NO_3)_3.5H_2O$ (0.05 M) and polyethylene glycol-8000 (1 g) were magnetically stirred together and heated. Drop-wise, 5 M NaOH (10 g NaOH in 50 mL H_2O) was included in the mixture at 80°C until yellow color appeared. After cooling the solution for some time, washing was given using ethanol and distilled water (thrice). The obtained solution was then filtered and dried by keeping overnight. Calcination of the procured yellow-colored product (**Scheme 3.1**) was done at 500°C for a time period of 2 h (10°C/min).[15]

3.2.2.2 Synthesis of g-C_3N_4

Urea was utilized for the synthesis of g-C_3N_4 via the recrystallization method. Urea (30g) was mixed with water (50 mL), transferred, and recrystallized in a silica crucible for 12 h. Calcination was done at 550°C for a time period of 2 h (10°C/min). The resultant yellow-brown-colored sample was grounded with a mortar pestle (**Scheme 3.1**).[3]

3.2.2.3 Synthesis of β-Bi_2O_3/g-C_3N_4

The in-situ precipitation of nanoflake g-C_3N_4 and NaOH was employed to fabricate β- Bi_2O_3/g-C_3N_4. The obtained yellow-brown-colored g-C_3N_4 powder was mixed with 10 mL $Bi(NO_3)_3.5H_2O$ (0.05 M), to which polyethylene glycol-8000 (1 g) was simultaneously added and heated. Lastly, 5 M NaOH solution (10 g NaOH in 50 mL H_2O) was added to the mixture drop-wise until a color change appears from "brown" to "tan", "hazelwood", and "biscotti" for 1:1, 3:1 and 1:3 β- Bi_2O_3/g-C_3N_4, respectively (**Scheme 3.1)**.[15] The schematic diagram for the synthesis of β-Bi_2O_3/g-C_3N_4 has been provided as **Scheme 3.2**.

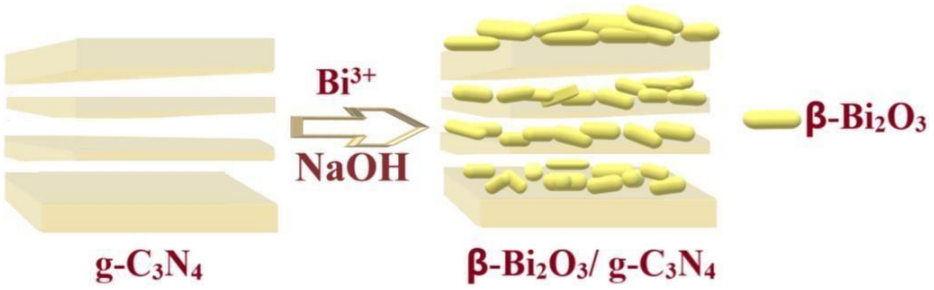

Scheme 3.2. Schematic illustration of β-Bi_2O_3/g-C_3N_4 fabrication.

3.2.3 Characterization

The BET N_2 adsorption-desorption isotherm at 77.3 K scrutinized the pore-size distribution and the surface area using Microtrac Belsorp Mini-II (Bel, Japan, Inc.). Before the analysis, pretreatment was performed at 100°C for 6 h. The Barrett-Joyner-Halenda (BJH) analysis technique investigated the pore-size distribution curves. PANanalytical X-ray diffractometer using Cu-Kα radiation was employed for the crystallinity of the prepared samples via the X-ray diffraction (XRD) process at 45 kV voltage and scan between 10-90°C. The microstructure and the surface morphology were investigated by employing transmission electron spectroscopy (TEM, JEM-2100F) and field emission scanning electron spectroscopy (FESEM SU8180, Hitachi, Tokyo, Japan) using Oxford INCTA energy dispersive spectrometer (EDS), respectively. X-ray photoelectron spectroscopy (XPS) analysis did an elaborated study of the elemental nature of the composite using PHI-5000 VersaProbe-III system with a monochromatic Al Kα X-ray source (1486.7 eV). The UV-Vis Diffusion Reflectance Spectroscopy (DRS) through a Hitachi-3900H spectrophotometer (Shimadzu, Japan) was performed with the diffusion absorbance mode. The photoluminescence (PL) analysis was done using the fluorescence spectrometer (F-4500, Hitachi, Japan). A cyber scanpH 1100 (Eutech, Singapore) for the computation and accommodation of pH was performed. Lastly, to measure the photodegradation activity of the pollutants, a UV-Vis spectrophotometer(Shimadzu, UV-2600) was utilized.

3.2.4 Photocatalytic Activity

The photocatalysts' solutions were put in a photoreactor to measure their degradation efficiency. The catalyst (2 mg) was thoroughly mixed with MB/FIP (15 mL) at concentrations of 5 ppm/600 ppm, respectively. The solutions were placed for 60 min in the dark establishing adsorption-desorption equilibrium which was then illuminated using a 65 W CFL lamp (k>400 nm at 125 W/m^2 intensity), 90 min for MB, and 120 min for FIP. At the maximum absorption bands, for MB (λ_{max} = 664) and FIP (λ_{max} =376 nm), the degradation activities were observed utilizing a UV-vis spectrophotometer. Under lambert beer's law, the solution's absorbance is directly related to the concentration, hence, the % photodegradation efficiency can be formulated via the following equation (**Eq. (3.1)**)[15]:

$$\% D = \{(A_o-A_t)/A_o\} \times 100 = \{(C_o-C_t)/C_o\} \times 100 \quad (3.1)$$

Where A_o signifies the absorbance of dye/pesticide at a time '0', A_t signifies the absorbance of dye/pesticide at a time 't', C_o signifies the concentration of dye/pesticide at a time '0', and C_t signifies the concentration of dye/pesticide at a time 't'.

Chemical Oxygen Demand (COD) analysis was done to confirm the degradation activity of the β-Bi_2O_3/g-C_3N_4 composite. 2mg of 1:3 Bi_2O_3/g-C_3N_4 (0.06 g/L) was added in MB and FIP (15 mL) and illuminated for 90 min (MB) and 120 min (FIP), respectively. To affirm the COD value, the titrimetric method was employed and COD was calculated before the catalytic treatment at a time '0' and after the catalytic treatment at a time 't'. The deduction in COD is formulated via **Eq. (3.2)**[29] as follows:

$$\text{COD} = \frac{(a-b)\times N\times 8000\times Dilution\ Factor}{Volume\ Of\ Sample} \quad (3.2)$$

Where a = Ferrous ammonium sulfate (FAS) used for the titration of the blank sample in mL; b = Ferrous ammonium sulfate (FAS) used for the titration of the sample in mL, N = Normality of FAS (0.1 N).

3.3 Results and Discussion

3.3.1 Characterizations

3.3.1.1 X-ray Diffraction Analysis

XRD study computed the crystal planes of g-C_3N_4, β-Bi_2O_3, and β-Bi_2O_3/g-C_3N_4. **Fig. 3.1 (a)** exhibited two peaks of g-C_3N_4 with a prominent peak at 26.69° relating to the (002) plane and the other at 13.1° relating to (100) planes (JCPDS card no. 87-1526).[14] For β-Bi_2O_3, peaks at positions 12.8°, 23.9°, 27.95°, 30.3°, 32.6°, 32.69°, 42.4°, 46.22°, 52.49°, 54.86°, 56°, 59° and 68.5° corresponding to (110), (210), (201), (211), (002), (220), (212), (222), (411), (203), (421), (402) and (440) planes (JCPDS card no. 27-0050), respectively were present associated with the tetragonal phase of β-Bi_2O_3 (**Fig. 3.1 (a)**).[15] Lastly, The XRD pattern of β-Bi_2O_3/g- C_3N_4 exhibited peaks of g-C_3N_4 nanoflakes and β-Bi_2O_3 nanorods, suggesting the creation of heterojunction.

Table 3.1. Total pore volume, Mesopore size, and Surface area of the catalysts.

Photocatalyst	Surface area (m^2/g)	Total pore volume (cm^3/g)	Mesopore size (nm)
β-Bi_2O_3	18	0.19	22.26
g-C_3N_4	88	0.44	20.37
1:1 β-Bi_2O_3/g-C_3N_4	43	0.14	13.75
1:3 β-Bi_2O_3/g-C_3N_4	63	0.40	25.59
3:1 β-Bi_2O_3/g-C_3N_4	20	0.19	39.46
1:4 β-Bi_2O_3/g-C_3N_4	48	0.56	46.58

3.3.1.2 Nitrogen Adsorption/Desorption Analysis

N_2 adsorption-desorption analysis (**Fig. 3.1 (b)**) demonstrated the type-IV isotherm, revealing the photocatalyst's mesoporous nature.[30] As depicted in **Fig. 3.1 (b)**, g-C_3N_4, 1:1 β- Bi_2O_3/g-C_3N_4,1:4 β-Bi_2O_3/g-C_3N_4, 3:1 β-Bi_2O_3/g-C_3N_4, and 1:3 β-Bi_2O_3/g-C_3N_4 shows H1 hysteresis loops[30] while β-Bi_2O_3 depicted H3 hysteresis loop comprising sharpened adsorption and desorption branches,[30] validating the structure and constancy of the catalysts. The BJH method (**Fig. 3.1 (c)**) illustrated the pore size distribution, depicting the catalysts' mesoporous kind. The BET method investigated the mean pore diameter, surface area, and mean pore volume. For β-Bi_2O_3, g-C_3N_4, 1:1 β-Bi_2O_3/g-C_3N_4, 1:3 β-Bi_2O_3/g-C_3N_4, 3:1 β-Bi_2O_3/g-C_3N_4, and 1:4 β-Bi_2O_3/g-C_3N_4 the surface areas were noted to be 18, 88, 43, 63, 20, and 48 m^2/g, respectively. The increased area from pureβ-Bi_2O_3 to 1:3 β-Bi_2O_3/g-C_3N_4 was noted with the maximum surface area for g-C_3N_4 (**Table 3.1**).

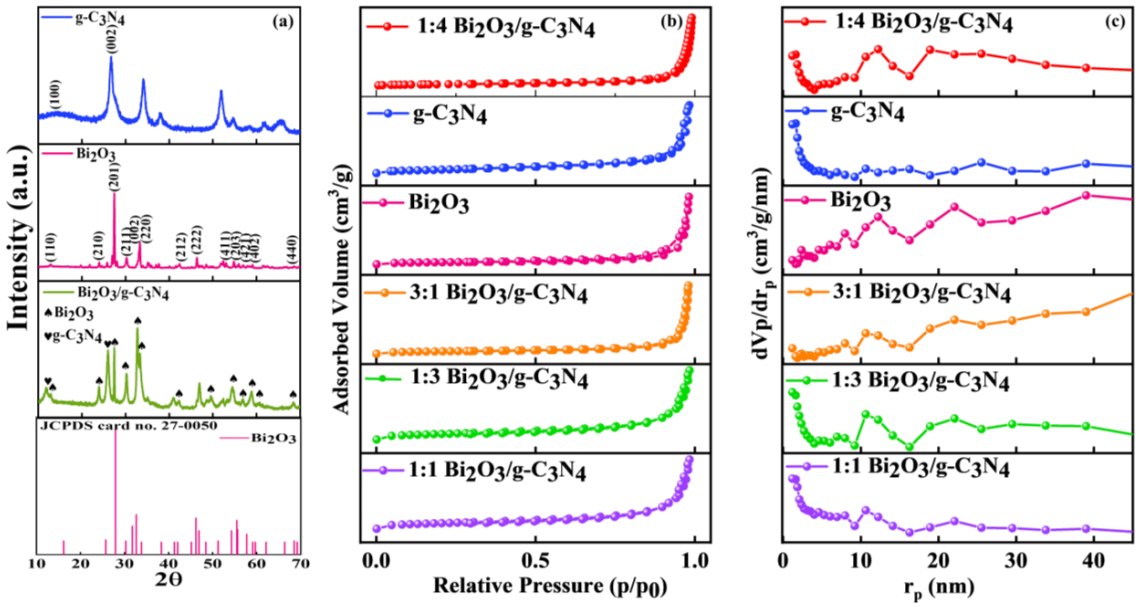

Fig. 3.1. (a) XRD patterns, (b) N_2 adsorption-desorption isotherms, and (c) pore size distribution curves of the photocatalysts.

3.3.1.3 XPS Studies

The elemental oxidation state in 1:3 β-Bi_2O_3/g-C_3N_4 was scrutinized via the XPS technique. The XPS spectrum demonstrated in **Fig. 3.2 (a)** illustrated the occurrence of Bi, C, O, and N. For β-Bi_2O_3, two peaks are present, one at 158.4 eV relating to Bi $4f_{7/2}$ and the otherat 163.7 eV relating to Bi $4f_{5/2}$, indicating the existence of Bi^{3+} in β-Bi_2O_3.[15] For the β-Bi_2O_3/g-C_3N_4 composite, Bi 4f spectra show two peaks (**Fig. 3.2 (b)**), one at 156.6 eV relating to Bi $4f_{7/2}$ and the other at 161.8 eV relating to Bi $4f_{5/2}$, suggesting the Bi^{3+} ion's existence in β- Bi_2O_3/g-C_3N_4. The O1s spectrum for β-Bi_2O_3 shows one peak at a binding energy of 529.7 eV relating to the lattice oxygen (Bi-O) and the second peak of 531.4 eV corresponding to the hydroxyl groups on the surface and adsorbed H_2O[22] while β-Bi_2O_3/g-C_3N_4 displays two peaksof O1s, one at 527.4 eV for lattice O and the other at 531.7 eV for the adsorbed O (**Fig. 3.2 (c)**). For g-C_3N_4, an evident peak present at 285.13 eV[27] ascribes to the C atoms in the C-C bond whereas the first peak at 398.5 eV ascribes to the pyridine N, the second peak at 399.2 eV relates to the pyrrolic N, and the third peak at 400.6 eV ascribes to the graphitic N.[31] The β-Bi_2O_3/g-C_3N_4 composite displays peak for C1s at 285 eV, indicating the C-C bond in g-C_3N_4 (**Fig. 3.2 (d)**) at 398.9 eV and N1s at 399.71 eV, indicating the existence of graphite-like sp^2- bonded g-C_3N_4 (**Fig. 3.2 (e)**) indicating the shift in binding energies in the composite. The shift in binding energies from pure β-Bi_2O_3 and pure g-C_3N_4 to β-Bi_2O_3/g-C_3N_4 heterostructure corresponds to the change in surface charge density. It had been illustrated that the binding energy shift of a specific element was associated with a change in surface electron density, from the incorporation of foreign material of different Fermi levels (E_f) resulting in direct charge transformation. The electron transfer will occur from a higher Fermi level to a lower Fermi level. This will cause the electron to transfer from g-C_3N_4 to β-Bi_2O_3 in β-Bi_2O_3/g -C_3N_4 heterostructure, and a decrease in electron density in g-C_3N_4 and an enhancement in β-Bi_2O_3.

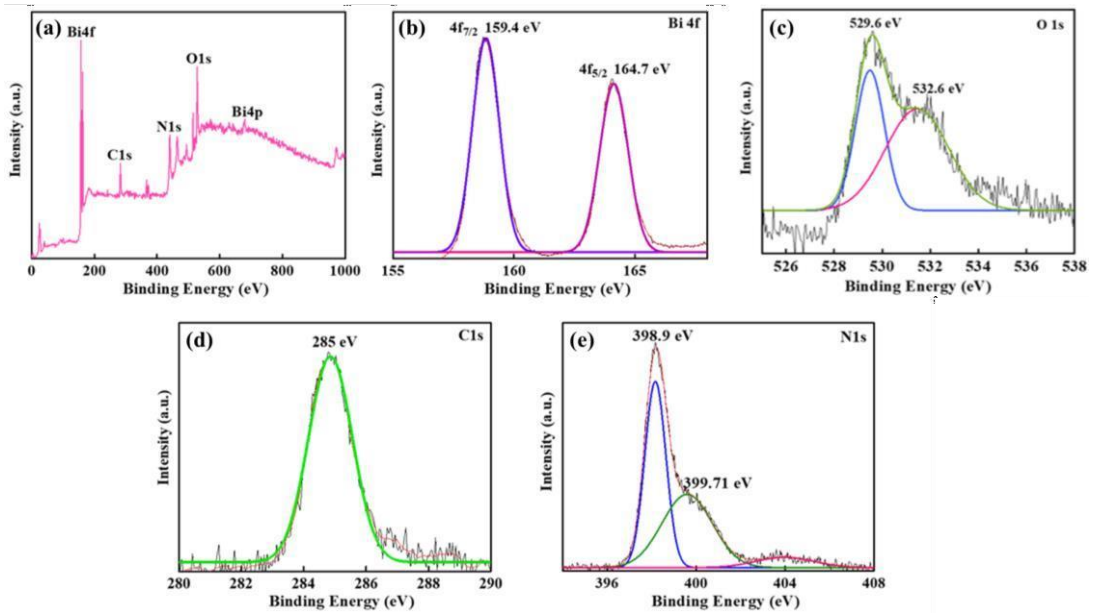

Fig. 3.2. (a) XPS spectrum, deconvoluted peaks of (b) Bi, (c) O, (d) C, and (e) N of 1:3 β-Bi_2O_3/g-C_3N_4 binary composite.

3.3.1.4 EDS and Elemental Mapping Analysis

Elemental mapping of the 1:3 β-Bi_2O_3/g-C_3N_4 binary composite is displayed in the **Fig. 3.3 (b-e)**, validating the presence of C, O, Bi, N. EDS analysis study the elemental structure of β-Bi_2O_3/g-C_3N_4 (**Fig. 3.3 (a)**). As shown in **Fig. 3.3 (a)**, the weight percentages of Bi, O, C, andN are 12.94, 12.17, 36.98, and 37.91, respectively, indicating a 3-fold increase in amounts from Bi_2O_3 to g-C_3N_4. The atomic percentages also increased from O to N. This validated the formation of the 1:3 β-Bi_2O_3/g-C_3N_4 composite.

3.3.1.5 FESEM and HRTEM Analysis

FESEM analysis investigated the surface morphology of β-Bi_2O_3, g-C_3N_4, and β-Bi_2O_3/g-C_3N_4. **Fig. 3.3 (f)** illustrates the nanorods-like structure for β-Bi_2O_3. **Fig. 3.3 (g)** depicts the nanoflakes-like structure for g-C_3N_4 having an enormous surface area, advantageous for the interfacial pollutant adsorption. The presence of a rod-flake-like

structure for the nanocomposite of β-Bi_2O_3/g-C_3N_4 (**Fig. 3.3 (h)**), suggested there is deposition of β-Bi_2O_3 nanorods on the g-C_3N_4 nanoflake layers. To further study the structure of the nanocomposite, the HRTEM analysis was carried out. **Fig. 3.3 (i-k)** depicts the transparent layer signifying g-C_3N_4 while the darker part signifies β-Bi_2O_3 owing to Bi's greater atomic mass than N and C and thereby, the difficult penetration of the electrons in the layers of Bi_2O_3. **Fig. 3.3 (k)** shows thelattice fringes with the spacing of 0.32 nm and 0.295 nm corresponding to (201) and (211) planes, respectively, for β-Bi_2O_3 nanorods. **Fig. 3.3 (j-inset)** shows a proximal interface between β-Bi_2O_3 and g-C_3N_4 (depicted via blue line), affirming the heterojunction formation and proximity of its components.

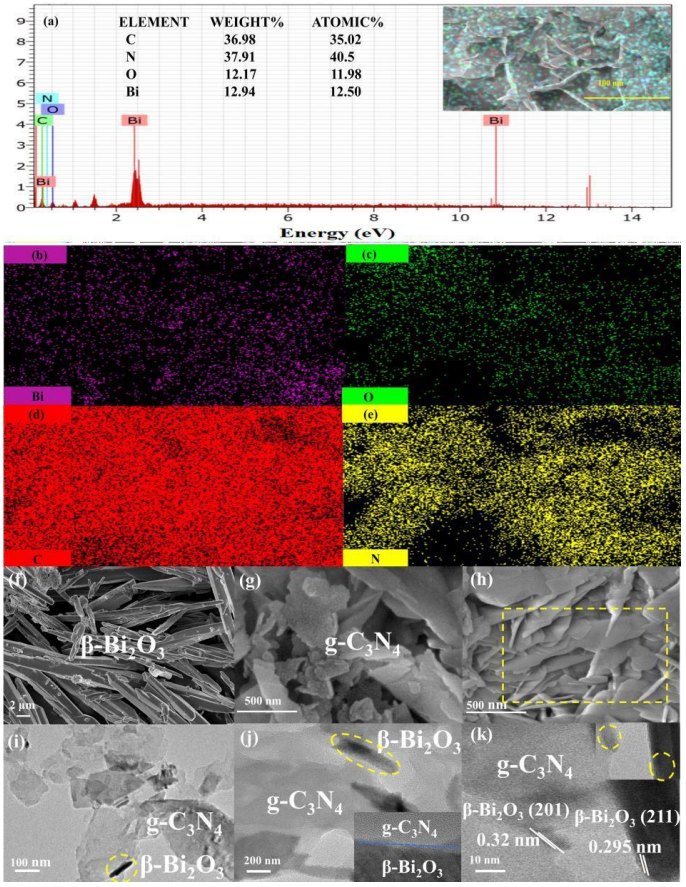

Fig. 3.3. (a) EDS spectrum, elemental mapping (b) Bi, (c) O, (d) C, and (e) N; FESEM illustrations of (f) β-Bi_2O_3, (g) g-C_3N_4, (h) 1:3 β-Bi_2O_3/ g-C_3N_4, and (i-k) HRTEM depictions of 1:3 β-Bi_2O_3/g-C_3N_4.

3.3.1.6 Optical Studies

The recombination of the e^--h^+ plays an active role in the degradation activity. When the photoluminescence (PL) intensity is low, the recombination capacity of the charge carriers is small, and the charge separation is large.[32] For the excitation wavelength (325 nm), the spectrawere obtained (**Fig. 3.4 (a)**). It was noted that the emission wavelength was 448 nm. The lower intensity of the β-Bi_2O_3/g-C_3N_4 nanocomposite than β-Bi_2O_3, g-C_3N_4 signified better charge carrier separation and lower recombination and thus photocatalytic achievement.[32]

UV-Visible diffuse reflectance spectroscopy (DRS) to measure the light absorption capacity of the photocatalysts was performed. For g-C_3N_4, β-Bi_2O_3, and β-Bi_2O_3/g-C_3N_4 composite, the absorption edges (**Fig. 3.4 (b)**) were found to be 490 nm,[33] 570 nm,[34] and 650 nm,[23] respectively. The introduction of g-C_3N_4 in β-Bi_2O_3 causes a redshift in the visible light region.[23] The bandgap of the prepared photocatalysts was formulated via DRS by plotting tauc's plot. The equation is as follows (Eq. (3.3))[23]:

$$(\alpha h\nu)^{1/2}=A(h\nu-E_g)n/2 \quad (3.3)$$

Where h, α, E_g, n, A, and ν are Planck constant, absorption coefficient, bandgap energy, optical transition type of semiconductors, proportionality constant, and light frequency, respectively. The optical bandgaps for g-C_3N_4, β-Bi_2O_3, and β-Bi_2O_3/g-C_3N_4 (**Fig. 3.4 (c)**) were calculated to be 2.88 eV,[35] 2.5 eV (equal to β-Bi_2O_3's literature value),[36] and 2.02 Ev,[23] respectively. Theresults signify that by coupling g-C_3N_4 with β-Bi_2O_3, alteration of the electronic structure of β-Bi_2O_3 occurs.[23]

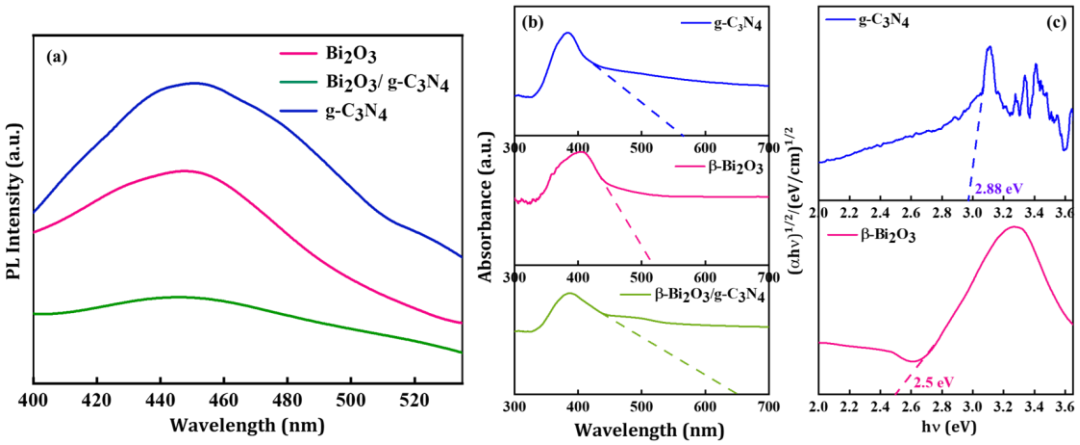

Fig. 3.4. (a) Photoluminescence spectra, (b) UV Visible diffuse reflectance spectra, and (c)Tauc's plot of the photocatalysts.

3.3.2 Methylene Blue and Fipronil Photocatalytic Activity

β-Bi_2O_3/g-C_3N_4's photocatalytic ability was investigated by pollutant degradation (MB,[14] and FIP[15] with concentrations of 5, and 600 mg/L, respectively). To set up the adsorption-desorption equilibrium, the solutions were placed for 60 min in the dark. The photodegradation efficacy without catalyst was scrutinized and was found to be almost same (5.07% for MB and 5.46% for FIP) (**Fig. 3.5 (a) and (c)**), emphasizing the role of β-Bi_2O_3/g- C_3N_4 composite in the photodegradation process. **Eq. (3.4)** was utilized to formulate the rate constant,[15] depicted as:

$$\ln (C/C_0) = -kt \qquad (3.4)$$

Where C denotes the concentration at a time 't', C_0 denotes the concentration at time = '0', and k denotes the rate constant.

Fig. 3.5 (a), and **Fig. 3.5 (c)** demonstrate the photocatalytic efficiency for MB, and FIP, respectively, both with and without catalyst. Remarkably, the efficiencies without any catalyst were merely 5.07% ($k = 5.228 \times 10^{-4}\ min^{-1}$) for MB (**Fig. 3.5 (b)**), and 5.46% ($k = 4.389 \times 10^{-4}\ min^{-1}$) for FIP (**Fig. 3.5 (d)**). The best results were shown by 1:3 β-Bi_2O_3/g-C_3N_4 composite for both the dyes MB and FIP with the degradation efficiencies of 97.58%

(k = 0.04066 min^{-1}) and 74.71% (k = 0.01068 min^{-1}), respectively as compared to g-C_3N_4, β-Bi_2O_3, 1:1 β-Bi_2O_3/g-C_3N_4composite, 1:4 β-Bi_2O_3/g-C_3N_4 composite, 3:1 β-Bi_2O_3/g-C_3N_4 composite. **Table 3.2** shows the rate constants of g-C_3N_4, β-Bi_2O_3, 1:1 β-Bi_2O_3/g-C_3N_4, 3:1 β-Bi_2O_3/g-C_3N_4, 1:4 β-Bi_2O_3/g- C_3N_4, 1:3 β-Bi_2O_3/g-C_3N_4 for pollutant degradation. Thus, as observed from the results, 1:3 β-Bi_2O_3/g-C_3N_4 displayed exceptional efficacy in the photodegradation of pollutants illuminated under visible light.

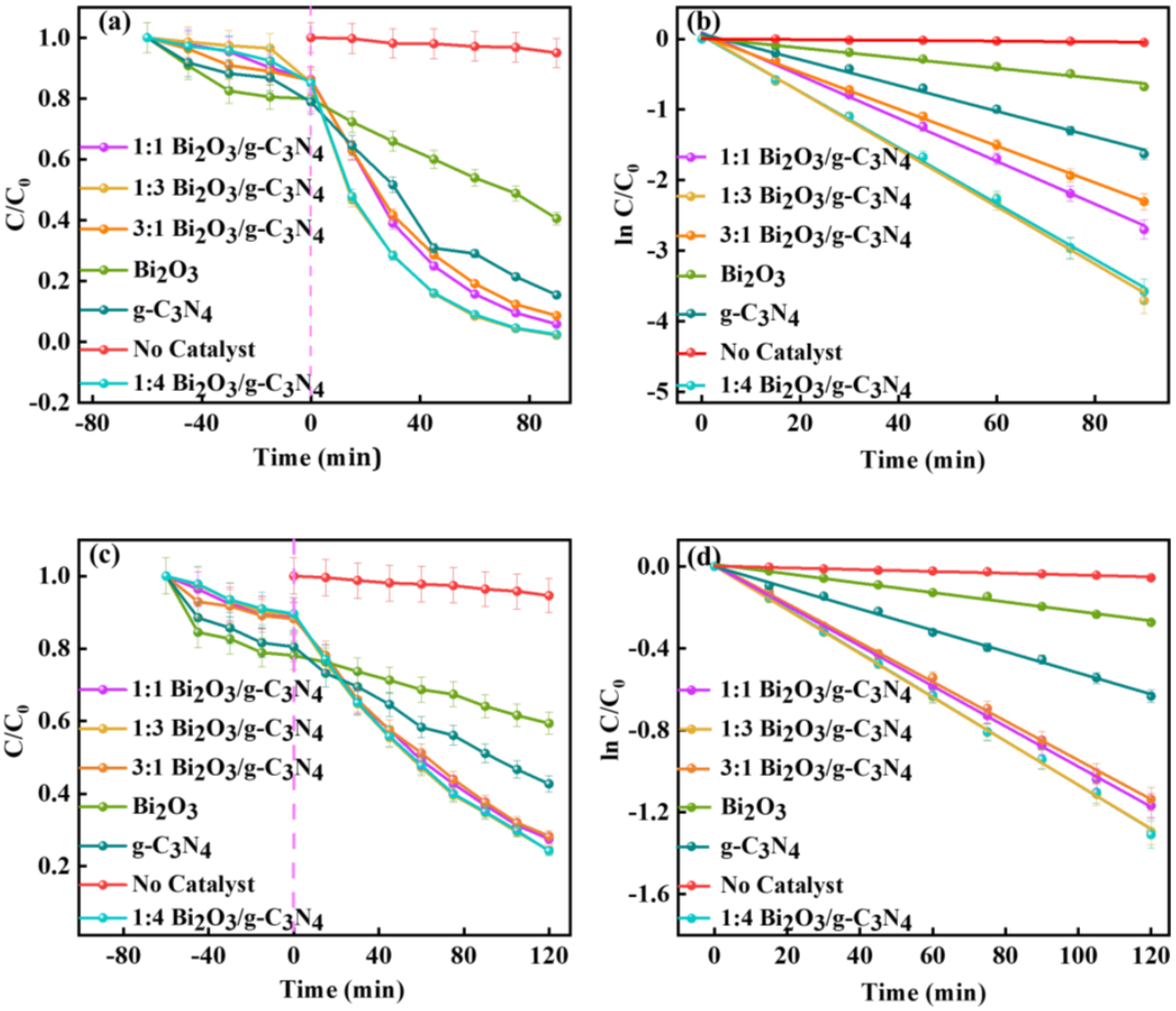

Fig. 3.5. Kinetic studies of the catalytic activity of (a, b) MB and (c, d) FIP.

Table 3.2. Rate constants for the degradation of MB and FIP.

Photocatalyst	Rate Constants		% Degradation	
	MB (min^{-1})	FIP (min^{-1})	MB	FIP
β-Bi_2O_3	0.00719	0.00229	52.41	46.33
g-C_3N_4	0.01824	0.0052	82.12	60.78
1:1 β-Bi_2O_3/g-C_3N_4	0.03037	0.00982	93.11	71.51
1:3 β-Bi_2O_3/g-C_3N_4	0.04066	0.01068	97.58	74.71
3:1 β-Bi_2O_3/g-C_3N_4	0.02605	0.00955	89.73	70.69
1:4 β-Bi_2O_3/g-C_3N_4	0.03962	0.01074	97.2	74.09

3.3.2.1 Catalyst Concentration Analysis

The catalyst concentration analysis was performed to scrutinize the part played by catalyst concentration in the photodegradation process. Different concentrations from 0.06 to 0.4 g/L were varied to study the degradation efficiency via 1:3 β-Bi_2O_3/g-C_3N_4 composite (**Fig. 3.6 (a)**). The efficacy was highest for MB and FIP at 0.06 g/L. This is attributed to the hike in the opaqueness of the solution and the scattering of light. Once, there is thorough adsorption of dye, any additional inclusion of the catalyst will avail no result on the photodegradation activity, owing to the deactivated sites.[15]

3.3.2.2 pH Studies

The formulation of point of zero charge (pzc) on β-Bi_2O_3/g-C_3N_4's surface (pH_{pzc}) was formulated to be ~pH 6 (**Fig. 3.6 (b)**), indicating the negatively charged surface of the composite when $pH>pH_{pzc}$ and positively charged when $pH<pH_{pzc}$. The effect on the degradation process via the change in pH (pH 1 to 12) using 0.06 g/L β-Bi_2O_3/g-C_3N_4 was

recorded (**Fig. 3.6 (c)**). In the solution, the pH was secured by adding NaOH and HCl. For MB, the highest efficacy (97.54%) was found at pH 8, suggesting cationic dye MB's interaction with the negative surface of β-Bi_2O_3/g-C_3N_4 binary composite.[37] The maximum efficacy (74.28%) for FIP was observed at pH 4, indicating anionic dye FIP's interaction with the positive surface of β-Bi_2O_3/g-C_3N_4 binary composite.[37]

3.3.2.3 Reusability

The separation of the β-Bi_2O_3/g-C_3N_4 binary composite after the photodegradation activity could be overcome via centrifugation. Since the MB dye gets temporarily adsorb on the surface of the catalyst, its separation is facile. To evaluate the efficacy of the catalyst, the retrieved material was washed with distilled water (thrice), later centrifuged and dried, then reutilized.[15] The efficacy reduced to 88.89% for MB and 71.84% for FIP after 4 repetitive cycles of degradation (**Fig. 3.6 (d)**). The firmness of the photocatalyst was established through XRD (**Fig. 3.6 (e)**), BET (**Fig. 3.7 (a-b)**), and FESEM (**Fig. 3.7 (c-d)**) analysis for 1:3 β- Bi_2O_3/g-C_3N_4 composite before and after degradation. The surface area analysis of the catalyst after degradation cycles indicates its surface area to be ~53 m^2/g, affirming the pollutants are not permanently adsorbed on the surface of the catalyst. The sorption isotherms before and after 4 cycles of degradation are shown in **Fig. 3.7 (a-b)**. The XRD analysis (**Fig. 3.6 (e)**) after degradation affirms the intactness of the crystallinity of the structure after degradation cycles. **Fig. 3.7 (c-d)** shows that the surface morphology of the catalyst remains intact, indicating the stability of the photocatalyst after degradation cycles. Thus, the studies confirm the reusability and stability of the photocatalyst with high efficiency.

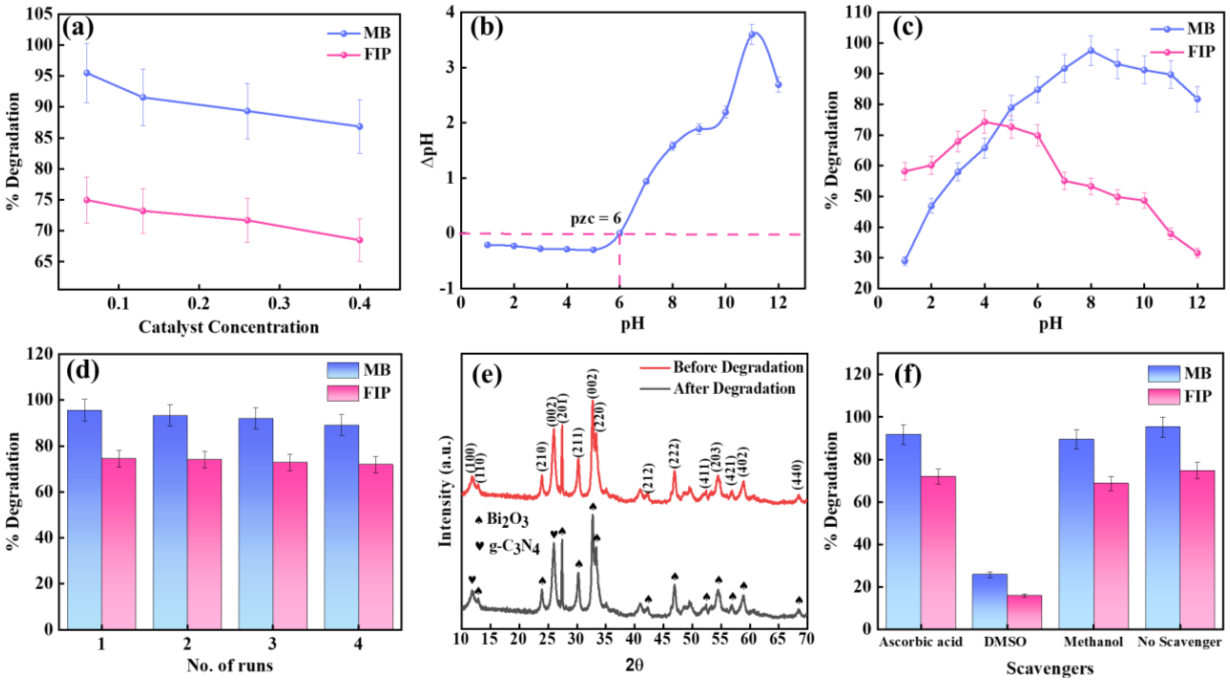

Fig. 3.6. Catalytic activity: (a) studies in catalyst concentration, (b) studies in pH_{PZC} calculation, (c) studies in pH variation, (d) studies of reusability, (e) XRD patterns of the β-Bi_2O_3/g-C_3N_4 before and after photodegradation, (f) scavenging experiment via 1:3 β-Bi_2O_3/g-C_3N_4 binary composite.

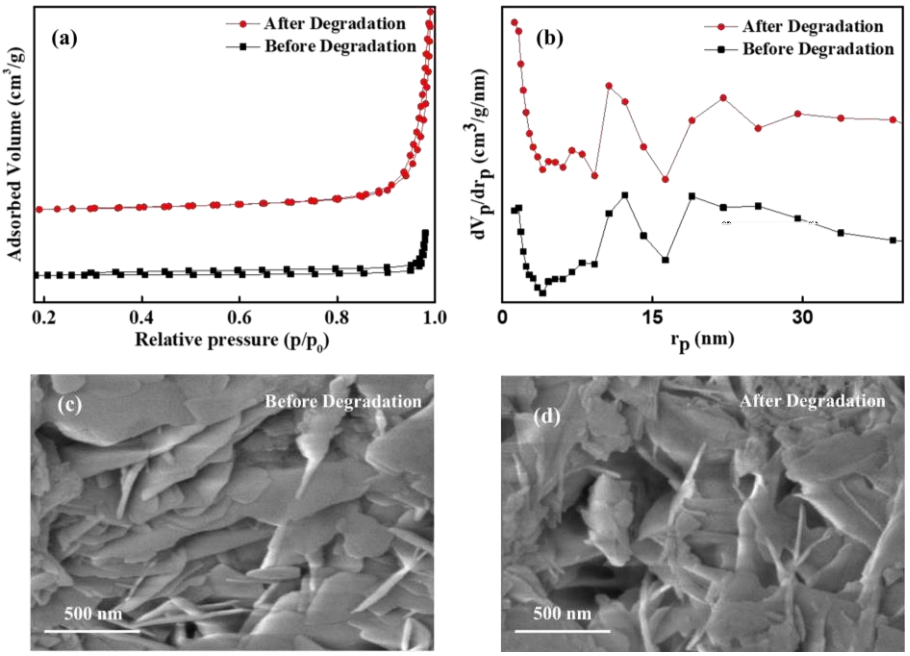

Fig. 3.7. (a) N_2 adsorption-desorption isotherms, (b) pore size distribution curves, (c-d) FESEM analysis of 1:3 β-Bi_2O_3/g-C_3N_4 before and after degradation.

3.3.2.4 Possible Mechanism

The scavenging experiments scrutinized the role played by the radical species in the photodegradation activity via ascorbic acid, DMSO, and methanol relating to superoxide radical ($O_2^{\bullet-}$), hydroxide radical ($^{\bullet}OH$), and quenching holes (h^+), respectively (**Fig. 3.6 (f)**).[38] The ability of ascorbic acid to scavenge both $O_2^{\bullet-}$ and $^{\bullet}OH$ poses a limitation because of the less reaction rate of ascorbate with $^{\bullet}OH$ to produce ascorbyl radicals.[39] The β-Bi_2O_3/g-C_3N_4 composite was utilized to carry out the studies. The radical species whose scavenger shows maximum inhibition in the degradation activity are considered responsible for the photodegradation process. In the process, equimolar amounts of ascorbic acid, DMSO, and methanol were put in the prepared solutions. Particularly, the MB degradation efficacies for ascorbic acid, methanol, and DMSO were 91.74%, 89.56%, and 25.87% suggesting the distinguished role played by $^{\bullet}OH$ in MB degradation. The degradation efficacies of FIP for ascorbic acid, methanol, and DMSO were noted to be 71.98%, 68.75%, and 15.87%, respectively, indicating the role of $^{\bullet}OH$ in FIP degradation.

The photocatalyst's band positions act as a vital part in determining the charge carrier partition. The valence band (VB) and the conduction band (CB) potentials for g-C_3N_4 and β-Bi_2O_3 were calculated via the **Eqs. (3.5 and 3.6)**[40]:

$$E_{CB} = X - E_c - 0.5E_g \quad (3.5)$$

$$E_{VB} = E_{CB} + E_g \quad (3.6)$$

Where E_{VB} signifies the valence band's position, X signifies the semiconductor's absolute electronegativity, E_{CB} signifies the conduction band's position, E_g signifies the semiconductor's bandgap, and E_c signifies the energy of the free-electron of hydrogen (~ 4.5 eV). The values of electronegativity for β-Bi_2O_3 and g-C_3N_4 are 5.95 eV[15] and 4.73 eV[41], respectively. As obtained from DRS Tauc Plot, β-Bi_2O_3's bandgap is 2.5 eV and g-C_3N_4's bandgap is 2.88 eV. Thus, by **Eq. (3.5) and (3.6)**, for β-Bi_2O_3, the CB, and VB potentials

are 0.2 eV, and 2.7 eV, respectively, while for g-C_3N_4 the CB, VB positions are -1.21 eV, 1.67 eV,respectively.

The visible-light-induced electrons move from the VB to the CB for photocatalysts. For pure g-C_3N_4 and pure β-Bi_2O_3, there is a recombination of the e^--h^+ pair, thus giving a restricted photocatalytic performance. While coupling g-C_3N_4 with β-Bi_2O_3 dramatically improved the performance. As depicted by the bandgap potentials of β-Bi_2O_3 and g-C_3N_4, the positioning of the novel catalysts is done (**Scheme 3.3**). The scavenging mechanism displayed the role played by $^{\bullet}OH$ in pollutant degradation by the heterojunction between β-Bi_2O_3 and g-C_3N_4. Therefore, a Z-scheme mechanism is proposed at the interface of g-C_3N_4 and β-Bi_2O_3 where oxidation occurs at the VB of β-Bi_2O_3 owing to the greater VB potential than $^{\bullet}OH/H_2O$ and reduction occurs at the CB of g-C_3N_4 due to the greater negative potential than $O_2/O_2^{\bullet-}$. The superoxide anion then forms H_2O_2 which eventually forms $^{\bullet}OH$ and hydroxyl radicals being the main species in the degradation activity by β-Bi_2O_3/g-C_3N_4.

Thus, g-C_3N_4 nanoflakes and β-Bi_2O_3 nanorods get excited upon illumination via visible light (**Eq. 3.7**). The electrons of the CB of β-Bi_2O_3 transfer to g-C_3N_4's VB and again combine with the holes on g-C_3N_4's VB (**Eq. 3.8**). The formation of $^{\bullet}OH$ radicals occurs when holes present on β-Bi_2O_3's VB react with OH^- (**Eq. 3.9**) owing to its higher VB (2.7 eV) position than $^{\bullet}OH/H_2O$ i.e., 1.99 V and 2.27 V *vs.* NHE, respectively. Superoxide radicals ($O_2^{\bullet-}$) are formed (**Eq. 3.10**) when CB electrons of g-C_3N_4 react with O_2 owing to its greater negative potential i.e., -1.21 eV than the redox potential of $O_2/O_2^{\bullet-}$ i.e. -0.33 V *vs.* NHE. Viewing the insignificant impact of superoxide radicals in the photodegradation process of pollutants (**Fig. 3.6 (f)**), $O_2^{\bullet-}$ forms $^{\bullet}OH$ radicals on reaction with water molecules and electrons (**Eq. 3.11- 13**).[23] Finally, the $^{\bullet}OH$ radicals degrade MB and FIP to lesser toxins such as CO_2 and H_2O (**Eq. 3.14**). Thus, there was an efficient separation of photogenerated e^--h^+ pairs favorable for generating $^{\bullet}OH$ radicals and strengthened photodegradation under visible light, supported by the high degradation efficiency of MB

(97.58%) and FIP (74.71%) via β-Bi_2O_3/g-C_3N_4 when illuminated under visible light (**Fig. 3.5 (a) and (c)**). The mechanism is as follows:

$$\beta\text{-}Bi_2O_3/g\text{-}C_3N_4 + h\nu \longrightarrow \beta\text{-}Bi_2O_3\ (e^- + h^+) + g\text{-}C_3N_4\ (e^- + h^+) \quad (3.7)$$

$$\beta\text{-}Bi_2O_3\ (e^-) + g\text{-}C_3N_4\ (h^+) \longrightarrow \beta\text{-}Bi_2O_3 + g\text{-}C_3N_4 \quad (3.8)$$

$$\beta\text{-}Bi_2O_3\ (h^+) + OH^- \longrightarrow {}^{\bullet}OH \quad (3.9)$$

$$g\text{-}C_3N_4\ (e^-) + O_2 \longrightarrow O_2^{\bullet-} \quad (3.10)$$

$$O_2^{\bullet-} + H^+ \longrightarrow HO_2^{\bullet} \quad (3.11)$$

$$2HO_2^{\bullet} \longrightarrow H_2O_2 + O_2 \quad (3.12)$$

$$H_2O_2 + e^- \longrightarrow OH^- + {}^{\bullet}OH \quad (3.13)$$

$$\bullet OH + MB/FIP \longrightarrow CO_2 + H_2O \quad (3.14)$$

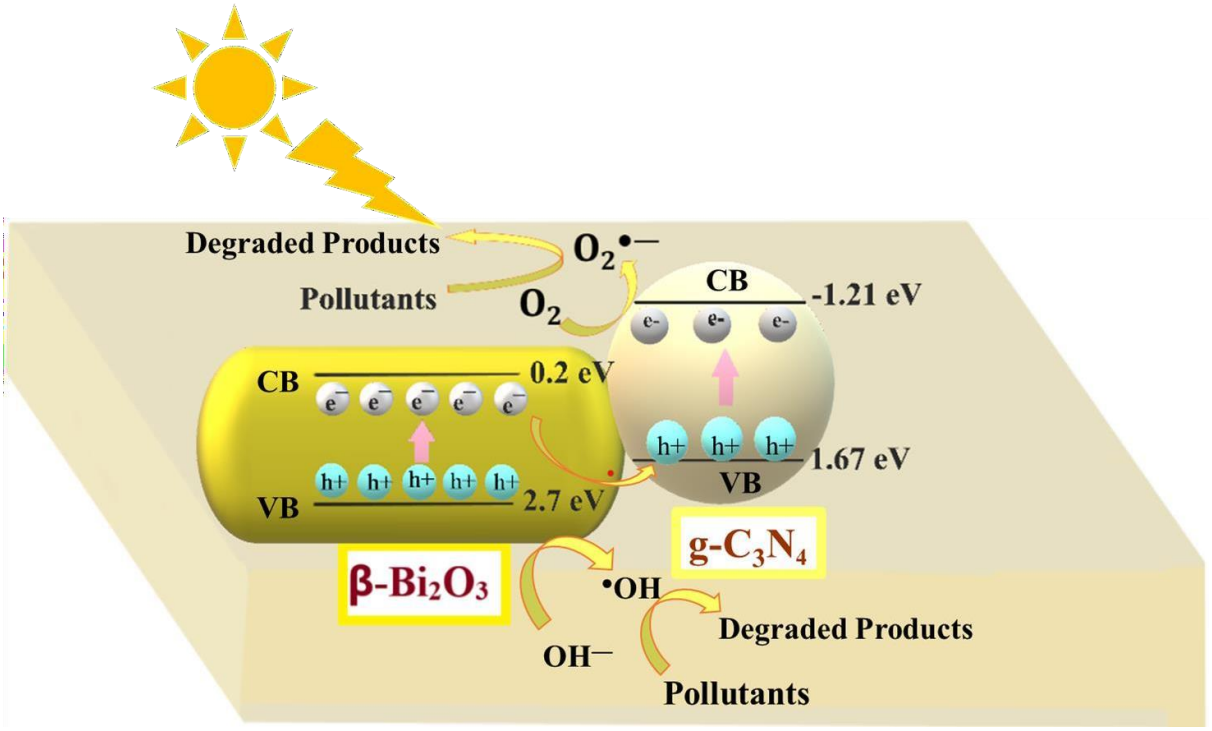

Scheme 3.3. Mechanism for visible-light pollutant degradation by nanoflake-nanorod-like β-Bi_2O_3/g-C_3N_4 composite.

The as-fabricated catalyst 1:3 β-Bi_2O_3/g-C_3N_4 composite was compared with the ones reported in the literature. Fan *et al.*[23] fabricated 0.5-Bi_2O_3/g-C_3N_4 to degrade MB with 100% efficiency but did not validate the mechanism by utilizing a colorless pollutant while Ghosh *etal.*[27] degraded MB with only 92% efficiency using Bi_2O_3/g-C_3N_4 composite without using a colorless pollutant. The authors have fabricated β-phased Bi_2O_3 and g-C_3N_4 heterojunction with varied weight ratios of the composite (1:1, 1:3, and 3:1 β-Bi_2O_3/g-C_3N_4), and their photodegradation efficiency for MB and FIP was noted. The degradation efficiencies for pollutants were remarkable at ~97% and ~74% for MB and FIP, respectively. Previously, no study was done with β-phased Bi_2O_3 for MB and FIP degradation. Moreover, FIP (a colorless insecticide) was used to validate the indirect mechanism. COD analysis was also performed to support the studies. A comparative study of the literature was done in the tabulated form for pollutants' degradation efficacy using bismuth composites (**Table 3.3**) confirming the visible-light degradation efficiency of our as-synthesized β-Bi_2O_3/g-C_3N_4 nanocomposites.

Table 3.3. Comparison of varied photocatalysts for pollutant degradation.

Catalyst	**Pollutant**	**Conc. (g/L)**	**Time (min)**	**Light source**	**Lamp**	***k* (min^{-1})**	**Efficiency (%)**	**Reference**
β-Bi_2O_3/g-C_3N_4	PNP, RhB	-	300,120	visible	-	0.0233	71.6, 94.8	22

Bi_2O_3/ g-C_3N_4	MB	1	90	visible	250 W Xe lamp	-	100	23
Bi_2O_3/ g-C_3N_4	MB	2	60	visible	18 W LED light	0.0400	-	27
Bi_2O_3/ g-C_3N_4	AB10B	0.2	120	visible	35 W Xe lamp	0.0172	88.7	28
Bi_2O_3/ g-C_3N_4	RB 5	1	120	UV-visible	120 W Xe lamp	-	84	26

3.3.2.5. COD Measurements

The COD analysis of the pollutants was performed using 0.06 g/L of 1:3 nanoflake-nanorod-like β-Bi_2O_3/g-C_3N_4 composite. Visible light illumination was done (90 min, MB and 120 min, FIP). COD with no pretreatment was found to be 1200 mg/L for MB, and 1600 mg/Lfor FIP, indicating the high amounts of organics' loading in the pollutants. While the final CODwas calculated to be 800 mg/L and 1200 mg/L for MB and FIP, respectively, suggesting the efficacy of β-Bi_2O_3/g-C_3N_4 composite in treating such pollutants (**Fig. 3.8**). The low degradation efficiency could be since no pretreatment of the sample was done before the degradation process.

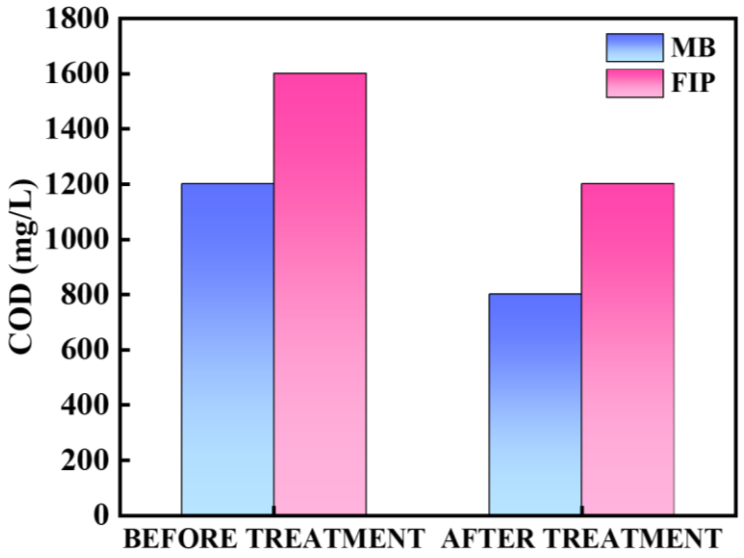

Fig. 3.8. COD analysis of MB and FIP by 1:3 β-Bi_2O_3/g-C_3N_4 binary composite.

3.3.3 Conclusion

The chapter includes the fabrication of flaky nanosheets-like β-Bi_2O_3/g-C_3N_4 binary composites through the in-situ precipitation technique, applied for MB and FIP photodegradation. Surface analysis displayed β-Bi_2O_3 nanorods deposited on g-C_3N_4's flaky nanolayers. The maximum proficiency was shown via 1:3 β-Bi_2O_3/g-C_3N_4 composite ascribed to the enhanced e^--h^+ pair separation with deduced recombination rate by forming Z-scheme heterojunction between nanorods of β-Bi_2O_3 and flaky nanosheets of g-C_3N_4. The pH and pzc investigation showcased that in the alkaline range, MB displayed maximum proficiency, whereas FIP favored acidic pH due to the interactions between catalyst's surface and cationic dye MB and anionic insecticide FIP, respectively. Active sites were deduced after the complete pollutant adsorption, shown by decreased efficacy as depicted through the feed concentration analysis. The capacity to reuse the β-Bi_2O_3/g-C_3N_4 composite was also affirmed. Scavenging investigations demonstrated the part played by $^{\bullet}OH$ in the degradation process. Thus, the technique provides a good way to design flaky nanosheets-like β-Bi_2O_3/g-C_3N_4 photocatalysts with high efficacy.

References

(1) Tang, K. Y.; Chen, J. X.; Legaspi, E. D. R.; Owh, C.; Lin, M.; Tee, I. S. Y.; Kai, D.; Loh, X. J.; Li, Z.; Regulacio, M. D.; Ye, E. Gold-Decorated TiO_2 Nanofibrous Hybrid for Improved Solar-Driven Photocatalytic Pollutant Degradation. *Chemosphere* **2021**, *265*, 129114. https://doi.org/10.1016/j.chemosphere.2020.129114.

(2) Sharma, S.; Basu, S. Fabrication of Centimeter-Sized Sb_2S_3/SiO_2 Monolithic Mimosa Pudica Nanoflowers for Remediation of Hazardous Pollutants from Industrial Wastewater. *J. Clean. Prod.* **2021**, *280*, 124525. https://doi.org/10.1016/j.jclepro.2020.124525.

(3) Nagar, A.; Basu, S. Ternary g-C_3N_4/Ag/$BiVO_4$ Nanocomposite: Fabrication and Implementation to Remove Organic Pollutants. *Environ. Technol. Innov.* **2021**, *23*, 101646. https://doi.org/10.1016/j.eti.2021.101646.

(4) Bhakare, M. A.; Lokhande, K. D.; Dhumal, P. S.; Bondarde, M. P.; Some, S. Multifunctional Heteroatom Doped Sustainable Carbon Nanocomposite for Rapid Removal of Persistent Organic Pollutant and Iodine from Water. *Sep. Purif. Technol.* **2022**, *278*, 119490. https://doi.org/10.1016/j.seppur.2021.119490.

(5) Contreras, M.; Grande-Tovar, C. D.; Vallejo, W.; Chaves-López, C. Bio-Removal of Methylene Blue from Aqueous Solution by Galactomyces Geotrichum KL20A. *Water* **2019**, *11*, 1. https://doi.org/10.3390/w11020282.

(6) Rathi, A.; Basu, S.; Barman, S. Adsorptive Removal of Fipronil from Its Aqueous Solution by Modified Zeolite HZSM-5: Equilibrium, Kinetic and Thermodynamic Study. *J. Mol. Liq.* **2019**, *283*, 867. https://doi.org/10.1016/j.molliq.2019.02.140.

(7) Monga, D.; Basu, S. Enhanced Photocatalytic Degradation of Industrial Dye by g-C_3N_4/TiO_2 Nanocomposite: Role of Shape of TiO_2. *Adv. Powder Technol.* **2019**, *30*, 1089. https://doi.org/10.1016/j.apt.2019.03.004.

(8) Sharma, S.; Basu, S. Highly Reusable Visible Light Active Hierarchical Porous WO_3/SiO_2 Monolith in Centimeter Length Scale for Enhanced Photocatalytic Degradation of Toxic Pollutants. *Sep. Purif. Technol.* **2020**, *231*, 115916. https://doi.org/10.1016/j.seppur.2019.115916.

(9) Pethsangave, D. A.; Khose, R. V.; Wadekar, P. H.; Kulal, D. K.; Some, S. One-Pot Synthetic Approach for Magnetically Separable Graphene Nanocomposite for Dye Degradation. *Chemistry Select* **2020**, *5*, 1516. https://doi.org/10.1002/slct.201903966.

(10) Dashairya, L.; Sharma, S.; Rathi, A.; Saha, P.; Basu, S. Solar-Light-Driven Photocatalysis by Sb_2S_3/Carbon Based Composites towards Degradation of Noxious Organic Pollutants. *Mater. Chem. Phys.* **2021**, *273*, 125120. https://doi.org/10.1016/j.matchemphys.2021.125120.

(11) Mushtaq, F.; Guerrero, M.; Sakar, M. S.; Hoop, M.; Lindo, A. M.; Sort, J.; Chen, X.; Nelson, B. J.; Pellicer, E.; Pané, S. Magnetically Driven Bi_2O_3/BiOCl-Based Hybrid Microrobots for Photocatalytic Water Remediation. *J. Mater. Chem. A* **2015**, *3*, 23670. https://doi.org/10.1039/c5ta05825b.

(12) Aanchal; Barman, S.; Basu, S. Complete Removal of Endocrine Disrupting Compound and Toxic Dye by Visible Light Active Porous g-C_3N_4/H-ZSM-5 Nanocomposite. *Chemosphere* **2020**, *241*, 124981. https://doi.org/10.1016/j.chemosphere.2019.124981.

(13) Garg, A.; Basu, S.; Shetti, N. P.; Reddy, K. R. 2D Materials and Its Heterostructured Photocatalysts: Synthesis, Properties, Functionalization and Applications in Environmental Remediation. *J. Environ. Chem. Eng.* **2021**, *9*, 106408. https://doi.org/10.1016/J.JECE.2021.106408.

(14) Monga, D.; Ilager, D.; Shetti, N. P.; Basu, S.; Aminabhavi, T. M. 2D/2D Heterojunction of MoS_2/g-C_3N_4 Nanoflowers for Enhanced Visible-Light-Driven Photocatalytic and Electrochemical Degradation of Organic Pollutants. *J. Environ. Manage.* **2020**, *274*,

111208. https://doi.org/10.1016/j.jenvman.2020.111208.

(15) Nagar, A.; Basu, S. Fabrication of 3D Porous Peony Flower-like β-Bi_2O_3/BiOCl Heterostructure for Synergistically Boosting the Visible-Light-Driven Degradation of Organic Pollutants. *Environ. Technol. Innov.* **2021**, *24*, 101956. https://doi.org/10.1016/j.eti.2021.101956.

(16) Chai, S. Y.; Kim, Y. J.; Jung, M. H.; Chakraborty, A. K.; Jung, D.; Lee, W. I. Heterojunctioned BiOCl/Bi_2O_3, a New Visible Light Photocatalyst. *J. Catal.* **2009**, *262*, 144. https://doi.org/10.1016/j.jcat.2008.12.020.

(17) Hou, J.; Yang, C.; Wang, Z.; Zhou, W.; Jiao, S.; Zhu, H. In Situ Synthesis of α-β Phase Heterojunction on Bi_2O_3 Nanowires with Exceptional Visible-Light Photocatalytic Performance. *Applied Catal. B: Environ.* **2013**, *142*, 504. https://doi.org/10.1016/j.apcatb.2013.05.050.

(18) Kong, S.; An, Z.; Zhang, W.; An, Z.; Yuan, M.; Chen, D. Preparation of Hollow Flower-like Microspherical β-Bi_2O_3/BiOCl Heterojunction and High Photocatalytic Property for Tetracycline Hydrochloride Degradation. *Nanomaterials* **2020**, *10*, 1. https://doi.org/10.3390/nano10010057.

(19) Kundu, A.; Sharma, S.; Basu, S. Modulated BiOCl Nanoplates with Porous g-C_3N_4 Nanosheets for Photocatalytic Degradation of Color/Colorless Pollutants in Natural Sunlight. *J. Phys. Chem. Solids* **2021**, *154*, 110064. https://doi.org/10.1016/j.jpcs.2021.110064.

(20) Si, Y. H.; Chen, W. M.; Shang, S. K.; Xia, Y.; Zeng, X. R.; Zhou, J.; Li, Y. Y. g-C_3N_4/Pt/$BiVO_4$ Nanocomposites for Highly Efficient Visible-Light Photocatalytic Removal of Contaminants and Hydrogen Generation. *Nanotechnology* **2020**, *31*, 125706. https://doi.org/10.1088/1361-6528/ab5bc5.

(21) Lin, X.; Xu, D.; Xi, Y.; Zhao, R.; Zhao, L.; Song, M.; Zhai, H.; Che, G.; Chang, L.

Construction of Leaf-like g-C_3N_4/Ag/$BiVO_4$ Nanoheterostructures with Enhanced Photocatalysis Performance under Visible-Light Irradiation. *Colloids Surfaces A: Physicochem. Eng. Asp.* **2017**, *513*, 117–124. https://doi.org/10.1016/j.colsurfa.2016.11.040.

(22) Wang, D.; Yu, X.; Feng, Q.; Lin, X.; Huang, Y.; Huang, X.; Li, X.; Chen, K.; Zhao, B.; Zhang, Z. In-Situ Growth of β-Bi_2O_3 Nanosheets on g-C_3N_4 to Construct Direct Z Scheme Heterojunction with Enhanced Photocatalytic Activities. *J. Alloys Compd.* **2021**, *859*, 157795. https://doi.org/10.1016/j.jallcom.2020.157795.

(23) Fan, G.; Ma, Z.; Li, X.; Deng, L. Coupling of Bi_2O_3 Nanoparticles with g-C_3N_4 for Enhanced Photocatalytic Degradation of Methylene Blue. *Ceram. Int.* **2021**, *47*, 5758. https://doi.org/10.1016/j.ceramint.2020.10.162.

(24) Liu, G.; Li, S.; Lu, Y.; Zhang, J.; Feng, Z.; Li, C. Controllable Synthesis of α-Bi_2O_3 and γ-Bi_2O_3 with High Photocatalytic Activity by α-Bi_2O_3→γ-Bi_2O_3→α-Bi_2O_3 transformation in a Facile Precipitation Method. *J. Alloys Compd.* **2016**, *689*, 787. https://doi.org/10.1016/j.jallcom.2016.08.047.

(25) Zhang, L.; Wang, G.; Xiong, Z.; Tang, H.; Jiang, C. Fabrication of Flower-like Direct Z-Scheme β-Bi_2O_3/g-C_3N_4 Photocatalyst with Enhanced Visible Light Photoactivity for Rhodamine B Degradation. *Appl. Surf. Sci.* **2018**, *436*, 162. https://doi.org/10.1016/j.apsusc.2017.11.280.

(26) Shafawi, A. N.; Mahmud, R. A.; Ahmed Ali, K.; Putri, L. K.; Md Rosli, N. I.; Mohamed, A. R. Bi_2O_3 Particles Decorated on Porous g-C_3N_4 Sheets: Enhanced Photocatalytic Activity through a Direct Z-Scheme Mechanism for Degradation of Reactive Black 5 under UV–Vis Light. *J. Photochem. Photobiol. A Chem.* **2020**, *389*, 112289. https://doi.org/10.1016/j.jphotochem.2019.112289.

(27) Ghosh, U.; Pal, A. Fabrication of a Novel Bi_2O_3 Nanoparticle Impregnated Nitrogen

Vacant 2D g-C_3N_4 Nanosheet Z Scheme Photocatalyst for Improved Degradation of Methylene Blue Dye under LED Light Illumination. *Appl. Surf. Sci.* **2020**, *507*, 144965. https://doi.org/10.1016/j.apsusc.2019.144965.

(28) Cui, Y.; Zhang, X.; Guo, R.; Zhang, H.; Li, B.; Xie, M.; Cheng, Q.; Cheng, X. Construction of Bi_2O_3/g-C_3N_4 Composite Photocatalyst and Its Enhanced Visible Light Photocatalytic Performance and Mechanism. *Sep. Purif. Technol.* **2018**, *203*, 301. https://doi.org/10.1016/j.seppur.2018.04.061.

(29) Raposo, F.; Delarubia, M.; Borja, R.; Alaiz, M. Assessment of a modified and optimised method for determining chemical oxygen demand of solid substrates and solutions with high suspended solid content. *Talanta* **2008**, 76, 448. https://doi.org/10.1016/j.talanta.2008.03.030.

(30) Balint, R.; Bartoli, M.; Jagdale, P.; Tagliaferro, A.; Memon, A. S.; Rovere, M.; Martin, M. Defective Bismuth Oxide as Effective Adsorbent for Arsenic Removal from Water and Wastewater. *Toxics* **2021**, *9*, 23. https://doi.org/10.3390/toxics9070158.

(31) Tan, L.; Xu, J.; Zhang, X.; Hang, Z.; Jia, Y.; Wang, S. Synthesis of g-C_3N_4/CeO_2 Nanocomposites with Improved Catalytic Activity on the Thermal Decomposition of Ammonium Perchlorate. *Appl. Surf. Sci.* **2015**, *356*, 447. https://doi.org/10.1016/j.apsusc.2015.08.078.

(32) Nguyen, V. H.; Bui, Q. T. P.; Vo, D. V. N.; Lim, K. T.; Bach, L. G.; Do, S. T.; Van Nguyen, T.; Doan, V. D.; Nguyen, T. D.; Nguyen, T. D. Effective Photocatalytic Activity of Sulfate-Modified $BiVO_4$ for the Decomposition of Methylene Blue under LED Visible Light. *Materials* **2019**, *12*, 2681. https://doi.org/10.3390/ma12172681.

(33) Zhang, Y.; Pan, Q.; Chai, G.; Liang, M.; Dong, G.; Zhang, Q.; Qiu, J. Synthesis and Luminescence Mechanism of Multicolor-Emitting g-C_3N_4 Nanopowders by Low Temperature Thermal Condensation of Melamine. *Sci. Rep.* **2013**, *3*, 1. https://doi.10.

1038/srep01943.

(34) Oudghiri-Hassani, H.; Rakass, S.; Al Wadaani, F. T.; Al-ghamdi, K. J.; Omer, A.; Messali, M.; Abboudi, M. Synthesis, Characterization and Photocatalytic Activity of α-Bi_2O_3 Nanoparticles. *J. Taibah Univ. Sci.* **2015**, *9*, 508. https://doi.org/10.1016/j.jtusci.2015.01.009.

(35) Shen, L.; Xing, Z.; Zou, J.; Li, Z.; Wu, X.; Zhang, Y.; Zhu, Q.; Yang, S.; Zhou, W. Black TiO_2 Nanobelts/g-C_3N_4 Nanosheets Laminated Heterojunctions with Efficient Visible-Light-Driven Photocatalytic Performance. *Sci. Rep.* **2017**, *7*, 1. https://doi.org/10.1038/srep41978.

(36) Gadhi, T. A.; Hernández-Gordillo, A.; Bizarro, M.; Jagdale, P.; Tagliaferro, A.; Rodil, S. E. Efficient α/β-Bi_2O_3 Composite for the Sequential Photodegradation of Two-Dyes Mixture. *Ceram. Int.* **2016**, *42*, 13065. https://doi.org/10.1016/j.ceramint.2016.05.087.

(37) Zhu, B.; Xia, P.; Ho, W.; Yu, J. Isoelectric Point and Adsorption Activity of Porous g-C_3N_4. *Appl. Surf. Sci.* **2015**, *344*, 188. https://doi.org/10.1016/j.apsusc.2015.03.086.

(38) Pelaez, M.; Falaras, P.; Likodimos, V.; O'Shea, K.; de la Cruz, A. A.; Dunlop, P. S. M.; Byrne, J. A.; Dionysiou, D. D. Use of Selected Scavengers for the Determination of NF-TiO_2 Reactive Oxygen Species during the Degradation of Microcystin-LR under Visible Light Irradiation. *J. Mol. Catal. A Chem.* **2016**, *425*, 183. https://doi.org/10.1016/j.molcata.2016.09.035.

(39) Pehlivan, F. E. Vitamin C: An Antioxidant Agent. *Vitamin C* **2017**, *Chapter 2*, 1. https://doi.org/10.5772/intechopen.69660.

(40) Li, Y.; Wang, J.; Yao, H.; Dang, L.; Li, Z. Chemical Etching Preparation of BiOI/Bi_2O_3 Heterostructures with Enhanced Photocatalytic Activities. *Catal. Commun.* **2011**, *12*, 660. https://doi.org/10.1016/J.CATCOM.2010.12.011.

(41) Liu, Q. Y.; Qi, Y. L.; Zheng, Y. F.; Song, X. C. Synthesis and Enhanced Photocatalytic Activity of g-C3N4 Hybridized CdS Nanoparticles. *Bull. Mater. Sci.* **2017**, *40*, 1329.

https://doi.org/10.1007/s12034-017-1513-y.

Chapter 4

Ternary g-C_3N_4/Ag/$BiVO_4$ nanocomposite: Fabrication and implementation to remove organic pollutants

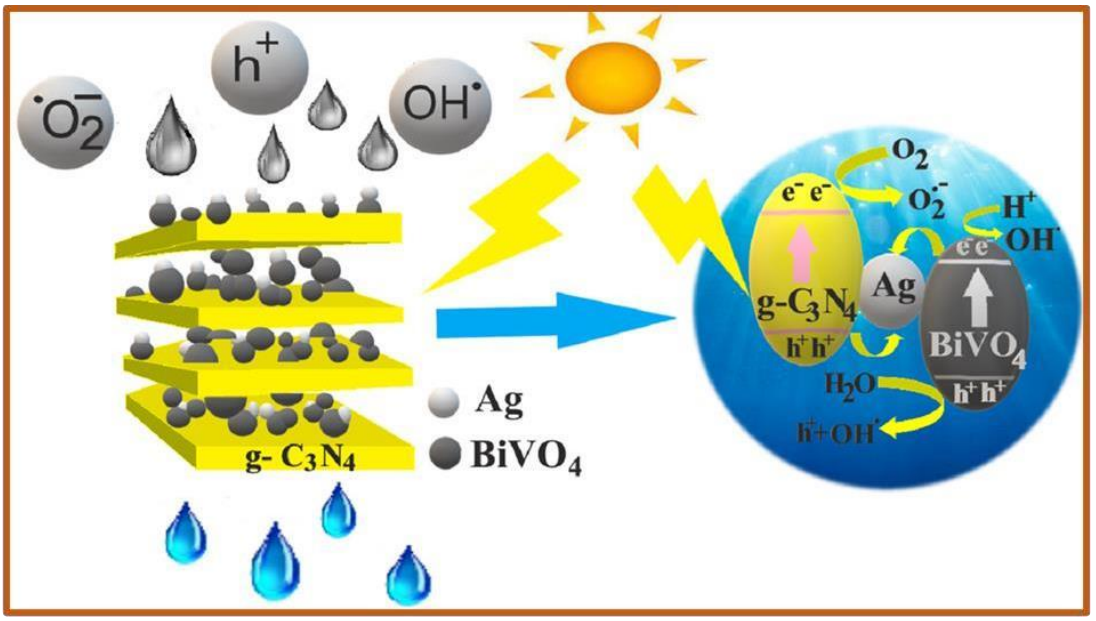

Highlights

- Z-scheme ternary g-C_3N_4/Ag/$BiVO_4$ nanocomposite fabricated via hydrothermal method.
- Ag was loaded on $BiVO_4$ via illumination under visible light.
- Ultrasonication technique employed to stack Ag-loaded $BiVO_4$ onto g-C_3N_4 plates.
- Visible-light degradation of MB dye and insecticide FIP was investigated.
- ~94% and 74% photodegradation efficiency for MB and FIP respectively.

4.1 Introduction

Population growth demands energy production and consumption which leads to the emergence of various toxic effluents having frenzied effects on human health.[1] Organic dye isone of the leading causes of contamination of the environment via discharge from textile, leather, and printing industries.[2] Although a large number of such synthetic dyes are either lesstoxic or rarely harmful, their presence increases the oxygen content in water, damaging aquatic life. About 70% of these dyes belong to the azo dye family, known to be cancer-inducing in the combined state and tumor-inducing in the cleaved state.[3] Methylene blue (MB), a synthetic basic azo dye, and fipronil (FIP), an insecticide, pose serious threats to living beings.[4] MB has a deleterious neurotic impact[5] on the central nervous system and with lingered exposure causesailments such as nausea, anemia, and hypertension.[5] While FIP leads to undesirable disorders such as cardiovascular, metabolic, reproductive, and neurological when used in crops. Therefore, it is requisite to eradicate such toxic pollutants,[6] making degradation of pollutants such as dyes,[4,7] pesticides,[6] microplastics[8] an epicenter of research.

Conventional methods like adsorption, microbial degradation, and precipitation are proposed for the purification of wastewater[8] but pose certain limitations such as expensiveness, or subsidiary pollutant formation.[9] Therefore, for the total or fractional disintegration of pollutants, photocatalytic means[10] seems like a viable process owing to its cost-effective, simple, and efficient nature.[5] Recently, consideration has been given to the advanced oxidation process[11] which relies immensely on reactive hydroxyl radicals for the disintegration of toxins to form CO_2 and H_2O.[3,12] In the process, optical energy is utilized to carry out chemical reactions. Hydroxyl radicals being strong oxidizing agents attack pollutants through electron transfer and produce radicals. These radicals further react, along with the formation of reactive species such as superoxide radicals and H_2O_2 responsible for pollutant degradation.[13]

In recent years, heterojunction catalysts have gained attention, owing to their ability to efficiently separate charge carriers rather than single catalysts. The oxidation reaction for the heterostructure catalyst occurs in the VB of photosystem I while reduction occurs in the CB of photosystem II, facilitating spatial charge separation. But due to the more negative valence band potential of the upper part of photosystem I than photosystem II and more positive conduction band potential of the lower part of photosystem II than photosystem I, redox properties of electron-hole pair get affected by spatial separation. A Z-type heterojunction catalyst bridges this gap, it not only improves charge separation but also enhances redox properties of electron-hole pair and thereby increasing photocatalytic performance.[14]

Bismuth vanadate ($BiVO_4$) has emerged as a popular photocatalyst, mainly in water oxidation half-reactions due to a bandgap of 2.4 eV and activity in visible light. Its valence band potential is more positive than that of $OH^-/{}^{\bullet}OH$ and the holes on the valence band of $BiVO_4$ possess enough oxidizing power to synthesize hydroxyl anions and to carry out photocatalytic reactions feasibly.[15] But the recombination rate of charge carriers is tremendous and therefore, heterojunction structures are suggested.

Graphitic carbon nitride ($g\text{-}C_3N_4$)[16] has surfaced as a budding photocatalyst comprising a 2D layered structure and graphene-like electronic properties.[7] It has a bandgap of 2.7 eV and visible light activity and is thus widely used for contaminant removal.[4] Furthermore, it is cheap, non-toxic, decay-free, and can last in both aqueous and aerobic conditions in a vast pH range.[4] Type-II heterojunction catalysts are significant in photocatalytic performance due to their ability to deduce the reconciliation of charge carriers[7] but the production of radicals ${}^{\bullet}OH$ and $O_2{}^{\bullet-}$ is troublesome in such semiconductors.[14] A Z-type heterojunction catalyst can overcome this limitation by constructing a ternary semiconductor-conductor-semiconductor trivia.[14] Noble metals such as Ag[2] are the most appropriate conductors for this purpose owing to their electron-transfer ability between semiconductor layers.[17] Due to the conductive property of metals, the

conduction electrons oscillate in resonance. This occurs at the interface of negative and positive permittivity material. The incident light facilitates the absorption capacity of photocatalysts and improves efficiency.[18]

The research was conducted to design such ternary composites with good photocatalytic performance. Lin *et al.*[19] fabricated leaf-like g-C_3N_4/Ag/$BiVO_4$ ternary composite via in situ precipitation method. On the leaf-like structure of $BiVO_4$, Ag metal was photo-deposited via $AgNO_3$ solution and further wrapped with g-C_3N_4. To carry out the comparative study, Ag (2wt%) $BiVO_4$ sample was fabricated excluding the enveloped g-C_3N_4 and g-C_3N_4 (2wt%) $BiVO_4$ sample was fabricated in the absence of Ag. The ternary composite displayed photocatalytic achievement with Rhodamine-B dye as compared to pure $BiVO_4$, g-C_3N_4, g- C_3N_4/$BiVO_4$, and Ag/$BiVO_4$. Ou *et al.*[15] constructed g-C_3N_4/Ag/$BiVO_4$ composite via reflux method by photo-depositing Ag on the (040) facets of $BiVO_4$ and eventually covering the surface of Ag/$BiVO_4$ via g-C_3N_4. Varying mass ratios of g-C_3N_4 produced varied photocatalysts. Amongst them, g-C_3N_4/Ag/$BiVO_4$ showed optimum performance for water splitting as well as NO oxidation than pure $BiVO_4$. The Z-scheme of the ternary composite g-C_3N_4/Ag/$BiVO_4$ (040) amplifies the photogenerated electron-hole pairs with Ag acting as an electron mediator. However, much literature is unavailable regarding photocatalytic degradation via g-C_3N_4/Ag/$BiVO_4$ ternary composite prepared by a facile and a more economical route. Therefore, a heterojunction catalyst that shows augmented photocatalytic activity with the transference of the photogenerated electrons occurring at the conduction band of $BiVO_4$ and holes at g-C_3N_4 is proposed.[20]

The chapter concerns the designing of the g-C_3N_4/Ag/$BiVO_4$ composite by a simple hydrothermal method and then utilized for the photodegradation of model pollutants, MB and FIP. Various parameters such as the pH of the solution and catalyst concentration were scrutinized. The trapping experiments were employed to investigate the degradation mechanism, along with the reusability of the ternary composite. The stability of the

composite was checked after performing photodegradation via XRD analysis to confirm its reusability efficiency. The uniqueness of the research is owed to the ultrasonically fabricated g-C_3N_4/Ag/$BiVO_4$ ternary composite employed for photocatalytic purposes and the detailed studyof factors influencing photodegradation.

4.2 Experimental

This section consists of chemicals, materials, and the methodologies used for the synthesis of catalysts.

4.2.1 Chemicals and Materials

Bismuth nitrate pentahydrate ($Bi(NO_3)_3.5H_2O$), sodium dodecylbenzene sulphonate ($C_{18}H_{29}NaO_3S$), ammonium vanadate (NH_4VO_3), urea (NH_2CONH_2), silver nitrate ($AgNO_3$), and methanol (CH_3OH) were bought through S D Fine-Chem Limited, Mumbai, and Thermo Fisher Scientific India Pvt. Ltd. respectively. The MB dye and FIP were procured from Merckand Bayer Crop Science Ltd., India respectively.

4.2.2 Synthesis

This section includes the synthesis methodologies of pure $BiVO_4$, pure g-C_3N_4, Ag/$BiVO_4$, and g-C_3N_4/Ag/$BiVO_4$ composite.

4.2.2.1 Synthesis of $BiVO_4$

$BiVO_4$ nanosheets were designed via the hydrothermal method. Two separate solutions were made, one with 5 mmol $Bi(NO_3)_3.5H_2O$ dissolved in 10 mL HNO_3 solution (4M) and the otherwith 5 mmol NH_4VO_3 dissolved in 10 mL NaOH solution (2M). To both the solutions, sodium dodecylbenzene sulphonate (0.25 g) was added with continuous stirring

for about 30 min[14] until the solutions become neutral. Thereafter, the stirring was continued for 30 min. The solution was poured into a Teflon-lined vessel (50 mL) and warmed (200°C) for nearly 1.5 h at a heating rate of 10°C/min. The resultant product was washed and filtered with ethanol (thrice) and deionized water (thrice) and finally dried at 80°C for 12 h. The product formed was Tuscany yellow.[14]

4.2.2.2 Synthesis of g-C_3N_4

The synthesis of g-C_3N_4 was carried out by heating urea. 30 g of urea dissolved in 50 mL H_2O was poured into a silica crucible and dried for 12 h for recrystallization. The sample was heated at 550°C for 2 h (10°C/min). To wash out alkaline residues, nitric acid was poured and the collected light-yellow product was grounded by a mortar pestle.[4]

4.2.2.3 Synthesis of Ag/$BiVO_4$

For synthesizing Ag-loaded $BiVO_4$, $BiVO_4$ nanosheets (0.5 g) were mixed ultrasonically in 70 mL methanol. In this solution, ~13.3 mg $AgNO_3$ was dissolved with continuous stirring and placed in a photo-reaction cell, and irradiated under visible light for 2 h. Centrifugation and drying of the solution at 80°C for 12 h formed a Bumblebee yellow product.

Ternary g-C_3N_4/Ag/$BiVO_4$ composite was obtained by ultrasonically dispersing 0.4 g g-C_3N_4 and 30% of Ag/$BiVO_4$ in methanol (50 mL) and stirred for 10 h. The suspension was poured into a beaker and dried at 80°C for the complete evaporation of the solvent. The sample thus obtained was calcined at 450°C for 2 h (10°C/min) and named as 1:1 g-C_3N_4/Ag/$BiVO_4$. Atortilla-colored product was obtained (**Scheme 4.1**).[14]

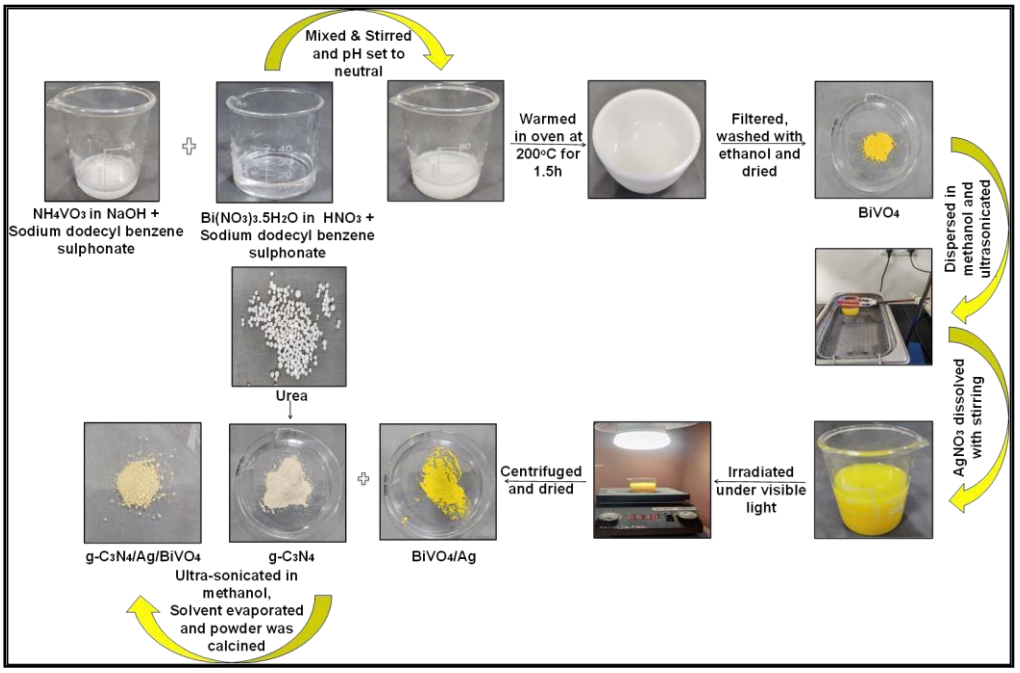

Scheme 4.1. Synthesis of ternary 1:1 g-C_3N_4 /Ag/$BiVO_4$ composite.

4.2.3 Characterization

To investigate the surface area and pore-size distribution, BET N_2 adsorption-desorption isotherm at 77.3 K was performed via a surface area analyzer Microtrac Belsorp Mini-II (Bel, Japan, Inc). Pre-treatment at 100°C for 6 h was carried out before the analysis. Barrett-Joyner-Halenda (BJH) method was utilized for the investigative study of pore size distribution curves. Also, to study the crystalline phase of the photocatalysts, x-ray diffractionanalysis was conducted via a PANanalytical X-ray diffractometer with Cu-Kα radiation, operating at 45kV at a scan range of 10-90° Field emission scanning electron microscopy (FESEM SU8180, Hitachi, Tokyo, Japan) with Oxford INCTA energy dispersive spectrometer (EDS) and transmission electron microscopy (TEM, JEM-2100F) investigated the morphologies of surface and microstructures. To study the elemental structure on the photocatalyst's surface, X-ray photoelectron spectroscopy (XPS) was done via PHI- 5000 VersaProbe III system containing a monochromatic Al Kα X-ray source (1486.7 eV). Hitachi-3900H spectrophotometer (Shimadzu, Japan) was utilized for

carrying out UV-Vis Diffusion Reflectance Spectroscopy (DRS) in diffuse absorbance mode. A fluorescence spectrometer (F- 4500, Hitachi, Japan) was utilized to get photoluminescence (PL) spectra. To adjust and measure the pH, a cyber scan pH 1100 (Eutech, Singapore) was used. UV-Vis spectrophotometer (Shimadzu, UV-2600) was employed for the kinetic investigation of photodegradation of MB and FIP.

4.2.4 Photocatalytic Activity Measurement

To investigate the photocatalytic activity of the catalyst, photo-degradation of MB, a model dye, and FIP, a colorless insecticide was monitored by keeping the solution in a photo- reactor. In the experiment, about 2 mg of the composite was dissolved in 15 mL MB/FIP solution (5 ppm). For the adsorption-desorption equilibrium to establish between the composite and pollutant, the solution was magnetically stirred for 45 min in dark and then stirred for 60 min under visible light (65W CFL lamp, Phillips, k> 400 nm with an intensity of 125 W/m^2). The complete degradation occurred (94.6% MB and 74.2% FIP). The degradation of MB and FIP was noted using a UV-Vis spectrophotometer with the maximum band absorption at 664 and 276 nm (λ_{max}), respectively. As stated by Lambert-Beer's law, the concentration of a solution depends directly on the absorbance, and therefore, the percent degradation (**Eq. 4.1**)
was noted as:

$$\%\,D = \{(A_o - A_t)/A_o\} \times 100 = \{(C_o - C_t)/C_o\} \times 100 \quad (4.1)$$

Where A_o and A_t denote the absorbance of dye/pesticide at a time '0' and 't' respectively, and C_o and C_t denote the concentration of dye/pesticide at a time '0' and 't' respectively.

4.3 Results and Discussion

4.3.1 Photocatalyst Characterizations

4.3.1.1 X-ray Diffraction Studies

XRD analysis was employed to measure the crystal planes of g-C_3N_4/Ag/$BiVO_4$, $BiVO_4$/Ag, g-C_3N_4, and $BiVO_4$. For the pure $BiVO_4$ sample (**Fig. 4.1 (a)**), the XRD peaks at 18.8°, 28.89°, 30.5°, 34.91°, 40.04°, 42.3°, 45.91°, 47.07°, 50.18°, 53.2°, 56.01°, 59.02° and 60°[14] corresponding to (011), (112), (004), (020), (121), (105), (123), (024), (220), (116), (215), (312) and (224) planes respectively, suggested $BiVO_4$ be in monoclinic phase (JCPDS No. 83-1699) while g-C_3N_4 displayed one evident peak at 26.69° corresponding to (002) plane. The XRD patterns of $BiVO_4$/Ag and g-C_3N_4/Ag/$BiVO_4$ displayed the peaks relating to g-C_3N_4 and$BiVO_4$. But it was noticed that no peaks were observed for Ag, this was could be due to eithera low percentage of Ag or rather its minute size on $BiVO_4$.[17]

4.3.1.2 Nitrogen Adsorption/Desorption Analysis

Fig. 4.1 (b) illustrated type IV isotherm as depicted from N_2 adsorption-desorption isotherm studies for the as-synthesized photocatalysts. This validated a mesoporous surface. The constancy of pore size and shape of the composite was confirmed by H1 hysteresis loops having sharpened adsorption and desorption branches while the BJH method depicted the pore size distribution, suggesting the mesoporous nature of the composite (**Fig. 4.1 (c)**). Surface area, mean pore volume, and mean pore diameter were scrutinized via the BET method analysis. The calculated surface area for $BiVO_4$, g-C_3N_4, $BiVO_4$/Ag, g-C_3N_4/Ag/$BiVO_4$ were 9 m^2/g, 88 m^2/g, 11 m^2/g, 47 m^2/g, respectively. An enhancement in surface area from $BiVO_4$ to $BiVO_4$/Ag to g-C_3N_4/Ag/$BiVO_4$ was observed. While for g-C_3N_4, the surface area was maximum (87.6 m^2/g) and the mesopore size minimum (20.378 nm) (**Table 4.1**).

Table 4.1. Surface area, Total pore volume and Mesopore size of different catalysts.

Photocatalyst	Surface area (m^2/g)	Total pore volume (cm^3/g)	Mesopore size (nm)
$BiVO_4$	9	0.10	46.28
g-C_3N_4	88	0.44	20.37
$BiVO_4$/Ag	11	0.08	30.77
g-C_3N_4/Ag/$BiVO_4$	47	0.55	46.78

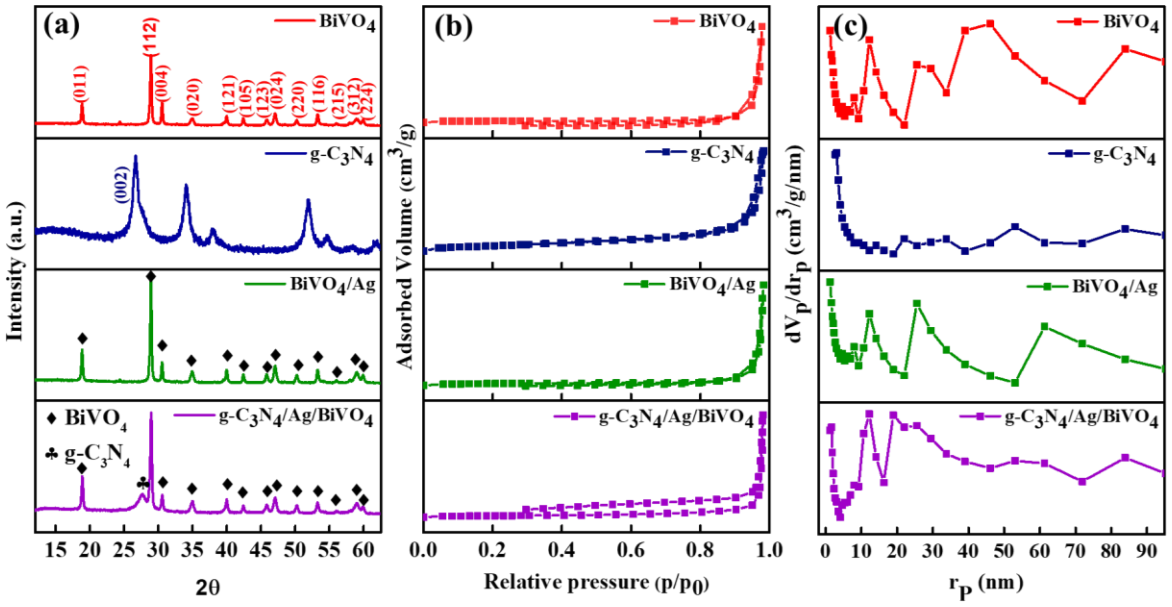

Fig. 4.1. (a) XRD patterns, (b) N_2 adsorption-desorption isotherms, and (c) pore size distribution curves of the as-synthesized photocatalysts.

4.3.1.3 XPS Analysis

XPS analysis was employed for a detailed understanding of the oxidation state of respective elements in the ternary composite. **Fig. 4.2 (a)** depicts the XPS survey spectrum forthe ternary composite. The spectrum shows the existence of Bi, Ag, C, V, O, and N. **Fig. 4.2 (b)** illustrates high-resolution Bi 4f spectra with a well-resolved doublet corresponding to Bi $4f_{7/2}$ and $4f_{5/2}$ at 159.4 eV and 164.7 eV, respectively which suggested the presence of Bi^{3+} in the composite.[15] In **Fig. 4.2 (c)**, the two characteristic peaks

corresponding to Ag $3d_{5/2}$ and $3d_{3/2}$ at 374.3 eV and 368.3 eV, respectively indicated the existence of metallic Ag in the 0 oxidation state in the ternary sample.[15] Similarly, 'V' was in +5 valence state, as verified by V $2p_{3/2}$ and $2p_{1/2}$ peaks at 516.8 eV and 524.4 eV, respectively (**Fig. 4.2 (e)**).[15] A peak at 530.2 eV was obtained for the O1s spectrum (**Fig. 4.2 (e)**). Finally, it was found that the binding energies for C1s and N1s were at 285 eV, 398.9 eV, and 399.71 eV, respectively (**Fig. 4.2 (d and f)**).[10]

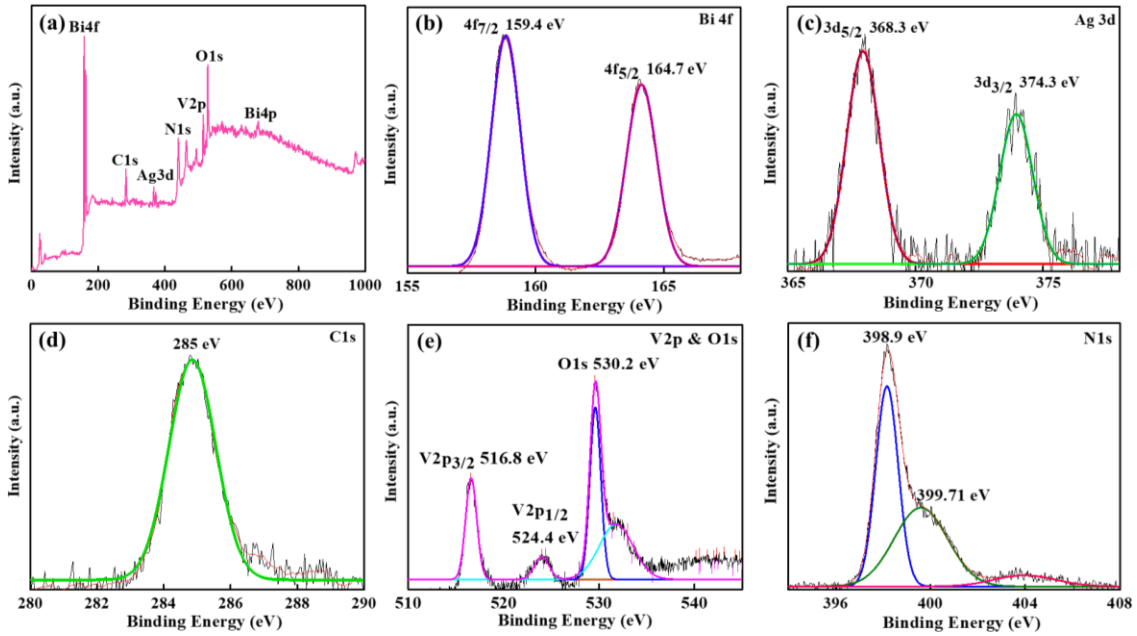

Fig. 4.2 (a) XPS survey, deconvoluted peaks of (b) Bi, (c) Ag, (d) C, (e) V and O, and (f) N of 1:1 g-C_3N_4/Ag/$BiVO_4$ ternary composite.

4.3.1.4 EDS and Elemental Mapping

The elemental mapping images for the ternary composite (**Fig. 4.3 (b-g)**) validated the existence of Ag, O, C, Bi, V, and N in the composite. Moreover, the dispersion of elements in the g-C_3N_4/Ag/$BiVO_4$ ternary composite is homogeneous.[21] The elemental composition was investigated by conducting the EDS analysis of the as-prepared ternary composite as shown in**Fig. 4.3 (a)**. The weight percentages of the elements in the ternary

composite are C with 8.59%, N with 0.01%, O with 9.28%, V with 5.69%, Ag with 0.34%, and Bi with 76%.

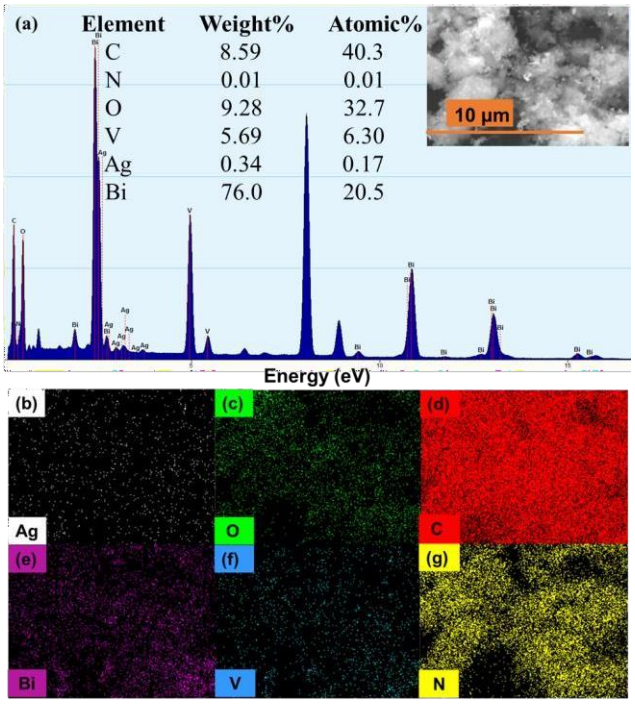

Fig. 4.3. (a) EDS spectrum, elemental mapping for (b) Ag, (c) O, (d) C, (e) Bi, (f) V and (g) N of 1:1 ternary composite g-C_3N_4 /Ag/$BiVO_4$.

4.3.1.5 FESEM and HRTEM Studies

To investigate the surface structure of the ternary composite, FESEM analysis was carried out. The studies revealed (**Fig. 4.4 (a-b)**) the deposition of spherical Ag onto $BiVO_4$ and this $BiVO_4$/Ag composite is accumulated on the plate-like surface of g-C_3N_4. This suggested an easy separation of charge carriers and their migration. The proximity existing between g-C_3N_4 and $BiVO_4$/Ag particles is vital owing to its capability to lessen the recombination tendency of photoinduced charge carriers. This enhances the participation of electron-hole pairs in photocatalysis.[22] **Fig. 4.4 (c)** exhibits the HR-TEM images for the as-prepared ternary nanocomposite. It displayed the existence of bismuth vanadate, silver,

and amorphous carbon nitride with the positioning of $BiVO_4$/Ag atop g-C_3N_4 plates. The plane lattices for Ag and $BiVO_4$ were (111) and (200) respectively at a distance of 0.24 nm and 0.26nm. The g-C_3N_4 nanosheets acted as a ground/base for both $BiVO_4$ and metallic Ag.[23]

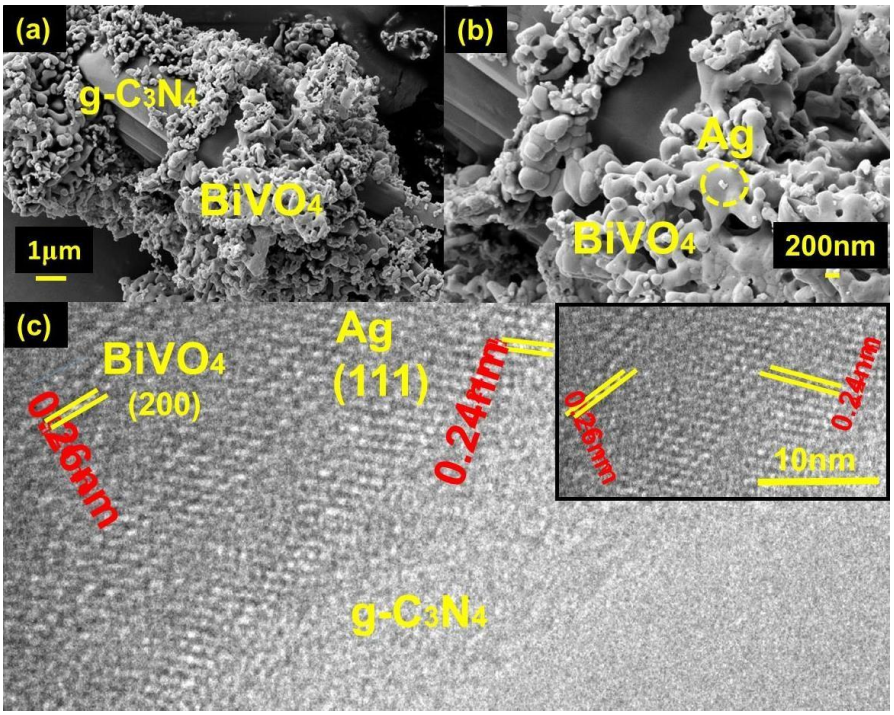

Fig. 4.4. (a, b) FESEM images, (c) HRTEM image of 1:1 ternary nanocomposite.

4.3.1.6 Optical Properties

The recombination of charge carriers in a catalyst plays a vital role in the photocatalytic process. A low PL intensity indicates efficient charge separation efficacy and reduced recombination of electron-hole pairs. Therefore, to investigate the charge separation, photoluminescence (PL) spectra were recorded at an excitation wavelength of 325 nm[19] as **Fig. 4.5 (a).** For g-C_3N_4, an intense emission peak appeared at around 490 nm, suggesting an electronic transition from n to π*. Notably, the peak intensity decreased for the $BiVO_4$ and Ag heterojunction, suggesting the reduced recombination of charge carriers.

The peak further decreased for the g-C_3N_4, Ag, and $BiVO_4$ heterojunction, suggesting the formation of a Schottky barrier between g-C_3N_4 and $BiVO_4$ via Ag which enhances the electron transfer. The movement promotes the efficient separation of photoinduced charge carriers and a deduced recombination rate.[14] Therefore, g-C_3N_4/Ag/$BiVO_4$ composite shows better photocatalytic performance and eventually promotes reactive species production.

The bandgap of the g-C_3N_4/Ag/$BiVO_4$ was investigated via UV-Visible diffuse reflectance spectroscopy (DRS). Tauc's plot was employed to formulate bandgap energy. The equation isshown in **Eq. (4.2)**[24]:

$$(\alpha h\nu)^{1/2}=A(h\nu-E_g)n/2 \quad (4.2)$$

Where α, h, ν, n and E_g are absorption coefficient, Planck constant, light frequency, optical transition type of semiconductors, and bandgap energy, respectively (**Fig. 4.5 (c)**). As illustrated in **Fig. 4.5 (b)**, the optical absorption edge of $BiVO_4$[25] is 600 nm and g-C_3N_4 [26]is 490 nm. The optical band gaps of $BiVO_4$,[27] g-C_3N_4,[28] $BiVO_4$/Ag,[17] and g-C_3N_4/Ag/$BiVO_4$[17] were formulated to be 2.90 eV, 2.88 eV, 2.45 eV, and 2.41 eV respectively (**Fig. 4.5 (c)**). The shift towards a longer wavelength in the ternary composite could be attributed to Ag nanoparticles owing to its visible light absorption through surface plasmon resonance.[15]

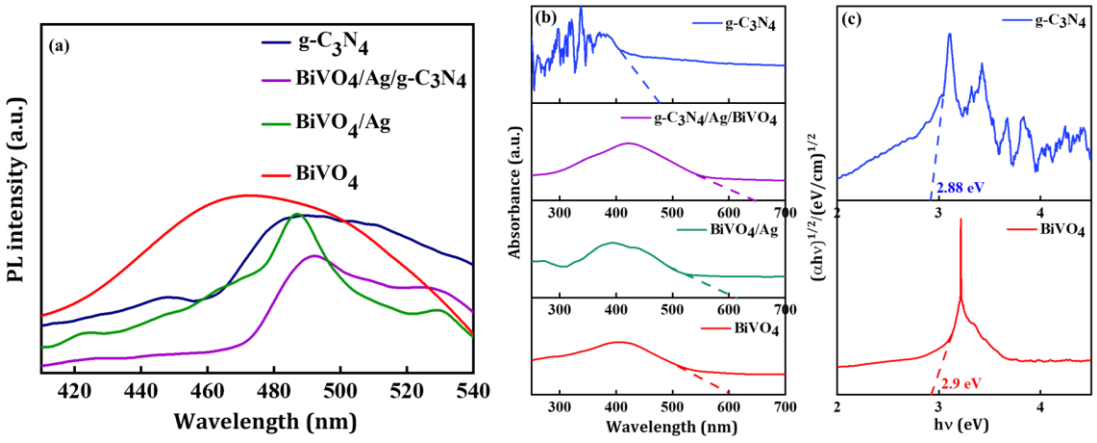

Fig. 4.5. (a) Photoluminescence spectra, (b) UV Visible diffuse reflectance spectra and (c) Tauc's plot of the as-prepared catalyst.

4.3.2 Photocatalytic Degradation of Methylene Blue and Fipronil

To scrutinize the photocatalytic nature of g-C_3N_4/Ag/$BiVO_4$ ternary composite, organic pollutants such as MB[29] and FIP were adopted for the photodegradation experiments under visible light. The initial concentration of MB taken was 5 mg/L and that of FIP was 600 mg/L.The adsorption-desorption equilibrium was attained in 45 min when placed in the dark. Then for degradation activity, 60 min illumination was performed. The photocatalytic degradation for dye and insecticide without ternary catalyst was also carried out. The solutions were illuminated under visible light for 60 min. It was inferred that the absorbance for both the pollutants MB and FIP maintains constancy (6.03% MB and 3.09% FIP) (**Fig. 4.6 (a) and (c)**),suggesting the necessity of g-C_3N_4/Ag/$BiVO_4$ ternary catalyst in the degradation process.

To formulate the rate constant, the following **Eq. (4.3)**[5] was followed:

$$\ln (C/C_0) = -kt \qquad (4.3)$$

Where k is the rate constant, C_0 and C are the initial concentration i.e., the concentration at time = '0' and 't' respectively.

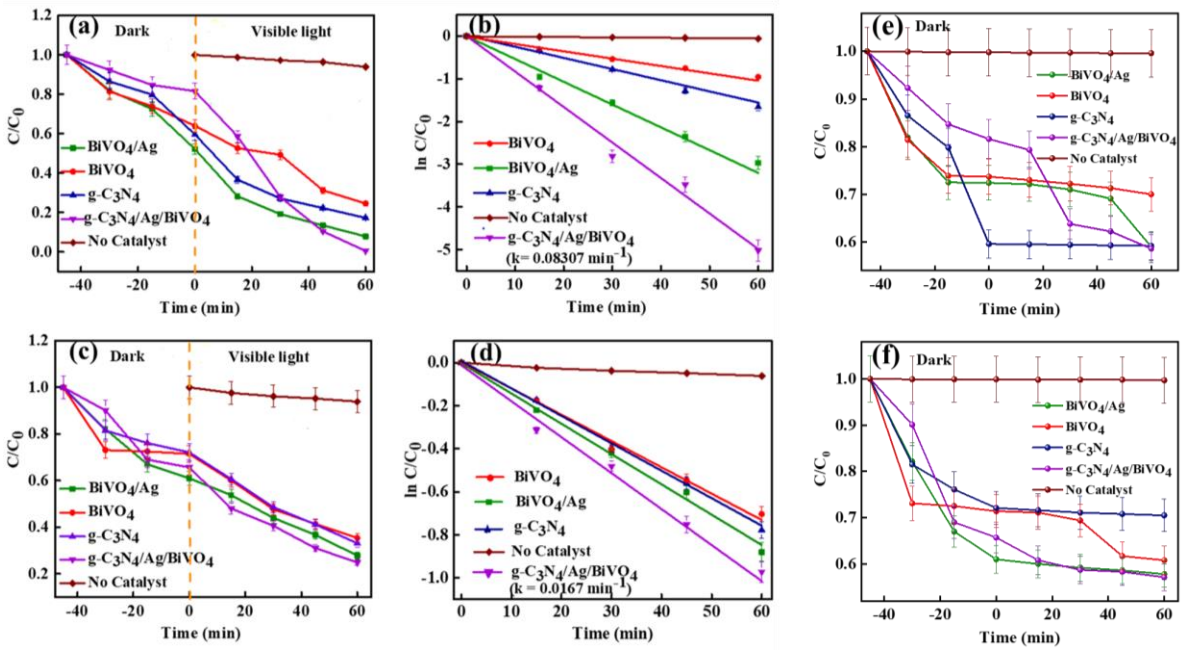

Fig. 4.6. Kinetic analysis for the photocatalytic degradation of (a, b, c) MB, (d, e, f) FIP.

Fig. 4.6 (a) and Fig. 4.6 (c) depict the kinetic survey for MB and FIP photodegradation, both with and without photocatalyst. It was notable that the absorbances without catalyst were only 6.03% ($k = 8.249 \times 10^{-4}\ min^{-1}$) and 3.09% ($k = 8.567 \times 10^{-4}\ min^{-1}$) for MB (**Fig. 4.6 (b)**) and FIP (**Fig. 4.6 (d)**), respectively. Also, the photodegradation efficiencies of the ternary composite were highest both in MB (94.56%; $k = 0.08307\ min^{-1}$) (**Fig. 4.6 (b)**) and FIP (74.2%;$k = 0.0167\ min^{-1}$) (**Fig. 4.6 (d)**) as compared to $BiVO_4$, g-C_3N_4, and $BiVO_4$/Ag. The rate constants of g-C_3N_4/Ag/$BiVO_4$, $BiVO_4$/Ag, g-C_3N_4, and $BiVO_4$ for MB and FIP degradation in **Table 4.2**. It was concluded that the ternary composite displayed good efficiency in visible-light-degradation of pollutants.

Table 4.2. Rate constants for the degradation of MB and FIP.

Photocatalyst	**Rate Constants**		**% Degradation**	
	MB (min^{-1})	**FIP (min^{-1})**	**MB**	**FIP**
$BiVO_4$	0.01940	0.01183	66.06	49.01
g-C_3N_4	0.01733	0.01286	81.52	59.02
$BiVO_4$/Ag	0.03000	0.01440	88.76	66.04
g-C_3N_4/Ag/$BiVO_4$	0.03500	0.01632	94.56	74.2

4.3.2.1 Effect of Catalyst Concentration

An investigation of the effect of catalyst concentration on the photodegradation activity was conducted. **Fig. 4.7 (a)** shows the graph regarding the photocatalyst concentration that changed from 0.06 to 0.4 g/L in both cases. It was observed that for MB, the degradation efficiency is maximum at 0.13 g/L and decreases from 0.26-0.40 g/L for

MB[10] while for FIP, the degradation efficiency is maximum at 0.06 g/L and decreases from 0.26-0.40 g/L. This was attributed to the fact that after the complete adsorption of dye on the surface, further integration of catalyst will have no effect owing to the deactivated sites causing opaqueness of the solution and scattering of light.[5]

4.3.2.2 Effect of pH

The pH_{pzc} value for g-C_3N_4/Ag/$BiVO_4$ was formulated[15] to be ~pH 5 (**Fig. 4.7 (b)**),[30] indicating the negative charge on the surface of the ternary composite at pH>pH_{pzc} (i.e., pH>5)and a positive charge at pH<pH_{pzc}.[31] The effect of change in pH (pH 1 to 12) was noted for the degradation activity by using 0.13 g/L ternary composite (**Fig. 4.7 (c)**). The pH of the solutions was secured with the addition of NaOH or HCl. In the case of MB, the highest degradation was at pH 8 (94.5%) which could be attributed to the interaction of cationic dye MB[12] and the negatively charged surface of the ternary composite.[32] While in the case of FIP, the maximum activity (72.6%) was in the acidic range (pH~4) owing to the interactions of anionic FIP and positively charged ternary catalyst.[33]

4.3.2.3 Reusability

The reusability of the photocatalysts is an important factor indicating stability. The stability and reusability of the catalysts were inspected for 4 successive runs in the degradation of MB.[4] It can be seen that the photodegradation efficiency decreased but not to a large extent i.e. 89.85% for MB after 4 cycles[14] (**Fig. 4.7 (d)**). XRD analysis (**Fig. 4.7 (e)**) before and after photocatalysis confirmed the intactness of the crystal structure for the ternary catalyst even after the photocatalytic reaction.[34]

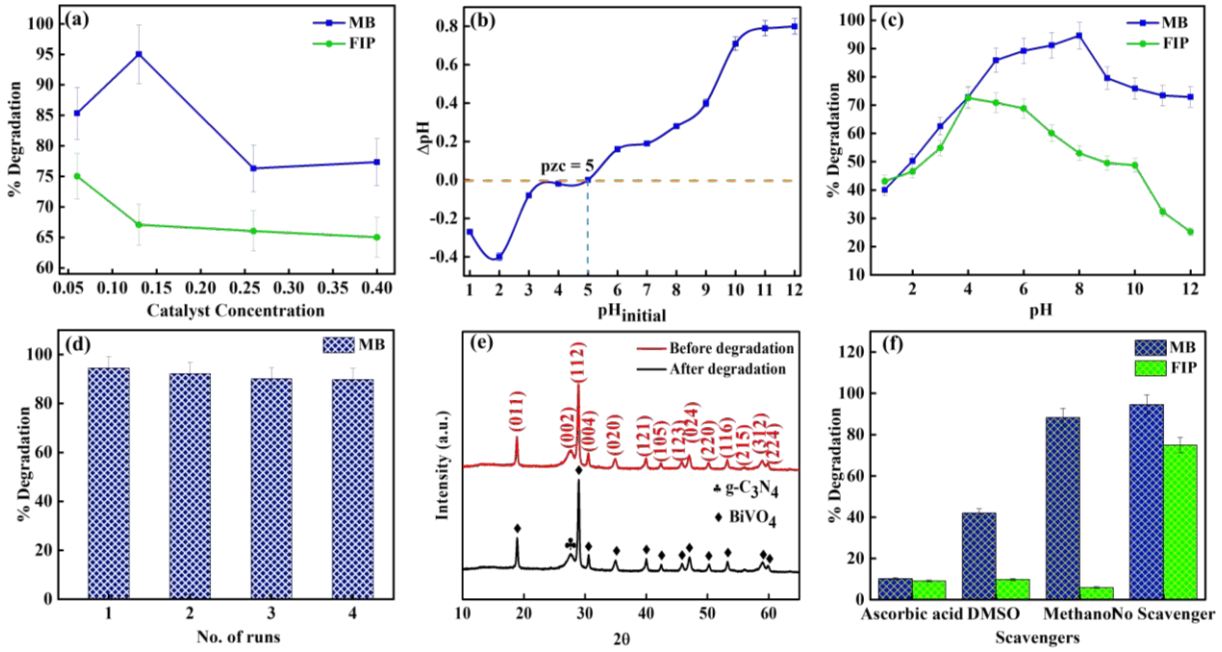

Fig. 4.7. Photocatalytic degradation: (a) catalyst dose studies, (b) pH_{PZC} studies, (c) pH studies, (d) reusability studies, (e) XRD spectra after 4 cycles of MB degradation, (f) scavenger studies on MB and FIP degradation by 1:1 g-C_3N_4 /Ag/$BiVO_4$ photocatalyst.

4.3.2.4 Plausible Mechanism

To investigate the main radical species in the degradation process, scavenger studies were carried out via ascorbic acid, methanol, and DMSO for superoxide radical ($O_2^{\bullet-}$), quenching holes (h^+), and hydroxide radical ($^{\bullet}OH$) (respectively)[35] (**Fig. 4.7 (f)**). Although ascorbic acid can scavenge both $O_2^{\bullet-}$and $^{\bullet}OH$ but ascorbate reacts with highly reactive $^{\bullet}OH$ to form ascorbyl radical which is not so reactive.[36]

The ternary g-C_3N_4/Ag/$BiVO_4$ composite was used as a research tool (**Fig. 4.7 (f)**). If the scavenger caused a major inhibition in the photocatalytic activity, the active species were responsible for the photodegradation process. Equimolar ascorbic acid, DMSO, and methanol were added to the reaction mixture and it was observed that the photodegradation efficiencies for MB by methanol, DMSO, and ascorbic acid were 88.3%, 41.97%, and

10.24% respectively, suggesting that hydroxide radical ($^{\bullet}OH$) and superoxide radical ($O_2^{\bullet}$) are the primary species in the MB degradation. For FIP, the photodegradation efficiencies by ascorbic acid, methanol, and DMSO were 9.09%. 9.81% and 5.97% respectively, indicating the participation of superoxide radical ($O2^{\bullet-}$), holes (h^+), and hydroxide radical ($^{\bullet}OH$) in the degradation process. A Z-scheme mechanism for g-C_3N_4/Ag/$BiVO_4$ ternary composite is suggested[23] (**Scheme 4.2**). Under visible light irradiation, the electrons present in the VB of g-C_3N_4 (**Eq.4.4**), and $BiVO_4$ are excited (**Eq. 4.5**), leaving behind holes. But owing to the rapid recombination of photogenerated charge carriers, low photocatalytic activity is observed.[37] Although the heterojunction of $BiVO_4$/Ag enhances the performance,[38] is still incompetent. **Scheme 4.2** depicts the inability of the CB electrons of $BiVO_4$ to synthesize $O_2^{\bullet-}$[25] and that of the VB holes of g-C_3N_4[39] to react with adsorbed H_2O and synthesize $^{\bullet}OH$. Thus, type II heterojunction semiconductors are unable to produce $O_2^{\bullet-}$ and $^{\bullet}OH$. Trapping experiments showed the vital role played by $O_2^{\bullet-}$ and $^{\bullet}OH$ in MB photodegradation and $O_2^{\bullet-}$, h^+, and $^{\bullet}OH$ in the photodegradation of FIP. This sufficiently proves the occurrence of the Z-scheme in photodegradation via g-C_3N_4/Ag/$BiVO_4$ ternary composite. Owing to the existence of Ag nanoparticles, CB electrons of $BiVO_4$ could be captured via the Schottky barrier established between BiVO4 and metallic Ag. The holes in the VB of g-C_3N_4 could transfer and recombine with the electrons of Ag nanoparticles due to the higher energy level of Ag than the VB of g-C_3N_4.[40] The electrons left in the CB of g-C_3N_4 are sufficient to form $O_2^{\bullet-}$ when reacting with O_2 (**Eq. 4.6**). The reaction between ascorbic acid (AH_2) and superoxide radical ($O_2^{\bullet-}$) follows second-order kinetics and produces ascorbate free radical (AH) ($k=8.2 \times 10^7\ M^{-1}\ s^{-1}$) (**Eq. 4.7**).[41] The VB holes of $BiVO_4$ have enough energy (2.5 eV)[42] to oxidize H_2O or OH^- and form $^{\bullet}OH$ (**Eq. 4.8**). When methanol reacts with quenching holes

CH_2O (formaldehyde) is formed, and the reaction obeys second-order kinetics ($k=8.3 \times 10^8$ M^{-1} s^{-1}) (**Eq. 4.9**).[43] Also, $O_2^{\bullet-}$ can protonate to form $^{\bullet}OH$. Finally, the second-order kinetics reaction between DMSO and $^{\bullet}OH$ forms MS^- (methane sulphonate) ($k=4.5 \times 10^9$ $M^{-1}s^{-1}$) (**Eq. 4.10**).[44] The produced radicals of $O_2^{\bullet-}$ (**Eq. 4.11**) and $^{\bullet}OH$ (**Eq. 4.12**) can finally degrade MB and FIP into harmless product such as CO_2 and H_2O.[14] The reaction mechanism[14] is depicted as:

$$g\text{-}C_3N_4 + h\nu \longrightarrow g\text{-}C_3N_4\,(h^+ + e^-) \quad (4.4)$$

$$BiVO_4 + h\nu \longrightarrow BiVO_4\,(h^+ + e^-) \quad (4.5)$$

$$g\text{-}C_3N_4\,(e^-) + O_2 \longrightarrow g\text{-}C_3N_4 + O_2^{\bullet-} \quad (4.6)$$

$$O_2^{\bullet-} + AH_2 + H^+ \longrightarrow AH + H_2O_2;\ k=8.2 \times 10^7\ M^{-1}\ s^{-1} \quad (4.7)$$

$$BiVO_4\,(h^+) + H_2O \longrightarrow BiVO_4 + {}^{\bullet}OH + H^+ \quad (4.8)$$

$$CH_3OH + 2h^+ \longrightarrow CH_2O + 2H^+;\ k=8.3 \times 10^8\ M^{-1}\ s^{-1} \quad (4.9)$$

$$DMSO + {}^{\bullet}OH \longrightarrow MS^-;\ k=4.5 \times 10^9\ M^{-1}s^{-1} \quad (4.10)$$

$$MB/FIP + O_2^{\bullet-} \longrightarrow CO_2 + H_2O \quad (4.11)$$

$$MB/FIP + {}^{\bullet}OH \longrightarrow CO_2 + H_2O \quad (4.12)$$

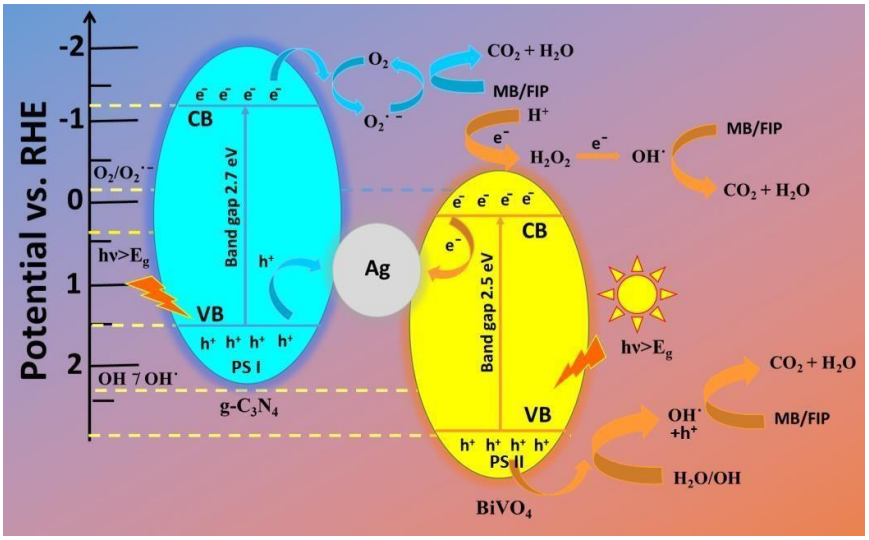

Scheme 4.2. The mechanism for photocatalytic degradation of organic pollutants by ternary composite.

Z-scheme[45] in the ternary composite not only helps in the partition of photogenerated charge carriers but supports the redox ability of the photogenerated charge carriers as well and thus enhancing photocatalytic performance.[15]

A comparison was performed with varied photocatalysts in literature for the photodegradation of pollutants (**Table 4.3**) which confirms the effectiveness of the proposedcatalyst towards pollutant degradation.

Table 4.3. Comparison of different photocatalysts for degradation of pollutants.

Catalyst	**Pollutant**	**Conc. (g/L)**	**Time (min)**	**Light source**	**Light intensity (mW/cm^2)**	***k*** **(min^{-1})**	**Efficie-ncy (%)**	**Reference**
g-C_3N_4/Ag/$BiVO_4$	RhB	0.02	40	visible	-	-	100	19
g-C_3N_4/Pt/$BiVO_4$	MB	0.02	130	visible	100	0.119	87.6	14
g-C_3N_4/TiO_2	Isoniazid	0.05	240	UV light	-	7.10 x 10^{-4}	13.5	21
P-g-C_3N_4/TiO_2	MB	0.20	135	visible	205	3.28 x 10^{-3}	19	28
$BiVO_4$/TiO_2	RhB	-	30	visible	100	-	-	25

g-C_3N_4/Ag/$BiVO_4$	TC	0.02	240	visible	-	-	90.7	14

4.3.3 Conclusion

The chapter involves the fabrication of a ternary nanocomposite g-C_3N_4/Ag/$BiVO_4$ viathe hydrothermal method which was used for MB and FIP degradation. The analysis of the surface proved the uniform dispersity of $BiVO_4$/Ag on g-C_3N_4 plates. The pH and pzc studies showed the maximum degradation for MB at a basic pH and FIP at an acidic pH due to the electrostatic interactions between the photocatalyst with cationic MB and anionic FIP respectively. The feed concentration studies revealed a decrease in degradation efficiency owing to the reduced active sites after the initial complete adsorption of pollutants, while the reusability studies confirmed the stability of the photocatalyst. To investigate the mechanism of the process, trapping experiments had been carried out, revealing the involvement of both holes and electrons in the photodegradation process. Sufficient partition of photogenerated charge carriers and the porosity of the ternary composite could be the reasons for the enhancedphotocatalytic performance. Moreover, by acting as a link between electrons and the conduction band, Ag NPs were major contributors to the photodegradation process. Also, owing to surface plasmon resonance, Ag NPs enhanced absorption in visible light. Thus, the technique provides a decent way to fabricate Z-scheme photocatalysts with high efficacy.

References

(1) Sharma, S.; Basu, S. Fabrication of Centimeter-Sized Sb_2S_3/SiO_2 Monolithic Mimosa Pudica Nanoflowers for Remediation of Hazardous Pollutants from Industrial Wastewater. *J. Clean. Prod.* **2021**, *280*, 124525. https://doi.org/10.1016/j.jclepro.2020.124525.

(2) Singh, S.; Parveen, N.; Gupta, H. Adsorptive Decontamination of Rhodamine-B from Water Using Banana Peel Powder: A Biosorbent. *Environ. Technol. Innov.* **2018**, *12*, 189. https://doi.org/10.1016/j.eti.2018.09.001.

(3) Gupta, N. K.; Ghaffari, Y.; Kim, S.; Bae, J.; Kim, K. S.; Saifuddin, M. Photocatalytic Degradation of Organic Pollutants over MFe_2O_4 (M = Co, Ni, Cu, Zn) Nanoparticles at Neutral pH. *Sci. Rep.* **2020**, *10*, 1. https://doi.org/10.1038/s41598-020-61930-2.

(4) Monga, D.; Ilager, D.; Shetti, N. P.; Basu, S.; Aminabhavi, T. M. 2D/2D Heterojunction of MoS_2/g-C_3N_4 Nanoflowers for Enhanced Visible-Light-Driven Photocatalytic and Electrochemical Degradation of Organic Pollutants. *J. Environ. Manage.* **2020**, *274*, 111208. https://doi.org/10.1016/j.jenvman.2020.111208.

(5) Sharma, S.; Basu, S. Highly Reusable Visible Light Active Hierarchical Porous WO_3/SiO_2 Monolith in Centimeter Length Scale for Enhanced Photocatalytic Degradation of Toxic Pollutants. *Sep. Purif. Technol.* **2020**, *231*, 115916. https://doi.org/10.1016/j.seppur.2019.115916.

(6) Rathi, A.; Basu, S.; Barman, S. Adsorptive Removal of Fipronil from Its Aqueous Solution by Modified Zeolite HZSM-5: Equilibrium, Kinetic and Thermodynamic Study. *J. Mol. Liq.* **2019**, *283*, 867. https://doi.org/10.1016/j.molliq.2019.02.140.

(7) Monga, D.; Basu, S. Enhanced Photocatalytic Degradation of Industrial Dye by g-C_3N_4/TiO_2 Nanocomposite: Role of Shape of TiO_2. *Adv. Powder Technol.* **2019**, *30*, 1089. https://doi.org/10.1016/j.apt.2019.03.004.

(8) Sharma, S.; Basu, S.; Shetti, N. P.; Nadagouda, M. N.; Aminabhavi, T. M. Microplastics in the Environment: Occurrence, Perils, and Eradication. *Chem. Eng. J.* **2021**, *408*, 127317. https://doi.org/10.1016/j.cej.2020.127317.

(9) Sharma, S.; Basu, S.; Shetti, N. P.; Kamali, M.; Walvekar, P.; Aminabhavi, T. M. Waste-to-Energy Nexus: A Sustainable Development. *Environ. Pollut.* **2020**, *267*, 115501. https://doi.org/10.1016/j.envpol.2020.115501.

(10) Aanchal; Barman, S.; Basu, S. Complete Removal of Endocrine Disrupting Compound and Toxic Dye by Visible Light Active Porous g-C_3N_4/H-ZSM-5 Nanocomposite. *Chemosphere* **2020**, *241*, 124981. https://doi.org/10.1016/j.chemosphere.2019.124981.

(11) Sidaraviciute, R.; Kavaliunas, V.; Puodziukynas, L.; Guobiene, A.; Martuzevicius, D.; Andrulevicius, M. Enhancement of Photocatalytic Pollutant Decomposition Efficiency of Surface Mounted TiO_2 via Lithographic Surface Patterning. *Environ. Technol. Innov.* **2020**, *19*, 100983. https://doi.org/10.1016/j.eti.2020.100983.

(12) Sharma, S.; Basu, S. Visible-Light-Driven Efficient Photocatalytic Abatement of Recalcitrant Pollutants by Centimeter-Length MoO_3/SiO_2 Monoliths with Long Service Life. *Appl. Mater. Today* **2021**, *23*, 101033. https://doi.org/10.1016/j.apmt.2021.101033.

(13) Saharan, V. K.; Pinjari, D. V.; Gogate, P. R.; Pandit, A. B. Advanced Oxidation Technologies for Wastewater Treatment: An Overview. *Industrial Wastewater Treatment, Recycling and Reuse* **2014**, *Chapter 3*, 141. https://doi.org/10.1016/B978-0-08-099968-5.00003-9.

(14) Si, Y. H.; Chen, W. M.; Shang, S. K.; Xia, Y.; Zeng, X. R.; Zhou, J.; Li, Y. Y. g-C_3N_4/Pt/$BiVO_4$ Nanocomposites for Highly Efficient Visible-Light Photocatalytic Removal of Contaminants and Hydrogen Generation. *Nanotechnology* **2020**, *31*, 125706. https://doi.org/10.1088/1361-6528/ab5bc5.

(15) Ou, M.; Wan, S.; Zhong, Q.; Zhang, S.; Song, Y.; Guo, L.; Cai, W.; Xu, Y. Hierarchical Z-Scheme Photocatalyst of g-C_3N_4@Ag/$BiVO_4$ (040) with Enhanced Visible-Light-Induced Photocatalytic Oxidation Performance. *Appl. Catal. B Environ.* **2018**, *221*, 97. https://doi.org/10.1016/j.apcatb.2017.09.005.

(16) Hassani, A.; Eghbali, P.; Kakavandi, B.; Lin, K. Y. A.; Ghanbari, F. Acetaminophen Removal from Aqueous Solutions through Peroxymonosulfate Activation by $CoFe_2O_4$/Mpg-C_3N_4 Nanocomposite: Insight into the Performance and Degradation Kinetics. *Environ. Technol. Innov.* **2020**, *20*, 101127. https://doi.org/10.1016/j.eti.2020.101127.

(17) Zeng, X.; Lan, S.; Lo, I. M. C. Rapid Disinfection of E. Coli by a Ternary $BiVO_4$/Ag/g-C_3N_4 Composite under Visible Light: Photocatalytic Mechanism and Performance Investigation in Authentic Sewage. *Environ. Sci. Nano* **2019**, *6*, 610. https://doi.org/10.1039/c8en01283k.

(18) Zheng, Z.; Huang, B.; Qin, X.; Zhang, X.; Dai, Y.; Whangbo, M. H. Facile in Situ Synthesis of Visible-Light Plasmonic Photocatalysts M@TiO_2 (M = Au, Pt, Ag) and Evaluation of Their Photocatalytic Oxidation of Benzene to Phenol. *J. Mater. Chem.* **2011**, *21*, 9079. https://doi.org/10.1039/c1jm10983a.

(19) Lin, X.; Xu, D.; Xi, Y.; Zhao, R.; Zhao, L.; Song, M.; Zhai, H.; Che, G.; Chang, L. Construction of Leaf-like g-C_3N_4/Ag/$BiVO_4$ Nanoheterostructures with Enhanced Photocatalysis Performance under Visible-Light Irradiation. *Colloids Surfaces A: Physicochem. Eng. Asp.* **2017**, *513*, 117. https://doi.org/10.1016/j.colsurfa.2016.11.040.

(20) Zhang, J.; Ren, F.; Deng, M.; Wang, Y. Enhanced Visible-Light Photocatalytic Activity of a g-C_3N_4/$BiVO_4$ Nanocomposite: A First-Principles Study. *Phys. Chem. Chem. Phys.* **2015**, *17*, 10218. https://doi.org/10.1039/c4cp06089j.

(21) Jo, W. K.; Natarajan, T. S. Influence of TiO_2 Morphology on the Photocatalytic

Efficiency of Direct Z-Scheme g-C_3N_4/TiO_2 Photocatalysts for Isoniazid Degradation. *Chem. Eng. J.* **2015**, *281*, 549. https://doi.org/10.1016/j.cej.2015.06.120.

(22) Chen, P.; Li, Y.; Xiao, C.; Chen, L.; Guo, J.; Shen, S.; Au, C.; Yin, S. Bond under Visible Light Irradiation. *ACS Sustain. Chem. Eng.* **2019**, *7*, 17500. https://doi.org/10.1021/acssuschemeng.9b04858.

(23) Chen, F.; Yang, Q.; Wang, Y.; Zhao, J.; Wang, D.; Li, X.; Guo, Z.; Wang, H.; Deng, Y.; Niu, C.; Zeng, G. Novel Ternary Heterojunction Photococatalyst of Ag Nanoparticles and g-C_3N_4 Nanosheets Co-Modified $BiVO_4$ for Wider Spectrum Visible-Light Photocatalytic Degradation of Refractory Pollutant. *Appl. Catal. B Environ.* **2017**, *205*, 133. https://doi.org/10.1016/j.apcatb.2016.12.017.

(24) Zanatta, A. R. Revisiting the Optical Bandgap of Semiconductors and the Proposal of a Unified Methodology to Its Determination. *Sci. Rep.* **2019**, *9*, 11225. https://doi.org/10.1038/s41598-019-47670-y.

(25) Phanichphant, S.; Nakaruk, A.; Chansaenpak, K.; Channei, D. Evaluating the Photocatalytic Efficiency of the $BiVO_4$/RGO Photocatalyst. *Sci. Rep.* **2019**, *9*, 1. https://doi.org/10.1038/s41598-019-52589-5.

(26) Zhang, Y.; Pan, Q.; Chai, G.; Liang, M.; Dong, G.; Zhang, Q.; Qiu, J. Synthesis and Luminescence Mechanism of Multicolor-Emitting g-C_3N_4 Nanopowders by Low Temperature Thermal Condensation of Melamine. *Sci. Rep.* **2013**, *3*, 1. https://doi.org/10.1038/srep01943.

(27) Fang, D.; Li, X.; Liu, H.; Xu, W.; Jiang, M.; Li, W.; Fan, X. $BiVO_4$-RGO with a Novel Structure on Steel Fabric Used as High-Performance Photocatalysts. *Sci. Rep.* **2017**, *7*, 1. https://doi.org/10.1038/s41598-017-07342-1.

(28) Shen, L.; Xing, Z.; Zou, J.; Li, Z.; Wu, X.; Zhang, Y.; Zhu, Q.; Yang, S.; Zhou, W. Black TiO_2 Nanobelts/g-C_3N_4 Nanosheets Laminated Heterojunctions with Efficient Visible-

Light-Driven Photocatalytic Performance. *Sci. Rep.* **2017**, *7*, 1. https://doi.org/10.1038/srep41978.

(29) Wang, L.; Zhou, H.; Zhang, H.; Song, Y.; Zhang, H.; Qian, X. SiO_2@TiO_2 Core@Shell Nanoparticles Deposited on 2D-Layered $ZnIn_2S_4$ to Form a Ternary Heterostructure for Simultaneous Photocatalytic Hydrogen Production and Organic Pollutant Degradation. *Inorg. Chem.* **2020**, *59*, 2278. https://doi.org/10.1021/acs.inorgchem.9b03007.

(30) Prakash, K.; Karuthapandian, S.; Senthilkumar, S. Zeolite Nanorods Decorated g-C_3N_4 Nanosheets: A Novel Platform for the Photodegradation of the Hazardous Water Contaminants. Mater. Chem. Phys. **2019**, 221, 34. https://doi.org/10.1016/j.matchemphys.2018.09.026.

(31) Ambrosio, F.; Wiktor, J.; Pasquarello, A. pH-Dependent Surface Chemistry from First Principles: Application to the $BiVO_4$ (010)-Water Interface. *ACS Appl. Mater. Interfaces* **2018**, *10*, 10011. https://doi.org/10.1021/acsami.7b16545.

(32) Gürses, A.; Doğar, Ç.; Yalçin, M.; Açikyildiz, M.; Bayrak, R.; Karaca, S. The Adsorption Kinetics of the Cationic Dye, Methylene Blue, onto Clay. *J. Hazard. Mater.* **2006**, *131*, 217. https://doi.org/10.1016/j.jhazmat.2005.09.036.

(33) Goyal, N.; Barman, S.; Bulasara, V. K. Quaternary Ammonium Salt Assisted Removal of Genistein and Bisphenol S from Aqueous Solution by Nanozeolite NaY: Equilibrium, Kinetic and Thermodynamic Studies. *J. Mol. Liq.* **2016**, *224*, 1154. https://doi.org/10.1016/j.molliq.2016.10.088.

(34) Sorathiya, K.; Mishra, B.; Kalarikkal, A.; Reddy, K. P.; Gopinath, C. S.; Khushalani, D. Enhancement in Rate of Photocatalysis Upon Catalyst Recycling. *Sci. Rep.* **2016**, *6*, 1. https://doi.org/10.1038/srep35075.

(35) Farooq, U.; Phul, R.; Alshehri, S. M.; Ahmed, J.; Ahmad, T. Electrocatalytic and Enhanced Photocatalytic Applications of Sodium Niobate Nanoparticles Developed by

Citrate Precursor Route. *Sci. Rep.* **2019**, *9*, 1. https://doi.org/10.1038/s41598-019-40745-w.

(36) Pehlivan, F. E. Vitamin C: An Antioxidant Agent. *Vitam. C* **2017**, *Chapter 2*, 1. https://doi.org/10.5772/intechopen.69660.

(37) Xu, J.; Teng, Y.; Teng, F. Effect of Surface Defect States on Valence Band and Charge Separation and Transfer Efficiency. *Sci. Rep.* **2016**, *6*, 1. https://doi.org/10.1038/srep32457.

(38) Zhao, W.; Hu, C. H.; Chen, R.; Lv, F. Z.; Zhong, Y.; Zhou, H. Y. Synthesis and Photocatalytic Activity of Ag - Doped $BiVO_4$. *Adv. Mater. Res.* **2013**, *734*, 2204. https://doi.org/10.4028/www.scientific.net/AMR.734-737.2204.

(39) Pawar, R. C.; Kang, S.; Park, J. H.; Kim, J. H.; Ahn, S.; Lee, C. S. Room-Temperature Synthesis of Nanoporous 1D Microrods of Graphitic Carbon Nitride (g-C_3N_4) with Highly Enhanced Photocatalytic Activity and Stability. *Sci. Rep.* **2016**, *6*, 1. https://doi.org/10.1038/srep31147.

(40) Orimolade, B. O.; Arotiba, O. A. Towards Visible Light Driven Photoelectrocatalysis for Water Treatment: Application of a FTO/$BiVO_4$/Ag_2S Heterojunction Anode for the Removal of Emerging Pharmaceutical Pollutants. *Sci. Rep.* **2020**, *10*, 1. https://doi.org/10.1038/s41598-020-62425-w.

(41) Nandi, A.; Chatterjee, I. B. Scavenging of Superoxide Radical by Ascorbic Acid. *J. Biosci.* **1987**, *11*, 435. https://doi.org/10.1007/BF02704692.

(42) Kamble, G. S.; Ling, Y. C. Solvothermal Synthesis of Facet-Dependent $BiVO_4$ Photocatalyst with Enhanced Visible-Light-Driven Photocatalytic Degradation of Organic Pollutant: Assessment of Toxicity by Zebrafish Embryo. *Sci. Rep.* **2020**, *10*, 1. https://doi.org/10.1038/s41598-020-69706-4.

(43) Mesa, C. A.; Kafizas, A.; Francàs, L.; Pendlebury, S. R.; Pastor, E.; Ma, Y.; Le Formal,

F.; Mayer, M. T.; Grätzel, M.; Durrant, J. R. Kinetics of Photoelectrochemical Oxidation of Methanol on Hematite Photoanodes. *J. Am. Chem. Soc.* **2017**, *139*, 11537. https://doi.org/10.1021/jacs.7b05184.

(44) Bardouki, H.; Da Rosa, M. B.; Mihalopoulos, N.; Palm, W. U.; Zetzsch, C. Kinetics and Mechanism of the Oxidation of Dimethylsulfoxide (DMSO) and Methanesulfinate (MSI-) by OH Radicals in Aqueous Medium. *Atmos. Environ.* **2002**, *36*, 4627. https://doi.org/10.1016/S1352-2310(02)00460-0.

(45) Wang, Y.; Shang, X.; Shen, J.; Zhang, Z.; Wang, D.; Lin, J.; Wu, J. C. S.; Fu, X.; Wang, X.; Li, C. Direct and Indirect Z-Scheme Heterostructure-Coupled Photosystem Enabling Cooperation of CO_2 Reduction and H_2O Oxidation. *Nat. Commun.* **2020**, *11*, 1. https://doi.org/10.1038/s41467-020-16742-3.

Chapter 5

2D-2D Bi_3TaO_7/BiOCl heterostructure with heightened charge segregation for Visible-light-driven photocatalytic pollutants degradation

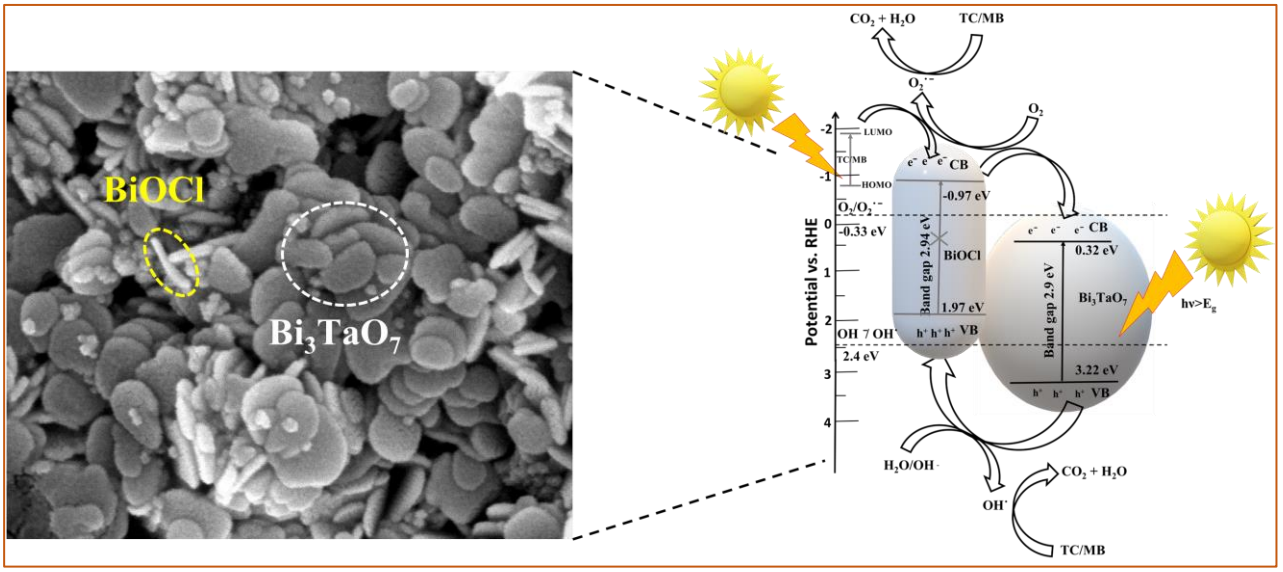

Highlights

- Bi_3TaO_7/BiOCl nano tablets were fabricated via the in-situ precipitation technique.
- BiOCl nanocapsules deposited on Bi_3TaO_7 nano tablets.
- Visible-light degradation of MB dye and antibiotic TC was investigated.
- ~99% and 90% photodegradation efficiency for MB and TC, respectively.

5.1 Introduction

The defilement of veterinary[1] and human pharmaceuticals[1] because of metabolic excretion[2] and industrial discharge[3] over the past years has posed a threat to both our environment and human survival.[4] The major concern with the presence of antibiotics in nature is their physiological effect on the non-target species even when present in low concentrations. Also, discharging waste directly into water bodies results in genotoxic, carcinogenic, and mutagenic effects.[5] One such pollutant is methylene blue (MB) dye having disastrous effects on the human body including anemia and hypertension[6] and the other is tetracycline (TC) usedas an antibiotic for humans, animals, and a promotor for livestock. TC is more harmful owing to its resistant and stubborn nature and subsequent accumulation in the environment leading to environmental toxicity.[7] Additionally, the complete elimination of antibiotics is arduous due totheir toxicity, stability of aromatic rings, solubility, and variable intermediates.[7] It is requisite to utilize efficient, reliable, and fast techniques to completely remove such pollutants from nature. Being an advanced oxidation process, photocatalysis has emerged as a potential methodfor water splitting, CO_2 reduction, and pollutant degradation purposes[8] owing to its eco- friendly, efficient and sustainable nature.[9] The process includes the removal of such pollutants to form less harmful products[10] by using optical energy for the chemical reaction to occur.[5] Hydroxyl radicals being a strong oxidizing agent induce a charge upon pollutants and produceradicals that further react and form radicals such as superoxide and hydrogen peroxide radicals engaged in the photodegradation process.[11] It poses a limitation due to the response of photocatalysts toward UV light comprising a small portion of the entire solar range.[12] The issue can be resolved by either doping or creating heterojunctions between semiconductors comprising different bandgaps making them visible-light-active.[13] Research has been conducted to utilize a large spectrum of visible light by designing such catalysts

having exceptional stability, as well as efficiency, known as visible-light-induced photocatalysts.[14]

In the recent past, two-dimensional (2D) nanostructures favored their hefty counterparts owing to the greater surface area with numerous activation sites and lower e^-/h^+ mitigation gap from bulk to catalyst's surface.[15] Moreover, semiconductors depending on Bi have a relatively narrow bandgap for a good photo-response owing to its valence band structure with Bi 6s and O 2p valence states. Owing to the non-toxic, photostable, and incomparable synthesis, Bi_3TaO_7 has emerged as a popular semiconductor-based catalyst with a small bandgap (2.7-2.9 eV).[16] It can decompose organic pollutants under acidic and alkaline mediums. Designed via high- temperature solid-state reaction, it has the limitation of fast charge carrier recombination, causing less photocatalytic activity.[17] The problem can be resolved by creating heterostructures with good efficiency.

BiOCl is one of the emerging photocatalysts due to its indirect bandgap, high optical activity, anisotropy, and chemical stability. Its layered structure facilitates electron-hole mobility and separation, thereby improving photocatalytic activity. However, it has a large bandgap of 3.2-3.5 eV, making it a poorer response catalyst towards photocatalytic activity than Bi_3TaO_7.[18] Thus, the heterojunction creation amongst BiOCl and Bi_3TaO_7 is suggested. This enhances charge carrier separation, reduces reconciliation rate, and improves photocatalytic performance. Also, the heterostructure formed has the advantage of utility in both visible and UV light, thereby utilizing the complete solar spectrum. Moreover, it provides a facile and inexpensive fabrication technique without intermediate formation. Theoretically, in the heterojunction formed the oxidation reaction falls in BiOCl's valence band (VB) and reduction in Bi_3TaO_7's conduction band (CB), facilitating charge separation. However, due to the lower BiOCl's VB position and more Bi_3TaO_7's CB position, the redox properties of e^-- h^+ pairs get modified through charge separation.

The problem can be resolved by creating a B-type heterojunction that enhances charge partition and reduces charge carrier recombination and thus, enhancing photocatalytic performance.[19] The Bi_3TaO_7/BiOCl heterostructure formed facilitates visible light absorption capacity and thereby, improves photodegradation efficiency.[20]

Research has been conducted in the past with heterostructures comprising Bi_3TaO_7 for pollutant degradation. Le *et al.*[21] deposited the stacked nanosheets of $BiVO_4$ with C-dots on the surface of stacked nanosheets of Bi_3TaO_7 to fabricate a C-sensitized $BiVO_4$/Bi_3TaO_7 using the hydrothermal method. Varied w/w of Bi_3TaO_7 and $BiVO_4$ (such as 5:5, 8:2, 2:8) were synthesized, as VT-5, VT-8, and VT-2. The composite 3CVT-5 (91.7%) displayed maximum efficiency in tetracycline degradation when illuminated via visible light for 120 min. Zhang *etal.*[22] designed Bi_3TaO_7 (fine powder) along with Bi_2O_3 (worm-like) and synthesized Bi_2O_3/Bi_3TaO_7 heterostructure using the calcination technique. Various mass ratios of Bi_2O_3:Bi_3TaO_7 were varied as 0.5:1, 2:1, 1:1, 2.5:1, 3.5:1, and 3:1 and labeled as $0.5Bi_2O_3$- Bi_3TaO_7, $2Bi_2O_3$-Bi_3TaO_7, $1Bi_2O_3$-Bi_3TaO_7, $2.5Bi_2O_3$-Bi_3TaO_7, $3.5Bi_2O_3$-Bi_3TaO_7, $3Bi_2O_3$-Bi_3TaO_7, respectively. The prepared catalysts were used to degrade antibiotic tetracycline with $2Bi_2O_3$-Bi_3TaO_7 composite showing maximum degradation efficiency (90.06%) when irradiation for 180 min under visible light. Luo *et al.*[23] deposited the Bi_3TaO_7 nanoparticles on g-C_3N_4's lamellar structure to design g-C_3N_4/Bi_3TaO_7 binary composite. Different ratios werefabricated via varied quantities of g-C_3N_4 (0%, 30%,10%, 70%, 50%, 90%) and labeled as BTO, CB-3, CB-1, CB-7, CB-5, CB-9, respectively to degrade tetracycline. It was observed that the CB-5 composite showed maximum efficacy when irradiation for 90 min under visiblelight. Yet, no work has been published regarding the fabrication and photocatalytic application of 2D-2D Bi_3TaO_7/BiOCl composite. Since the CB of Bi_3TaO_7 is less negative than BiOCl CBand the VB of Bi_3TaO_7 is more positive than BiOCl's VB. Therefore, the heterostructure of Bi_3TaO_7 and BiOCl not only deduces

the charge carrier reconciliation but also enhances interfacial electron transfer, thereby, promoting photocatalytic performance. The present work involves the fabrication of 2D-2D Bi_3TaO_7/BiOCl nano tablets via the hydrothermal method by coupling Bi_3TaO_7 nano-aggregates and BiOCl nanocapsules. Theas-prepared 2D-2D Bi_3TaO_7/BiOCl nano tablets photodegraded model pollutants, TC, and MB. Factors, such as pH and catalyst concentration were scrutinized. To study the degradation mechanism and stability of the composite, trapping analysis and reusability of the composite were done. The XRD study supported the stability of the used catalyst. COD analysis validated the degradation performance of the fabricated Bi_3TaO_7/BiOCl nano tablets with different weight ratios for the degradation of an antibiotic and a dye and its varied factors affecting degradation.

5.2 Experimental

This section consists of chemicals, materials, and the methodologies used for the synthesis of catalysts.

5.2.1 Chemicals and Materials

Tantalum chloride ($TaCl_5$), potassium hydroxide (KOH), ethanol (C_2H_5OH), bismuth nitrate pentahydrate ($Bi(NO_3)_3.5H_2O$), methanol (CH_3OH), ethylene glycol ($C_2H_6O_2$), and potassium chloride (KCl) were obtained via S. D. Fine-Chem. Limited, India and Thermo Fisher Scientific India Pvt. Ltd. MB and TC were obtained through Merck and Bayer Crop Science Ltd., India. The solutions were prepared via double distilled water.

5.2.2 Synthesis

This section consists of methodologies to synthesize Bi_3TaO_7/BiOCl composite, pure BiOCland pure Bi_3TaO_7.

5.2.2.1 Synthesis of Bi_3TaO_7

3 mmol $TaCl_5$ (1.0745 g) and $Bi(NO_3)_3.5H_2O$ (2.4255 g) were mixed in ethanol (10 mL) with continuous mixing for 60 min. To the solution, $TaCl_5$ was added drop-wise and stirred for another 30 min. Finally, 7M KOH solution was included gradually in the solution with pH set to 10. It was again stirred for 60 min. The solution thus obtained was poured into an autoclave and at atemperature of 220°C heated for a period of 24 h. Washing of the solution was done using distilled water and ethanol (thrice). Lastly, the solution was placed in an oven overnight at 60°C.A "grey" color product was obtained (**Scheme 5.1**).

5.2.2.2 Synthesis of BiOCl

$Bi(NO_3)_3.5H_2O$ (2 mmol) was added to 80 mL ethylene glycol. The solution was magnetically mixed for 30 min. To this, KCl (0.149 g) dissolved in water (10 mL) was included dropwise. Finally, heating in an oil bath (5 min) was done and then magnetically stirred for 12 h. Lastly, centrifugation was done and dried at 60°C. The "white" colored product was procured (**Scheme 5.1**).

5.2.2.3 Synthesis of Bi_3TaO_7/BiOCl

2 mmol of $Bi(NO_3)_3.5H_2O$, Bi_3TaO_7 in a 1:1 stoichiometric weight ratio was mixed in ethylene glycol (80mL), magnetically mixed (30 min). To this, KCl (0.149 g) dissolved in

water (10 mL) was included dropwise. Finally, heating in an oil bath for 5 min was done and then magnetically stirred for 12h. Lastly, centrifugation and drying (at 60°C) were done. Procured products were "white", "light-grey", and "dark-grey" in color for 1:3 Bi_3TaO_7/BiOCl, 1:1 Bi_3TaO_7/BiOCl, and 3:1 Bi_3TaO_7/BiOCl, respectively (**Scheme 5.1**).

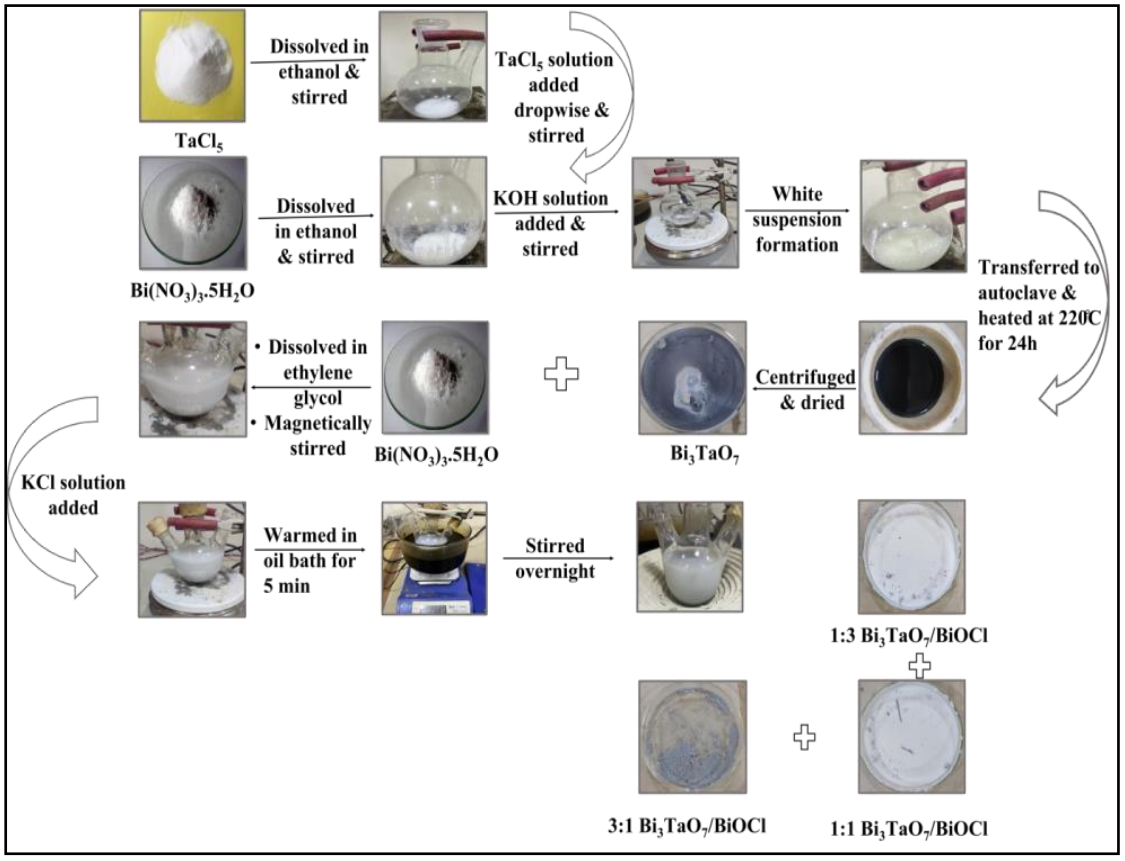

Scheme 5.1. Synthesis of Bi_3TaO_7/BiOCl binary composite.

5.2.3 Characterization

The size distribution curves were investigated via Barrett-Joyner-Halenda (BJH) method. The X-ray diffraction analysis determined the crystallinity of the photocatalyst using a PANanalytical X-ray diffractometer with Cu-Kα radiation at 45kV and scan range 10-90°. The surface morphologies and microstructure of the nanocomposite were studied using the field emission scanning electron microscopy (FESEM SU8180, Hitachi, Tokyo, Japan) and

with Oxford INCTA energy dispersive spectrometer (EDS) and transmission electron microscopy (TEM, JEM-2100F), respectively. By using a PHI- 5000 VersaProbe III system containing a monochromatic Al Kα X-ray source (1486.7 eV), X-ray photoelectron spectroscopy (XPS) was performed to determine the elemental structure of the composite. UV-Vis Diffusion Reflectance Spectroscopy (DRS) in diffuse absorbance mode was carried out by a Hitachi-3900H model spectrophotometer (Shimadzu, Japan). Photoluminescence (PL) spectra were obtained using afluorescence spectrometer (F-4500, Hitachi, Japan). A cyber scan pH 1100 (Eutech, Singapore)was employed to adjust and measure the pH. For the kinetic analysis of pollutant degradation, a UV-Vis spectrophotometer (Shimadzu, UV-2600) was employed.

5.2.4 Photocatalytic Process

The degradation performance was tested via photodegrading MB and TC by putting the solutions in a photoreactor. MB/TC solution with 5 ppm concentration and 2 mg catalysts were mixed and stirred for 90 min in visible light (65W CFL lamp, Phillips, 125 W/m^2, k> 400 nm). The adsorption-desorption equilibrium amongst the catalysts and TC/MB was established by placing the solutions in dark for 60 min. MB (99.6%) and TC (90.22%) were completely degraded. The efficacy for TC (λ_{max} = 357 nm) and MB (λ_{max} = 664 nm) was recorded via a UV-Vis spectrophotometer. According to Lambert Beer's law, absorbance depends upon the concentration, accordingly, the percentage degradation (**Eq. (5.1)**) is as follows[24]:

$$\% D = \{(A_o-A_t)/A_o\} \times 100 = \{(C_o-C_t)/C_o\} \times 100 \quad (5.1)$$

Where A_o and A_t signify the absorbance of dye/pesticide at a time '0' and 't', respectively whereas C_o and C_t signify the concentration of dye/pesticide at a time '0' and 't', respectively.

The Chemical Oxygen Demand (COD) study validated the degradation efficiency of the Bi_3TaO_7/BiOCl binary composite. About 2mg of 0.06 g/L Bi_3TaO_7/BiOCl (1:1) composite was included in 15 ml of TC/MB solution, finally irradiated under visible light (90 min). The titrimetric technique was used to calculate the COD value after and before the catalytic treatment at a time 't', and '0', respectively. The final reduction is calculated using the following **Eq. (5.2)**[25]:

$$\text{COD} = \frac{(a-b)\times N\times 8000\times Dilution\ Factor}{Volume\ Of\ Sample} \quad (5.2)$$

Where b = Ferrous ammonium sulfate (FAS) is used for the titration of the sample in mL, a = Ferrous ammonium sulfate (FAS) was used for the titration of the blank sample in mL, N = Normality of FAS (0.1 N).

5.3 Results and Discussion

5.3.1 Characterization Analysis

5.3.1.1 X-ray Diffraction Analysis

XRD was performed to calculate the lattice planes of Bi_3TaO_7/BiOCl, Bi_3TaO_7, and BiOCl. **Fig. 5.1 (a)** illustrates the XRD pattern for pure Bi_3TaO_7 at 28°, 32.7°, 55.5°, 48.5°, and 57.5° relating to (111), (200), (311), (202), and (222) planes respectively, suggesting Bi_3TaO_7 to be in cubic phase (JCPDS No. 44-0202).[22] The XRD peaks for pure BiOCl (**Fig. 5.1 (a)**) were present at 12°, 32.58°, 25.93°, 24.15°, 33.5°, 36.5°, 46.7°, 41°, 48.4°, 49.8°, 53.35°, 55.2°, 58.7°,60.54°, 68.2°, 54.2°, and 34.81° relating to (001), (110), (101), (002), (102), (003), (200), (112), (201), (113), (202), (104), (212), (114), (220), (211), and (111) lattice planes, respectively indicating the tetragonal phase of BiOCl (JCPDS card no. 06-0249).[26] Lastly, the XRD pattern of Bi_3TaO_7/BiOCl displayed peaks of Bi_3TaO_7 and BiOCl, suggesting the heterojunction formation. The other peaks present in Bi_3TaO_7 and Bi_3TaO_7/BiOCl were probably due to the formation of impurities of $Bi_7Ta_3O_{18}$.[27]

Table 5.1. Mesopore size, total pore volume, and surface area of the prepared photocatalysts.

Photocatalyst	**Surface Area (m^2/g)**	**Total pore volume (cm^3/g)**	**Mesopore size (nm)**
Bi_3TaO_7	26	0.22	20.01
BiOCl	11	0.04	14.68
1:1 Bi_3TaO_7/BiOCl	74	0.55	46.01
1:3 Bi_3TaO_7/BiOCl	61	0.44	43.00
3:1 Bi_3TaO_7/BiOCl	45	0.43	33.69

5.3.1.2 Nitrogen Adsorption/Desorption Studies

To study the catalysts' mesoporous nature, N_2 adsorption-desorption analyses were carried out. The studies illustrated the type-IV isotherm (**Fig. 5.1 (b)**).[9] **Fig. 5.1 (b)** illustrates Bi_3TaO_7, BiOCl, 1:1 Bi_3TaO_7/BiOCl, 1:3 Bi_3TaO_7/BiOCl, and 3:1 Bi_3TaO_7/BiOCl as H3 hysteresis loop, consisting of sharpened desorption and adsorption branches,[22] confirming the constancy and structure of the photocatalysts. The BJH method illustrating the mesoporous nature demonstrated the pore size of the photocatalysts. To scrutinize the mean pore diameter, mean pore volume, and surface area, the BET technique was employed and the surface area for Bi_3TaO_7, BiOCl, 1:1 Bi_3TaO_7/BiOCl, 1:3 Bi_3TaO_7/BiOCl, and 3:1 Bi_3TaO_7/BiOCl were noted to be 26, 11, 74, 61, and 45 m^2/g, respectively. From pure Bi_3TaO_7 and pure BiOCl to 1:1 Bi_3TaO_7/BiOCl, enhancement in surface area was noted (**Table 5.1**).

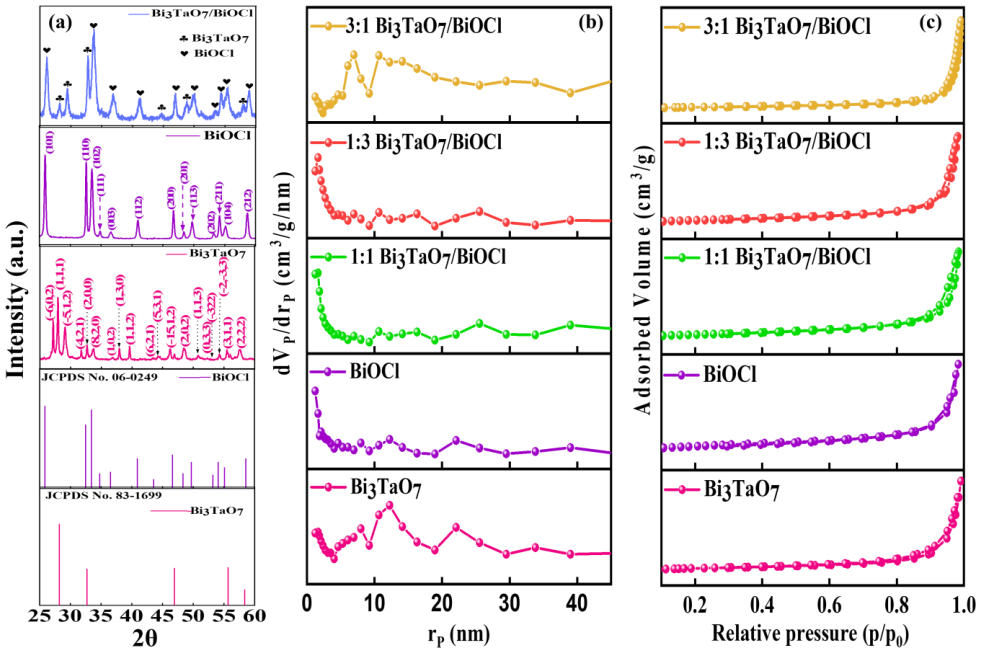

Fig. 5.1. (a) XRD patterns, (b) N_2 adsorption-desorption isotherms, and (c) pore size distribution graphs for the prepared catalysts.

5.3.1.3 XPS Studies

The 1:1 Bi_3TaO_7/BiOCl's elemental state was studied using the XPS analysis. **Fig. 5.2 (a)** demonstrated the presence of Cl, Bi, Ta, and O. For pure Bi_3TaO_7 and pure BiOCl,[9] peaks are situated at 158.8 eV, and 165.9 eV relating to Bi $4f_{7/2}$, Bi $4f_{5/2}$, respectively. The Bi_3TaO_7/BiOCl composite (**Fig. 5.2 (b)**) depicts a Bi 4f spectra with two peaks relating to Bi $4f_{7/2}$ at 159.4 eV and Bi and $4f_{5/2}$ at 164.7 eV, demonstrating Bi^{3+}'s existence in Bi_3TaO_7/BiOCl. The two peaks of Ta in Bi_3TaO_7 are present at 29 eV and 26 eV, respectively relating to Ta $4f_{5/2}$, and Ta $4f_{7/2}$[21] while Ta $4f_{7/2}$ and Ta $4f_{5/2}$ in the composite correspond to 25.9 eV, and 28.4 eV depicting the occurrence of Ta (+5 valence state) in Bi_3TaO_7/BiOCl (**Fig. 5.2 (c)**).[21] This depicts a blue shift in the binding energy. The O1s spectra for Bi_3TaO_7 and BiOCl display peaks at 529.5 eV, 531.4 eV corresponding to Bi-O (lattice O), O-H on the surface and H_2O adsorbed, respectively,[5] while the two peaks of O1s

in the composite are present at the 529.6 eV, and 532.6 eV relating to Bi-O (lattice O), O-H on the surface and H_2O adsorbed, respectively (**Fig. 5.2 (d)**),[6] showing a redshift in the binding energy. The Cl 2p spectra for BiOCl display peaks at 198.1 eV corresponding to Cl $2p_{3/2}$, at 199.7 eV corresponding to Cl $2p_{1/2}$ [26] while the composite displays peaks at 195.4 eV corresponding to Cl $2p_{3/2}$, at 197.6 eV corresponding to Cl $2p_{1/2}$. (**Fig. 5.2 (e)**),[19] suggesting the blue shift. The shift in binding energies is mentioned in **Table 5.2**. The binding energy alteration through pure Bi_3TaO_7 and pure BiOCl to Bi_3TaO_7/BiOCl composite relates to the surface charge density modification by a different material embodiment with varied Fermi levels (E_f) causing direct charge alteration.[28]

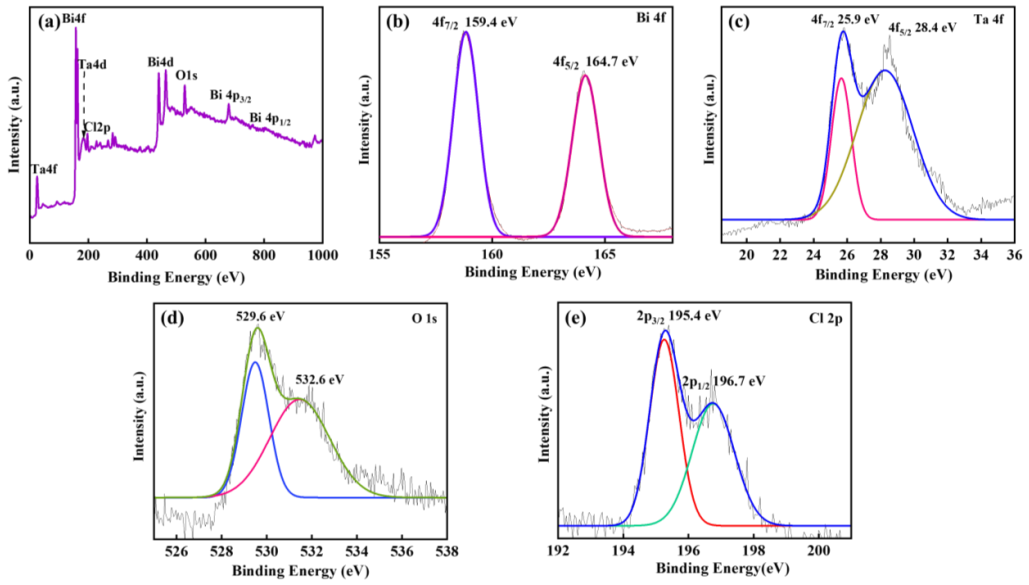

Fig. 5.2. (a) XPS spectrum, and deconvoluted peaks of (b) Bi, (c) Ta, (d) O, (e) Cl of 1:1 Bi_3TaO_7/BiOCl composite.

Table 5.2. Shift in Binding Energies for Elements of 1:1 Bi_3TaO_7/BiOCl composite.

Element	**Binding Energy**	
Bi	$4f_{7/2}$ at 159.4 eV	$4f_{5/2}$ at 164.7 eV
Ta	$4f_{7/2}$ at 25.9 eV	$4f_{5/2}$ at 28.4 eV
O	529.6 eV (lattice O)	532.6 eV (adsorbed O)
Cl	$2p_{3/2}$ at 195.4 eV	$2p_{1/2}$ at 197.6 eV

5.3.1.4 Elemental Mapping and EDS Studies

The elemental mapping of the 1:1 Bi_3TaO_7/BiOCl composite is depicted in **Fig. 5.3 (b-e)**, supporting the occurrence of Bi, Ta, O, and Cl. The EDS studies investigated the elemental structure of Bi_3TaO_7/BiOCl (**Fig. 5.3 (a)**). To investigate the elements' composition EDS analysis of the 1:1 Bi_3TaO_7/BiOCl composite was done and it was observed that the weight % of Bi, Cl, O, Ta was found to be 59.64%, 9.69%, 7.49%, and 23.19%, respectively.

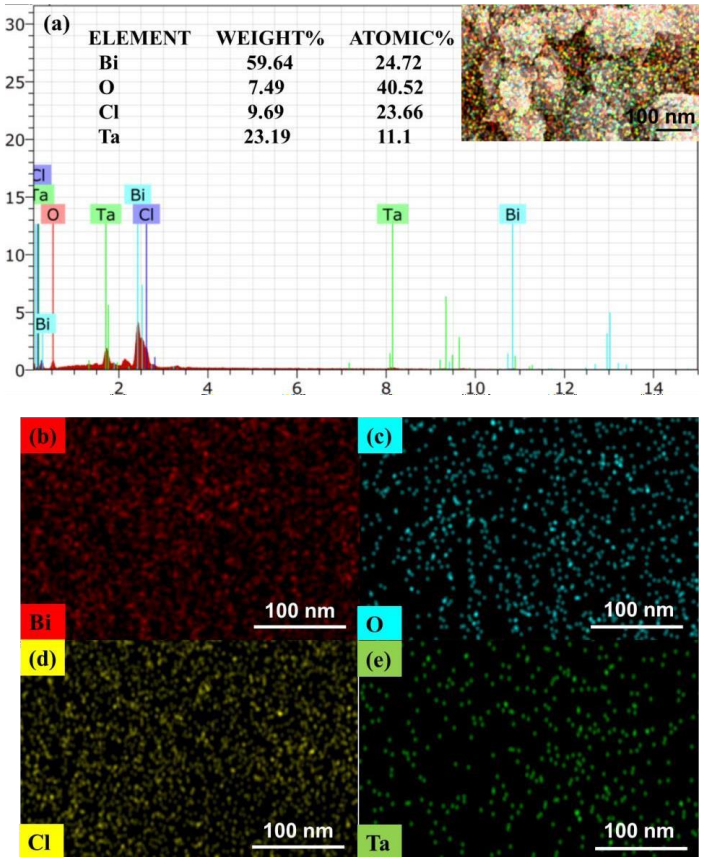

Fig. 5.3. (a) EDS spectrum, elemental mapping images for (b) Bi, (c) O, (d) Cl, and (e) Ta of 1:1 Bi_3TaO_7/BiOCl binary composite.

5.3.1.5 FESEM and HRTEM Studies

FESEM studies were done to study the surface morphology of pure Bi_3TaO_7, pure BiOCl, and Bi_3TaO_7/BiOCl. **Fig. 5.4 (a)** shows the aggregated-like molecules for pure

Bi_3TaO_7. Capsule-like structures (**Fig. 5.4 (b)**) were obtained for BiOCl. **Fig. 5.4 (c)** illustrates the deposition of BiOCl nanocapsules on the Bi_3TaO_7 nano tablets formed. For the detailed structural study of the nanocomposite, HR-TEM analysis was also done. **Fig. 5.4 (d-f)** shows the presence of BiOCl nanocapsules (dark grey portion) along with Bi_3TaO_7 (light grey portion). The lattice planes for Bi_3TaO_7 and BiOCl were found to be (111), (001), and (002) at 0.315 nm, 0.73 nm, and 0.35 nm, respectively.

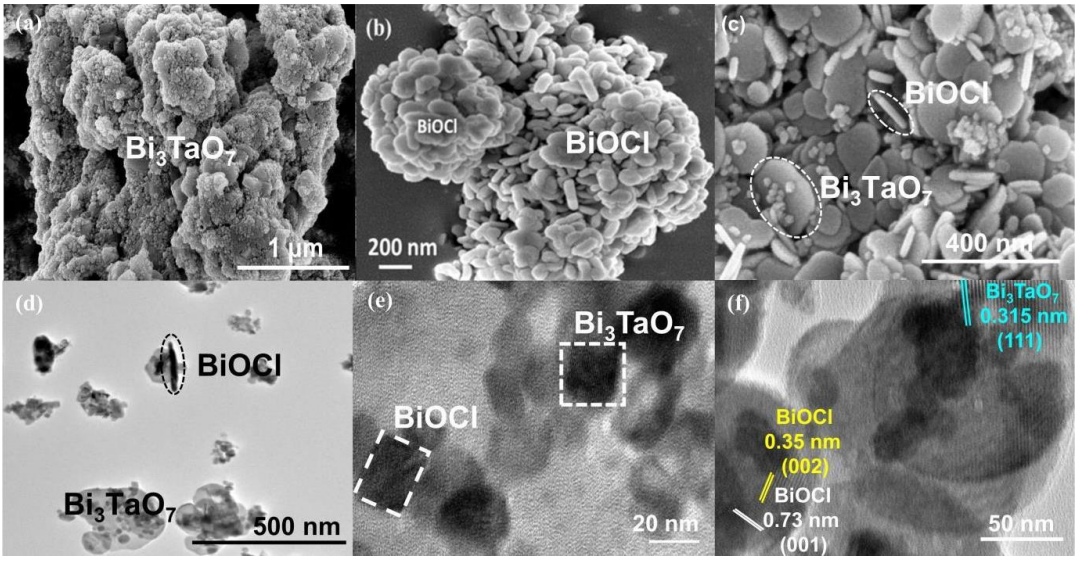

Fig. 5.4. FESEM illustrations of (a) Bi_3TaO_7, (b) BiOCl, (c) 1:1 Bi_3TaO_7/BiOCl, and (d-f) HRTEM images of 1:1 Bi_3TaO_7/BiOCl.

5.3.1.6 Optical Studies

The e^--h^+ reconciliation is predominant in the degradation process. The e^--h^+ recombination is less with less photoluminescence (PL) intensity and more charge separation.[29] PL spectra were recorded to scrutinize the charge separation at 315 nm (excitation wavelength) (**Fig. 5.5 (a)**). Bi_3TaO_7/BiOCl's PL intensity was lower than that of Bi_3TaO_7, and BiOCl, suggesting better charge segregation with lesser reconciliation capacity and therefore better photocatalytic performance.[9]

UV-Visible diffuse reflectance spectroscopy evaluated Bi_3TaO_7/BiOCl's bandgap. Theabsorption edges for Bi_3TaO_7, BiOCl, and Bi_3TaO_7/BiOCl were formulated as 490 nm, 390 nm, and 680 nm (**Fig. 5.5 (b)**), respectively. Bi_3TaO_7's incorporation in BiOCl leads to a shifttowards a longer wavelength in the visible region.[21] To calculate the bandgap energy, tauc's plot was drawn. The **Eqn. (5.3)** is:

$$(\alpha h\nu)^{1/2} = A(h\nu - E_g)n/2 \quad (5.3)$$

Where ν denotes light frequency, h denotes Planck constant, α denotes absorption coefficient, n = optical transition type of semiconductors, A = proportionality constant and E_g donates bandgap energy. The bandgaps for Bi_3TaO_7, BiOCl, Bi_3TaO_7/BiOCl were calculated as 2.9 eV, 3.1 eV, and 2.34 eV, respectively (**Fig. 5.5 (c)**). Due to the introduction of Bi_3TaO_7 in BiOCl, a change in the electronic structure occurs.[21]

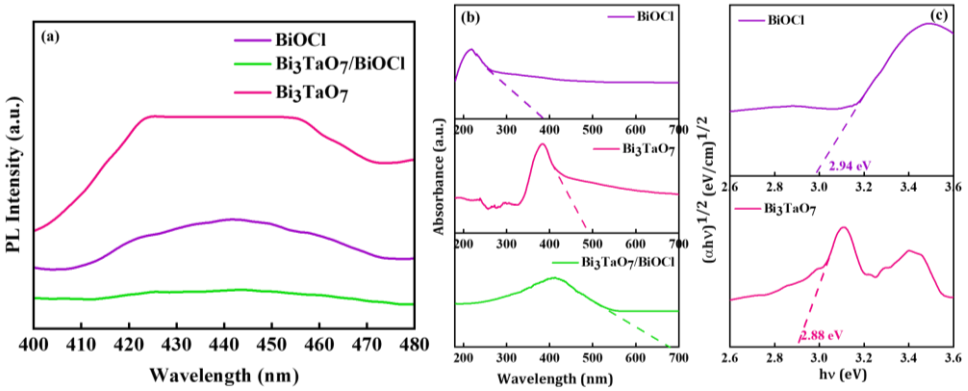

Fig. 5.5. (a) Photoluminescence spectra, (b) UV Visible diffuse reflectance spectra, and (c)Tauc's plot of the photocatalysts.

5.3.2 Methylene Blue and Tetracycline Photocatalytic Process

The photocatalytic degradation of Bi_3TaO_7/BiOCl was scrutinized by degrading model pollutants, MB (5 mg/L),[30] and TC (600 mg/L).[21] The solution was put in the dark (60 min) to set the adsorption-desorption equilibrium. The efficiency with no composite

was almost the same (4.15% for MB and 2.90% for TC) (**Fig. 5.6 (a) and (c)**), emphasizing the role of Bi_3TaO_7/BiOCl composite in the photocatalytic process. **Eq. (5.4)** formulated the rate constant,[31] as follows:

$$\ln (C/C_0) = -kt \quad (5.4)$$

Where C signifies the concentration at a time 't', k signifies the rate constant, C_0 signifies the concentration at time = '0'.

Fig. 5.6 (a) and Fig. 5.6 (c) demonstrated the efficiencies for the pollutants with and without photocatalyst. Notably, as such no degradation was seen with no catalyst for MB (**Fig.5.6 (b)**) (4.15%; $k = 3.93 \times 10^{-4}\ min^{-1}$), and for TC (**Fig. 5.6 (d)**) (2.90%; $k = 3.01 \times 10^{-4}\ min^{-1}$). 1:1 Bi_3TaO_7/BiOCl composite displayed optimum efficiency for MB with of 99.6% (k = 0.05622 min^{-1}), TC with 90.22% efficiency ($k = 0.02541\ min^{-1}$) when equated with Bi3TaO7, BiOCl, 1:3 Bi3TaO7/BiOCl, 3:1 Bi3TaO7/BiOCl. For Bi3TaO7, BiOCl, 1:1 Bi3TaO7/BiOCl, 1:3 Bi3TaO7/BiOCl, 3:1 Bi3TaO7/BiOCl, the rate constants are provided in **Table 5.3**. Thus, the 1:1 composite displayed exceptional degradation efficacy for pollutants under visible light.

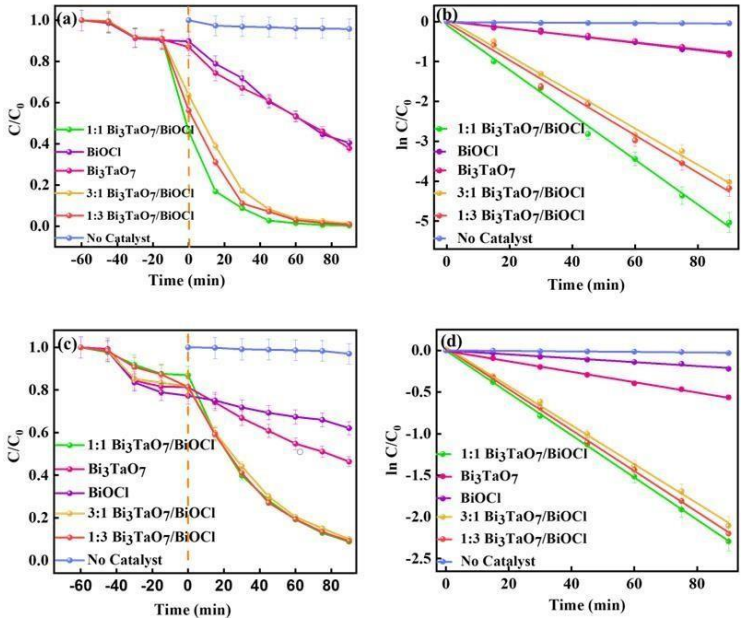

Fig. 5.6. Kinetic investigation of the photocatalytic degradation of (a, b) MB and (c, d) TC.

Table 5.3. Rate constants for the degradation of MB and TC.

Photocatalyst	Rate Constants		% Degradation	
	TC (min^{-1})	MB (min^{-1})	TC	MB
Bi_3TaO_7	0.00626	0.00875	50.11	30.67
BiOCl	0.00234	0.00909	33.88	27.89
1:1 Bi3TaO7/BiOCl	0.02541	0.05622	90.22	99.6
1:3 Bi3TaO7/BiOCl	0.02457	0.0471	90	98.94
3:1 Bi3TaO7/BiOCl	0.02343	0.0455	89.11	98.62

5.3.2.1 Catalyst Concentration Studies

Catalyst concentration studies investigated the role of catalysts in the degradation activity by changing the concentrations (0.06 to 0.4 g/L) using a 1:1 Bi_3TaO_7/BiOCl composite (**Fig. 5.7 (a)**). The efficiency was maximum for the pollutants at 0.13 g/L concentration. The reason could be owed to the opaqueness of the solution and light's scattering.[24] It was inferred that beyond the initial dye adsorption, further addition of the photocatalyst will furnish no resultin the degradation due to the reduced active sites.[30]

5.3.2.2 pH Studies

The point of zero charges (pzc) on Bi_3TaO_7/BiOCl's surface was found as ~pH 6 (pH_{pzc})(**Fig. 5.7 (b)**), suggesting Bi_3TaO_7/BiOCl's negatively charged surface if $pH>pH_{pzc}$, Bi_3TaO_7/BiOCl's positively charged if $pH<pH_{pzc}$.[32] Different pH was varied (pH 1 to 12) (**Fig. 5.7 (c)**) to examine the pH's consequence in the activity via 0.13 g/L Bi_3TaO_7/BiOCl. The maintenance of pH was done by altering the addition of dilute HCl

and NaOH solution.[33] Owing to the cationic nature of MB, the efficiency was highest (99.6%) in the basic range (pH 9), indicating the electrostatic interaction amongst MB and Bi_3TaO_7/BiOCl's negative surface[34] while owing to the anionic nature of TC, the efficiency was highest (90.22%) in basic range (pH 4), indicating the electrostatic interaction amongst TC and Bi_3TaO_7/BiOCl's positive surface.[35]

5.3.2.3 Reusability Studies

Bi_3TaO_7/BiOCl after the activity was segregated by centrifugation. This segregation was facile owing to the dye's temporary adsorption on Bi_3TaO_7/BiOCl's surface. The obtained sample was washed thrice (distilled water), centrifuged, finally kept in the oven, and used.[24] After 4 continuous cycles, the efficiency did not decrease much (92.46% for MB and 86.59% for TC) (Fig. 5.7 (d)). The stability of the reused catalyst was affirmed using XRD (Fig. 5.7 (e)), confirming the firmness and reusability of the composite.

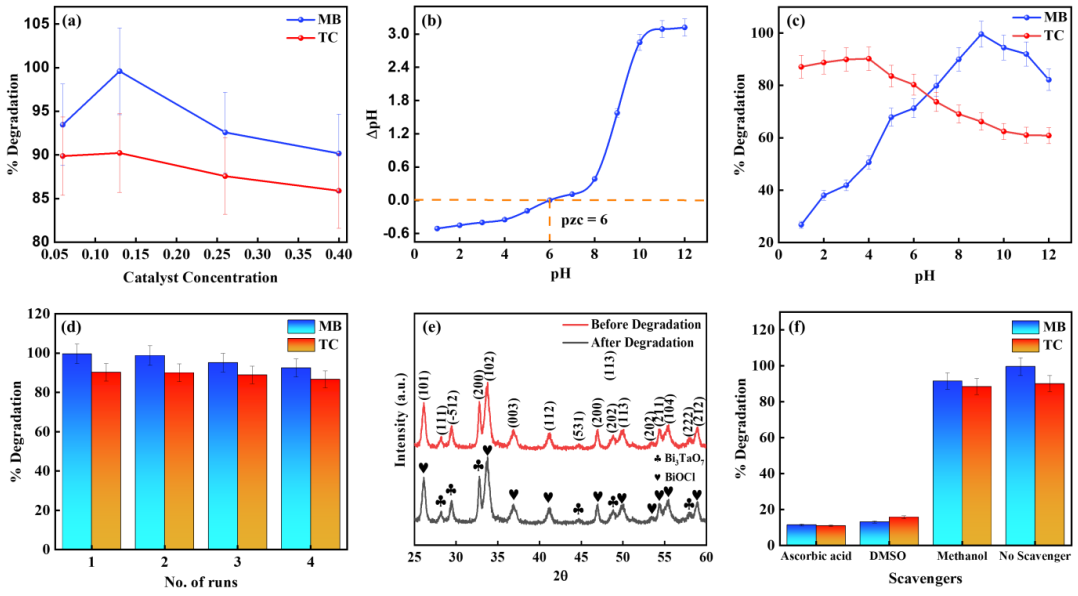

Fig. 5.7. Catalytic analysis: (a) catalyst concentration studies, (b) pH_{PZC} calculation, (c) pHvariation, (d) reusability, (e) XRD patterns of the 1:1 Bi_3TaO_7/BiOCl before and after photodegradation, (f) scavenging analysis via 1:1 Bi_3TaO_7/BiOCl.

5.3.2.4 Plausible Mechanism

To examine the role of radical species in the degradation activity, scavenging analysis was conducted with methanol relating to quenching holes (h^+), and ascorbic acid corresponding to superoxide radical ($O_2^{\bullet-}$), DMSO relating to hydroxide radical ($^{\bullet}OH$) (**Fig. 5.7 (f)**).[5] The 1:1 Bi_3TaO_7/BiOCl composite was used to carry out the degradation activity and the scavenger responsible for the degradation process, its radical species accounts for the activity. Equimolar amounts of ascorbic acid, methanol, and DMSO were included in the prepared solutions. The photodegradation efficacy for MB for methanol was 91.48%, ascorbic acid was 11.45%, and DMSO was 13.09%, indicating $O_2^{\bullet-}$ and $^{\bullet}OH$'s role in MB removal while in the case of TC, the efficacies for methanol were 88.47%, ascorbic acid was 10.99%, and DMSO was 15.76%,indicating $O_2^{\bullet-}$ and $^{\bullet}OH$'s role in TC removal.

The catalyst's band potentials help in understanding the charge carrier partition. For the Bi_3TaO_7 and BiOCl, the VB position and the CB potential were calculated using the **Eqns. (5.5) and (5.6)**[36]:

$$E_{CB} = X - E_c - 0.5E_g \quad (5.5)$$

$$E_{VB} = E_{CB} + E_g \quad (5.6)$$

Where X denotes the absolute electronegativity of the semiconductor, E_{VB} denotes the valence band's potential, E_{CB} denotes the conduction band's position, and E_c denotes hydrogen's free- electron energy (~ 4.5 eV), and E_g denotes the bandgap of the semiconductor. The electronegativity value for BiOCl was 5 eV[5] and for Bi_3TaO_7 it was 6.27 eV.[22] As stated by DRS analysis, the bandgap of BiOCl and Bi_3TaO_7 is 2.94 eV and 2.9 eV, respectively. Therefore, as per **Eqns. (5.5) and (5.6)**, the CB positions for BiOCl and Bi_3TaO_7 are -0.97 eV and 0.32 eV while the VB position for BiOCl and Bi_3TaO_7 are 1.97 eV and 3.22 eV. On this basis, it was inferred that the p-n type heterojunction creation amongst BiOCl and Bi_3TaO_7 is responsible for the enhanced performance. A mechanism

proposed is depicted in **Scheme 5.2**. The E_f is nearer to the n-type Bi_3TaO_7's CB while E_f is nearer to the p-type BiOCl's VB. When Bi_3TaO_7 and BiOCl are in a heterojunction, holes diffuse from BiOCl to Bi_3TaO_7 and electrons from Bi_3TaO_7 to BiOCl. The positive charges gather around Bi_3TaO_7 and negative charges around BiOCl. A built-in electric field produces if the E_f of Bi_3TaO_7 and BiOCl attain equilibrium with an opposing internal electric field to prevent further diffusion of charge amongst them. The E_f becomes flat when there is a mobility of the band levels in the opposite directions. Therefore, a built-in electric field is produced at the interface of the p-n junction through Bi_3TaO_7 to BiOCl. The catalyst's band potential is important in the production, and electron-hole pair segregation. Moreover, the minimum of the CB and the maximum of the VB determine the transference path of the electrons and holes. Once there is the formation of heterojunction, BiOCl's CB becomes more negative than Bi_3TaO_7 and Bi_3TaO_7's VB becomes more positive than BiOCl. Such a type of heterostructure is known as a B-type heterojunction.

With the visible-light illumination of Bi_3TaO_7/BiOCl, the excitation of Bi_3TaO_7 occurs through the photons to produce holes and electrons owing to the narrow bandgap of 2.34 eV (**Eq. 5.9**). While Bi_3TaO_7's VB electrons get transferred to the CB leaving behind holes. As such no excitation occurs for BiOCl because of the large bandgap.[5] Owing to Bi_3TaO_7's greater positive CB potential than O_2/ $O_2^{\bullet-}$ i.e -0.33 eV,[37] the Bi_3TaO_7's CB electrons cannot react with O_2 to synthesize $O_2^{\bullet-}$. Owing to the greater VB position of Bi_3TaO_7 than BiOCl, Bi_3TaO_7's VB holes move to BiOCl's VB by heterojunction creation at the interface of the catalysts, facilitating charge carrier separation.[26] Also, the molecules of the pollutant situated on the surface of the photocatalysts become excited via irradiation to synthesize electrons which move to BiOCl's CB (**Eq. 5.8**) owed to the greater LUMO position of pollutants[38] than BiOCl's CB.[26] The O_2 then reacts with the electrons to produce $O_2^{\bullet-}$ (**Eq. 5.10**). This is owed to the BiOCl's greater CB position than O_2/ $O_2^{\bullet-}$.[26] Likewise, the holes present on Bi_3TaO_7's valence band produce $^{\bullet}OH$ radicals from OH^-

due to the more valence band potential of Bi_3TaO_7 than $^{\bullet}OH/H_2O$ (**Eq. 5.11**). Finally, the $O_2^{\bullet-}$ and $^{\bullet}OH$ radicals produced oxidize the pollutants and decompose them into lesser toxic products like CO_2 and H_2O (**Eq. 5.12- 5.13**).[6] The reaction mechanism is as follows:

$$MB/TC + h\nu \longrightarrow MB'/TC' \quad (5.7)$$

$$MB'/TC' + Bi_3TaO_7/BiOCl \longrightarrow MB^{+\bullet}/TC^{+\bullet} + Bi_3TaO_7/BiOCl\ (e^-) \quad (5.8)$$

$$Bi_3TaO_7/BiOCl + h\nu \longrightarrow h^+ + e^- \quad (5.9)$$

$$O_2 + e^-\ (CB_{BiOCl}) \longrightarrow O_2^{\bullet-} \quad (5.10)$$

$$BiOCl(h^+)/Bi_3TaO_7(h^+) + H_2O \longrightarrow BiOCl/Bi_3TaO_7 + {}^{\bullet}OH + H^+ \quad (5.11)$$

$$MB\ (MB^{+\bullet})/FIP\ (FIP^{+\bullet}) + O_2^{\bullet-}\ (CB_{BiOCl}) \longrightarrow CO_2 + H_2O \quad (5.12)$$

$$MB\ (MB^{+\bullet})/FIP\ (FIP^{+\bullet}) + {}^{\bullet}OH\ (CB_{BiOCl}) \longrightarrow CO_2 + H_2O \quad (5.13)$$

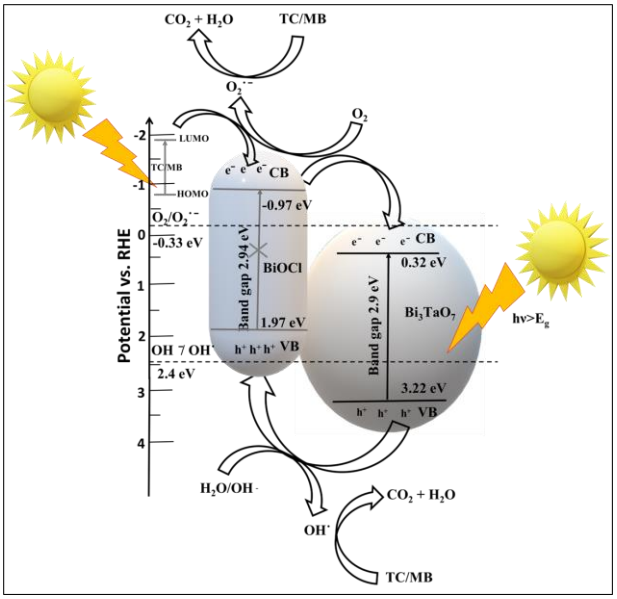

Scheme 5.2. Mechanism for visible-light-induced pollutant removal by Bi_3TaO_7/BiOCl nanotablet.

A comparative study was done with various photocatalysts for pollutant removal (**Table 5.4**), confirming the usefulness of the composite for pollutant degradation.

Table 5.4. Comparison of varied photocatalysts for pollutant degradation.

Catalyst	Pollutant	Conc. (g/L)	Time (min)	Light source	Light intensity (mW/cm^2)	*k* (min^{-1})	Efficie-ncy (%)	Reference
Bi_2O_3/Bi_3TaO_7	TC	0.50	210	visible	-	0.54	90.0	22
g-C_3N_4/Bi_3TaO_7	TC	0.05	90	visible	15	-	89.2	23
C-$Bi_3TaO_7/BiVO_4$	TC	0.50	120	visible	-	-	91.7	21
Bi_3TaO_7	TC	0.50	120	visible	-	-	74.9	16
β-Bi_2O_3/BiOCl	TC HCl	0.20	180	visible	-	0.02	99.5	19

5.3.2.5. COD Analysis

The pollutants were analyzed by COD using 1:1 Bi_3TaO_7/BiOCl (0.13 g/L) by visible-light irradiation (90 min). It was seen that the COD value without any pre-treatment for MB was 1200 mg/L, and for TC, it was 1800 mg/L, suggesting the high quantity of organic content loading in MB and TC. The final COD value after photodegradation activity was

125 mg/L (MB) and 220 mg/L (TC), suggesting that the 1:1 Bi_3TaO_7/BiOCl composite is highly efficient in treating pollutants with huge organic contents (**Fig. 5.8**).

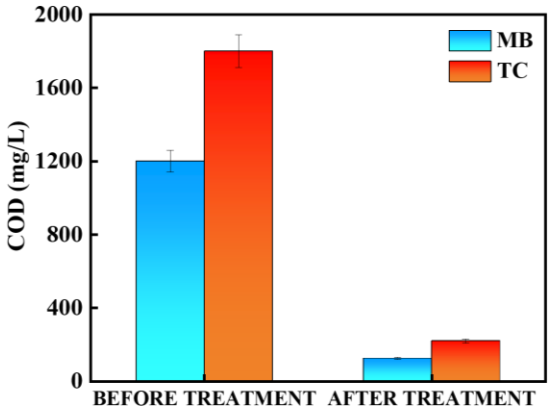

Fig. 5.8. COD analysis for visible-light-induced pollutant removal by Bi_3TaO_7/BiOCl nanotablet.

5.3.3 Conclusion

The chapter comprises the fabrication of a novel binary composite of Bi_3TaO_7/BiOCl with various weight ratios using the in-situ precipitation technique. It was used for antibiotic and dye degradation. The surface analysis showed nanocapsules of BiOCl deposited on the nano tablets of Bi_3TaO_7. The pzc and pH analysis displayed the maximum removal for MB and TC in the basic and acidic range, respectively. It was because of the ionic interactions betweenthe composite's surface and the pollutants. A reduction in efficacy in the feed concentration studies demonstrated the lesser activation sites once there is complete pollutant adsorption. Thecatalysts' stability was affirmed via the reusability analysis. COD studies displayed the efficiency of the composite in removing organic pollutants. The scavenging experiments implored the mechanism suggesting the role of $^{\bullet}OH$ and $O_2^{\bullet-}$ in the activity. The reason maybe because of the large area, charge carrier separation, and less charge carrier reconciliation. Therefore, due to the optical,

morphological, and electronic properties, the composite showed high efficiency for pollutant removal.

References

(1) Wilkinson, J. L.; Boxall, A. B. A.; Kolpin, D. W.; Leung, K. M. Y.; Lai, R. W. S.; Wong, D.; Ntchantcho, R.; Pizarro, J.; Mart, J.; Echeverr, S.; Garric, J.; Chaumot, A.; Gibba, P.; Kunchulia, I.; Seidensticker, S.; Lyberatos, G.; Morales-salda, J. M.; Kang, H. Pharmaceutical Pollution of the World's Rivers. *Environmnetal Sciences* **2022**, *119*, 1. https://doi.org/10.1073/pnas.2113947119.

(2) Plattard, N.; Dupuis, A.; Migeot, V.; Haddad, S.; Venisse, N. An Overview of the Literature on Emerging Pollutants: Chlorinated Derivatives of Bisphenol A (Cl_xBPA). *Environ. Int.* **2021**, *153*, 106547. https://doi.org/10.1016/j.envint.2021.106547.

(3) Wei, H.; Zhang, Y.; Xiu, P.; Zhang, H.; Zhu, S. Index-Based Analysis of Industrial Structure and Environmental Efficiency Based on Sewage Discharge Assessment in China. *Alexandria Eng. J.* **2022**, *61*, 493. https://doi.org/10.1016/j.aej.2021.06.006.

(4) Bello, N. I. Environmental Problems as a Threat to Sustainable Urban Development in Kano Metropolitan- A Review. International Journal of Energy and Environmental Research **2021**, *9*, 33. https://doi.org/10.37745/ijeer.13.

(5) Nagar, A.; Basu, S. Fabrication of 3D Porous Peony Flower-like β-Bi_2O_3/BiOCl Heterostructure for Synergistically Boosting the Visible-Light-Driven Degradation of Organic Pollutants. *Environ. Technol. Innov.* **2021**, *24*, 101956. https://doi.org/10.1016/j.eti.2021.101956.

(6) Nagar, A.; Basu, S. Ternary g-C_3N_4/Ag/$BiVO_4$ Nanocomposite: Fabrication and Implementation to Remove Organic Pollutants. *Environ. Technol. Innov.* **2021**, *23*,

101646. https://doi.org/10.1016/j.eti.2021.101646.

(7) Majumdar, A.; Ghosh, U.; Pal, A. Novel 2D/2D g-C_3N_4/Bi_4NbO_8Cl Nano-Composite for Enhanced Photocatalytic Degradation of Oxytetracycline under Visible LED light Irradiation. J. Colloid Interface Sci. 2021, 584, 320. https://doi.org/10.1016/j.jcis.2020.09.101.

(8) Li, Z.; Zhang, Z.; Dong, Z.; Wu, Y.; Liu, J.; Cheng, Z.; Liu, Y.; Wang, Y.; Zheng, Z.; Cao, X.; Wang, Y.; Liu, Y. Synthesis of MoS_2/P-g-C_3N_4 Nanocomposites with Enhanced Visible-Light Photocatalytic Activity for the Removal of Uranium (VI). *J. Solid State Chem.* **2021**, *302*, 122305. https://doi.org/10.1016/j.jssc.2021.122305.

(9) Nagar, A.; Basu, S. Deciphering the Role of β-Phase Bi_2O_3 Nanorods Incorporated on g-C_3N_4 Nanosheets for Efficient Pollutant Removal. *J. Phys. Chem. Solids* **2022**, *164*, 110625. https://doi.org/10.1016/j.jpcs.2022.110625.

(10) Garg, A.; Basu, S.; Shetti, N. P.; Reddy, K. R. 2D Materials and Its Heterostructured Photocatalysts: Synthesis, Properties, Functionalization and Applications in Environmental Remediation. *J. Environ. Chem. Eng.* **2021**, 106408. https://doi.org/10.1016/J.JECE.2021.106408.

(11) Narenuch, T.; Senasu, T.; Chankhanittha, T.; Nanan, S. Solvothermal Synthesis of CTAB Capped and SDS Capped BiOCl Photocatalysts for Degradation of Rhodamine B (RhB) Dye and Fluoroquinolone Antibiotics. *J. Solid State Chem.* **2021**, *294*, 121824. https://doi.org/10.1016/j.jssc.2020.121824.

(12) Hou, C.; Liu, H.; Mohammad, F. B. Preparation of Ordered Mesoporous F–$H_2Ti_3O_7$ Nanosheets Using Orthorhombic $HTiOF_3$ as a Precursor and Their Highly Efficient Degradation of Tetracycline Hydrochloride under Simulated Sunlight. *J. Solid State Chem.* **2021**, *300*, 122288. https://doi.org/10.1016/j.jssc.2021.122288.

(13) Senasu, T.; Youngme, S.; Hemavibool, K.; Nanan, S. Sunlight-Driven Photodegradation

of Oxytetracycline Antibiotic by $BiVO_4$ Photocatalyst. *J. Solid State Chem.* **2021**, *297*, 122088. https://doi.org/10.1016/j.jssc.2021.122088.

(14) Peng, L. G.; Wang, H.; Liu, J.; Sun, M.; Ni, F. R.; Chang, M. J.; Du, H. L.; Yang, J. Fabrication of Fibrous $BiVO_4/Bi_2S_3/MoS_2$ Heterojunction and Synergetic Enhancement of Photocatalytic Activity towards Pollutant Degradation. *J. Solid State Chem.* **2021**, *299* (April). https://doi.org/10.1016/j.jssc.2021.122195.

(15) Israr, M.; Iqbal, J.; Arshad, A.; Gómez-Romero, P. Sheet-on-Sheet like Calcium Ferrite and Graphene Nanoplatelets Nanocomposite: A Multifunctional Nanocomposite for High-Performance Supercapacitor and Visible Light Driven Photocatalysis. *J. Solid State Chem.* **2021**, *293* (April 2020). https://doi.org/10.1016/j.jssc.2020.121646.

(16) Song, Q.; Wu, P.; Sarkar, S.; Zhao, Y.; Liu, Z. T. C. Bi3TaO7 Film: A Promising Photoelectrode for Photoelectrochemical Water Splitting. *Dalt. Trans.* **2019**, *49* (1), 147–155. https://doi.org/10.1039/c9dt03953h.

(17) Li, K.; Lu, X.; Zhang, Y.; Liu, K.; Huang, Y.; Liu, H. Bi_3TaO_7/Ti_3C_2 Heterojunctions for Enhanced Photocatalytic Removal of Water-Borne Contaminants. *Environ. Res.* **2020**, *185* (November 2019), 109409. https://doi.org/10.1016/j.envres.2020.109409.

(18) Gao, X.; Gong, C.; Wang, X.; Zhu, W.; Luo, Y. Facile Synthesis of Cobalt Doped BiOCl Ultrathin Nanosheets as Superior Photocatalyst for Degradation of Carbamazepine under Visible Light. *J. Solid State Chem.* **2021**, *298* (March), 122131. https://doi.org/10.1016/j.jssc.2021.122131.

(19) Kong, S.; An, Z.; Zhang, W.; An, Z.; Yuan, M.; Chen, D. Preparation of Hollow Flower-Like Microspherical β-Bi_2O_3/BiOCl Heterojunction and High Photocatalytic Property for Tetracycline Hydrochloride Degradation. *Nanomaterials* **2020**, *10* (1), 1–19. https://doi.org/10.3390/nano10010057.

(20) Tang, M.; Ao, Y.; Wang, C.; Wang, P. Rationally Constructing of a Novel Dual Z-Scheme Composite Photocatalyst with Significantly Enhanced Performance for Neonicotinoid Degradation under Visible Light Irradiation. *Appl. Catal. B Environ.* **2020**, *270* (February), 118918. https://doi.org/10.1016/j.apcatb.2020.118918.

(21) Le, S.; Li, W.; Wang, Y.; Jiang, X.; Yang, X.; Wang, X. Carbon Dots Sensitized 2D-2D Heterojunction of $BiVO_4/Bi_3TaO_7$ for Visible Light Photocatalytic Removal towards the Broad-Spectrum Antibiotics. *J. Hazard. Mater.* **2019**, *376* (May), 1–11. https://doi.org/10.1016/j.jhazmat.2019.04.088.

(22) Zhang, J.; Qu, L.; Wu, Y.; Ma, Y.; Chai, Z.; Wang, X. Journal of Solid State Chemistry Fabrication of Visible-Light-Driven Bi_2O_3-Bi_3TaO_7 Nanocomposite for Tetracycline Degradation with Enhanced Photocatalytic Ef Fi Ciency. *J. Solid State Chem.* **2019**, *278* (July), 120894. https://doi.org/10.1016/j.jssc.2019.120894.

(23) Manuscript, A. Dalton Transactions. **2017**. https://doi.org/10.1039/C7DT01250K.

(24) Dashairya, L.; Sharma, S.; Rathi, A.; Saha, P.; Basu, S. Solar-Light-Driven Photocatalysis by Sb2S3/Carbon Based Composites towards Degradation of Noxious Organic Pollutants. *Mater. Chem. Phys.* **2021**, *273* (June), 125120. https://doi.org/10.1016/j.matchemphys.2021.125120.

(25) Tasnim, A. Estimation of Chemical Oxygen Demand in WasteWater Using UV-VIS Spectroscopy. *Sch. Mechatron. Syst. Eng.* **2015**, 10–18.

(26) Tang, X.; Ma, C.; Liu, N.; Liu, C.; Liu, S. Visible Light β-Bi_2O_3/BiOCl Heterojunction Photocatalyst with Highly Enhanced Photocatalytic Activity. *Chem. Phys. Lett.* **2018**, *709*, 82–87. https://doi.org/10.1016/j.cplett.2018.08.045.

(27) Firman, K.; Tan, K. B.; Khaw, C. C.; Zainal, Z.; Tan, Y. P.; Chen, S. K. Doping Mechanisms and Electrical Properties of Bismuth Tantalate Fluorites. *J. Mater. Sci.*

2017, *52* (17), 10106–10118. https://doi.org/10.1007/s10853-017-1216-1.

(28) Si, Y. H.; Chen, W. M.; Shang, S. K.; Xia, Y.; Zeng, X. R.; Zhou, J.; Li, Y. Y. g-C_3N_4/Pt/$BiVO_4$ Nanocomposites for Highly Efficient Visible-Light Photocatalytic Removal of Contaminants and Hydrogen Generation. *Nanotechnology* **2020**, *31* (12). https://doi.org/10.1088/1361-6528/ab5bc5.

(29) Nguyen, V. H.; Bui, Q. T. P.; Vo, D. V. N.; Lim, K. T.; Bach, L. G.; Do, S. T.; Van Nguyen, T.; Doan, V. D.; Nguyen, T. D.; Nguyen, T. D. Effective Photocatalytic Activity of Sulfate-Modified $BiVO_4$ for the Decomposition of Methylene Blue under LED Visible Light. *Materials (Basel).* **2019**, *12* (7). https://doi.org/10.3390/ma12172681.

(30) Monga, D.; Ilager, D.; Shetti, N. P.; Basu, S.; Aminabhavi, T. M. 2D/2d Heterojunction of MoS_2/g-C_3N_4 Nanoflowers for Enhanced Visible-Light-Driven Photocatalytic and Electrochemical Degradation of Organic Pollutants. *J. Environ. Manage.* **2020**, *274*, 111208. https://doi.org/10.1016/j.jenvman.2020.111208.

(31) Sharma, S.; Basu, S. Highly Reusable Visible Light Active Hierarchical Porous WO_3/SiO_2 Monolith in Centimeter Length Scale for Enhanced Photocatalytic Degradation of Toxic Pollutants. *Sep. Purif. Technol.* **2020**, *231* (June 2019), 115916. https://doi.org/10.1016/j.seppur.2019.115916.

(32) Ambrosio, F.; Wiktor, J.; Pasquarello, A. pH-Dependent Surface Chemistry from First Principles: Application to the $BiVO_4$(010)-Water Interface. *ACS Appl. Mater. Interfaces* **2018**, *10* (12), 10011–10021. https://doi.org/10.1021/acsami.7b16545.

(33) Rathi, A.; Basu, S.; Barman, S. Adsorptive Removal of Fipronil from Its Aqueous Solution by Modified Zeolite HZSM-5: Equilibrium, Kinetic and Thermodynamic Study. *J. Mol. Liq.* **2019**, *283*, 867–878. https://doi.org/10.1016/j.molliq.2019.02.140.

(34) Zhu, B.; Xia, P.; Ho, W.; Yu, J. Isoelectric Point and Adsorption Activity of Porous g-C_3N_4. *Appl. Surf. Sci.* **2015**, *344*, 188–195. https://doi.org/10.1016/j.apsusc.2015.03.086.

(35) Han, W.; Wu, T.; Wu, Q. Fabrication of WO_3/Bi_2MoO_6 Heterostructures with Efficient and Highly Selective Photocatalytic Degradation of Tetracycline Hydrochloride. *J. Colloid Interface Sci.* **2021**, *602*, 544–552. https://doi.org/10.1016/j.jcis.2021.05.128.

(36) Li, Y.; Wang, J.; Yao, H.; Dang, L.; Li, Z. Chemical Etching Preparation of BiOI/Bi_2O_3 Heterostructures with Enhanced Photocatalytic Activities. *Catal. Commun.* **2011**, *12* (7), 660–664. https://doi.org/10.1016/J.CATCOM.2010.12.011.

(37) Wang, Z.; Huang, Y.; Ho, W.; Cao, J.; Shen, Z.; Lee, S. C. Fabrication of $Bi_2O_2CO_3$/g-C_3N_4 Heterojunctions for Efficiently Photocatalytic NO in Air Removal: In-Situ Self-Sacrificial Synthesis, Characterizations and Mechanistic Study. *Appl. Catal. B Environ.* **2016**, *199*, 123–133. https://doi.org/10.1016/j.apcatb.2016.06.027.

(38) Wang, C. C.; Zhang, Y. Q.; Zhu, T.; Wang, P.; Gao, S. J. Photocatalytic Degradation of Methylene Blue and Methyl Orange in a Zn(II)-Based Metal–Organic Framework. *Desalin. Water Treat.* **2016**, *57* (38), 17844–17851. https://doi.org/10.1080/19443994.2015.1088807.

Chapter 6

Fabrication of $Bi_3TaO_7/Ag/BiVO_4$ ternary photocatalyst for boosting pollutants degradation under visible light

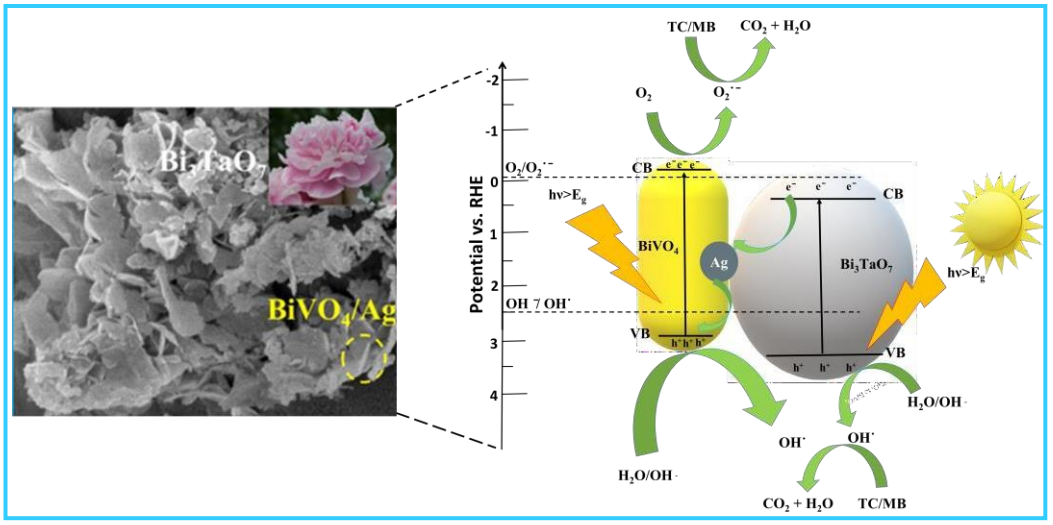

Highlights

- Z-scheme ternary $Bi_3TaO_7/Ag/BiVO_4$ nanoflowers fabricated via hydrothermal method.
- Ag was loaded on $BiVO_4$ via illumination under visible light.
- Ultrasonication technique employed to stack Ag-loaded $BiVO_4$ onto Bi_3TaO_7 clusters.
- Visible-light degradation of MB dye and antibiotic TC was investigated.
- ~99% and 92% photodegradation efficiency for MB and TC, respectively.

6.1 Introduction

Metabolic excretion and extensive industrial waste discharge and veterinary pharmaceutical contamination[1] have caused a severe menace to living beings.[2] The predominant issue with the existence of antibiotics in nature is their hidden physiological damage to the non-targeted species.[3] Moreover, industrial discharge directly with no pre-treatment has led to genotoxic, carcinogenic, and mutagenic consequences.[4] One such industrial dye is methylene blue (MB) having damaging effects on the human body.[5] Tetracycline (TC), a surfacing pollutant is widely used in veterinary and human medicine, andas a livestock growth influencer. Owing to its tenacious and resistant nature, TC is present in high concentrations in aqueous bodies leading to environmental catastrophes such as ecotoxicity and bacterial antibiotic resistance.[6] Therefore, it is essential to focus on issues concerning antibiotics and industrial dyes with efficient and less time-consuming methods to purify toxic water. Furthermore, the antibiotics pose difficulty in degradation owing to their highly stable aromatic rings, biotoxicity, variable intermediates, and solubility.[7]

Compared to conventional methods, photocatalysis via semiconductors has been acclaimed as a suitable technique by researchers, being a green, efficient, and sustainable technique to eradicate pollutants, particularly, pharmaceuticals from aqueous matrices.[6] It involves the removal of toxins to produce less harmful products.[8] Here the chemical reaction occurs by utilizing optical energy. Being a strong oxidizing agent, hydroxyl radicals induce a charge upon the pollutants and form radicals.[9] The as-synthesized radicals further form radicals such as H_2O_2 and superoxide radicals accountable for the photodegradation process.[9] But owing the responsive nature of photocatalysts towards UV radiation comprising merely 5% of the complete solar range poses difficulty.[10] The problem was solved by making them active in visible light via doping or forming heterojunctions between different semiconductors with unequal band gaps.[10] Thus, to harvest a huge spectrum of visible light,

work has been done to fabricate catalysts that are highly stable and efficient, called visible-light-catalyzed photocatalysts. Such photocatalysts are practical due to the large percentage of visibly-active light present in solar radiation.[10]

Recently, two-dimensional (2D) nanostructures are favored over their bulk counterparts owing to their greater surface area that gives additional reactive sites and lessens charge carrier mitigation distance from bulk to the surface.[6] Bismuth vanadate ($BiVO_4$)[11] has been viewed as a celebrated catalyst by researchers owing to a small bandgap (2.4 eV) and its visible-light activity. It has functioning significantly for water oxidation half-reactions. Its VB position is greater than $OH^-/OH^\bullet$ with the holes present on $BiVO_4$'s VB having enough power to produce hydroxyl radicals and achieve photocatalysis.[12] But $BiVO_4$ has insufficient electron transport and less electron mobility, limiting its applicability in photocatalysis.[12] To overcome this, the formation of heterojunction is suggested due to the fast reconciliation of the e^--h^+ pair in $BiVO_4$.[5] Bi_3TaO_7 has gained widespread attention as a semiconductor-based photocatalyst because of its photostability, non-toxic nature, and incomparable formation.[5] With a small bandgap (2.7-2.8 eV), Bi_3TaO_7 has visible-light activity.[13] Owing to the high band potential, Bi_3TaO_7 is suitable to decompose organic pollutants under strong alkaline and acidic conditions.[5] But Bi_3TaO_7 is unable to separate charge carriers efficiently, normally fabricated by high-temperature solid-state reaction leading to low photocatalytic activity.[13] Generally, individual catalysts face the limitation of charge carrier reconciliation and utilization of visible light. To overcome this barrier, heterostructure construction with optimum efficacy is suggested.[14]

Furthermore, numerous heterojunction formations such as type II, type I, and Z- schemes via coupling of various semiconductors have been seen as popular methods by researchers to enhance photocatalytic performance. Also, a 2D-2D nanocomposite benefits because of the enhanced contact area of the semiconductors for the promotion of charge carrier mitigation

and enhanced electron-hole separation.[6] In the heterostructure, the oxidation reaction befalls in photosystem I's VB and reduction befalls in photosystem II's CB, accommodating charge carrier partition. But owing to the lesser VB potential of photosystem I and greater CB potential of photosystem II, the charge carrier's redox properties get manipulated via partition. This can be overcome by designing a Z-type heterostructure that enhances both charge separation and electron-hole pair's redox properties and thus, acquiring photocatalytic achievement.[15] Although type-II heterostructures are prominent in catalytic action because of the reduction in e^{-}-h^{+} pair reconciliation,[5] they have the limitation of $OH^{\bullet}$ and $O_2^{\bullet -}$ production in such semiconductors.[15] Such an obstruction can also be subdued via a Z-type heterostructure by designing a semiconductor-conductor-semiconductor scheme.[5] It is established that the alignment of bands for $BiVO_4$ and Bi_3TaO_7 is appropriate for type-II heterostructure formation while Ag nanoparticles are the most suitable noble metals due to their electron transferability to form this trivia.[16] There is the vibration of electrons between the surface of positive and negative permittivity material owing to the metal's conductive property. The absorption capability of the photocatalyst gets facilitated via incident light, thus improving efficiency.[17]

Work has been done to fabricate such ternary heterojunctions with heightened activity. Ou *et al.*[12] designed a ternary composite of g-C_3N_4/Ag/$BiVO_4$ where deposition of Ag was done via illuminating on $BiVO_4$'s surface and here after covered Ag/$BiVO_4$'s surface via g-C_3N_4. Different composites were fabricated by varying mass ratios with 100% g-C_3N_4/Ag/$BiVO_4$ showcasing heightened efficacy for NO oxidation and water splitting purposes. Here, Ag worksas an electron mediator in the Z-type heterostructure enhancing the partition of charge carriers. Lin *et al.*[18] utilized the precipitation technique to design g-C_3N_4/Ag/$BiVO_4$ ternary composite. g-C_3N_4 wrapped leaf-like $BiVO_4$ with photo deposited Ag. A comparative study was carried out with 2wt% of Ag along with leaf-like $BiVO_4$ without

any g-C_3N_4 and on the other hand design of 2wt% g-C_3N_4/$BiVO_4$ was done with no Ag. The optimum performance was shown by the prepared ternary composite, when equated with g-C_3N_4, Ag/$BiVO_4$, $BiVO_4$, $BiVO_4$/g-C_3N_4. Le *et al.*[2] designed a 2D-2D heterostructure of C-sensitized $BiVO_4$/Bi_3TaO_7 via the hydrothermal method. Stacked nanosheets of $BiVO_4$ with C-dots were found to be present on the surface of stacked nanosheets of Bi_3TaO_7. Different w/w of Bi_3TaO_7 and $BiVO_4$ (such as 5:5, 8:2, 2:8) werefabricated, namely, VT-5, VT-8, VT-2. A comparison was made between pure Bi_3TaO_7, pure $BiVO_4$, $BiVO_4$/Bi_3TaO_7 (VT-5), and C-$BiVO_4$/Bi_3TaO_7 (3CVT-5) with the maximum efficiencyof 3CVT-5 (91.7%) tetracycline deterioration when visible light illumination was done for 120 min. This study presents a novel 2D-2D Bi_3TaO_7/Ag/$BiVO_4$ ternary composite for pollutant degradation, beneficial for charge separation and accommodating electron transfer. Also, a 2D- 2D heterostructure designed by coupling Bi_3TaO_7 and $BiVO_4$ with appropriately aligned band structures is unfavorable for pollutant degradation since the reduced redox potentials may not entirely perform pollutant oxidation. Therefore, an Ag-mediated electron shuttle between the 2D-2D heterostructure is suggested where Ag when coupled with the semiconductors forms a nanocomposite that could absorb in the longer wavelength of the visible spectrum and therefore, act as an excellent harvester and mediator. Hence, a ternary composite with enhanced pollutant degradation efficiency through the transference of electrons at $BiVO_4$'s CB and Bi_3TaO_7's VB with Ag asa mediator has been proposed.

The present chapter involves the construction of a 2D-2D carnation nanoflower-like Bi_3TaO_7/Ag/$BiVO_4$ ternary composite by the hydrothermal method via coupling of Bi_3TaO_7 nano-aggregates and $BiVO_4$/Ag nanocapsules. The as-prepared composite was utilized to degrade model pollutants, TC, and MB under visible light. Factors, such as catalyst concentration and solution pH were investigated. To scrutinize the degradation mechanism and stability of the composite, trapping analysis and reusability of the composite were

done. To affirm the catalyst's stability after the degradation activity, the XRD analysis was performed. COD studies were done to verify the degradation efficiency of the ternary composite. The novelty of the research lies in the synthesis of the ultrasonically-fabricated nanoflower-like ternary composite Bi_3TaO_7/Ag/$BiVO_4$ with different weight ratios for the deterioration of an antibiotic and a dye and its varied factors affecting degradation.

6.2 Experimental

This section includes the chemicals, materials, and methodologies used for the synthesis of the catalysts.

6.2.1 Chemicals and Materials

Tantalum chloride ($TaCl_5$), nitric acid (HNO_3), ammonium vanadate (NH_4VO_3), potassium hydroxide (KOH), ethanol (C_2H_5OH), methanol (CH_3OH), sodium dodecylbenzene sulphonate ($C_{18}H_{29}NaO_3S$), silver nitrate ($AgNO_3$), sodium hydroxide (NaOH), bismuth nitratepentahydrate ($Bi(NO_3)_3.5H_2O$) was procured from Thermo Fisher Scientific India Pvt. Ltd. and S. D. Fine-Chem. Limited, India. Merck and Bayer Crop Science Ltd., India supplied the pollutants used. Aqueous solutions were prepared using double distilled water.

6.2.2 Synthesis

This section consists of the synthesis methodologies of pure $BiVO_4$, pure Bi_3TaO_7, $BiVO_4$/Ag,and Bi_3TaO_7/Ag/$BiVO_4$ composite.

6.2.2.1 Synthesis of $BiVO_4$

$BiVO_4$ nanorods were synthesized using the simple hydrothermal process. Two different mixtures, a 5 mmol $Bi(NO_3)_3.5H_2O$ solution mixed in 4M HNO_3 (4 mL) and a 5 mmol NH_4VO_3 mixed in 2M NaOH (10 mL) solution were prepared. The prepared solutions were mixed with the addition of 0.25 g sodium dodecylbenzene sulphonate and further stirred for 30 min. The solution's pH was adjusted to neutral. A Teflon-lined vessel (50 mL) was used to transfer the obtained solution and heated (200°C) for 1.5 h at the rate of 10°C/min. The solution was washed thrice and put in an oven to dry at 80°C for 12 h. A "Tuscany yellow" product was obtained.[5]

6.2.2.2 Synthesis of Bi_3TaO_7

2 mmol $TaCl_5$ (1.0745 g) and $Bi(NO_3)_3.5H_2O$ (2.4255 g) were mixed in ethanol (10 mL) with continuous mixing for a period of 60 min. The $TaCl_5$ solution was poured drop-wise into the Bi $(NO_3)_3.5H_2O$ solution and stirred for another 30 min. About 7M KOH solution was poured slowly into this solution and set the pH to 10 and further stirred for 60 min. In an autoclave (50 mL), the prepared solution was poured and heated at 220°C for 24 h. Ethanol and distilled water were used to wash the solution (thrice). The obtained mixture was finally placed in an oven for a time period of 12 h at 60°C. A "greyish" product was obtained.

6.2.2.3 Synthesis of $BiVO_4$/Ag

To synthesize Ag deposited $BiVO_4$, ultrasonication of $BiVO_4$ nanorods (0.5 g) was done in 70 mL methanol. 13.3 mg of $AgNO_3$ was included and mixed continuously and then put in a photo-reactor cell. It was illuminated for 2 h using visible light (65W CFL lamp,

Phillips, 125 W/m^2, k> 400 nm). A bumblebee-yellow product was obtained after the centrifugation and drying at 80°C for 12 h.[5]

Bi_3TaO_7/Ag/$BiVO_4$ (BABV) composite was synthesized by ultrasonically mixing Bi_3TaO_7 and $BiVO_4$/Ag in a stoichiometric weight ratio of 1:1 and dissolved in 50 mL methanol with stirring for 10 h. It was named as 1:1 Bi_3TaO_7/Ag/$BiVO_4$ composite (Bi_3TaO_7:$BiVO_4$/Ag as 1:1). It was poured into a beaker and kept in an oven at 80°C until the solution is evaporated. Calcination of the product was done at 450°C for a period of 2 h at the rate of 10°C/min. Different stoichiometric weight ratios such as 1:3, and 3:1 was formed by varying the weight ratios of Bi_3TaO_7 and $BiVO_4$/Ag and named 1:3 Bi_3TaO_7/Ag/$BiVO_4$, and 3:1 Bi_3TaO_7/Ag/$BiVO_4$, respectively. The obtained products for 1:1, 3:1, and 1:3 was "shade","grey", and "Versaille" in color, respectively (**Scheme 6.1**).

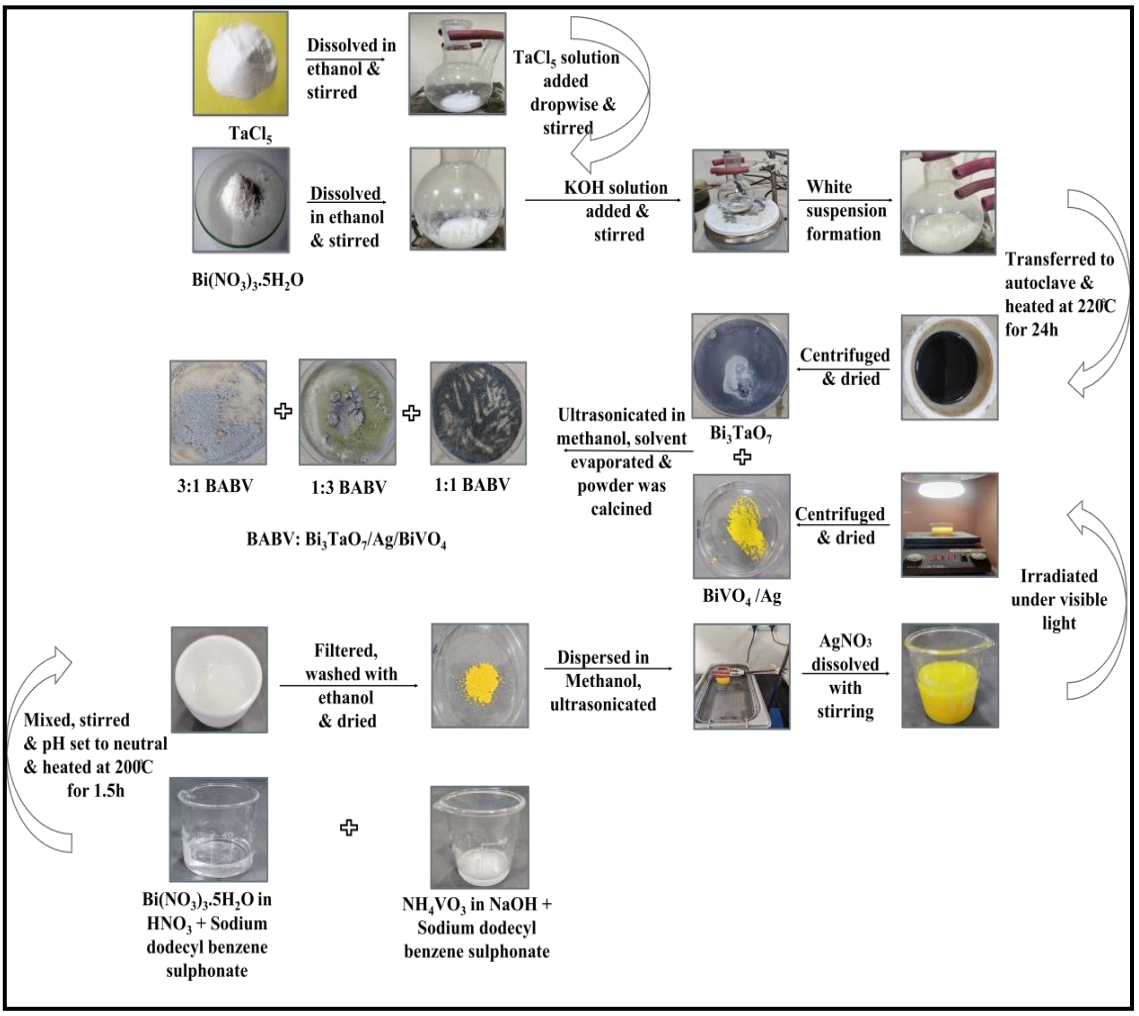

Scheme 6.1. Synthesis of ternary $Bi_3TaO_7/Ag/BiVO_4$ composite.

6.2.3 Characterization

BET N_2 adsorption-desorption isotherm was performed at 77.3 K to scrutinize the surface area and pore size distribution using a surface area analyzer Microtrac Belsorp Mini-II (Bel, Japan, Inc). Before the analysis, pre-treatment was done at 100°C for 6 h. Pore size distribution curves were investigated via Barrett-Joyner-Halenda (BJH) method. X-ray diffraction analysis determined the crystallinity of the photocatalyst using a PANanalytical X-ray diffractometer with Cu-Kα radiation at 45kV and scan range 10-90°. The surface morphologies and microstructure of the composite were studied via field emission scanning

electron microscopy (FESEM SU8180, Hitachi, Tokyo, Japan) with Oxford INCTA energy dispersive spectrometer (EDS) and transmission electron microscopy (TEM, JEM-2100F), respectively. By using a PHI- 5000 VersaProbe III system containing a monochromatic Al KαX-ray source (1486.7 eV),X-ray photoelectron spectroscopy (XPS) was performed to determine the elemental structure of the composite. UV-Vis Diffusion Reflectance Spectroscopy (DRS) in diffuse absorbance mode was carried out by a Hitachi-3900H spectrophotometer (Shimadzu, Japan). Photoluminescence (PL) spectra were obtained using a fluorescence spectrometer (F-4500, Hitachi, Japan). A cyber scan pH 1100 (Eutech, Singapore) was employed to adjust and measurethe pH. For the kinetic analysis of pollutant degradation, a UV-Vis spectrophotometer (Shimadzu, UV-2600) was employed.

6.2.4 Photocatalytic Process

The photocatalytic study was done by degrading a model dye, MB, and a colorless antibiotic, TC. The solutions were evaluated by placing them in a photoreactor. The photocatalysts were put in 5 ppm of MB/TC solution (15 mL) and mixed for 60 min and 120 min in dark and visible light (65W CFL lamp, Phillips, 125 W/m^2, k> 400 nm), for the adsorption-desorption equilibrium to establish amongst the catalysts and MB/TC. The full photodegradation occurred with 99.85% for MB and 92.94% for TC. The degradation efficiency for TC and MB was recorded via a UV-Vis spectrophotometer (λ_{max} at 357 and 664 nm, respectively). As per Lambert Beer's law,[19] the concentration depends on the absorbance, and thus, the percentage degradation (**Eq. 6.1**) is:

$$\% D = \{(A_o-A_t)/A_o\} \times 100 = \{(C_o-C_t)/C_o\} \times 100, \quad (6.1)$$

Where A_o and A_t signify the absorbance of dye/pesticide at a time '0' and 't', respectively whereas C_o and C_t signify the concentration of dye/pesticide at a time '0' and 't', respectively.

Chemical Oxygen Demand (COD) studies were executed to assert the photodegradation process of Bi_3TaO_7/Ag/$BiVO_4$ composite. About 2mg of 0.06 g/L Bi_3TaO_7/Ag/$BiVO_4$ composite was included in 15 mL of MB/TC solution and irradiated (120 min). The titrimetric method was utilized to confirm the COD value and was calculated after the catalytic treatment time 't' and at an initial time '0'. The COD depletion is found via the following **Eq. 6.2**[20]:

$$\text{COD} = \frac{(a-b)\times N\times 8000\times Dilution\ Factor}{Volume\ Of\ Sample} \quad (6.2)$$

Where a = Ferrous ammonium sulphate (FAS) used for the titration of the blank sample (mL); N = Normality of FAS (0.1 N); b = Ferrous ammonium sulphate (FAS) used for the titration of the sample (mL).

6.3 Results and Discussion

6.3.1 Characterization Analysis

6.3.1.1 X-ray Diffraction Studies

XRD analysis was done to compute the planes of 1:1 Bi_3TaO_7/Ag/$BiVO_4$, 1:3 Bi_3TaO_7/Ag/$BiVO_4$, and 3:1 Bi_3TaO_7/Ag/$BiVO_4$, $BiVO_4$/Ag, Bi_3TaO_7, and $BiVO_4$. **Fig. 6.1** illustrate the XRD pattern for pure $BiVO_4$ at 30.5°, 28.89°, 34.91°, 40.04°, 42.3°, 45.91°, 47.07°, 50.18°, 53.2°, 56.01°, 59.02° and 60° relating to (0,0,4), (1,1,2), (0,2,0), (1,2,1), (1,0,5), (1,2,3), (0,2,4), (2,2,0), (1,1,6), (2,1,5), (3,1,2), (2,2,4) planes respectively. This indicated that $BiVO_4$ exists in the monoclinic phase (JCPDS No. 83-1699).[15] The XRD peaks of pure Bi_3TaO_7 at 28°,55.5°, 32.7°, 48.5°, and 57.5° relating to (1,1,1), (3,1,1), (2,0,0), (2,0,2), and (2,2,2) planes respectively, indicated Bi_3TaO_7 to be in cubic phase (JCPDS No. 44-0202).[21] Lastly, the XRDpattern of Bi_3TaO_7/Ag/$BiVO_4$ exhibited peaks of Bi_3TaO_7 and $BiVO_4$, suggesting the creation of heterojunction. The other peaks present in Bi_3TaO_7 and Bi_3TaO_7/Ag/$BiVO_4$

were probably due to the formation of impurities of $Bi_7Ta_3O_{18}$.[22] No peaks of Ag were observed, and it is probably owed to the small amount of Ag or rather the small size of Ag.[16] It was observed that the peak intensities for 1:1 Bi_3TaO_7/Ag/$BiVO_4$, 1:3 Bi_3TaO_7/Ag/$BiVO_4$, and 3:1 Bi_3TaO_7/Ag/$BiVO_4$ varied.

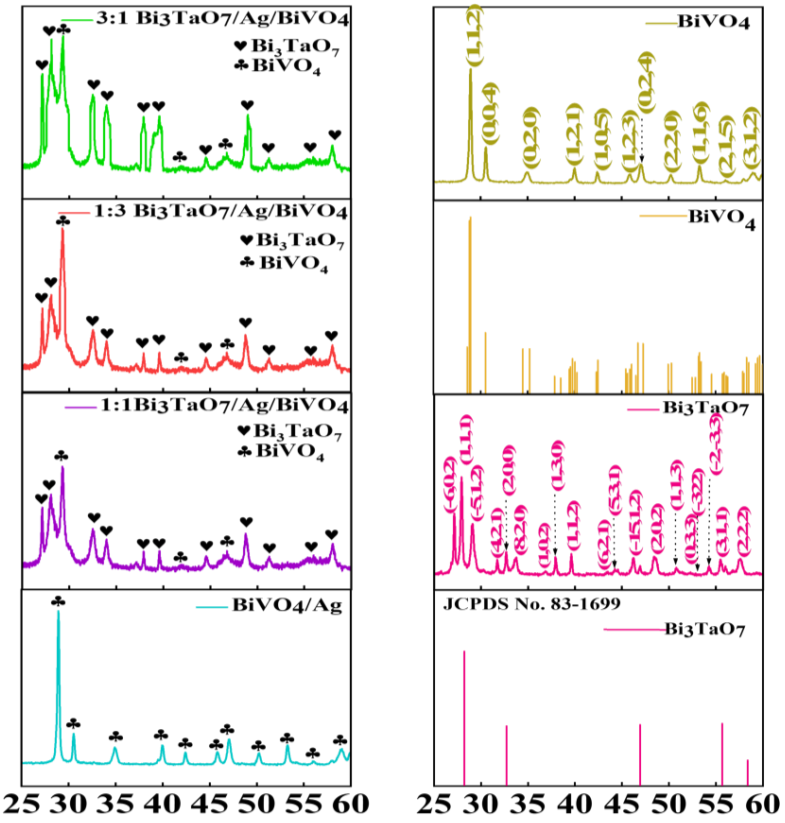

Fig. 6.1 XRD patterns of the prepared catalysts.

Table 6.1. Total pore volume, mesopore size, and the surface area of the prepared photocatalysts.

Photocatalyst	**Surface area (m^2/g)**	**Total pore volume (cm^3/g)**	**Mesopore size (nm)**
Bi_3TaO_7	26	0.22	33.69
$BiVO_4$	9	0.04	14.70
$BiVO_4$/Ag	11	0.10	46.28

1:1 Bi_3TaO_7/Ag/$BiVO_4$	88	0.45	25.60
1:3 Bi_3TaO_7/Ag/$BiVO_4$	62	0.41	23.38
3:1 Bi_3TaO_7/Ag/$BiVO_4$	76	0.43	22.28

6.3.1.2 Nitrogen Adsorption/Desorption Studies

Fig. 6.2 (a) displays N_2 adsorption-desorption studies illustrating the type-IV isotherm, demonstrating the catalyst's mesoporous nature.[5] As shown in **Fig. 6.2 (a)**, Bi_3TaO_7, 1:1 Bi_3TaO_7/Ag/$BiVO_4$, 1:3 Bi_3TaO_7/Ag/$BiVO_4$, 3:1 Bi_3TaO_7/Ag/$BiVO_4$ displayed H3 hysteresis loop, while $BiVO_4$ and $BiVO_4$/Ag depicted H1 type hysteresis loop with sharpened desorption-adsorption curves,[21] confirming the structure and constancy of the photocatalysts. For the mesoporous nature, the BJH method demonstrated the photocatalysts' pore size (**Fig. 6.2 (b)**).Mean pore volume, surface area, and mean pore diameter were investigated utilizing the BET method. For Bi_3TaO_7, $BiVO_4$, 1:1 Bi_3TaO_7/Ag/$BiVO_4$, 1:3 Bi_3TaO_7/Ag/$BiVO_4$, and 3:1 Bi_3TaO_7/Ag/$BiVO_4$, the areas were estimated to be 26, 9, 11, 88, 62, and 76 m^2/g, respectively.From pure Bi_3TaO_7 and pure $BiVO_4$ to 1:1 Bi_3TaO_7/Ag/$BiVO_4$, the surface area is enhanced with the maximum total pore volume (**Table 6.1**).

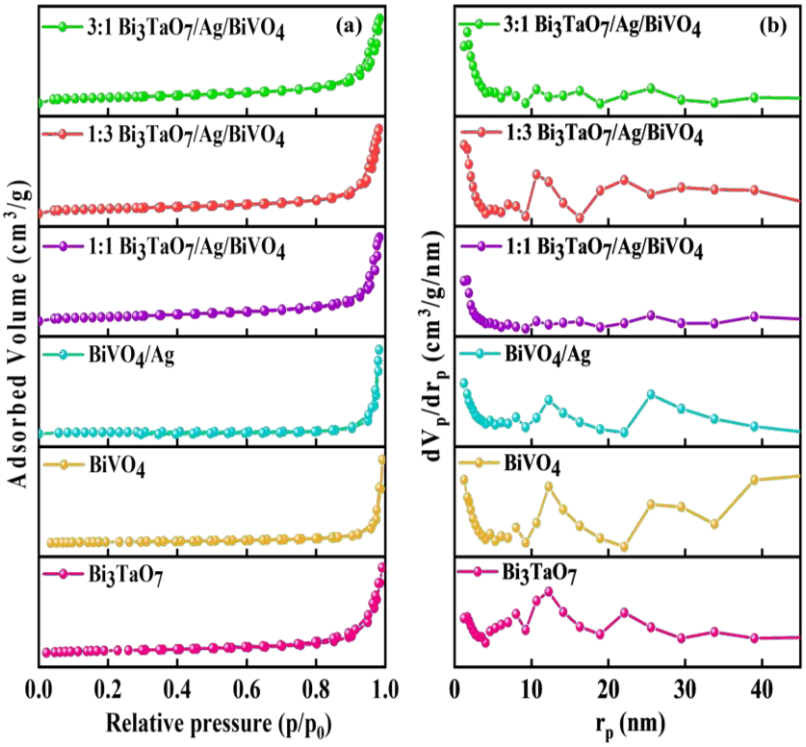

Fig. 6.2. (a) N_2 adsorption-desorption isotherms, and (c) pore size distribution curves for the prepared catalysts.

6.3.1.3 XPS Studies

The XPS method was employed to scrutinize the elemental valence state in 1:1 Bi_3TaO_7/Ag/$BiVO_4$. **Fig. 6.3 (a)** depicting the survey curve showed the existence of V, Ta, Bi, Ag, and O. For pure Bi_3TaO_7 and pure $BiVO_4$,[23] peaks are present at 165.9 eV, 158.8 eV relating to Bi $4f_{5/2}$, Bi $4f_{7/2}$, respectively. The Bi_3TaO_7/Ag/$BiVO_4$ composite depicts a Bi 4f spectrum with two peaks at 164.7 eV, 159.4 eV corresponding to Bi $4f_{5/2}$, Bi $4f_{7/2}$ (**Fig. 6.3 (b)**), respectively, suggesting Bi^{3+} ion's occurrence in Bi_3TaO_7/Ag/$BiVO_4$, depicting shift in binding energies. For V, in pure $BiVO_4$ displayed peaks at 518.5 eV and 526 eV relating to V $2p_{3/2}$ and V $2p_{1/2}$ peaks while V present in Bi_3TaO_7/Ag/$BiVO_4$ (in +5 valence state) displayed peaks for V $2p_{1/2}$, V $2p_{3/2}$ at 523.9 eV, 516.8 eV, respectively (**Fig. 6.3 (c)**).[5] This depicts a blue shift. The two peaks of Ta in Bi_3TaO_7 are present at 29 eV and 26 eV, respectively relating to Ta $4f_{7/2}$, Ta $4f_{5/2}$[13] while the Ta $4f_{7/2}$, Ta $4f_{5/2}$ in the composite

correspond to 25.9 eV, 28.4 eV, depicting the presence of Ta (+5 valence state) in $Bi_3TaO_7/Ag/BiVO_4$ composite (**Fig. 6.3 (d)**).[2] This depicts a blue shift. The O1s spectra for Bi_3TaO_7 and $BiVO_4$ display peaks at 529.5eV, 531.4 eV corresponding to Bi-O (lattice O), O-H on the surface, and H_2O adsorbed, respectively,[4] while $Bi_3TaO_7/Ag/BiVO_4$ shows peaks at 529.6 eV, 532.6 eV for lattice O, adsorbed O, respectively (**Fig. 6.3 (e)**),[5] illustrating a redshift. The peaks relating to Ag $3d_{3/2}$, Ag $3d_{5/2}$ at a binding energy of 374.3 eV, 368.3 eV, respectively suggest the occurrence of 0 valence state of Ag in $Bi_3TaO_7/Ag/BiVO_4$ (**Fig. 6.3 (f)**).[18] The shift in binding energies is depicted in **Table 6.2**. The binding energies shift from pureBi_3TaO_7 and pure $BiVO_4$ to $Bi_3TaO_7/Ag/BiVO_4$ heterostructure owing to the surface charge density alteration by the embodiment of a different material with varied Fermi levels (E_f). It leads to direct charge conversion. The mobility of electrons then occurs via upper E_f towards the lower E_f. Therefore, the mobility occurs from Bi_3TaO_7 to $BiVO_4$ in $Bi_3TaO_7/Ag/BiVO_4$ heterostructure, and a reduction in density of electrons in Bi_3TaO_7 and a boost in $BiVO_4$.[15]

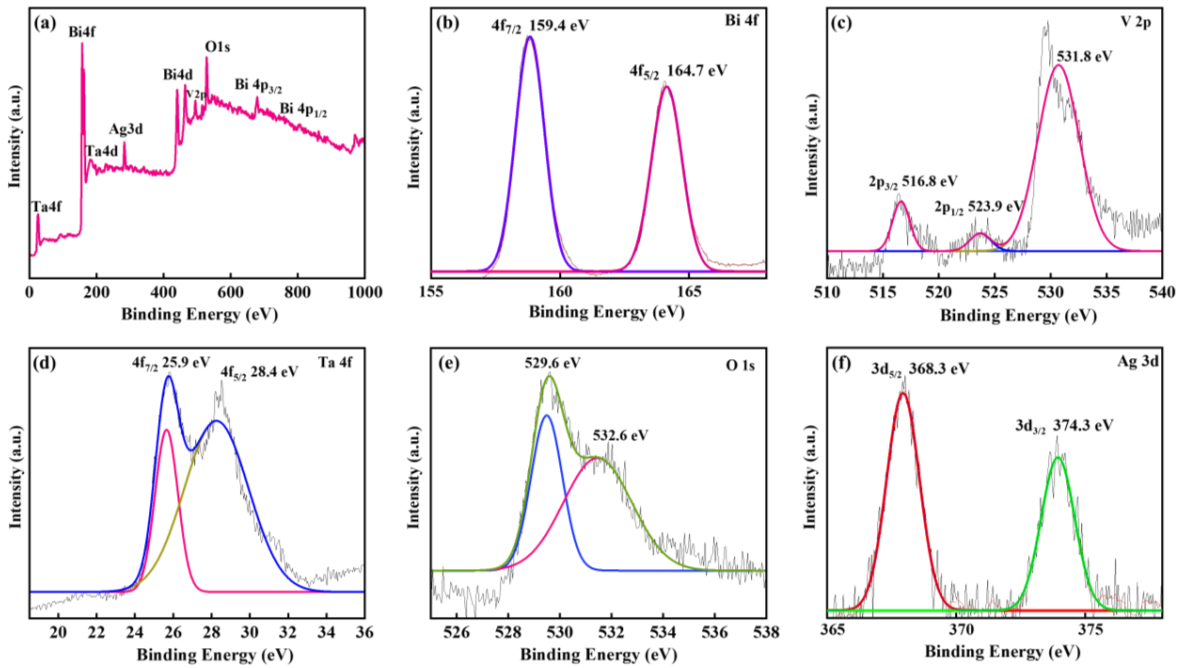

Fig. 6.3. (a) XPS spectrum, and deconvoluted peaks of (b) Bi, (c) V, (d) Ta, (e) O, (f) Ag of 1:1 $Bi_3TaO_7/Ag/BiVO_4$ ternary composite.

Table 6.2. Shift in Binding Energies for Elements of 1:1 $Bi_3TaO_7/Ag/BiVO_4$ composite.

Element	Binding Energy	
Bi	$4f_{7/2}$ at 159.4 eV	$4f_{5/2}$ at 164.7 eV
V	$2p_{1/2}$ at 523.9 eV	$2p_{3/2}$ at 516.8 eV
Ta	$4f_{7/2}$ at 25.9 eV	$4f_{5/2}$ at 28.4 eV
O	529.6 eV (lattice O)	532.6 eV (adsorbed O)
Ag	$3d_{3/2}$ at 374.3 eV	$3d_{5/2}$ at 368.3 eV

6.3.1.4 Elemental Mapping and EDS Studies

Fig. 6.4 (b-e) illustrates the existence of Ta, O, Bi, Ag, and V by performing elemental mapping of the ternary composite. **Fig. 6.4 (a)** illustrates the EDS analysis to investigate $Bi_3TaO_7/Ag/BiVO_4$'s elemental structure. The composition of elements was scrutinized via EDS studies of 1:1 composite. The weight % of Bi, Ta, V, O, and Ag are 48.49%, 37.06%, 3.01%, 11.1%, and 0.34%, respectively.

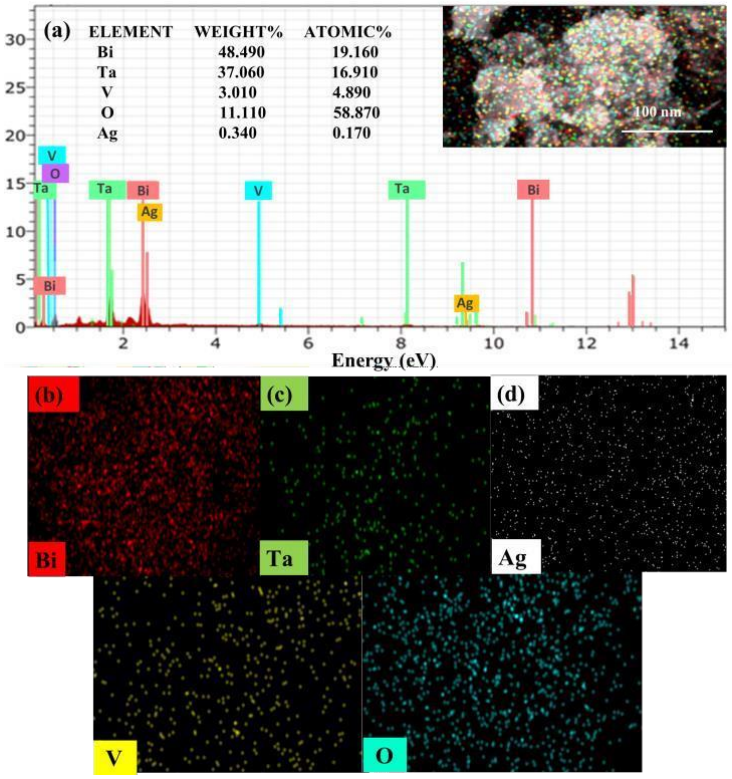

Fig. 6.4. (a) EDS spectrum, elemental mapping images for (b) Bi, (c) Ta, (d) Ag, (e) V, and (f) O of 1:1 ternary composite $Bi_3TaO_7/Ag/BiVO_4$.

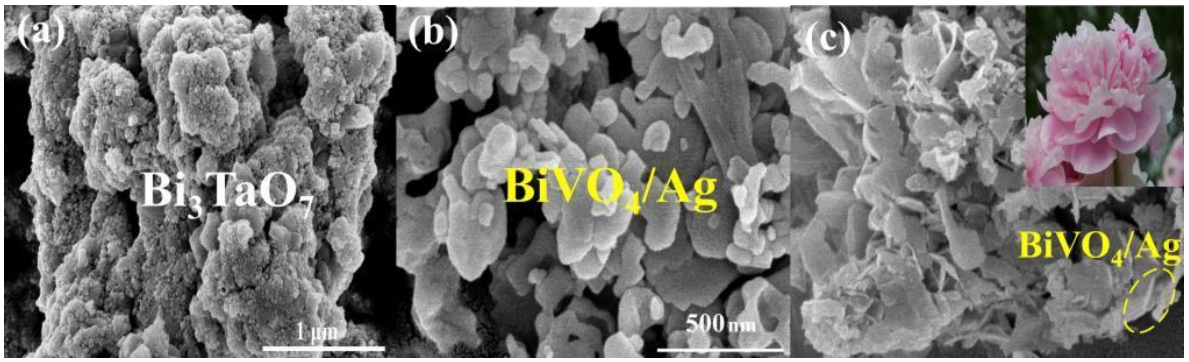

Fig. 6.5. FESEM illustrations of (a) Bi_3TaO_7, (b) $BiVO_4$/Ag, (c) 1:1 Bi_3TaO_7/Ag/$BiVO_4$.

6.3.1.5 FESEM and HRTEM Studies

FESEM studies were used for the surface study of Bi_3TaO_7, $BiVO_4$/Ag, and Bi_3TaO_7/Ag/$BiVO_4$. **Fig. 6.5 (a)** illustrates the aggregated-like molecules for Bi_3TaO_7. **Fig. 6.5 (a)** depicts the capsule-like nanostructures for $BiVO_4$ with deposition of Ag nanospheres. **Fig. 6.5 (c)** demonstrates carnation flower-like nanostructure for Bi_3TaO_7/Ag/$BiVO_4$ ternary composite with capsule-like $BiVO_4$/Ag, present on the nanoflower. To further elaborate on thestructural study of the nanocomposite, HR-TEM analysis was carried out. **Fig. 6.6 (a-c)** illustrates the presence of $BiVO_4$/Ag (dark grey portion) along with Bi_3TaO_7 (light grey portion). The planes for Bi_3TaO_7, $BiVO_4$, Ag were found to be (2,0,0), (0,4,0), (1,1,1) at 0.27 nm, 0.29 nm, and 0.24 nm, respectively.

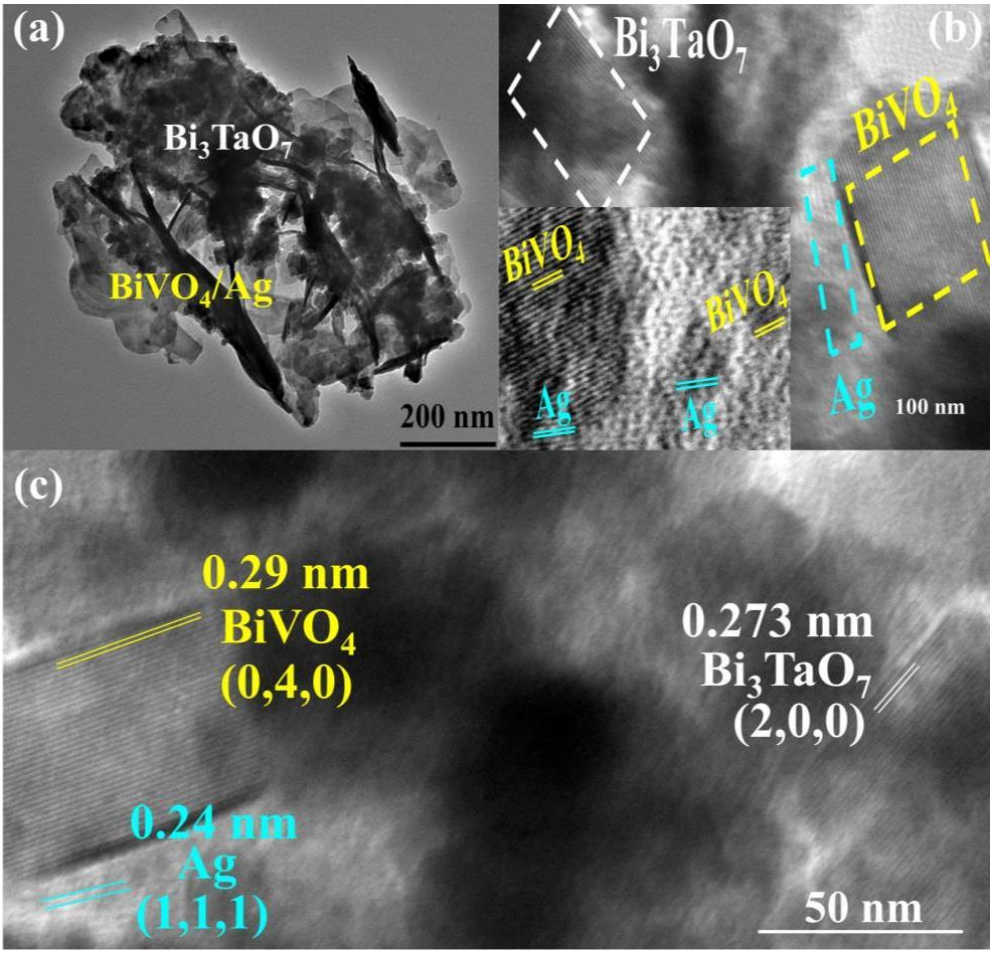

Fig. 6.6. HRTEM images of 1:1 Bi_3TaO_7/Ag/$BiVO_4$.

6.3.1.6 Optical Studies

The electron-hole pair reconciliation has a dominant task in the photodegradation process. The charge carrier reconciliation tendency is low at low photoluminescence (PL) intensity, and thus, sufficient charge partition.[24] Therefore, the charge separation was scrutinized by recording PL spectra when excited at 315 nm wavelength (**Fig. 6.7 (a)**). Bi_3TaO_7/Ag/$BiVO_4$'s PL curve was lower than that of Bi_3TaO_7, $BiVO_4$, and $BiVO_4$/Ag, indicating better charge separation with lesser recombination capacity resulting in high photocatalytic performance.[5]

To compute the bandgap of Bi_3TaO_7/Ag/$BiVO_4$, UV-Visible diffuse reflectance spectroscopy was done. For $BiVO_4$, Bi_3TaO_7, $BiVO_4$/Ag, and Bi_3TaO_7/Ag/$BiVO_4$

composites, the absorption edges were formulated as 600 nm, 490 nm, 620 nm, and 690 nm, respectively (**Fig. 6.7 (b)**). It was observed that the incorporation of Bi_3TaO_7 in $BiVO_4$/Ag brings a shift in the longer wavelength of the visible region.[2] To calculate the bandgap energy, tauc's plot was used. The equation is as follows (**Eq. (6.3)**):

$$(\alpha h\nu)^{1/2}=A(h\nu-E_g)n/2 \quad (6.3)$$

Where h denotes Planck constant, ν denotes light frequency, α denotes absorption coefficient, n = optical transition type of semiconductors, A = proportionality constant, and E_g donates bandgap energy. The bandgaps for Bi_3TaO_7, $BiVO_4$, $BiVO_4$/Ag, and Bi_3TaO_7/Ag/$BiVO_4$ were estimated as 2.86 eV, 2.9 eV, 2.45 eV, 2.18 eV, respectively (**Fig. 6.7 (c)**). The results signify that, by introducing Ag in $BiVO_4$, diminishing of the bandgap occurs. Further, with the introduction of Bi_3TaO_7 in $BiVO_4$/Ag, alteration of the electronic structure occurs.[2]

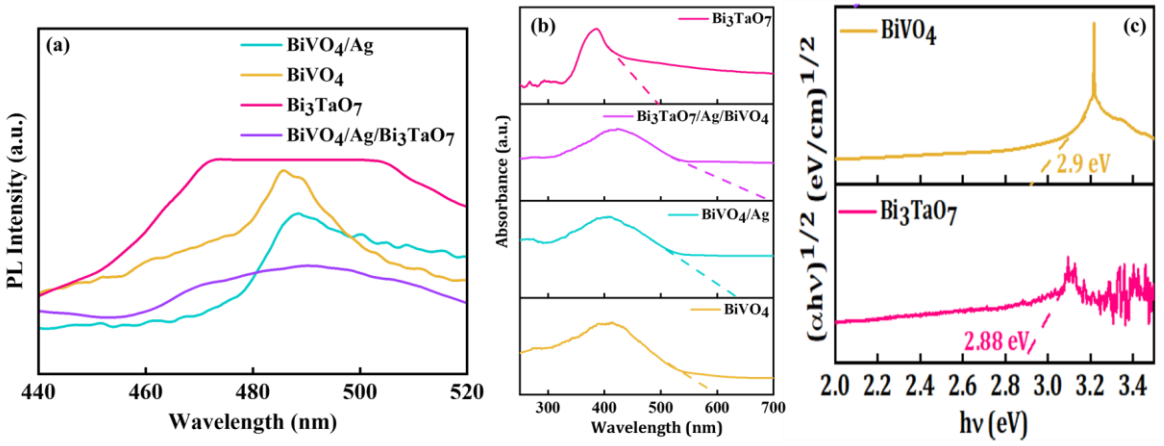

Fig. 6.7. (a) Photoluminescence spectra, (b) UV Visible diffuse reflectance spectra, and (c) Tauc's plot of the photocatalysts.

6.3.2 Methylene Blue and Tetracycline Photocatalytic Activity

Bi_3TaO_7/Ag/$BiVO_4$'s photocatalytic tendency was scrutinized by pollutant deterioration MB[25] with a concentration of 5 mg/L and TC[26] with a concentration of 600 mg/L. The solutions put in the dark for a period of 60 min facilitated the adsorption-desorption

equilibrium. As such no reduction in the degradation efficacy was found with no catalyst **(Fig. 6.8 (a and c))** (1.09% for TC and 2.29% for MB), depicting the importance of Bi_3TaO_7/Ag/$BiVO_4$ ternary photocatalyst in the activity. The rate constants were calculated,[27] via **Eq. 6.4**:

$$\ln (C/C_0) = -kt \qquad (6.4)$$

Where C_0 denotes the concentration at time = '0', k denotes the rate constant, and C denotes the concentration at a time 't'.

Fig. 6.8 (a) and Fig. 6.8 (c) illustrate the catalytic efficiency for TC and MB with and without photocatalysts. It was hardly 2.29% ($k = 3.386 \times 10^{-4}\ min^{-1}$) for MB (**Fig. 6.8 (b)**), 1.09% ($k = 1.472 \times 10^{-4}\ min^{-1}$) for TC (**Fig. 6.8 (d)**). 1:1 Bi_3TaO_7/Ag/$BiVO_4$ composite showed optimum efficiencies for MB with 99.85% degradation ($k = 0.05439\ min^{-1}$), TC with 92.94% degradation ($k = 0.02128\ min^{-1}$) as equated with Bi_3TaO_7, $BiVO_4$, $BiVO_4$/Ag, 1:3 composite, and 3:1 composite. The rate constants for Bi_3TaO_7, $BiVO_4$, $BiVO_4$/Ag, 1:1 composite, 1:3 composite, and 3:1 composite is given in **Table 6.3**. Thus, the 1:1 composite exhibited phenomenal degradation efficiency for pollutants irradiated using visible light.

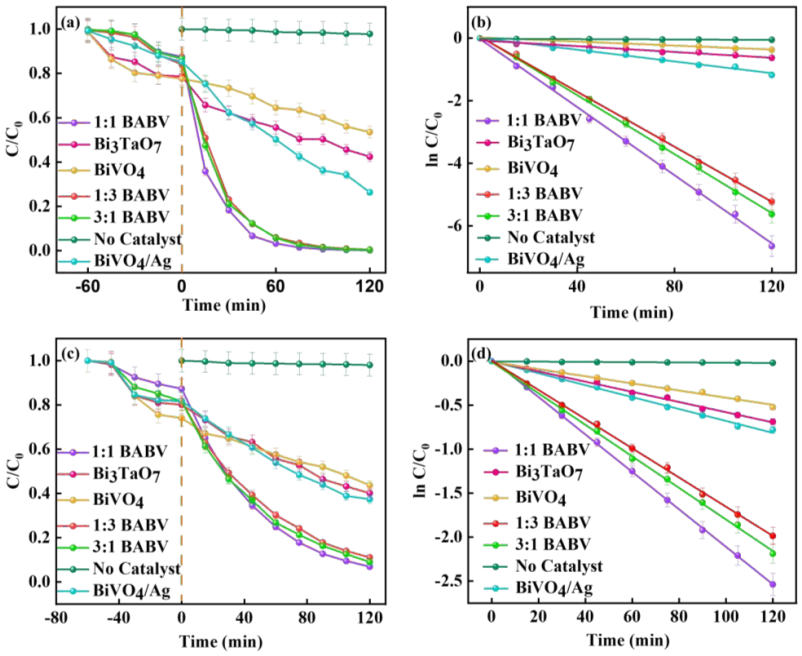

Fig. 6.8. Kinetic photocatalytic degradation of (a, b) MB and (c, d) TC.

Table 6.3. Rate constants for the degradation of MB and TC.

Sample	Rate Constants		% Degradation	
	TC (min^{-1})	MB (min^{-1})	TC	MB
Bi_3TaO_7	0.00578	0.00436	53.01	48.67
$BiVO_4$	0.00406	0.00374	49.63	35.26
$BiVO_4$/Ag	0.00677	0.00938	64	68.23
1:1 Bi_3TaO_7/Ag/$BiVO_4$	0.02128	0.05439	92.94	99.85
1:3 Bi_3TaO_7/Ag/$BiVO_4$	0.01793	0.0436	86.83	99.4
3:1 Bi_3TaO_7/Ag/$BiVO_4$	0.01659	0.04713	89.25	99.61

6.3.2.1 Catalyst Concentration Studies

The catalyst concentration studies were conducted to analyze the role of catalysts in the activity. Catalyst concentrations were changed (0.06 to 0.4 g/L) to investigate the photodegradation efficacy using a 1:1 Bi_3TaO_7/Ag/$BiVO_4$ composite (**Fig. 6.9 (a)**). The efficiency was maximum for TC and MB at a concentration of 0.06 g/L. The solution's opaqueness and light's scattering could be attributing factors.[28] This occurs because of dye adsorption initially, then any furthermore incorporation of the catalyst will furnish no results on the photodegradation process due to the lesser sites available.[29]

6.3.2.2 pH Studies

The point of zero charges (pzc) was calculated on Bi_3TaO_7/Ag/$BiVO_4$'s surface. It was found as ~pH 4 (pH_{pzc}) (**Fig. 6.9 (b)**). This was suggested to Bi_3TaO_7/Ag/$BiVO_4$'s negatively charged surface if $pH>pH_{pzc}$ and positively charged if $pH<pH_{pzc}$.[30] The pH was varied from pH 1 to 12 to evaluate the consequence of pH in the degradation activity

via 0.06 g/L $Bi_3TaO_7/Ag/BiVO_4$ (**Fig. 6.9 (c)**). The maintenance of pH was done by pouring dilute HCl and NaOH solution.[31] It was observed that being a cationic dye, MB displays maximum efficiency at pH 9 (99.82%), owing to the electrostatic interaction between the dye and $Bi_3TaO_7/Ag/BiVO_4$ ternary composite's negative surface[32] while anionic TC displays the highest efficiency at pH 3 (92.12%), owing to the electrostatic interaction between TC and $Bi_3TaO_7/Ag/BiVO_4$ ternary composite's positive surface.[33]

6.3.2.3 Reusability Studies

The $Bi_3TaO_7/Ag/BiVO_4$ ternary composite segregation could be performed using centrifugation once the photodegradation process is done. This segregation is quite easy owing to the temporary MB adsorption. The efficiency of the photocatalyst was examined after washing the acquired sample was done thrice using distilled water, centrifuged, and finally dried and reused.[3] It was seen that not much reduction in efficiency was recorded (90.99% for MB and 88.84% for TC) after 4 continuous cycles (**Fig. 6.9 (d)**). XRD validated the intactness of the ternary composite (**Fig. 6.9 (e)**) after the 4 cycles of degradation. Hence, a ternary composite with high stability and reusability was achieved.

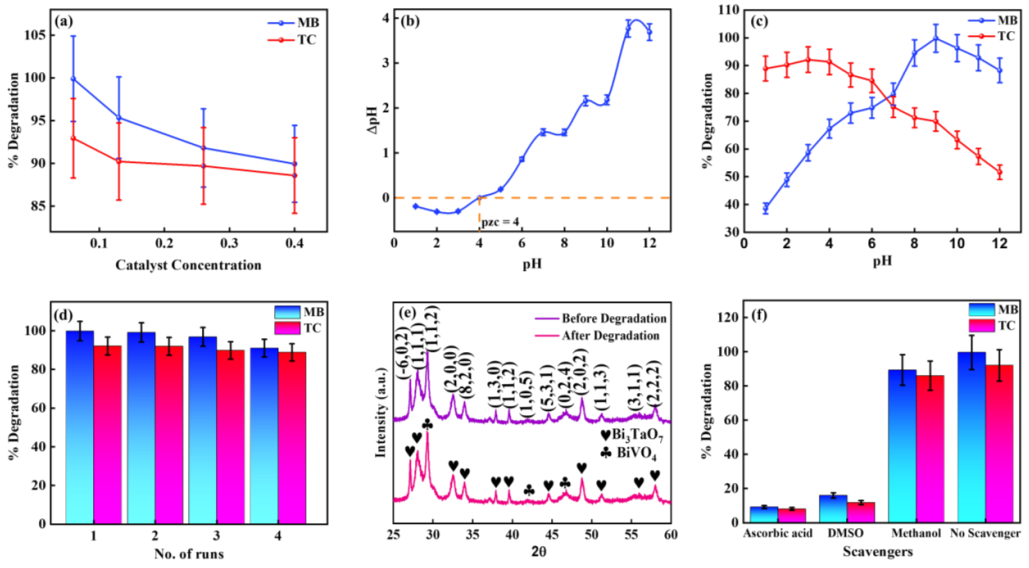

Fig. 6.9. Catalytic process: (a) catalyst concentration studies, (b) pH_{PZC} calculation, (c) pH variation, (d) reusability, (e) XRD patterns of the 1:1 $Bi_3TaO_7/Ag/BiVO_4$ before and after photodegradation, (f) scavenging mechanism using 1:1 $Bi_3TaO_7/Ag/BiVO_4$.

6.3.2.4 Plausible Mechanism

The scavenging mechanism investigated the part of the radical species in the degradation activity with ascorbic acid corresponding to superoxide radical ($O_2^{\bullet-}$), methanol relating to quenching holes (h^+), DMSO relating to hydroxide radical ($^{\bullet}OH$) (**Fig. 6.7 (f)**).[34] The 1:1 $Bi_3TaO_7/Ag/BiVO_4$ ternary sample was used as an instrument for the analysis. The scavenger, which inhibits the degradation activity, and its radical species are accountable for photocatalytic activity. In this process, equal molars of methanol, DMSO, and ascorbic acid were included in these solutions. Notably, the MB efficacy for ascorbic acid was 9.14%, methanol was 89.3%, and DMSO was 15.97% indicating the part played by $^{\bullet}OH$ and $O_2^{\bullet-}$ in the activity. The degradation efficiencies of TC for methanol, ascorbic acid, and DMSO were 85.97%, 8.09%, and 11.81%, respectively, indicating the part played by $^{\bullet}OH$ and $O_2^{\bullet-}$ in the photodegradation of TC.

The photocatalyst's band potentials act prominently in understanding the charge carrier partition. For Bi_3TaO_7 and $BiVO_4$, the VB position and the CB position were formulated via the **Eqns. (6.5) and (6.6)**[35]:

$$E_{CB} = X - E_c - 0.5E_g \quad (6.5)$$

$$E_{VB} = E_{CB} + E_g \quad (6.6)$$

Where X denotes the semiconductor's absolute electronegativity, E_{CB} denotes the conduction band's position, E_{VB} denotes the valence band's position, E_c denotes hydrogen's free-electron energy (~ 4.5 eV), and E_g denotes the bandgap of semiconductors. The electronegativity

value for $BiVO_4$ was 5.65 eV[34] and for Bi_3TaO_7 it was 6.27 eV.[21] As stated by DRS analysis, the bandgap of $BiVO_4$ and Bi_3TaO_7 is 2.9 eV, and 2.86 eV, respectively. Therefore, using **Eq. (6.5)and (6.6)**, the CB, and VB positions for $BiVO_4$ are -0.3 eV, and 2.6 eV, respectively, and the CB and VB potentials for Bi_3TaO_7 are 0.34 eV, 3.2 eV, respectively.

When forming a heterojunction of Bi_3TaO_7 and $BiVO_4$, h^+ and e^- move from Bi_3TaO_7 to $BiVO_4$ in terms of levels of band potential. Thus, h^+ and e^- combine rapidly and give a low photocatalytic performance. Therefore, a ternary heterojunction between Bi_3TaO_7 to $BiVO_4$ is devised using Ag, which provides spatial segregation of e^--h^+ pairs and therefore reduces the recombination rate. For Bi_3TaO_7, the VB potential is greater than the position of $OH^-/^{\bullet}OH$, indicating the part played by h^+ in hydroxyl anion's oxidation to synthesize $^{\bullet}OH$. The transference of electrons from Bi_3TaO_7 to $BiVO_4$ synthesized $O_2^{\bullet-}$ using Ag as an electron mediator.[36] Thus, a Z-scheme mechanism is proposed for pollutant degradation using Bi_3TaO_7/Ag/$BiVO_4$ ternary composite (**Scheme 6.2**). In the ternary heterostructure, Ag acts as a good electron acceptor and can quickly behave as a mediator for e^- transference from $Bi_3TaO_7$and $BiVO_4$ and thus enhancing carrier charge separation and thereby, improving photocatalytic performance. Upon illumination by visible light, Bi_3TaO_7 and $BiVO_4$ get excited (**Eq. 6.7 and6.8**). The e^- present on the CB of Bi_3TaO_7 gets transferred to $BiVO_4$'s CB via Ag and oxidizes O_2 to form $O_2^{\bullet-}$ (**Eq. 6.9**) owing to its greater negative potential i.e., -0.3 eV than $O_2/O_2^{\bullet-}$´s redox potential i.e. -0.28 V *vs.* NHE., which eventually decomposes the pollutants (MB/TC) to synthesize lesser toxic pollutants such as CO_2 and H_2O (**Eq. 6.10**). Similarly, the holes present on the VB of Bi_3TaO_7 and $BiVO_4$ synthesize $^{\bullet}OH$ radicals from OH^- due to the greater VB position of Bi_3TaO_7 and $BiVO_4$ than $^{\bullet}OH/H_2O$ (**Eq. 6.11**). The $^{\bullet}OH$ radicals thus produced decompose MB/TC to form CO_2 and H_2O (**Eq. 6.12**).[2]

$$BiVO_4 + h\nu \longrightarrow BiVO_4 (h^+ + e^-) \quad (6.7)$$

$$Bi_3TaO_7 + h\nu \longrightarrow Bi_3TaO_7 (h^+ + e^-) \quad (6.8)$$

$$BiVO_4\ (e^-) + O_2 \longrightarrow BiVO_4 + O_2^{\cdot -} \quad (6.9)$$

$$MB/TC + O_2^{\cdot -} \longrightarrow CO_2 + H_2O \quad (6.10)$$

$$BiVO_4(h^+)/Bi_3TaO_7(h^+) + H_2O \longrightarrow BiVO_4/Bi_3TaO_7 + OH^{\cdot} + H^+ \quad (6.11)$$

$$MB/TC + OH^{\cdot} \longrightarrow CO_2 + H_2O \quad (6.12)$$

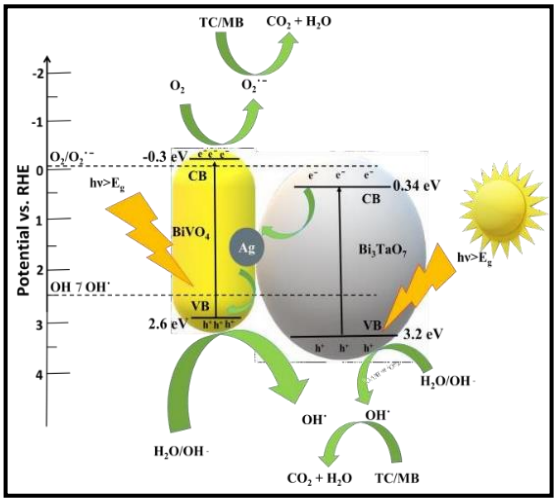

Scheme 6.2. Z-scheme mechanism for visible-light-induced pollutants degradation by carnation flower-like Bi_3TaO_7/Ag/$BiVO_4$ composite.

The Z-scheme mechanism in the ternary composite facilitates[37] both e^-h^+ partition and their redox properties, thereby, enhancing photocatalytic performance.[12]

A collative study of literature was done with different photocatalysts for pollutant removal (**Table 6.4**), affirming the usefulness of the fabricated ternary catalyst for pollutant degradation.

Table 6.4. Comparison of varied photocatalysts for pollutant degradation.

Catalyst	**Pollutant**	**Conc. (g/L)**	**Time(min)**	**Light source**	**Light intensity**	***k*** **(min$^-$**	**Effici -ency**	**Refere nce**

					(mW/cm^2)	^{1})	(%)	
g-C_3N_4/Ag/$BiVO_4$	RhB	0.02	40	visible	-	-	100	18
g-C_3N_4/Pt/$BiVO_4$	MB	0.02	130	visible	100	0.119	87.6	15
C-Bi_3TaO_7/$BiVO_4$	TC	0.5	120	visible	-	-	91.7	2
Bi_3TaO_7	TC	0.5	120	visible	-	-	74.9	23
Bi_3TaO_7/Bi_2O_3	TC	0.0005	210	visible	-	-	90	21
g-C_3N_4/Ag/$BiVO_4$	TC	0.02	240	visible	-	-	90.7	18

6.3.2.4 COD Studies

The COD measurements of TC and MB were done with a 1:1 Bi_3TaO_7/Ag/$BiVO_4$ ternary sample (0.06 g/L). The visible-light irradiation was performed for 120 min for pollutants. The COD, without any pre-treatment for MB, was found to be 1200 mg/L, and for TC, it was found to be 1800 mg/L, suggesting the high quantity of organic content present in TC and MB. The COD after photodegradation was 100 mg/L (MB; 91.66%), and 200

mg/L (TC; 83.33%), suggesting the high efficiency of 1:1 Bi_3TaO_7/Ag/$BiVO_4$ composite in treating pollutants with huge organic contents (**Fig. 6.10**).

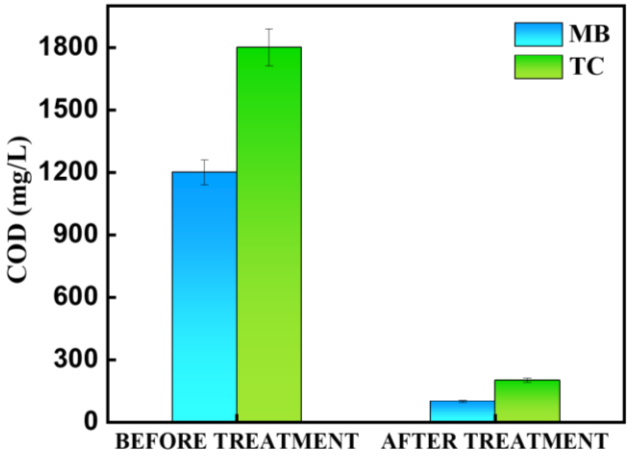

Fig. 6.10. COD analysis of MB and TC by 1:1 Bi_3TaO_7/Ag/$BiVO_4$ ternary composite.

6.3.3 Conclusion

The chapter involves the designing of a novel ternary nanocomposite Bi_3TaO_7/Ag/$BiVO_4$ with different weight ratios of Bi_3TaO_7 and $BiVO_4$/Ag using the hydrothermal method, employed for antibiotic and dye removal. The surface studies of the composites displayed a carnation flower-like ternary composite with capsule-like nanostructures of $BiVO_4$/Ag. The pzc and pH analysis depicted the highest removal for TC and MB in the acidic range and basic range, respectively owing to the ionic interactions amongst the ternary composite with the anionic TC and cationic MB. The feed concentration analysis of the catalyst disclosed a reduction in efficacy due to the decline in surface active sites, once the pollutants have been completely adsorbed, whereas the composite's stability was affirmedby the reusability studies. COD analysis showed the composite's efficiency in removing organic pollutants. The trapping experiments explored the scavenging mechanism and showed the part of $^{\bullet}OH$ and $O_2^{\bullet-}$ for photodegradation. Enough e^--h^+ partition, enhanced area, and reduced e^--h^+ reconciliation might have led to exceptional performance. Moreover,

the performance was owed to Ag NPs' role in the conduction bands of the semiconductors andthe electrons. Additionally, Ag NPs cause augmented visible-light absorption through surface plasmon resonance. Thus, the morphological, electronic, and optical properties construed that the Z-type ternary composite displayed high efficacy in antibiotic and dye removal.

References

(1) Garg, A.; Basu, S.; Shetti, N. P.; Reddy, K. R. 2D Materials and Its Heterostructured Photocatalysts: Synthesis, Properties, Functionalization and Applications in Environmental Remediation. *J. Environ. Chem. Eng.* **2021**, 106408. https://doi.org/10.1016/J.JECE.2021.106408.

(2) Le, S.; Li, W.; Wang, Y.; Jiang, X.; Yang, X.; Wang, X. Carbon Dots Sensitized 2D-2D Heterojunction of $BiVO_4/Bi_3TaO_7$ for Visible Light Photocatalytic Removal towards the Broad-Spectrum Antibiotics. *J. Hazard. Mater.* **2019**, *376*, 1. https://doi.org/10.1016/j.jhazmat.2019.04.088.

(3) Dashairya, L.; Sharma, S.; Rathi, A.; Saha, P.; Basu, S. Solar-Light-Driven Photocatalysis by Sb_2S_3/Carbon Based Composites towards Degradation of Noxious Organic Pollutants. *Mater. Chem. Phys.* **2021**, *273*, 125120. https://doi.org/10.1016/j.matchemphys.2021.125120.

(4) Nagar, A.; Basu, S. Fabrication of 3D Porous Peony Flower-like β-Bi_2O_3/BiOCl Heterostructure for Synergistically Boosting the Visible-Light-Driven Degradation of Organic Pollutants. *Environ. Technol. Innov.* **2021**, *24*, 101956. https://doi.org/10.1016/j.eti.2021.101956.

(5) Nagar, A.; Basu, S. Ternary g-C_3N_4/Ag/$BiVO_4$ Nanocomposite: Fabrication and Implementation to Remove Organic Pollutants. *Environ. Technol. Innov.* **2021**, *23*,

101646. https://doi.org/10.1016/j.eti.2021.101646.

(6) Majumdar, A.; Ghosh, U.; Pal, A. Novel 2D/2D g-C_3N_4/Bi_4NbO_8Cl Nano-Composite for the Enhanced Photocatalytic Degradation of Oxytetracycline under Visible LED Light Irradiation. *J. Colloid Interface Sci.* **2021**, *584*, 320. https://doi.org/10.1016/j.jcis.2020.09.101.

(7) Mirzaei, A.; Yerushalmi, L.; Chen, Z.; Haghighat, F. Photocatalytic Degradation of Sulfamethoxazole by Hierarchical Magnetic ZnO@g-C_3N_4: RSM Optimization, Kinetic Study, Reaction Pathway and Toxicity Evaluation. *J. Hazard. Mater.* **2018**, *359*, 516. https://doi.org/10.1016/j.jhazmat.2018.07.077.

(8) Kundu, A.; Sharma, S.; Basu, S. Modulated BiOCl Nanoplates with Porous g-C_3N_4 Nanosheets for Photocatalytic Degradation of Color/Colorless Pollutants in Natural Sunlight. *J. Phys. Chem. Solids* **2021**, *154*, 110064. https://doi.org/10.1016/j.jpcs.2021.110064.

(9) Ajmal, A.; Majeed, I.; Malik, R. N.; Idriss, H.; Nadeem, M. A. Principles and Mechanisms of Photocatalytic Dye Degradation on TiO_2 Based Photocatalysts: A Comparative Overview. *RSC Adv.* **2014**, *4*, 37003. https://doi.org/10.1039/c4ra06658h.

(10) Mushtaq, F.; Guerrero, M.; Sakar, M. S.; Hoop, M.; Lindo, A. M.; Sort, J.; Chen, X.; Nelson, B. J.; Pellicer, E.; Pané, S. Magnetically Driven Bi_2O_3/BiOCl-Based Hybrid Microrobots for Photocatalytic Water Remediation. *J. Mater. Chem. A* **2015**, *3*, 23670. https://doi.org/10.1039/c5ta05825b.

(11) Zhao, W.; Hu, C. H.; Chen, R.; Lv, F. Z.; Zhong, Y.; Zhou, H. Y. Synthesis and Photocatalytic Activity of Ag - Doped $BiVO_4$. *Adv. Mater. Res.* **2013**, *734*, 2204. https://doi.org/10.4028/www.scientific.net/AMR.734-737.2204.

(12) Ou, M.; Wan, S.; Zhong, Q.; Zhang, S.; Song, Y.; Guo, L.; Cai, W.; Xu, Y. Hierarchical Z-Scheme Photocatalyst of g-C_3N_4@Ag/$BiVO_4$ (040) with Enhanced Visible-Light-

Induced Photocatalytic Oxidation Performance. *Appl. Catal. B Environ.* **2018**, *221*, 97. https://doi.org/10.1016/j.apcatb.2017.09.005.

(13) Abrahams, I.; Krok, F.; Struzik, M.; Dygas, J. R. A Defect Structure and Electrical Conductivity in Bi_3TaO_7. *Solid State Ionics* **2008**, *179*, 1013. https://doi.org/10.1016/j.ssi.2008.02.002.

(14) Sharma, S.; Basu, S. Fabrication of Centimeter-Sized Sb_2S_3/SiO_2 Monolithic Mimosa Pudica Nanoflowers for Remediation of Hazardous Pollutants from IndustrialWastewater. *J. Clean. Prod.* **2021**, *280*, 124525. https://doi.org/10.1016/j.jclepro.2020.124525.

(15) Si, Y. H.; Chen, Y. M.; Zhong, Q.; Xia, Y.; Zeng, X. R.; Zhou, J.; Li, Y, Y. g-C_3N_4/Pt/$BiVO_4$ Nanocomposites for Highly Efficient Visible-Light Photocatalytic Removal of Contaminants and Hydrogen Generation. *Nanotechnology* **2020**, 31, 125706. https://doi.org/10.1008/1361-6528/ab5bc5.

(16) Zeng, X.; Lan, S.; Lo, I. M. C. Rapid Disinfection of E. Coli by a Ternary $BiVO_4$ /Ag/g-C_3N_4 Composite under Visible Light: Photocatalytic Mechanism and Performance Investigation in Authentic Sewage. *Environ. Sci. Nano* **2019**, *6*, 610. https://doi.org/10.1039/c8en01283k.

(17) Zheng, Z.; Huang, B.; Qin, X.; Zhang, X.; Dai, Y.; Whangbo, M. H. Facile in Situ Synthesis of Visible-Light Plasmonic Photocatalysts M@TiO2 (M = Au, Pt, Ag) and Evaluation of Their Photocatalytic Oxidation of Benzene to Phenol. *J. Mater. Chem.* **2011**, *21*, 9079. https://doi.org/10.1039/c1jm10983a.

(18) Lin, X.; Xu, D.; Xi, Y.; Zhao, R.; Zhao, L.; Song, M.; Zhai, H.; Che, G.; Chang, L. Construction of Leaf-like g-C_3N_4/Ag/$BiVO_4$ Nanoheterostructures with Enhanced Photocatalysis Performance under Visible-Light Irradiation. *Colloids Surfaces A: Physicochem. Eng. Asp.* **2017**, *513*, 117. https://doi.org/10.1016/j.colsurfa.2016.11.040.

(19) Chai, S. Y.; Kim, Y. J.; Jung, M. H.; Chakraborty, A. K.; Jung, D.; Lee, W. I.

Heterojunctioned BiOCl/Bi_2O_3, a New Visible Light Photocatalyst. *J. Catal.* **2009**, *262*,144. https://doi.org/10.1016/j.jcat.2008.12.020.

(20) Saleh, B.; Kayi, H. Prediction of Chemical Oxygen Demand from the Chemical Composition of Wastewater by Artificial Neural Networks. *J. Phys.* **2020**, *1818*, 012035. https://doi.org/ 10.1088/1742-6596/1818/1/012035.

(21) Zhang, J.; Qu, L.; Wu, Y.; Ma, Y.; Chai, Z.; Wang, X. Journal of Solid State Chemistry Fabrication of Visible-Light-Driven Bi_2O_3-Bi_3TaO_7 Nanocomposite for Tetracycline Degradation with Enhanced Photocatalytic Efficiency. *J. Solid State Chem.* **2019**, *278*, 120894. https://doi.org/10.1016/j.jssc.2019.120894.

(22) Firman, K.; Tan, K. B.; Khaw, C. C.; Zainal, Z.; Tan, Y. P.; Chen, S. K. Doping Mechanisms and Electrical Properties of Bismuth Tantalate Fluorites. *J. Mater. Sci.* **2017**, *52*, 10106. https://doi.org/10.1007/s10853-017-1216-1.

(23) Luo, B.; Chen, M.; Zhang, Z.; Hong, Y.; Lv, T.; Shi, W. Characterization and Photocatalytic Activity of Bi_3TaO_7 Prepared by Hydrothermal Method. *J. Solid State Chem.* **2017**, *256*, 203. https://doi.org/10.1016/j.jssc.2017.08.016.

(24) Nguyen, V. H.; Bui, Q. T. P.; Vo, D. V. N.; Lim, K. T.; Bach, L. G.; Do, S. T.; Van Nguyen, T.; Doan, V. D.; Nguyen, T. D.; Nguyen, T. D. Effective Photocatalytic Activity of Sulfate-Modified $BiVO_4$ for the Decomposition of Methylene Blue under LED Visible Light. *Materials* **2019**, *12*, 2681. https://doi.org/10.3390/ma12172681.

(25) Monga, D.; Basu, S. Enhanced Photocatalytic Degradation of Industrial Dye by g-C_3N_4/TiO_2 Nanocomposite: Role of Shape of TiO2. *Adv. Powder Technol.* **2019**, *30*, 1089. https://doi.org/10.1016/j.apt.2019.03.004.

(26) Kong, S.; An, Z.; Zhang, W.; An, Z.; Yuan, M.; Chen, D. Preparation of Hollow Flower-like Microspherical β-Bi_2O_3/BiOCl Heterojunction and High Photocatalytic Property for Tetracycline Hydrochloride Degradation. *Nanomaterials* **2020**, *10*, 1.

https://doi.org/10.3390/nano10010057.

(27) Sharma, S.; Basu, S. Highly Reusable Visible Light Active Hierarchical Porous WO_3/SiO_2 Monolith in Centimeter Length Scale for Enhanced Photocatalytic Degradation of Toxic Pollutants. *Sep. Purif. Technol.* **2020**, *231*, 115916. https://doi.org/10.1016/j.seppur.2019.115916.

(28) Sharma, S.; Basu, S. Visible-Light-Driven Efficient Photocatalytic Abatement of Recalcitrant Pollutants by Centimeter-Length MoO_3/SiO_2 Monoliths with Long Service Life. Appl. Mater. Today 2021, 23, 101033. https://doi.org/10.1016/j.apmt.2021.101033.

(29) Monga, D.; Ilager, D.; Shetti, N. P.; Basu, S.; Aminabhavi, T. M. 2D/2D Heterojunctionof MoS_2/g-C_3N_4 Nanoflowers for Enhanced Visible-Light-Driven Photocatalytic and Electrochemical Degradation of Organic Pollutants. *J. Environ.Manage.* **2020**, *274*, 111208. https://doi.org/10.1016/j.jenvman.2020.111208.

(30) Ambrosio, F.; Wiktor, J.; Pasquarello, A. PH-Dependent Surface Chemistry from First Principles: Application to the $BiVO_4$ (010)-Water Interface. *ACS Appl. Mater. Interfaces* **2018**, *10*, 10011. https://doi.org/10.1021/acsami.7b16545.

(31) Rathi, A.; Basu, S.; Barman, S. Adsorptive Removal of Fipronil from Its AqueousSolution by Modified Zeolite HZSM-5: Equilibrium, Kinetic and ThermodynamicStudy. *J. Mol. Liq.* **2019**, *283*, 867. https://doi.org/10.1016/j.molliq.2019.02.140.

(32) Zhu, B.; Xia, P.; Ho, W.; Yu, J. Isoelectric Point and Adsorption Activity of Porousg- C_3N_4. *Appl. Surf. Sci.* **2015**, *344*, 188. https://doi.org/10.1016/j.apsusc.2015.03.086.

(33) Han, W.; Wu, T.; Wu, Q. Fabrication of WO_3/Bi_2MoO_6 Heterostructures with Efficient and Highly Selective Photocatalytic Degradation of Tetracycline Hydrochloride. *J. Colloid Interface Sci.* **2021**, *602*, 544. https://doi.org/10.1016/j.jcis.2021.05.128.

(34) Wang, D.; Yu, X.; Feng, Q.; Lin, X.; Huang, Y.; Huang, X.; Li, X.; Chen, K.; Zhao, B.; Zhang,

Z. In-Situ Growth of β-Bi_2O_3 Nanosheets on g-C_3N_4 to Construct Direct Z-Scheme Heterojunction with Enhanced Photocatalytic Activities. *J. Alloys Compd.* **2021**, *859*, 157795. https://doi.org/10.1016/j.jallcom.2020.157795.

(35) Li, Y.; Wang, J.; Yao, H.; Dang, L.; Li, Z. Chemical Etching Preparation of BiOI/Bi_2O_3 Heterostructures with Enhanced Photocatalytic Activities. *Catal. Commun.* **2011**, *12*, 660. https://doi.org/10.1016/J.CATCOM.2010.12.011.

(36) Sturini, M.; Speltini, A.; Maraschi, F.; Pretali, L.; Profumo, A.; Fasani, E.; Albini, A.; Migliavacca, R.; Nucleo, E. Photodegradation of Fluoroquinolones in Surface Water and Antimicrobial Activity of the Photoproducts. *Water Res.* **2012**, *46*, 5575. https://doi.org/10.1016/j.watres.2012.07.043.

(37) Wang, Y.; Shang, X.; Shen, J.; Zhang, Z.; Wang, D.; Lin, J.; Wu, J. C. S.; Fu, X.; Wang, X.; Li, C. Direct and Indirect Z-Scheme Heterostructure-Coupled Photosystem Enabling Cooperation of CO_2 Reduction and H_2O Oxidation. *Nat. Commun.* **2020**, *11*, 1. https://doi.org/10.1038/s41467-020-16742-3.

Conclusion and Future Perspectives

It was observed that the composite Bi_3TaO_7/Ag/$BiVO_4$ displayed maximum methylene blue degradation efficiency amongst all the prepared photocatalysts. This couldbe attributed to the maximum surface area of the ternary composite as compared to the other photocatalysts with greater number of active sites and thus, higher photocatalytic performance.

Table 7.1. Comparative table for bismuth-based nanocomposites for MB removal.

Photocatalyst	**% Degradation (MB)**
β-Bi_2O_3/BiOCl	~93%
β-Bi_2O_3/g-C_3N_4	~97%
g-C_3N_4/Ag/$BiVO_4$	~94%
Bi_3TaO_7/BiOCl	~99%
Bi_3TaO_7/Ag/$BiVO_4$	~100%

The future opportunities for the work lie in the purification of wastewater. The research can be extended to the treatment of colorless and obstinate pollutants such as insecticides and pharmaceuticals. The photocatalytic scope of the photocatalysts can further be explored in CO_2 reduction and water splitting processes owing to its facile synthesis, low production cost, and mass production feasibility.

List of Publications

1. Nagar, A.; Basu, S. Ternary g-C_3N_4/Ag/$BiVO_4$ nanocomposite: Fabrication and implementation to remove organic pollutants**.** *Environ. Technol. Innov.* **2021**, *23*. 101646. https://doi.org/10.1016/j.eti.2021.101646. (IF 7.758)
2. Nagar, A.; Basu, S. Fabrication of 3D porous peony flower-like β-Bi_2O_3/BiOCl heterostructure for synergistically boosting the visible-light-driven degradation of organic pollutants. *Environ. Technol. Innov.* **2021**, *24*, 101956. https://doi.org/10.1016/j.eti.2021.101956. (IF 7.758)
3. Nagar, A.; Basu, S. Deciphering the Role of β-phase Bi_2O_3 Nanorods incorporated ong-C_3N_4 Nanosheets for Efficient Pollutant Removal**.** *Journal of Physics and Chemistryof Solids* **2022**, *164*, 110625. https://doi.org/10.1016/j.jpcs.2022.110625. (IF 4.383)
4. Nagar, A.; Basu, S. Novel tablet-like Bi_3TaO_7/BiOCl 2D-2D heterostructure with heightened charge segregation for Visible-light-driven photocatalytic pollutants degradation**.** *Journal of Solid State Chemistry* **2022**, *312*, 123249. https://doi.org/10.1016/j.jssc.2022.123249. (IF 3.656)
5. Nagar, A.; Basu, S. Fabrication of carnation flower-like Bi_3TaO_7/Ag/$BiVO_4$ ternary photocatalyst for boosting pollutants degradation under visible light**.** *Journal of Solid State Chemistry* **2022**, *313*, 123294. https://doi.org/10.1016/j.jssc.2022.123294. (IF 3.656)

Conferences and Workshops

1. National Virtual Conference on Recent Advances in Analytical Techniques – 2020 heldon August 16th-17th, 2020.
2. International e-seminar on Solar Activities in 21st century held on September 8th, 2020.
3. International Webinar on Advanced Functional Materials held on August 18th-21st, 2020.
4. Webinar series Practicing Chemdraw, Origin and Mendeley tools in research held on August 8th-10th, 2020.